

ALMA MATER STUDIORUM
UNIVERSITÀ DI BOLOGNA

DOTTORATO DI RICERCA
IN ASTROFISICA

Ciclo 34

Settore Concorsuale: 02/C1 - ASTRONOMIA, ASTROFISICA, FISICA DELLA
TERRA E DEI PIANETI

Settore Scientifico Disciplinare: FIS/05 - ASTRONOMIA E ASTROFISICA

**NON-STANDARD SIGNATURES FROM
COSMIC MICROWAVE BACKGROUND
POLARISATION**

Presentata da:
Dr. Matteo Billi

Coordinatore Dottorato:
Prof. Andrea Miglio

Supervisore:
Dr. Alessandro Gruppuso

Co-supervisore:
Prof. Lauro Moscardini

Esame Finale anno 2022

*Ai miei genitori, ai miei nonni e
a Valentina.*

4 Ottobre 2014
Ci guadagniamo il colore del grano.

Abstract

In this Thesis we focus on non-standard signatures from CMB polarisation, which might hint at the existence of new phenomena beyond the standard models for Cosmology (Λ CDM) and Particle physics. With the Planck ESA mission, CMB temperature anisotropies have been observed at the cosmic variance limit, but polarisation remains to be further investigated. CMB polarisation data are important not only because they contribute to provide tighter constraints of cosmological parameters but also because they allow the investigation of physical processes that would be precluded if just the CMB temperature maps were considered. We take polarisation data into account to assess the statistical significance of the anomalies currently observed only in the CMB temperature map and to constrain the Cosmic Birefringence (CB) effect, which is expected in parity-violating extensions of the standard electromagnetism.

We propose a new one-dimensional estimator for the lack of power anomaly capable of taking both temperature and polarisation into account jointly. By employing this estimator on Planck 2015 low- ℓ data, we find that the probability that a random Λ CDM realisation is statistically accepted decreases by a factor of two when the polarisation is taken into account. Moreover, we forecast that for future experiments, such as the LiteBIRD satellite, the contribution coming from the polarisation can increase by of factor 6.

With the aim of studying the power spectrum of the CB effect we develop and perform two different and complementary methods. In the first one using the "localisation" of the so-called D -estimators, a class of harmonic estimators for the isotropic birefringence, we build maps of the birefringence angle, evaluating the CB spectrum on angular scales larger than ~ 7 degrees. In the second approach we derive a novel class of linear and quadratic harmonic-based estimators which are able to directly evaluate the power spectrum of the CB from the EE, BB and EB observed angular power spectra of the CMB anisotropies. By employing these two methodologies on Planck 2018 Release (PR3) we provide new constraints on the CB spectrum with Planck data.

The measure of CMB polarisation represents a technological challenge,

since the polarised signal is much fainter than the signal in temperature and to make accurate estimates in polarisation, one has to keep an exquisite control of the systematic effects. In order to investigate the impact of spurious signal in forthcoming CMB polarisation experiments, we study the interplay between half-wave plates (HWP) non-idealities and the beams. We extend the capabilities of the publicly available `beamconv` code to produce the first time-domain simulations that include both HWP non-idealities and realistic full-sky beam convolution. Our analysis suggests that certain HWP configurations, depending on the complexity of Galactic foregrounds and the beam models, significantly impacts the B-mode reconstruction fidelity and could limit the capabilities of next-generation CMB experiments. We provide also a first study of the impact of non-ideal HWPs on CB, both isotropic and anisotropic.

Contents

1	Executive summary	1
2	Cosmic Microwave Background	11
2.1	Standard Cosmological Model	11
2.1.1	Friedmann Equations	12
2.1.2	Inflationary Paradigm	15
2.1.3	Inflation and cosmological perturbations	19
2.2	Introduction to CMB	20
2.2.1	CMB Black Body Spectrum	21
2.2.2	CMB temperature anisotropies	23
2.3	CMB polarisation	28
2.3.1	Thomson Scattering	28
2.3.2	Polarisation E and B modes	31
2.3.3	Observations	33
3	CMB anomalies: lack of power anomaly	37
3.1	Introduction	38
3.2	A new one-dimensional joint estimator	39
3.2.1	Optimised estimator	42
3.3	Dataset and simulations	44
3.4	Results of the analyses	49
3.4.1	Results for P	49
3.4.2	Results for \tilde{P}	51
3.5	Conclusions	53
3.6	Outlooks	55
3.6.1	Application to PR3 and PR4 data set	55
3.6.2	Lack of correlation anomaly with the NAPS	55
4	Cosmic Birefringence	59
4.1	Introduction	62
4.1.1	Physical origin of Cosmic Birefringence	62

4.1.2	CB impact on CMB	65
4.2	Formalism for the estimators	72
4.2.1	D-estimators	72
4.2.2	Localisation approach with the D-estimators	75
4.2.3	C_L^α estimators	76
4.3	Planck 2018 dataset (PR3)	88
4.4	Data analysis: localisation approach with PR3	89
4.5	Data analysis: C_ℓ^α estimators	95
4.5.1	Implemented formalism	95
4.5.2	Validation in a nearly-ideal case	100
4.5.3	Application to Planck Data	111
4.6	Conclusions	125
5	Half-wave plate non-idealities	129
5.1	Introduction	129
5.2	HWPs systematics with <code>beamconv</code>	131
5.2.1	Mathematical Framework	131
5.2.2	Simulation setup	145
5.2.3	Analysis Results	154
5.3	Impact of HWPs non-idealities on Cosmic Birefringence	162
5.3.1	Isotropic birefringence	164
5.3.2	Anisotropic birefringence	165
5.4	Conclusions	166
6	Conclusions and outlook	171
A	Appendix	197
A.1	Correlation between CB multipoles for the "vanilla" case	197
A.2	Correlation between F-matrix and uncertainties in the FFP10 analysis	206

Chapter 1

Executive summary

The Cosmic Microwave Background (CMB), discovered by Penzias and Wilson in 1965 [1], provides one of the most fundamental probes for the standard cosmological model, i.e. the Λ CDM model. The CMB originated in the early stages of Big Bang model and preserves the imprints of various physical early Universe processes. One of the most important scientific evidences achieved by the analysis of the CMB observations is the overall agreement of its statistical properties with the predictions of homogeneity and isotropy of the Universe made by the cosmic inflation.

In the past 30 years continually more sophisticated experimental techniques have been developed for the measurement of the CMB, using ground-based antennae, rockets, balloons and satellites. In May 2009 it was launched the Planck satellite (ESA), which had a combination of sensitivity, angular resolution and frequency coverage never achieved before. With the Planck ESA mission, CMB temperature anisotropies have been observed at the cosmic variance limit, but polarisation remains to be further investigated: in particular, information in the E modes have not been fully extracted yet and the primordial B modes have not been detected and only upper limits are provided. There have been four major data releases of Planck products available on the Planck Legacy Archive (PLA)¹: PR1 in 2013 [2], PR2 in 2015 [3], PR3 in 2018 [4] e PR4 (NPIPE) in 2020 [5]. Fig 1.1 shows the CMB temperature and polarisation anisotropy maps as observed by Planck 2018 [4].

The CMB radiation possesses a near-perfect black-body spectrum, which is an evidence that the Big Bang model is correct: its near-perfect black-body spectrum means that when the CMB was produced matter and radiation were in thermal equilibrium. According to the standard cosmology, after the

¹<https://www.cosmos.esa.int/web/planck/pla>

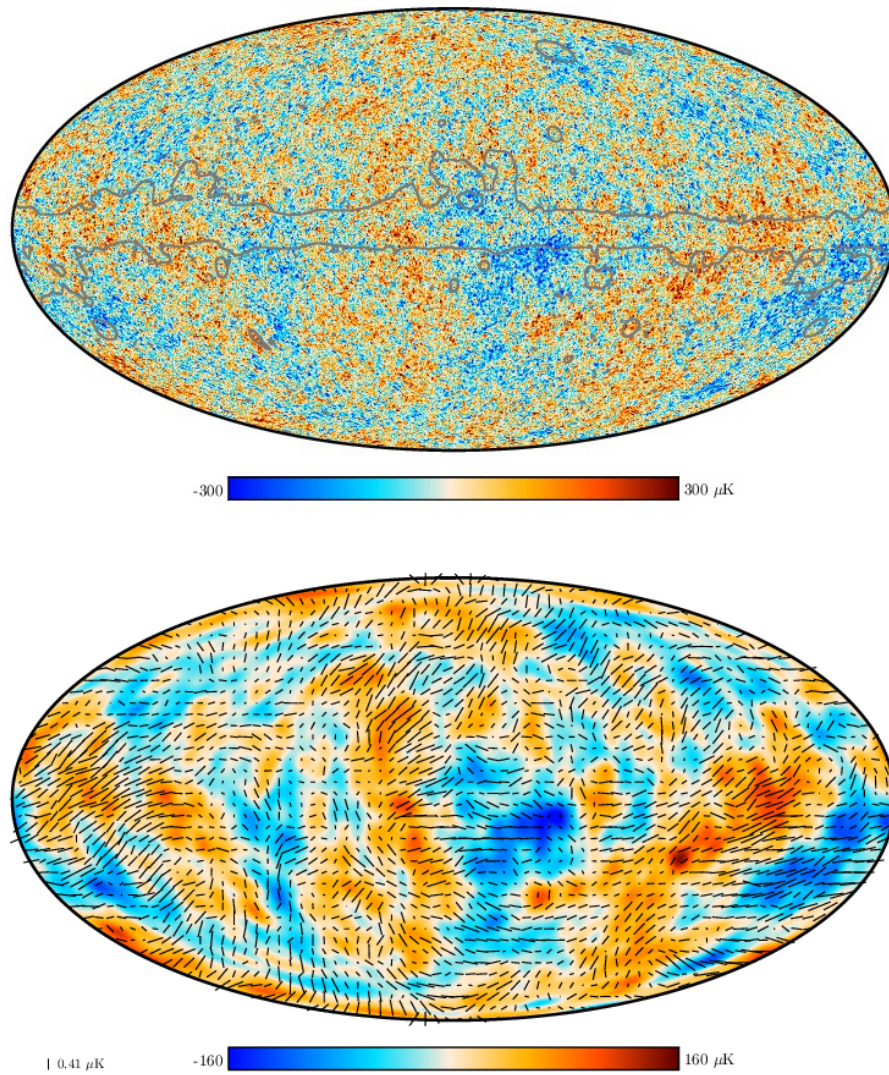


Figure 1.1: CMB maps obtained with the `smica` component-separation algorithm. Upper panel: map of the CMB temperature anisotropies. The grey line outlines the masked and inpainted regions where residuals from galactic and extra-galactic foreground emission are expected to be substantial. Lower panel: large-scale map of the CMB polarisation anisotropies. The polarisation field, described by vectors of varying length, is superimposed on the CMB temperature map (upper panel), both smoothed on a scale of 5° . Image credits: The Planck Collaboration (ESA) [4].

recombination of electrons and protons into neutral hydrogen, the Universe becomes transparent for CMB photons and they move along geodesics of the perturbed Friedman geometry. This corresponds to the so-called surface of last-scattering at a redshift of about $z_{ls} \simeq 1100$, when the Universe had an age of about 380000yr. From the epoch of last-scattering onwards, photons free-stream and reach us basically untouched. Detecting primordial photons is therefore equivalent to take a picture of the early Universe when the CMB photons was generated. A fundamental characteristic of the CMB are the fluctuations of the temperature observed in its pattern. These anisotropies are smaller than about one part over 10^5 and are usually expressed in terms of the quantity:

$$\frac{\Delta T(\theta, \varphi)}{T_0} = \frac{T(\theta, \varphi) - T_0}{T_0} \simeq 10^{-5}, \quad (1.1)$$

which gives the temperature fluctuation as a fraction of the mean temperature T_0 and as a function of the angular position on the sky (θ, φ) . The primary anisotropies are believed to have been generated from quantum fluctuations in the very early Universe by a nearly scale-invariant mechanism. The most prominent context is cosmological inflation. If inflation lasts long enough, the spatial geometry of the Universe is generally predicted to be indistinguishable from Euclidean, and the topology of the observable Universe is expected to be trivial (simply connected). The COBE [6, 7] discovery revealed the long-expected temperature anisotropies and confirmed that they are consistent with an almost scale-invariant power spectrum of temperature fluctuations.

Thomson scattering of temperature anisotropies on the last scattering surface produces a linear polarisation pattern on the sky that can be simply read off from their quadrupole moments (see e.g. [8] and references therein). If the temperature anisotropies are indeed the result of primordial fluctuations, their presence at last scattering would polarise the CMB anisotropies themselves. Therefore the polarisation of the CMB represents a fundamental check on our basic assumptions about the behavior of fluctuations in the Universe.

The polarisation power spectrum provides information complementary to the temperature one. The former can be used not only to provide tighter constraints of cosmological parameters but also to investigate physical processes that would be precluded if just the CMB temperature maps were considered. In particular, my research has been focusing on non-standard signatures from CMB polarisation, which might hint at the existence of new phenomena beyond the Λ CDM cosmological model and the standard model of particle physics (SM). In this Thesis, I took polarisation data into account

to assess the statistical significance of the anomalies currently observed only in the CMB temperature map and to constrain the Cosmic Birefringence (CB) effect, which is expected in parity-violating extensions of the standard electromagnetism. Anyway, the measure of CMB polarisation represents a technological challenge, since the polarised signal is much fainter than the signal in temperature, and to make accurate estimates of this signal, one has to keep an exquisite control of the systematic effects. One of the latter that I have investigated, in collaboration with Dr A. J. Duivenvoorden and the CMB group led by Dr J. E. Gudmundsson at the Stockholm University, is the interplay between half-wave plates (HWP) non-idealities and the beams for forthcoming CMB experiments.

The CMB observations have greatly contributed to build the Λ CDM cosmological model. However several unexpected features have been observed in the CMB anisotropy temperature maps at large angular scales, both by WMAP and by Planck. In Chapter 3, one of them: the lack of power anomaly is introduced and investigated. This anomaly consists in a missing of power at large scales with respect to what foreseen by the cosmological Λ CDM model. This effect has been studied with the variance estimator in WMAP data [9, 10, 11] and in Planck 2013 [12] and Planck 2015 [13] data, measuring a lower-tail-probability of the order of few per cent. WMAP and Planck agree well on this feature, so it is very hard, albeit not impossible, to attribute this anomaly to instrumental effects. Moreover it is also difficult to believe that a lack of power could be generated by residuals of astrophysical emission, since the latter is not expected to be correlated with the CMB and therefore an astrophysical residual should increase the total power rather than decreasing it. Hence, it appears natural to accept this as a real feature present in the CMB pattern. An early fast-roll phase of the inflaton could naturally explain such missing power, see e.g. [14, 15, 16, 17, 18]: therefore this anomaly might witness a new cosmological phase before the standard inflationary era (see e.g. [19, 20, 21] and references therein). However, with only the observations based on the temperature map, this anomaly has not the statistical significance needed to be considered the imprint of new physics beyond the standard cosmological model and is conservatively interpreted as a simple statistical fluke of the Λ CDM. In Chapter 3 we present our work [22], where we revisit the former statement by also considering polarisation data. To this aim, we propose a new one-dimensional estimator (defined in section 3.30, Eq. 3.2.1) capable to take jointly into account both temperature and polarisation. Once validated, this estimator has been applied on PLANCK 2015 low- ℓ dataset, following a frequentist approach, in the harmonic range $2 \leq \ell \leq 30$, with ℓ being the multipole moment. We find that considering the PLANCK 2015 data in the harmonic range mentioned above,

noise dominated polarisation provides an information content at the level of 4% to this estimator which, even though small, has a non-negligible impact on the analysis, the lower-tail-probability shifting downward from 7.22% (obtained considering only temperature data) to 3.68% C.L. (obtained considering jointly temperature and polarisation data), see Figure 3.7. Moreover, we have forecasted that future CMB polarised measurements, as those expected by the LiteBIRD satellite, can increase the polarisation contribution up to 6 times further, see Figure 3.8. We argue that the large-scale E-mode polarisation may play an important role in analysing CMB temperature anomalies with future mission.

Cosmic Birefringence, the in vacuum rotation of the linear polarisation direction of a photon during propagation, is a tracer for new parity-violating physics beyond the standard model of particle physics [23, 24]. Different models for dark matter and dark energy introduce scalar fields ϕ , which can couple to the photons through a Chern-Simons term, adding new parity violating terms to the Lagrangian of standard electromagnetism. Such a phenomenon, naturally measured with an angle α , might signal the presence of new interactions beyond the standard electrodynamics and to provide constraints on different theoretical models for dark energy, dark matter, axions and axion-like particles. Moreover, it is important to constrain the CB because this effect produces B-modes which can screen the primordial signal. The detection of the latter is fundamental to probe primordial gravitational waves and other properties of inflation, as its energy scale. Several astrophysical sources of linearly polarised photons can be used to investigate this phenomenon [24, 25, 26, 27, 28, 29, 30]. CMB is linearly polarised due to Thomson scattering (see section 2.3.1) and therefore it represents a good candidate to perform these investigations. CB is dubbed isotropic if the rotation angle does not depend on the direction of observation. CB is instead called anisotropic if the rotation is a function of the direction of observations. The isotropic CB is expected when the pseudo-scalar field ϕ , that sources CB, is spatially independent, instead a spatially-varying ϕ produces the anisotropic effect. In Chapter 4, after having recovered the main equations relating the birefringence effect to the observed CMB angular power spectra, we focus on evaluating the birefringence power spectrum. In our analysis we develop a novel class of linear and quadratic harmonic-based estimators which are able to directly evaluate the power spectrum of Cosmic Birefringence rotation angle starting from the EE, BB and EB observed angular power spectra of the CMB anisotropies [31]. We have employed these estimators on Planck 2018 data (PR3) [32] with the configuration reported in tables 4.1 and 4.2, evaluating the CB spectrum in the harmonic range $L \in [1, 1000]$. Considering the more constraining estimator, the linear one based on the BB power

spectrum see Eq. 4.175, we find a compatibility with the null effect better than 0.009 deg^2 for $L > 400$. The level of the uncertainties presented here is worse than previous analyses, but we have been able to explore a much wider harmonic range of C_B^α with the Planck data [33]. The region from $L=700$ to $L=1000$ was not cover before. In addition, in collaboration with Dr Marco Bortolami, Prof Luca Pagano and Prof Paolo Natoli, within the Cosmology group of the University of Ferrara, we developed a complementary methodology. In this approach we use the localisation of the so-called D-estimators (see section 4.2.2) to build maps of the birefringence angle evaluating CB spectrum on angular scales larger than ~ 7 degrees. This analysis extends the paper [34], along various directions, in particular providing the cross-correlation between polarised CMB and CB [35]. In particular in this Thesis we focus on constraining the CB auto-spectrum from the Planck 2018 data (PR3) in the harmonic range $L \in [1 - 24]$, finding a compatibility with the null effect with a precision better than 0.01 deg^2 , see Figure 4.8.

In Chapter 5 we investigate the interplay between half-wave plates (HWP) non-idealities and the beams for forthcoming CMB experiments and provide a first estimate of the impact of non-ideal HWPs on constraining the Cosmic Birefringence (CB), both isotropic and anisotropic. Half-wave plates (HWP) is a polarisation modulator which is currently used in various CMB experiments, such as SPIDER [36], MAXIPOL [37], POLARBEAR [38, 39], and may be employed in several forthcoming CMB missions as LiteBIRD satellite [40, 41], Simon Observatory [42] and CMB-S4 project [43]. An ideal rotating HWP only modulates the linearly polarised sky signal and therefore allows one to cleanly separate this desired signal from unpolarised sky signal. Non-ideal HWPs impede perfectly controlled modulation and indirectly cause spurious polarised signal of their own. The merit of a HWP has to be carefully weighed against the downsides. There exists a rich literature that describes the impact of HWPs and their associated non-idealities on the signal that they are supposed to modulate (see e.g. [44, 45, 46, 43, 47, 48, 49, 50]). In the first part of this chapter we report the outcome of this collaboration with Dr A. J. Duivenvoorden, Dr A. E. Adler, Dr. N. Dachlythra, Dr J. E. Gudmundsson at the Stockholm University, published in [51]. We study how different HWP configurations optimised for detectors sensitive to both 95 and 150 GHz impact our ability to reconstruct primordial B-mode polarisation in the CMB, paying particular attention to possible biases arising from the interaction of frequency dependent HWP non-idealities with polarised Galactic dust emission and the interaction between the HWP and the instrumental beam. In order to do this we extended the capabilities of the publicly

available `beamconv` code² [52]. To our knowledge, we produced the first time-domain simulations that include both HWP non-idealities and realistic full-sky beam convolution. With the upgraded version of `beamconv`, we have been able to estimate the contamination of the BB power spectrum due to the interplay between dust modelling, beam and HWP non-idealities. Our analysis suggests that certain HWP configurations, depending on the complexity of Galactic foregrounds and the beam models, significantly impact the B-mode reconstruction fidelity and could limit the capabilities of next-generation CMB experiments. We conclude this chapter providing an interesting application of the realistic CMB simulations produced with `beamconv`. We use the latter to investigate instrumental contamination which could specifically bias the measure of the CB effect in view of future and present CMB missions. Such an analysis, which is not fully covered in literature to our knowledge, in future could allow us to provide more robust constraints on different theoretical models which makes predictions for this phenomenon. In order to obtain the level of systematics that impact on the birefringence angle and spectra, we apply the statistical estimators for CB effect, described in Chapter 4, taking as an input the residual power spectra in Figure 5.11, obtained considering a co-polar polarised and azimuthally symmetric Gaussian beam model and observing the CMB (without foreground) in the 150 GHz band with the HWP configurations in table 4.2. Such a preliminary analysis shows that for this setup, all the HWPs configurations do not impact the evaluation of both the CB isotropic angle and its power spectrum.

Included papers

- **Paper 1**

M. Billi, A. Gruppuso, N. Mandolesi, L. Moscardini, P. Natoli.

"Polarisation as a tracer of CMB anomalies: Planck results and future forecasts",

Phys. Dark Univ. 26 (2019) 00327;

arXiv:1901.04762, doi:10.1016/j.dark.2019.100327

I have been the main contributor to this project. Under the guidance of my collaborators, I developed the code and the formalism of the new one-dimensional estimator, presented in this paper, capable to take jointly into account both temperature and polarisation in constraining the lack

²<https://github.com/AdriJD/beamconv>

of power anomaly. I have written the majority of the paper, my collaborators helped me by providing comments to the manuscript.

- **Paper 2**

A. J. Duivenvoorden, A. E. Adler, M. Billi, N. Dachlythra, J. E. Gudmundsson.

Probing frequency-dependent half-wave plate systematics for CMB experiments with full-sky beam convolution simulations,

Mon.Not.Roy.Astron.Soc. 502 (3) (2021) 4526-4539.

arXiv:2012.10437, doi:10.1093/mnras/stab317.

I contributed to the modeling and optimisation of HWP in Mueller matrix formalism, and assisted at the employment of the latter in the beamconv algorithm. I contributed to the analysis pipeline that calls the upgraded version of beamconv code to calculate the residuals of HWPs systematics for the satellite test case. I collaborated to the writing of the paper presenting the outcome of this analysis.

- **Paper 3**

M. Billi, M. Bortolami, A. Gruppuso, P. Natoli, L. Pagano.

"New estimators for anisotropic birefringence from CMB observations: the formalism and the application to Planck 2018 data."

To be submitted.

I have been the main contributor to this project. Starting from the initial idea provided by my supervisor, I formulated the statistical framework of the linear and quadratic estimators aiming at the evaluation of CB spectrum. I developed the python implementations of the latter helped by my collaborators. I assisted in the production of the CMB power spectra from Planck 2018 data, on which are applied the developed estimators. My collaborators assisted me in the writing of the paper by providing comments to drafts of the manuscript.

- **Paper 4**

M. Bortolami, M. Billi, A. Gruppuso, P. Natoli, L. Pagano.

"Constraints on anisotropic birefringence and its cross-correlation with CMB temperature and polarization fields."

To be submitted.

I assisted to the analysis pipeline used to derive the constrain on the anisotropic CB presented in this paper, focusing in particular on the

evaluation of the CB auto-spectrum. I have contributed to the writing of the paper by providing comments to drafts of the manuscript.

Chapter 2

Cosmic Microwave Background

The Cosmic Microwave Background (CMB), discovered by Penzias and Wilson in 1965 [1], provides one of the most fundamental proofs for the standard cosmological model, i.e. the Λ CDM model. The CMB did originate in the early stages of Big Bang model and preserves the imprints of various early Universe physical processes. One of the most important scientific evidences achieved by the analysis of the CMB observations is the overall agreement of its statistical properties with the predictions of homogeneity and isotropy of the Universe made by the cosmic inflation. In this chapter we general describe the Hot Big-Bang model, the Inflationary Universe and the CMB, introducing the concept and the mathematical formalism of its polarised component.

2.1 Standard Cosmological Model

The evolution of our Universe is described by the Hot Big Bang model [53, 54, 55, 56]. This model is based on the so-called Cosmological Principle: the Universe is, on large scales, homogeneous and isotropic. The best evidence for the isotropy is the uniformity of the temperature of the Cosmic Microwave Background (CMB) radiation: intrinsic temperature anisotropies are smaller than 10^{-5} . Other recent probes confirm that at scale larger than ($\sim 100h^{-1}$ Mpc) the Universe is well compatible with the cosmological principle [57].

The most generic metric that satisfies the condition of homogeneity and isotropy on large scales is the Friedmann-Lemaitre-Robertson-Walker (FLRW)

metric:

$$\begin{aligned} ds^2 &= \sum_{\mu,\nu=0}^3 g_{\mu\nu} dx^\mu dx^\nu \\ &= c^2 dt^2 - a^2(t) \left[\frac{dr^2}{1 - kr^2} + r^2 d\theta^2 + r^2 \sin^2 \theta d\phi^2 \right], \end{aligned} \quad (2.1)$$

where $g_{\mu\nu}$ is the metric tensor, (t, r, θ, ϕ) are comoving coordinates, $a(t)$ is the cosmic scale factor and k can be chosen to be $+1$, -1 , or 0 for closed, open or flat spaces, respectively. The coordinate r is taken to be dimensionless and $a(t)$ has dimensions of length. The time coordinate is the proper time measured by an observer at rest in the comoving frame, i.e. $(r, \theta, \phi) = \text{constant}$. Instead of the cosmic time it is customary to use the redshift z which is the shift of spectral lines to longer wavelengths caused by the recession of Galaxies from our Galaxy in the uniform expansion of the Universe. The redshift is defined to be:

$$z \equiv \frac{\lambda_0 - \lambda_e}{\lambda_e}, \quad (2.2)$$

where λ_e is the wavelengths of the line as emitted and λ_0 the observed wavelength. It follows directly from the FLRW metric that the redshift z is directly related to the scalar factor $a(t)$ through the relation:

$$1 + z = \frac{a_0}{a(t)}, \quad (2.3)$$

where a_0 is the scale factor at the present-day. The redshift determines the scale factor $a(t)$ (or the cosmic time once the function $a(t)$ is known) of the Universe when the light was emitted from distant sources.

2.1.1 Friedmann Equations

The FLRW models are relativistic models, based on the solutions of the field equations of Einstein General Relativity [56]:

$$R_{\mu\nu} - \frac{1}{2} g_{\mu\nu} R = \frac{8\pi G}{c^4} T_{\mu\nu} - \Lambda g_{\mu\nu}, \quad (2.4)$$

where $R_{\mu\nu}$ is the Ricci tensor, R is the Ricci scalar, $T_{\mu\nu}$ is the stress-energy tensor for all the fields present in the Universe, G is the Newton constant of gravitation and c is the speed of light. We have included the presence of a cosmological constant Λ . In standard cosmology $T_{\mu\nu}$ is taken to be the energy-momentum tensor of a perfect fluid:

$$T_{\mu\nu} = -P g_{\mu\nu} + (P + \rho c^2) u_\mu u_\nu, \quad (2.5)$$

where P and ρ are respectively the pressure and the density of the fluid and the four-vector u_μ is the velocity field of the fluid. To solve the Einstein equations it is necessary to introduce a relationship between the pressure and the density of the cosmic fluid which, in the standard models, is linear and parameterised through the parameter w :

$$P = w\rho c^2. \quad (2.6)$$

In general for physical matter one requires $\rho > 0$, i.e. positive energy, and also $P > 0$, implying that $w > 0$. In particular, the non-relativistic particles (m), usually called dust, are assumed to have a negligible pressure:

$$w_m = 0, \quad P_m = 0. \quad (2.7)$$

Relativistic particles (r), e.g. radiation, have the following equation of state:

$$w_r = \frac{1}{3}, \quad P_r = \frac{1}{3}\rho c^2. \quad (2.8)$$

A cosmological constant, instead, corresponds to a contribution with:

$$w_\Lambda = -1, \quad P_\Lambda = -\rho c^2. \quad (2.9)$$

In standard cosmology it is assumed that the expansion of the Universe is adiabatic¹:

$$d(\rho c^2 a^3) = -P da^3. \quad (2.10)$$

From this equation we can obtain the relation:

$$\rho_w a^{3(1+w)} = \rho_{0,w} a_0^{3(1+w)} = \text{const}, \quad (2.11)$$

where $\rho_{0,w}$ is the density at the present time of the component having equation of state parameter w . Under this assumption the matter, radiation and cosmological constant have different behaviour with the redshift:

$$\rho_m = \rho_{0,m} \left(\frac{a_0}{a} \right)^3 = \rho_{0,m} (1+z)^3, \quad (2.12)$$

$$\rho_r = \rho_{0,r} \left(\frac{a_0}{a} \right)^4 = \rho_{0,r} (1+z)^4, \quad (2.13)$$

$$\rho_\Lambda = \rho_{0,\Lambda}, \quad (2.14)$$

¹The adiabatic expansion is a consequence of the equation of continuity, condition satisfied by the Einstein field equations with a perfect fluid as source.

and contribute differently during the evolution of the Universe. The early Universe was radiation dominated, the “adolescent” Universe was matter dominated and the present-day Universe is dominated by the cosmological constant.

Because the isotropy and homogeneity only the diagonal components survive and all the "spatial " equations give the same one. From these two equations we obtain the so-called *I* and the *II* Friedmann equations:

$$\ddot{a} = -\frac{4\pi G}{3} \left(\rho + \frac{3P}{c^2} \right) a + \frac{\Lambda c^2}{3} a, \quad (2.15)$$

$$\dot{a}^2 + kc^2 = \frac{8\pi G}{3} \rho a^2 + \frac{\Lambda c^2}{3} a^2; \quad (2.16)$$

given the equation of state $P = P(\rho)$, Eqs. (2.15), (2.16) can be solved for $a(t)$, which describes the evolution of the expansion factor of the Universe.

The Friedmann equations can be recast in terms of the Hubble parameter $H(t)$ and the critical density parameter Ω :

$$H(t) \equiv \frac{\dot{a}}{a}; \quad (2.17)$$

$$\Omega \equiv \frac{\rho}{\rho_c}, \quad \rho_c \equiv \frac{3H^2}{8\pi G}. \quad (2.18)$$

The Hubble parameter is not a constant and its value at the present time it is called the Hubble constant:

$$H_0 = \frac{\dot{a}_0}{a_0}. \quad (2.19)$$

The geometry of the Universe can be expressed in terms of Ω , or $\Omega_k \equiv 1 - \Omega$:

- $\Omega > 1 \quad \rightarrow \quad \Omega_k < 0$: Closed Universe;
- $\Omega = 1 \quad \rightarrow \quad \Omega_k = 0$: Flat Universe;
- $\Omega < 1 \quad \rightarrow \quad \Omega_k > 0$: Open Universe.

For a multi-components fluid model Universe we have:

$$\Omega = \sum \Omega_i. \quad (2.20)$$

The *II* equation of Friedmann becomes:

$$H^2(t) = H_0^2 \left(\frac{a_0}{a} \right)^2 \left[1 - \sum_i \Omega_{0,i} + \sum_i \Omega_{0,i} \left(\frac{a_0}{a} \right)^{1+3\omega_i} \right]; \quad (2.21)$$

or as a function of the redshift:

$$\begin{aligned} H^2(t) &= H_0^2 (1+z)^2 \left[1 - \sum_i \Omega_{0,i} + \sum_i \Omega_{0,i} (1+z)^{1+3\omega_i} \right] = \\ &= H_0^2 E^2(z). \end{aligned} \quad (2.22)$$

For the Universe at the present time the component of radiation is negligible so we can consider a Universe composed only by the components of matter and cosmological constant. The evolution of the Hubble parameter is described by:

$$H^2(z) = H_0^2 \left[\Omega_{0,m}(1+z)^3 + \Omega_{0,k}(1+z)^2 + \Omega_{0,\Lambda} \right]. \quad (2.23)$$

Through independent observations, measures of luminosity distance by means SNIa, surveys of clusters of Galaxies and CMB radiation, it was possible to put constraints on the cosmological parameters $\Omega_{0,m}$ and $\Omega_{0,\Lambda}$, see Figure 2.1. In table 2.1 it is reported the values of $\Omega_{0,m}$ and $\Omega_{0,k}$ obtained from the CMB as measured by the Planck satellite [59] and from the observations of SNIa Supernovae made by Cosmology Project SCP 2011[58]. So the Universe at

	$\Omega_{0,m}$	$\Omega_{0,k}$
Planck Mission	$0.315 \pm +0.007$	$0.040^{+0.038}_{-0.041}$
SCP 2011	$0.282^{+0.015}_{-0.014}$	$-0.004^{+0.006}_{-0.006}$

Table 2.1: Cosmological parameters as measured by Planck and by the observations of SNIa.

the present time is compatible with a flat geometry and is composed by matter for about 30% and by dark energy for about 70%.

Anyway, the Hot Big Bang Model presents some shortcomings, as the Horizon and the flatness problem that can be solved by introducing the Inflationary Paradigm.

2.1.2 Inflationary Paradigm

The inflationary paradigm is based upon the idea that during an early era, the so-called Inflation, before the era of primordial nucleosynthesis, the expansion of the Universe was accelerated. In this epoch the vacuum energy of a scalar quantum field, called inflaton ϕ , dominates over other forms of energy, hence giving rise to a quasi-exponential expansion. This phase of rapid acceleration of the Universe can solve the flatness, the horizon and the monopole problems of the Hot Big Bang model. For more details, see e.g. [60, 61] and references therein.

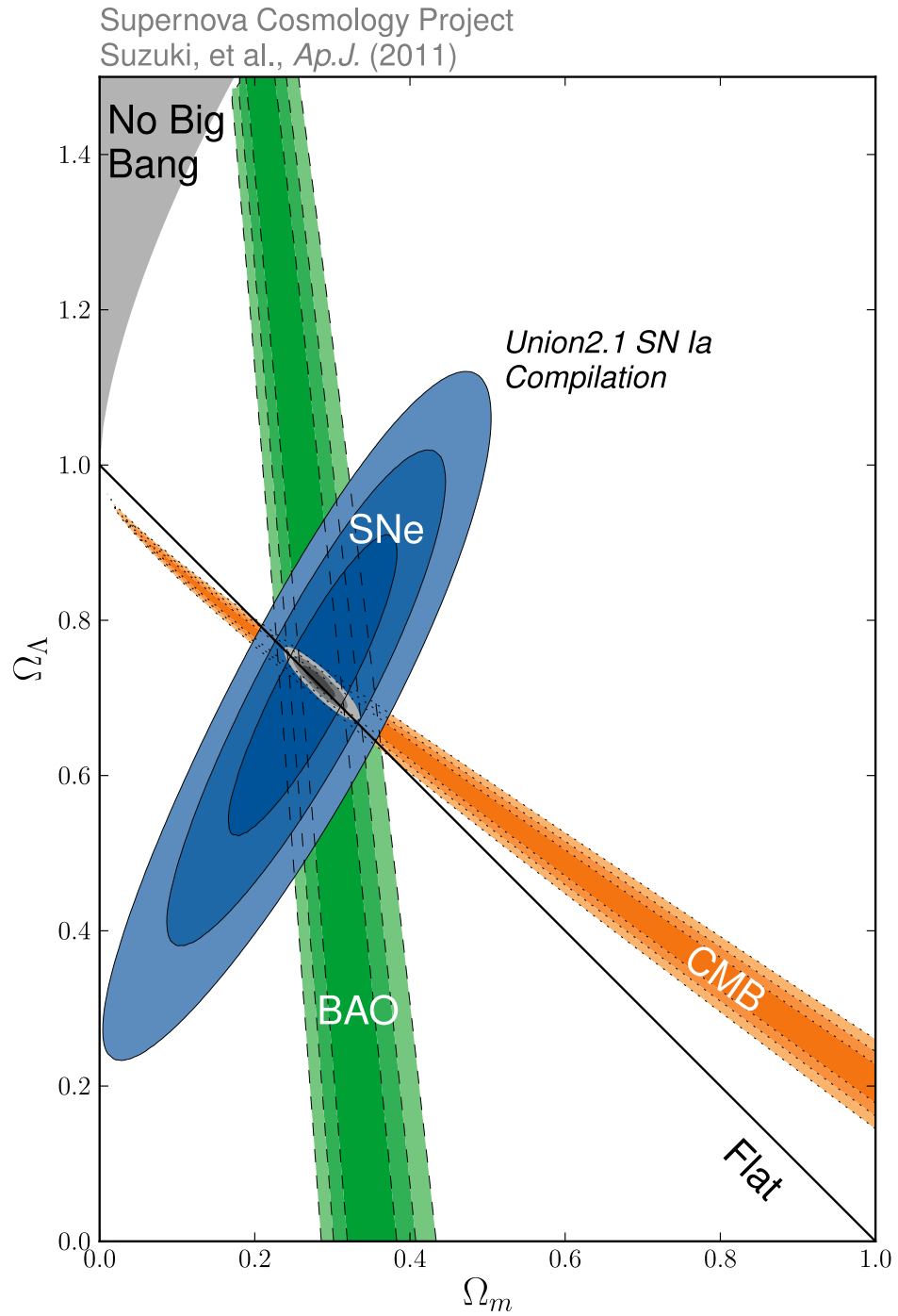


Figure 2.1: Confidence levels for the cosmological parameters, obtained from observations of SNIa (blue), CMB (orange) and BAO (green). Image credits: Supernova Cosmology Project [58].

2.1.2.1 Inflationary solution at the horizon and at the flatness problems

The Horizon Problem is a problem of causality. The Universe appears extremely smooth over very large distance scales, even though, according to the Hot Big Bang model, such distant regions had not been able to establish mutual correlation by exchanging any causal signal. A direct proof of this problem comes from the observations of the CMB maps: the surface of the last scattering, which is much larger than the Hubble radius ($r_H(t) = c/H(t)$) at the time of last scattering, is homogeneous and isotropic. To explain the Inflationary solution to this problem we introduce the comoving Hubble radius:

$$\tilde{r}_H(t) = \frac{c}{\dot{a}}, \quad (2.24)$$

which sets the effective comoving scale of causal connection. In a Universe dominated by a perfect fluid with $w > -1/3$, $\tilde{r}_H(t)$ grows with time, therefore larger and larger scales get in causal connection with increasing time as soon as they enter the horizon, i.e. cross the Hubble radius. According to the inflationary paradigm, in the early Universe $\tilde{r}_H(t)$ had decreased for some time, thus those scales which enters the horizon now may have actually been in causal contact in the past. A decrease of the Hubble radius with time:

$$\dot{\tilde{r}}_H(t) < 0, \quad (2.25)$$

corresponds to:

$$\ddot{a} > 0 \quad (2.26)$$

i.e. an acceleration. This is the main characteristic which defines the inflationary paradigm.

Another shortcoming of the Hot Big Bang Model is the so-called flatness problem, that is a fine-tuning problem. In order to get the observed value at the present time of $(\Omega_0 - 1) \sim 0$, the value of $(\Omega - 1)$ at the early Universe has to be fine-tuned to values amazingly close to zero ($\sim 10^{-64}$). The solution of the horizon problem also solves the flatness one. Since \tilde{r}_H decreases because of the accelerated expansion, at the end of the Inflation, $|\Omega - 1|$ gains such a tiny value that it can easily accommodate for the present observation of an almost flat Universe.

2.1.2.2 Slow-Roll dynamics of the inflaton field

The standard model of Inflation is the so-called slow-roll scenario, associated to a single scalar field. During the Inflation one can consider a homogeneous and isotropic Universe described by the FLRW metric (see Eq. 2.1). One

takes the Universe dominated by the vacuum energy of a scalar field, therefore the Friedmann equations become (in this section we use units such that $c = h = k_B = G = 1$):

$$\ddot{a} = -\frac{4\pi G}{3}(\rho + 3P)a, \quad (2.27)$$

$$\dot{a}^2 + k = \frac{8\pi G}{3}\rho a^2, \quad (2.28)$$

where ρ and P are the density and pressure of the scalar field. Eq. (2.27) implies that a period of accelerated expansion, $\ddot{a} > 0$, takes place only if:

$$P < -\frac{1}{3}\rho. \quad (2.29)$$

The condition (2.29) can be satisfied by a homogeneous scalar field, the inflaton ϕ , which behaves like a perfect fluid with energy density and pressure given by:

$$P_\phi = \frac{\dot{\phi}^2}{2} - V(\phi), \quad (2.30)$$

$$\rho_\phi = \frac{\dot{\phi}^2}{2} + V(\phi), \quad (2.31)$$

where $V(\phi)$ specifies the scalar field potential. Hence if we require the so-called slow-roll condition:

$$V(\phi) \gg \dot{\phi}^2, \quad (2.32)$$

we obtain:

$$P_\phi \simeq -\rho_\phi. \quad (2.33)$$

Thus, we realize that a scalar field whose energy is dominant in the Universe and whose potential energy dominates over the kinetic term gives inflation. The equation of motion of the scalar field ϕ is:

$$\ddot{\phi} + 3H\dot{\phi} + \frac{\partial V(\phi)}{\partial \phi} = 0, \quad (2.34)$$

where $3H\dot{\phi}$ is the friction term of a scalar field rolling down its potential due to the expansion of the Universe. The condition (2.32) requires the scalar field slowly rolls down its potential. Such a slow-roll period can be achieved if the inflaton field ϕ is in a region where the potential is sufficiently flat. The flatness condition of the potential could be parametrised in terms of the

so-called slow-roll parameters:

$$\epsilon \equiv \frac{1}{16\pi} \left(\frac{V'}{V} \right)^2, \quad (2.35)$$

$$\eta \equiv \frac{1}{8\pi} \left(\frac{V''}{V} \right). \quad (2.36)$$

Achieving a successful period of inflation requires the slow-roll parameters to be $\epsilon, |\eta| \ll 1$; when this condition fails, inflation ends.

It has been proposed a really large number of inflationary models, differing for the underlying particle physics theory and for the kind of potential. These models could be classified into three broad groups as “small field”, “large field” and “hybrid” type, according to the region occupied in the space $(\epsilon - \eta)$ by a given inflationary potential. The Planck dataset allowed to extract the parameters necessary for distinguishing among single-field inflation models [62].

The period of accelerated expansion of the Universe must last enough to solve the horizon and flatness problems. It is customary to measure the duration of inflation in terms of the number of e-foldings, defined as:

$$N = \ln \left(\frac{a_f}{a_i} \right), \quad (2.37)$$

where a_f and a_i are respectively the scale factors at the beginning and at the end of the inflation. It is requested that:

$$N \gg N_{min}, \quad (2.38)$$

where $N_{min} \sim 60$ is the number of e-foldings before the end of inflation when the present Hubble radius leaves the horizon. When the inflaton field starts to roll fast along its potential, Inflation ends. When inflation ends, the inflaton ϕ oscillates about the minimum of its potential $V(\phi)$ and decays, thereby reheating the Universe. After this phase the Universe is repopulated by a hot radiation fluid.

2.1.3 Inflation and cosmological perturbations

The Inflation generates also the primordial fluctuations. According to the inflationary paradigm, primordial density and gravitational-waves perturbations were generated from quantum fluctuations redshifted out of the Hubble radius, were they remain “frozen”: quantum vacuum oscillations of the inflaton give rise to classical fluctuations in the energy density, which provide the seeds for CMB radiation temperature anisotropies and polarisation,

as well as for the formation of Large Scale Structures (LSS) in the present Universe.

The generation of gravity-wave fluctuations is a generic prediction of an accelerated expansion of the Universe whatever mechanism for the generation of cosmological perturbations is operative. Gravitational waves, whose possible observation might come from the detection of the B-mode of polarisation in the CMB anisotropy (which are explained in chapter 3) may be viewed as ripples of space-time around the background metric.

2.2 Introduction to CMB

The CMB radiation, discovered by Penzias and Wilson in 1965 [1], provides one of the most important pieces of evidence for the Hot Big Bang model. Penzias and Wilson, which were radio engineers, investigating the properties of the atmospheric noise in connection with the Telstar communication satellite project, found an apparently uniform background signal at microwave frequencies which could not be explained by instrumental noise or by any known radio sources. They admitted the possibility that they had discovered a thermal radiation background left as a relic of the primordial fireball phase. A group of theorists at Princeton University, including Dicke and Peebles, soon gave the interpretation of the background “hiss” as relic radiation [63].

The CMB is a source of enormous observational and theoretical interest: the CMB actually did originate in the early stages of a Big Bang, thus it conserves the imprints of various physical early Universe processes.

In the past 30 years continually more sophisticated experimental techniques have been directed at the measurement of the CMB, using ground-based antennae, rockets, balloons and satellites. The first satellite was COBE (USA) [6, 7], launched in the 1989. It had an enormous advantage over previous experiments: it was able to avoid atmospheric absorption, which is an important systematic effect for ground-based experiments at microwave and submillimetric frequencies. The CMB spectrum observed by COBE reveals just how close to an ideal black body the radiation background is, with a mean the temperature of $2.726 \pm 0.005K$ [7]. In the 2001 it was launched the satellite WMAP (USA) [64] which had a resolution really better than COBE. Finally 14 May 2009 it was launched the Planck satellite (ESA) [2, 3, 4, 5] which had a combination of sensitivity, angular resolution, and frequency coverage never achieved before. Planck carried an array of 74 detectors sensitive to a range of frequencies between ~ 25 and ~ 1000 GHz, which scanned the sky simultaneously and continuously with an angular resolution varying

between ~ 5 arcmin at the highest frequencies and ~ 30 arcmin at the lowest. The array was arranged into two instruments: the Low Frequency Instrument (LFI), which covered three bands (centred at 30, 44, and 70 GHz) and the High Frequency Instrument (HFI) which covered six bands (centred at 100, 143, 217, 353, 545 and 857 GHz).

2.2.1 CMB Black Body Spectrum

The CMB radiation possesses a near-perfect black-body spectrum, which is a good evidence that the Big Bang model is correct: its near-perfect black-body spectrum means that when the CMB was produced matter and radiation were at the thermal equilibrium. According to the standard cosmology, after recombination of electrons and protons into neutral hydrogen, the Universe becomes transparent for CMB photons and they move along geodesics of the perturbed Friedman geometry. This corresponds to the so-called surface of last-scattering at a redshift of about $z_{ls} \simeq 1100$ and an age of about $380000yr$. From the epoch of last-scattering onwards, photons free-stream and reach us basically untouched. Detecting primordial photons is therefore equivalent to take a picture of the early Universe when the CMB photons were generated. Assuming thermal equilibrium, the intensity of the radiation is given by a black-body spectrum:

$$I(T_i, \nu) = \frac{4\pi\hbar\nu^3}{c} \left[e^{\left(\frac{h\nu}{k_B T_i}\right)} - 1 \right]^{-1}, \quad (2.39)$$

where \hbar is the Planck constant, ν is the radiation frequency, c is the speed of light, k_B is the Boltzmann constant and T_i is the temperature of the radiation. During the expansion of the Universe the form of the spectrum $I(T, \nu)$ remains the same (because both T and ν have the same dependence on the redshift) with the replacement of T_i by:

$$T = T_i \frac{a(t_i)}{a(t)}. \quad (2.40)$$

Figure 2.2 shows the results obtained by the FIRAS instrument on the COBE satellite [65], together with the results in different wavelength regions obtained by other experiments. The quality of the fit of the observed CMB spectrum to a black-body curve provides clear evidence of the Big Bang scenario.

The black-body spectrum of the CMB has the peak at the wavelength

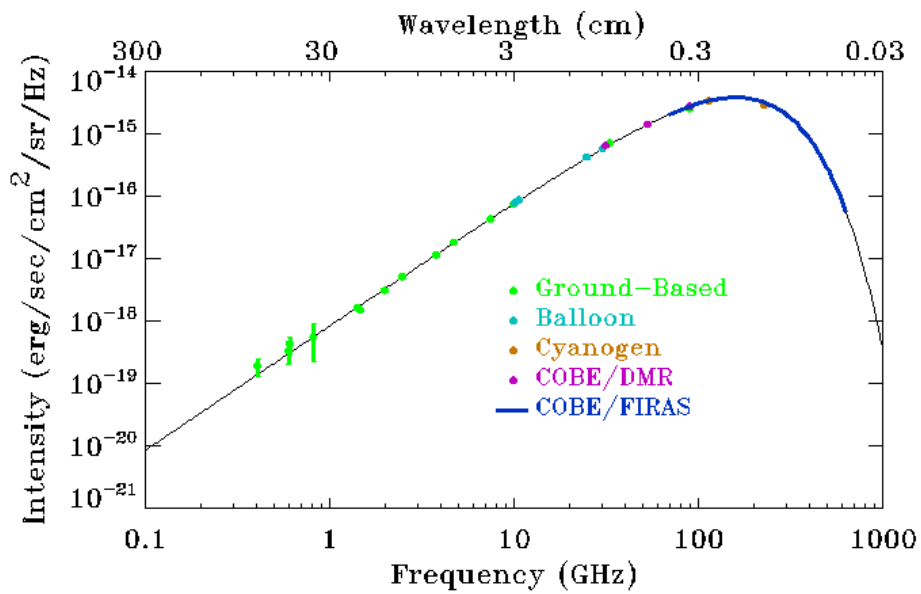


Figure 2.2: CMB spectrum as measured by the FIRAS instrument aboard COBE satellite. FIRAS determined the CMB temperature to be 2.726 ± 0.005 K, with deviations from a perfect blackbody limited to less than $5 \cdot 10^{-5}$ in intensity. Image credits: COBE collaboration [65].

$\lambda = 0.2 \text{ mm}$, which corresponds to the temperature of ²:

$$T_{0,CMB} = 2.726 \pm 0.005K. \quad (2.41)$$

The observation of an isotropic CMB provides strong support for the cosmological principle, which states that the Universe is statistically isotropic and homogeneous at large scales.

2.2.2 CMB temperature anisotropies

A fundamental characteristic of the CMB are the fluctuations of the temperature observed in its pattern. These anisotropies are smaller than about one part in 10^5 and are usually expressed in terms of the quantity:

$$\frac{\Delta T(\theta, \varphi)}{T_0} \simeq 10^{-5}, \quad (2.42)$$

which gives the temperature fluctuation as a fraction of the mean temperature T_0 and as a function of angular position (θ, φ) on the sky. Figure 2.3 shows the CMB temperature anisotropy maps as observed by the third Planck Data Release (PR3) [4].

These anisotropies are classified in two main categories: primary and secondary. The first ones are all those anisotropies produced at the redshift of the last-scattering (z_{LS}) and the second ones are the fluctuations generated by the interactions that the CMB made in the space-time path from z_{LS} and z_0 ($z_0 \equiv 0$). The primary anisotropies are believed to have been produced during the Inflation by a nearly scale-invariant mechanism. The inflationary theory predicts that the CMB temperature fluctuations should be:

- statistically isotropic,
- almost Gaussian,
- almost scale invariant,
- coherent in phase,
- dominated by the adiabatic mode,

Furthermore, it is expected:

- the non-existence of rotational modes at large scales,

²For a black-body spectrum the wavelength of the peak and the temperature of the radiation are connected by the law: $\lambda_{peak} \cdot T = b$, with $b = 2.8977685 \cdot 10^{-3}m \cdot K$.

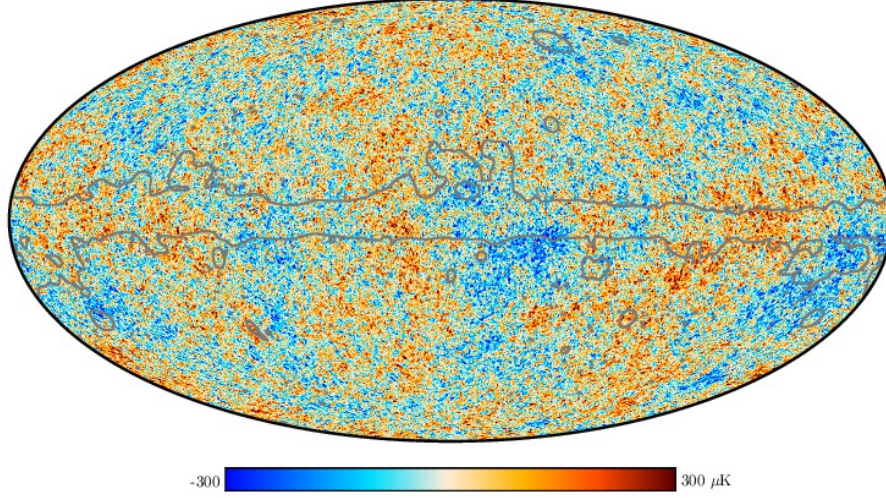


Figure 2.3: CMB temperature anisotropy map from `smica` component-separation algorithm. The grey line outlines the region of the Galactic plane filled in by a constrained realisation that has the same statistical properties as the rest of the sky. Image credits: The Planck Collaboration (ESA) [4].

- a detectable stochastic background of gravitational waves.

The CMB temperature anisotropies depend on the direction of the observations, hence they are defined on a sphere. We can expand them in terms of the spherical harmonic functions $Y_{\ell m}(\hat{n})$ [55]:

$$\frac{\Delta T}{T}(\hat{n}) = T(\hat{n}) \equiv \sum_{\ell=0}^{\infty} \sum_{m=-\ell}^{m=+\ell} a_{T,\ell m} Y_{\ell m}(\hat{n}), \quad (2.43)$$

where the unit-vector \hat{n} is the direction on the sky³, $a_{\ell m}$ are the coefficients of the spherical harmonic $Y_{\ell m}$. Here the index ℓ represents the multipole and corresponds to the inverse of the angular distance between two point on the sky. By inverting Eq. (2.43), one can find the expression of the harmonic coefficients:

$$a_{T,\ell m} = \int d\Omega Y_{\ell m}^*(\hat{n}) T(\hat{n}). \quad (2.44)$$

For statistically isotropic fluctuations the harmonic coefficients are orthogonal, therefore:

$$\langle a_{T,\ell m} (a_{T,\ell' m'})^* \rangle = C_{\ell}^{TT} \delta_{\ell\ell'} \delta_{mm'}, \quad (2.45)$$

³The unit-vector \hat{n} in spherical coordinates is: $\hat{n} = (\sin \theta \cos \varphi, \sin \theta \sin \varphi, \cos \theta)$

the average is taken over an ensemble of realisations. The quantity C_ℓ^{TT} is the angular power spectrum, which can be estimated by

$$\hat{C}_\ell^{TT} = \frac{1}{2\ell + 1} \sum_{m=-\ell}^{m=+\ell} a_{T,\ell m} (a_{T,\ell m})^*. \quad (2.46)$$

The estimation of the angular power spectrum C_ℓ^{TT} , for statistically isotropic and Gaussian skies, is limited by the fact that we can only observe one particular realisation of the Universe. For full sky observations, \hat{C}_ℓ is unbiased ($\langle \hat{C}_\ell^{TT} \rangle = C_\ell^{TT}$) and minimises the variance⁴:

$$\text{var}(\hat{C}_\ell^{TT}) = \frac{2}{2\ell + 1} (C_\ell^{TT})^2. \quad (2.47)$$

Eq. (2.47) represents the sample variance, the so-called cosmic variance. It is an irreducible lower bound, especially for low multipoles, on the error in the measurements of the angular power spectrum coming from the fact that we observe fluctuations in only one Universe.

Usually the angular power spectrum is written in the form of the angular band power, defined as:

$$D_\ell^{TT} = \frac{\ell(\ell + 1)}{2\pi} C_\ell^{TT}, \quad (2.48)$$

because for almost-scale-invariant fluctuations the angular band power spectrum D_ℓ^{TT} is almost-constant for low multipole. Figure 2.4 shows the band power spectrum for temperature, as published by Planck 2018 Release (PR3) [66].

If the distribution of fluctuations is almost-Gaussian (as predicted by inflation and as current data suggest [67]) then only the even order correlation functions are non-zero and all of them can be directly expressed through the two-point correlation function $C(\phi)$ ⁵, which, considering Eq.(2.45) can be written as:

$$\begin{aligned} C(\phi) &= \langle T(\hat{n}) T(\hat{n}') \rangle = \\ &= \sum_\ell \frac{2\ell + 1}{4\pi} C_\ell^{TT} P_\ell(\hat{n} \cdot \hat{n}'), \end{aligned} \quad (2.49)$$

⁴For $\ell = 1$ the cosmic variance does not apply if the CMB dipole is caused by the proper-motion of the Solar System.

⁵Therefore the three-point correlation function, also known as the bispectrum, is a sensitive test for a non-Gaussian contribution to the fluctuation spectrum since it would be precisely zero in the Gaussian limit.

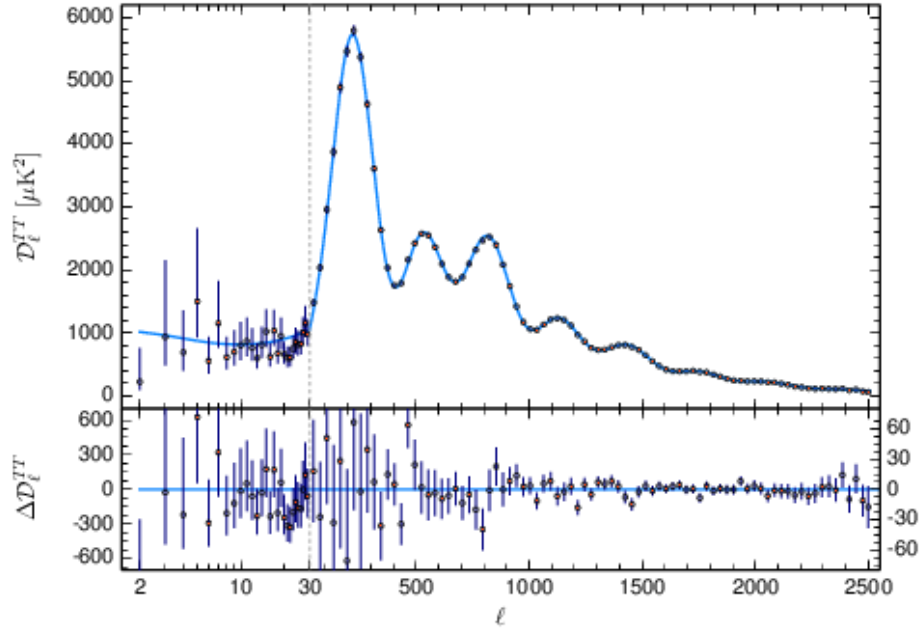


Figure 2.4: Angular band power (upper panel) and residual with respect to the model (lower panel) of the CMB temperature anisotropies as presented in the Planck 2018 release [66]. The blue line in the upper panel is Λ CDM theoretical spectrum best fit to the PLANCK likelihoods. The error bars show $\pm 1\sigma$ diagonal uncertainties, including cosmic variance, the latter being the dominant source of uncertainty at large angular scales (small ℓ). Note that the vertical scale changes at $\ell = 30$, where the horizontal axis switches from logarithmic to linear. Image credits: Planck ESA Collaboration [66].

where $\hat{n} \cdot \hat{n}' = \cos \phi$ and $P_\ell(\hat{n} \cdot \hat{n}')$ are the Legendre Polynomials:

$$P_\ell(\hat{n} \cdot \hat{n}') = \frac{4\pi}{2\ell + 1} \sum_{m=-\ell}^{+\ell} Y_{\ell m}(\hat{n}) Y_{\ell m}^*(\hat{n}'). \quad (2.50)$$

If we consider the same direction on the sky, i.e. $\hat{n} \cdot \hat{n}' = 1$, the two-point correlation function becomes the variance in the space of pixels:

$$V_{TT} = C_2(0) = \sum_l \frac{2l + 1}{4\pi} C_l^{TT}. \quad (2.51)$$

We list now all the sources of anisotropy. First, on a scale of $\ell = 1$ there is the dipole anisotropy. The dipole, which is at the level of $\sim 3\text{mK}$, is one of the most important calibrators in modern cosmology. In fact, it is interpreted as the effect of Doppler shift and aberration due to the proper motion of the Solar System with respect to a cosmological rest frame fixed using the CMB. The amplitude of the dipole anisotropy is around $\Delta T_D/T_0 = 10^{-3} = v/c$, where v is the velocity of the observer. After subtracting the Earth's motion around the Sun, and the Sun's motion around the galactic centre, one can determine the velocity of our Galaxy with respect to this cosmological rest frame, which is of $v \approx 600 \text{ km s}^{-1}$ in the direction of the constellations of Hydra-Centaurus.

On smaller scales, from the quadrupole ($\ell = 2$), there are the following sources of primary anisotropies:

- Sachs-Wolfe effect [68]: inhomogeneities in the distribution of matter on the surface of last scattering can generate anisotropies by the redshift or blueshift of photons from regions of different gravitational potential;
- Doppler effect: material moving on the last scattering induces temperature fluctuations by the Doppler effect;
- density contribution: the coupling between matter and radiation at last scattering means that overdense regions are intrinsically hotter than underdense regions if we assume adiabatic fluctuations;

and secondary ones:

- Sunyaev-Zel'dovich effect [69]: anisotropy produced by inverse Compton scattering of CMB photons by free electrons in a hot intergalactic plasma, between the observer and the last scattering surface;
- Integrated Sachs-Wolfe (ISW) effect [70]: photons passing through a time-varying gravitational potential field along the line of sight also suffer an effect similar to the Sachs-Wolfe effect.

On scales that are super-horizon at recombination the Sachs-Wolfe and the late-time Integrated Sachs-Wolfe (ISW) dominate the photon redshifting effects. On sub-horizon scales overdensities recombine later and are redshifted less and hence appear hot. At around $\ell \sim 60$ the anisotropies are dominated by Doppler signals from velocities at last-scattering because the density contribution cancels with the Sachs-Wolfe. As shown in Figure 2.5 there is no scale on which the Sachs-Wolfe limit is accurate, and only at $\ell \ll 60$ are Doppler effects negligible. In the region $10 \leq \ell \leq 100$ the signal has contributions from Doppler, Sachs-Wolfe and density perturbations of comparable magnitudes, as well as a significant early Sachs-Wolfe contribution.

2.3 CMB polarisation

The CMB is also weakly linearly polarised. Thomson scattering of temperature anisotropies on the last scattering surface produces a linear polarisation pattern on the sky that can be simply read off from their quadrupole moments (see e.g. [8] and references therein). Figure 2.6 shows the polarisation anisotropy field as measured by the Planck Satellite [4].

The gravitational instability paradigm predicts that the CMB anisotropies are polarised. According to this paradigm, small fluctuations in the early Universe grow into the large scale structure we observe in the present day Universe. If the temperature anisotropies are indeed the result of primordial fluctuations, their presence at last scattering would polarise the CMB anisotropies themselves. Therefore the polarisation of the CMB represents a fundamental check of our basic assumptions about the behavior of fluctuations in the Universe. The polarisation power spectrum provides information complementary to the temperature power spectrum. The former can be used not only to provide tighter constraints of cosmological parameters but also to investigate physical processes that had would be precluded if just the CMB temperature map were considered. Unfortunately, the polarised signal is really fainter than the signal in temperature: it is at the 10^{-6} level, representing a significant experimental challenge.

2.3.1 Thomson Scattering

The Thomson scattering cross section depends on polarisation as (see e.g. [72]):

$$\frac{d\sigma_T}{d\Omega} \propto |\hat{\epsilon} \cdot \hat{\epsilon}'|, \quad (2.52)$$

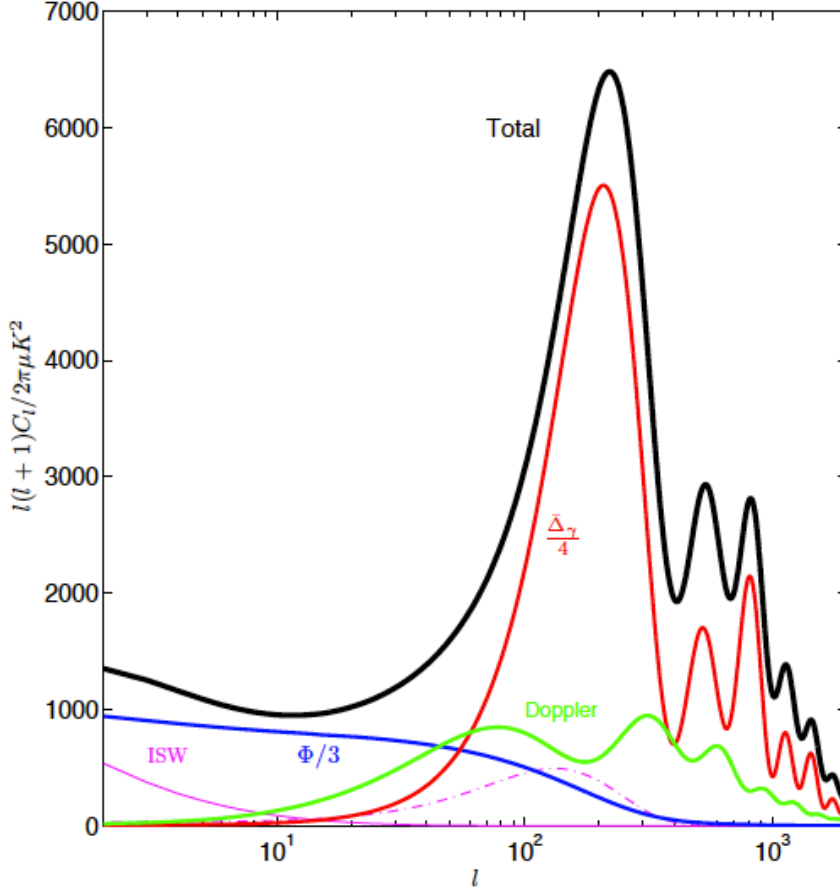


Figure 2.5: Power spectrum of the contributions to the total CMB temperature anisotropy D_ℓ^{TT} . At the small-scale, the density $\bar{\Delta}_\gamma$ (red solid line) is the main contribution from the comoving temperature perturbations at last-scattering. $\Phi/3$ (blue solid line) is the net large-scale contribution from photons climbing out of potential wells (Sachs-Wolf and ISW). $\Phi/3$ and $\bar{\Delta}_\gamma$ source terms have opposite sign, thus their total contribution to the power spectrum is nearly zero at $\ell \sim 60$, where the total signal is then dominated by the Doppler term (green solid line). The magenta ISW contributions come from the late-time change in the potentials when dark energy becomes important at low redshift (magenta solid line), and the early contribution (magenta dash-dotted line) from time-varying potentials soon after recombination as the Universe became fully matter rather than radiation dominated. Image credits: [71].

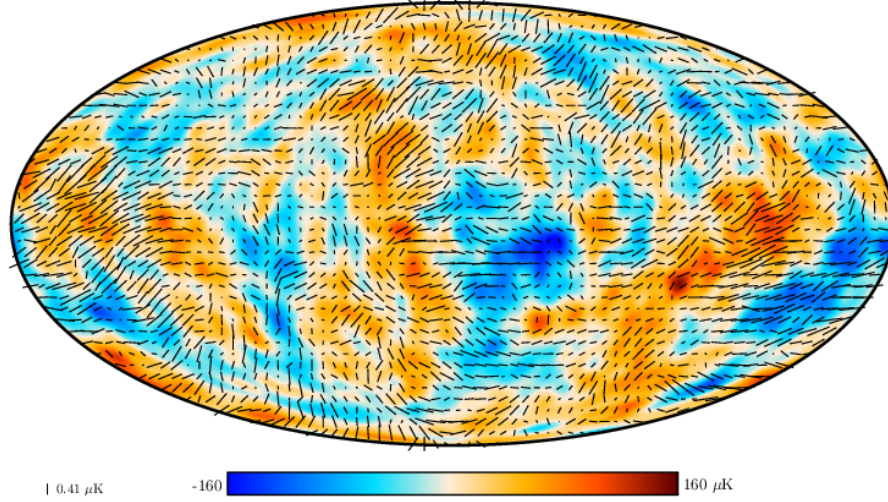


Figure 2.6: Large-scale map of the CMB polarisation anisotropies. The polarisation field, described by vectors of varying length, is superimposed on the CMB temperature map (upper panel), both smoothed to 5° . Image credits: The Planck Collaboration (ESA) [4].

where $\hat{\epsilon}$ ($\hat{\epsilon}'$) are the incident (scattered) polarisation directions. The incident light sets up oscillations of the target electron in the direction of the electric field vector \vec{E} . Thus, the scattered radiation intensity peaks in the direction normal to, with polarisation parallel to, the incident polarisation. More formally, the polarisation dependence of the cross section is dictated by electromagnetic gauge invariance.

If the incoming radiation field were isotropic, orthogonal polarisation states from incident directions separated by $\pi/2$ would balance so that the outgoing radiation would remain unpolarised. Conversely, if the incident radiation field possesses a quadrupolar variation in intensity or temperature (which possesses intensity peaks at $\pi/2$ separations), the result is a linear polarisation of the scattered radiation. If Thomson scattering is rapid, then the randomisation of photon directions that results destroys any quadrupole anisotropy and polarisation. The problem of understanding the polarisation pattern of the CMB thus reduces to understanding the quadrupolar temperature fluctuations at last scattering.

2.3.2 Polarisation E and B modes

The CMB linear polarisation can be described using the Stokes parameters Q and U (whereas the Stokes parameter V defines the circular polarisation state) or in terms of the E - and B -mode scalar field. The Stokes Q and U parameters, typically used to express measurements, are defined with respect to a fixed coordinate system in the sky. In such a coordinate system it is not possible to define a rotationally invariant orthogonal basis on a sphere, so it results to be well defined over a small patch in the sky, but becomes ambiguous once the whole sky is considered. Therefore, in order to formulate cosmological predictions are commonly used two rotationally invariant quantities: the electric and magnetic-type parity fields E and B , which can be derived from the usual Q and U Stokes parameters [73].

The CMB radiation field is characterised by a 2×2 intensity tensor I_{ij} . The Stokes parameters Q and U are defined as:

$$Q = \frac{(I_{11} - I_{22})}{4}, \quad (2.53)$$

$$U = \frac{I_{12}}{2}, \quad (2.54)$$

while the temperature anisotropy is given by:

$$T = \frac{(I_{11} + I_{22})}{4}. \quad (2.55)$$

While the temperature is invariant under a right-handed rotation in the plane perpendicular to direction \hat{n} , Q and U transform under rotation by an angle ϕ as:

$$\begin{aligned} Q' &= Q \cos 2\phi + U \sin 2\phi, \\ U' &= -Q \sin 2\phi + U \cos 2\phi, \end{aligned} \quad (2.56)$$

where $\hat{e}'_1 = \hat{e}_1 \cos \phi + \hat{e}_2 \sin \phi$ and $\hat{e}'_2 = -\hat{e}_1 \sin \phi + \hat{e}_2 \cos \phi$. This means we can construct two quantities from the Stokes Q and U parameters that have spin-2:

$$(Q \pm iU)'(\hat{n}) = e^{\mp 2i\phi} (Q \pm iU)(\hat{n}). \quad (2.57)$$

We may therefore expand each of the quantities in the appropriate spin-weighted basis:

$$(Q \pm iU)(\hat{n}) = \sum_{\ell m} a_{\pm 2, \ell m \pm 2} Y_{\ell m}(\hat{n}), \quad (2.58)$$

where ${}_{\pm 2}Y_{\ell m}(\hat{n})$ are the spin-2 spherical harmonic functions. By inverting Eq. (2.58) one finds the expression for the harmonic coefficients:

$$\begin{aligned} a_{2,\ell m} &= \int d\Omega {}_2Y_{\ell m}^*(\hat{n})(Q + iU)(\hat{n}), \\ a_{-2,\ell m} &= \int d\Omega {}_{-2}Y_{\ell m}^*(\hat{n})(Q - iU)(\hat{n}), \\ &\cdot \end{aligned} \tag{2.59}$$

Linearly combining the quantities $a_{2,\ell m}$ and $a_{-2,\ell m}$, we can introduce the E - and B - harmonic coefficients:

$$a_{E,\ell m} = -\frac{1}{2}(a_{2,\ell m} + a_{-2,\ell m}), \tag{2.60}$$

$$a_{B,\ell m} = -\frac{1}{2i}(a_{2,\ell m} - a_{-2,\ell m}). \tag{2.61}$$

These two combinations behave differently under parity transformation: while E remains unchanged, B changes the sign, in analogy with the electric and magnetic fields. From Eqs. (2.60) and (2.61), one may define the E - and B -mode scalar fields:

$$E(\hat{n}) = \sum_{\ell m} a_{E,\ell m} Y_{\ell m}(\hat{n}), \tag{2.62}$$

$$B(\hat{n}) = \sum_{\ell m} a_{B,\ell m} Y_{\ell m}(\hat{n}). \tag{2.63}$$

Figure 2.7 shows a schematic description of the E - and B -mode patterns. While E -mode is characterised by polarisation vectors radial around cold spots and tangential around hot spots on the sky, B -polarisation is a curl-mode and its vectors have vorticity around any given point on the sky.

The E - and B -mode power spectra can be estimated by:

$$\hat{C}_\ell^{EE} \equiv \frac{1}{2\ell + 1} \sum_{m=-\ell}^{m=+\ell} a_{E,\ell m} (a_{E,\ell m})^*, \tag{2.64}$$

$$\hat{C}_\ell^{BB} \equiv \frac{1}{2\ell + 1} \sum_{m=-\ell}^{m=+\ell} a_{B,\ell m} (a_{B,\ell m})^*, \tag{2.65}$$

while the the cross-correlation of E -modes with the temperature by:

$$\hat{C}_\ell^{TE} \equiv \frac{1}{2\ell + 1} \sum_{m=-\ell}^{m=+\ell} a_{T,\ell m} (a_{E,\ell m})^*. \tag{2.66}$$

Note that the other cross-correlations, i.e. TB and EB, vanish if parity is conserved. Figure 2.8 shows the spectra D_ℓ^{TE} and D_ℓ^{EE} as measured by Planck 2018 Release (PR3) [66].

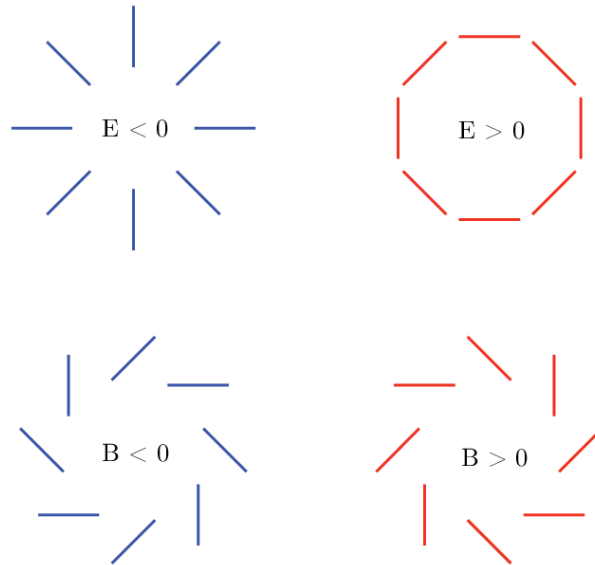


Figure 2.7: . Schematic description of E - and B -mode polarisation pattern. Image credits: [74].

2.3.3 Observations

While the theoretical case for observing polarisation is strong, it is a difficult experimental task to observe its signals. Given that the amplitude of the polarisation is so small the question of foregrounds is even more important than for the temperature anisotropy. Moreover, the level and structure of the various foreground polarisation in the CMB frequency bands is currently not well known. Atmospheric emission is believed to be negligibly polarised, leaving the main astrophysical foregrounds: dust, free-free ⁶, point source emissions and synchrotron, which is the most important polarisation foreground (see e.g. [12, 13, 75]).

At the large angular scales the observations in temperature, as measured by Planck, are limited by the cosmic variance whereas for the polarisation the instrumental noise is several times bigger than the level of the cosmic variance. Polarisation remains to be further investigated: in particular, information in the E modes have not been fully extracted yet and the primordial B modes have not been detected and only upper limits are provided. For this reason the future CMB missions, like the satellite Litebird [76], are so im-

⁶Bremsstrahlung emission is intrinsically unpolarised but can be partially polarised by Thomson scattering within the HII regions. This is a small effect which is expected to polarise the emission by less than 10%.

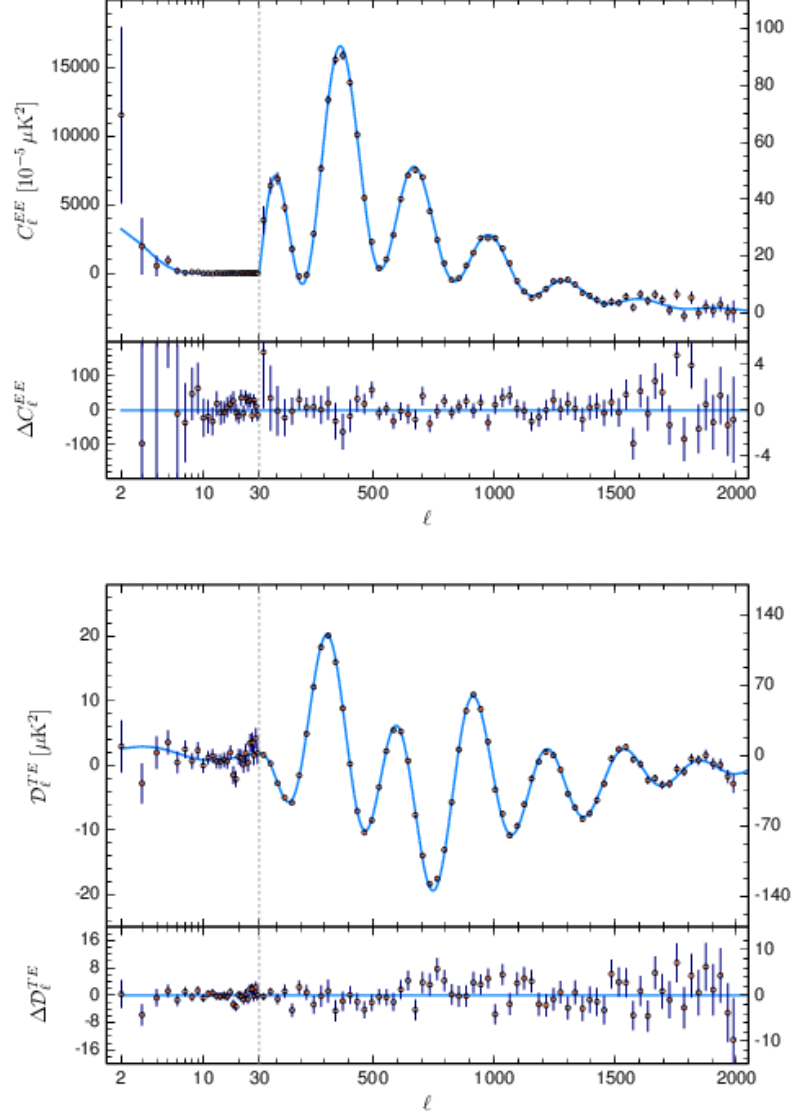


Figure 2.8: Frequency-averaged EE (upper panel) and TE (lower panel) band power. Blue lines in upper boxes represent the TE and EE theoretical spectra computed from the best-fit model of Fig 2.4. Residuals with respect to this theoretical model are shown in the lower boxes. The error bars show $\pm 1\sigma$ uncertainties. The blue lines in the lower boxes show the best-fit temperature-to-polarisation ($T \rightarrow P$) leakage model, fitted separately to the TE and EE spectra. Image credits: Planck ESA Collaboration [66].

portant for the observation of the CMB polarisation. In these experiments, aimed at detecting the primordial B-modes, the focus is on the best technologies that allow the minimization of both instrumental and astrophysical systematics.

Chapter 3

CMB anomalies: lack of power anomaly

The so-called CMB anomalies are unexpected features observed at large angular scale in the CMB maps (above a few degrees), as observed by the COBE, WMAP and Planck satellites, that deviate from the cosmological model Λ CDM with a statistical significance typically around 2-3 σ C.L.. These anomalies are not all independent and a certain degree of correlation exists. In particular, the maps of temperature anisotropies exhibit low variance, a lack of correlation on the largest angular scales [77], a preference for odd parity modes [78], a hemispherical power asymmetry [79], an alignment between various low multipole moments [80], an alignment between those low multipole moments and the motion and geometry of the Solar System [81], and an unexpectedly large cold spot in the Southern hemisphere [82]. Historically, the first observed anomalous feature, already within the COBE data, was the smallness of the quadrupole moment. It confirmed to be low when WMAP released its data [64]. However it was also shown that cosmic variance allows for such a small value. Another rediscovery in the first release of WMAP [64] was that the angular two-point correlation function, at angular scales larger than 60 degrees is unexpectedly close to zero, where a non-zero correlation signal was expected. This feature had already been observed by COBE [83], and was rediscovered by WMAP. Detailed further investigations of the lack of angular correlation have been presented in [81, 84, 85].

The possibility that these large-scale CMB features are due to instrumental systematics is quite low since independent experiments, COBE, WMAP and Planck, agree on these features. Better understanding of the anomalies will be driven in the future by observations of new quantities on very large spatial scales, such as lensing [86] and CMB polarisation [87], as well as large-scale structure of the Universe[88].

3.1 Introduction

In this chapter we focus on the lack of power anomaly, an intriguing feature that seems to be correlated with a low quadrupole, although it cannot be explained by a lack of quadrupole power alone. This anomaly consists in a missing of power with respect to what foreseen by Λ CDM model. This effect has been studied with the variance estimator in WMAP data [9, 10, 11] and in Planck 2013 [12] and Planck 2015 [13] data, measuring a lower-tail-probability of the order of few per cent. Such a percentage can become even smaller, below 1%, once only regions at high Galactic latitude are taken into account [11].

WMAP and Planck agree well on this feature, so it is very hard, albeit not impossible, to attribute this anomaly to instrumental effects. Moreover it is also difficult to believe that a lack of power could be generated by residuals of astrophysical emission, since the latter is not expected to be correlated¹ with the CMB and therefore an astrophysical residual should increase the total power rather than decreasing it. Hence, it appears natural to accept this as a real feature present in the CMB pattern.

An early fast-roll phase of the inflaton could naturally explain such a lack of power, see e.g. [14, 15, 16, 17, 18]: this anomaly might then witness a new cosmological phase before the standard inflationary era (see e.g. [19, 20, 21]).

However, with only the observations based on the temperature map, this anomaly is not statistically significant enough to be used to claim new physics beyond the standard cosmological model. Therefore, it is legitimate to conservatively interpret it as a statistical fluke of the Λ CDM concordance model.

We revisit here the former statement by also considering the counterpart in polarisation of this anomaly. In this chapter we propose a new one-dimensional estimator which combines information from the CMB TT, EE and TE angular power spectra at the largest angular scales, i.e. $2 \leq \ell \leq 30$, with ℓ being the multipole moment. We anticipate that the outcomes of this analysis show that considering PLANCK 2015 data in the harmonic range mentioned above, noise dominated polarisation provides an information content at the level of 4% to this estimator which, even though small, has a non-negligible impact on the analysis, the lower-tail-probability shifting downward from 7.22% (obtained considering only temperature data) to 3.68% C.L. (obtained considering jointly temperature and polarisation data). Furthermore, we forecast that for future CMB observations, polarisation at the largest angular scales can weight as much as $\sim 23\%$ of the total information entering our estimator.

¹In particular they should be anti-correlated to produce a decrease of the total power.

We argue that the inclusion of large-scale E-mode polarisation could crucially help in changing the interpretation from a simple statistical fluke into the detection of a new physical phenomenon. Therefore, future CMB large-scale polarised observations, which are typically aimed at primordial B-modes, might provide signals of new physics also through the other polarised CMB mode, i.e. the E-mode.

The chapter is organised as follows: in Section 3.2 we introduce the algebra needed to build the new estimator which condensates all the TT, EE and TE information into a 1-D object and in Section 3.2.1 we elaborate on its optimised (i.e. minimum variance) version; Section 3.3 is devoted to the description of the dataset used and of the simulations employed; in Section 3.4 we present the results on PLANCK data and provide estimates of the improvement expected with future CMB polarised observations, as the Lite-BIRD satellite [76]; conclusions and outlooks are drawn in Section 3.5 and 3.6 respectively.

3.2 A new one-dimensional joint estimator

The idea of this joint estimator starts from the usual equations employed to simulate temperature and E-mode CMB maps, see e.g. [89]:

$$a_{T,\ell m} = \sqrt{C_\ell^{TT,th}} \xi_{\ell m}^1, \quad (3.1)$$

$$a_{E,\ell m} = \frac{C_\ell^{TE,th}}{\sqrt{C_\ell^{TT,th}}} \xi_{\ell m}^1 + \sqrt{C_\ell^{EE,th} - \frac{(C_\ell^{TE,th})^2}{C_\ell^{TT,th}}} \xi_{\ell m}^2, \quad (3.2)$$

where $a_{\ell m}^{T,E}$ are the coefficients of the Spherical Harmonics (with ℓ, m being integers numbers so that $\ell \in \{0, 1, 2, 3, \dots\}$ and $-\ell \leq m \leq \ell$), $C_\ell^{TT,th}$, $C_\ell^{EE,th}$ and $C_\ell^{TE,th}$ are the theoretical angular power spectra (APS) for TT , EE and TE and with $\xi_{\ell m}^{1,2}$ being Gaussian random variables, uncorrelated, with zero mean and unit variance:

$$\langle \xi_{\ell m}^1 \rangle = 0, \quad (3.3)$$

$$\langle \xi_{\ell m}^2 \rangle = 0, \quad (3.4)$$

$$\langle \xi_{\ell m}^1 \xi_{\ell' m'}^2 \rangle = 0, \quad (3.5)$$

$$\langle \xi_{\ell m}^1 \xi_{\ell' m'}^1 \rangle = \langle \xi_{\ell m}^2 \xi_{\ell' m'}^2 \rangle = \delta_{\ell \ell'} \delta_{m m'}. \quad (3.6)$$

From equations (3.1),(3.2) one can compute the corresponding APS, defined as:

$$C_\ell^{TT,sim} = \frac{1}{2\ell+1} \sum_{m=-\ell}^{\ell} a_{T,\ell m} (a_{T,\ell m})^*, \quad (3.7)$$

$$C_\ell^{TE,sim} = \frac{1}{2\ell+1} \sum_{m=-\ell}^{\ell} a_{T,\ell m} (a_{E,\ell m})^*, \quad (3.8)$$

$$C_\ell^{EE,sim} = \frac{1}{2\ell+1} \sum_{m=-\ell}^{\ell} a_{E,\ell m} (a_{E,\ell m})^*, \quad (3.9)$$

where the label *sim* stands for ‘‘simulated’’, i.e. realised randomly from the theoretical spectra $C_\ell^{TT,th}$, $C_\ell^{EE,th}$ and $C_\ell^{TE,th}$, finding the following expressions,

$$C_\ell^{TT,sim} = C_\ell^{TT,th} \frac{|\vec{\xi}_\ell^{(1)}|^2}{2\ell+1}, \quad (3.10)$$

$$C_\ell^{EE,sim} = \frac{(C_\ell^{TE,th})^2}{C_\ell^{TT,th}} \left[\frac{|\vec{\xi}_\ell^{(1)}|^2}{2\ell+1} - \frac{|\vec{\xi}_\ell^{(2)}|^2}{2\ell+1} \right] + C_\ell^{EE,th} \frac{|\vec{\xi}_\ell^{(2)}|^2}{2\ell+1} + 2a_\ell \frac{C_\ell^{TE,th}}{C_\ell^{TT,th}} \frac{\vec{\xi}_\ell^{(1)} \cdot \vec{\xi}_\ell^{(2)}}{2\ell+1}, \quad (3.11)$$

$$C_\ell^{TE,sim} = C_\ell^{TE,th} \frac{|\vec{\xi}_\ell^{(1)}|^2}{2\ell+1} + a_\ell \frac{\vec{\xi}_\ell^{(1)} \cdot \vec{\xi}_\ell^{(2)}}{2\ell+1}, \quad (3.12)$$

where $\vec{\xi}_\ell^{(1/2)}$ are vectors with $2\ell+1$ components, i.e.

$$\vec{\xi}_\ell^{(1/2)} = \left(\xi_{-\ell}^{(1/2)}, \xi_{-\ell+1}^{(1/2)}, \dots, \xi_0^{(1/2)}, \dots, \xi_{\ell-1}^{(1/2)}, \xi_\ell^{(1/2)} \right), \quad (3.13)$$

and a_ℓ is defined as:

$$a_\ell \equiv \sqrt{C_\ell^{EE,th} C_\ell^{TT,th} - (C_\ell^{TE,th})^2}. \quad (3.14)$$

It is easy to check that taking the ensemble average of equations (3.10),(3.11) and (3.12) yields to:

$$\langle C_\ell^{TT,sim} \rangle = C_\ell^{TT,th}, \quad (3.15)$$

$$\langle C_\ell^{EE,sim} \rangle = C_\ell^{EE,th}, \quad (3.16)$$

$$\langle C_\ell^{TE,sim} \rangle = C_\ell^{TE,th}, \quad (3.17)$$

since for each ℓ , as a consequence of equations (3.5),(3.6),

$$\left\langle \frac{|\bar{\xi}_\ell^{(1)}|^2}{2\ell+1} \right\rangle = 1, \quad (3.18)$$

$$\left\langle \frac{|\bar{\xi}_\ell^{(2)}|^2}{2\ell+1} \right\rangle = 1, \quad (3.19)$$

$$\langle \bar{\xi}_\ell^{(1)} \cdot \bar{\xi}_\ell^{(2)} \rangle = 0. \quad (3.20)$$

Equations (3.10),(3.11) and (3.12) can be inverted, giving the following set of equations:

$$\frac{|\bar{\xi}_\ell^{(1)}|^2}{2\ell+1} = \frac{C_\ell^{TT}}{C_\ell^{TT,th}}, \quad (3.21)$$

$$\begin{aligned} \frac{|\bar{\xi}_\ell^{(2)}|^2}{2\ell+1} &= \frac{C_\ell^{EE}}{a_\ell^2} C_\ell^{TT,th} - \frac{C_\ell^{TT,th}}{a_\ell^2} \left(\frac{C_\ell^{TE,th}}{C_\ell^{TT,th}} \right)^2 C_\ell^{TT} \\ &\quad - 2 \frac{C_\ell^{TE,th}}{a_\ell^2} \left[C_\ell^{TE} - \frac{C_\ell^{TE,th}}{C_\ell^{TT,th}} C_\ell^{TT} \right], \end{aligned} \quad (3.22)$$

$$\frac{\bar{\xi}_\ell^{(1)} \cdot \bar{\xi}_\ell^{(2)}}{2\ell+1} = \frac{1}{a_\ell} \left[C_\ell^{TE} - \frac{C_\ell^{TE,th}}{C_\ell^{TT,th}} C_\ell^{TT} \right], \quad (3.23)$$

where we have dropped out the label “*sim*” for sake of simplicity. Now, we can interpret C_ℓ^{TT} , C_ℓ^{EE} and C_ℓ^{TE} as the CMB APS recovered by a CMB experiment under realistic circumstances, i.e. including noise residuals, incomplete sky fraction, finite angular resolution and also residuals of systematic effects. Once the model is chosen, i.e. once the spectra $C_\ell^{TT,th}$, $C_\ell^{EE,th}$ and $C_\ell^{TE,th}$ are fixed, for example to Λ CDM model, one can compute the following objects:

$$x_\ell^{(1)} \equiv \frac{|\bar{\xi}_\ell^{(1)}|^2}{2\ell+1}, \quad (3.24)$$

$$x_\ell^{(2)} \equiv \frac{|\bar{\xi}_\ell^{(2)}|^2}{2\ell+1}, \quad (3.25)$$

$$x_\ell^{(3)} \equiv \frac{\bar{\xi}_\ell^{(1)} \cdot \bar{\xi}_\ell^{(2)}}{2\ell+1}, \quad (3.26)$$

for the observations and/or for the corresponding realistic simulations.

In the following we will call the variables $x_\ell^{(1)}$, $x_\ell^{(2)}$ and $x_\ell^{(3)}$ as APS of the normal random variables or normalised APS (henceforth NAPS). The advantage of using NAPS, instead of the standard APS, is that they are

dimensionless and similar amplitude numbers. For these reasons they can be easily combined to define a 1-D estimator in harmonic space, which depends on temperature, E-mode polarisation and their cross-correlation. A natural definition of this 1-D estimator, called P , is the following:

$$P = \frac{1}{(\ell_{max} - 1)} \sum_{\ell=2}^{\ell_{max}} (x_{\ell}^{(1)} + x_{\ell}^{(2)}). \quad (3.27)$$

The estimator P could be interpreted as a dimensionless normalised mean power, which jointly combines the temperature and polarisation data. The expectation value of P is:

$$\langle P \rangle = 2, \quad (3.28)$$

regardless of the value of ℓ_{max} . Note that a definition of the following type:

$$S = \frac{1}{(\ell_{max} - 1)} \sum_{\ell=2}^{\ell_{max}} (x_{\ell}^{(1)} + x_{\ell}^{(2)} + x_{\ell}^{(3)}), \quad (3.29)$$

is expected to have less signal-to-noise ratio with respect to P because while S and P have the same expectation value, the intrinsic variance of P is in general smaller than the one of S .

We will see in the following that Eq. (3.27) is noise-limited for Planck data due to $x_{\ell}^{(2)}$ (its polarisation part) and in practice can be employed only up to $\ell_{max} = 6$. An optimised version of this estimator, given in next Section 3.2.1, does not suffer from this issue and can be employed up to the maximum multipole considered in this analysis, i.e. $\ell_{max} = 30$.

3.2.1 Optimised estimator

In equation (3.27) the NAPS $x_{\ell}^{(1)}$ and $x_{\ell}^{(2)}$ are combined with equal weights. However the signal-to-noise ratios of the two NAPS are different even in the cosmic variance limit case: therefore one might wonder which are the best weights that we can use in the definition of the joint estimator in order to make it optimal, i.e. with minimum variance. We define the optimised estimator \tilde{P} as:

$$\tilde{P} \equiv \frac{1}{(\ell_{max} - 1)} \sum_{\ell=2}^{\ell_{max}} (\alpha_{\ell} x_{\ell}^{(1)} + \beta_{\ell} x_{\ell}^{(2)}). \quad (3.30)$$

We use the method of the Lagrange multipliers to minimise the variance of \tilde{P} , i.e. $var(\tilde{P})$, keeping fixed the expected value of \tilde{P} . This can be achieved by requiring that

$$\alpha_{\ell} + \beta_{\ell} = const = 2, \quad (3.31)$$

for each multipole ℓ . The choice of the value for the constant is totally arbitrary, setting $const = 2$ allows to make the comparison between P and \tilde{P} more easily. Replacing the definition of \tilde{P} , see equation (3.30), in the expression of $var(\tilde{P})$, one obtains:

$$\begin{aligned} var(\tilde{P}) &\equiv \langle (\tilde{P} - \langle \tilde{P} \rangle)^2 \rangle = \langle (\tilde{P})^2 \rangle - \langle \tilde{P} \rangle^2 = \\ &= \sum_{\ell} var(\tilde{P}_{\ell}), \end{aligned} \quad (3.32)$$

where the cross-terms among different multipoles go exactly to zero in the full sky case, and with $var(\tilde{P}_{\ell})$ defined as:

$$var(\tilde{P}_{\ell}) = \bar{\alpha}_{\ell}^2 var(x_{\ell}^{(1)}) + \bar{\beta}_{\ell}^2 var(x_{\ell}^{(2)}) + 2\bar{\alpha}_{\ell}\bar{\beta}_{\ell} cov(x_{\ell}^{(1)}, x_{\ell}^{(2)}), \quad (3.33)$$

where the barred quantities are defined as $\bar{y} = y/(\ell_{max} - 1)$ and where $var(x_{\ell}^{(1)})$ and $var(x_{\ell}^{(2)})$ are the variance of $x_{\ell}^{(1)}$ and $x_{\ell}^{(2)}$ respectively, and $cov(x_{\ell}^{(1)}, x_{\ell}^{(2)})$ is their covariance

$$cov(x_{\ell}^{(1)}, x_{\ell}^{(2)}) = \langle (x_{\ell}^{(1)} - \langle x_{\ell}^{(1)} \rangle)(x_{\ell}^{(2)} - \langle x_{\ell}^{(2)} \rangle) \rangle. \quad (3.34)$$

Because of Eq. (3.32), the minimisation of $var(\tilde{P})$ is equivalent to the minimisation of each $var(\tilde{P}_{\ell})$. As it is customary in the Lagrange multiplier method, for each multipole ℓ we introduce a new variable $\bar{\lambda}_{\ell}$, known as the Lagrange multiplier, and minimise the function $F(\bar{\alpha}_{\ell}, \bar{\beta}_{\ell}, \bar{\lambda}_{\ell})$ which is defined as:

$$F(\bar{\alpha}_{\ell}, \bar{\beta}_{\ell}, \bar{\lambda}_{\ell}) = var(\tilde{P}_{\ell}) + \bar{\lambda}_{\ell} \left(\bar{\alpha}_{\ell} + \bar{\beta}_{\ell} - \frac{2}{(\ell_{max} - 1)} \right). \quad (3.35)$$

This is equivalent to minimise the variance of \tilde{P}_{ℓ} on the constrain given by equation (3.31) (multiplied by $1/(\ell_{max} - 1)$). Therefore we compute the partial derivatives with respect to the coefficients $\bar{\alpha}_{\ell}$, $\bar{\beta}_{\ell}$ and $\bar{\lambda}_{\ell}$ and set them to be zero:

$$\frac{\partial F(\bar{\alpha}_{\ell}, \bar{\beta}_{\ell}, \bar{\lambda}_{\ell})}{\partial \bar{\alpha}_{\ell}} = 2\bar{\alpha}_{\ell} var(x_{\ell}^{(1)}) + 2\bar{\beta}_{\ell} cov(x_{\ell}^{(1)}, x_{\ell}^{(2)}) + \bar{\lambda}_{\ell} = 0, \quad (3.36)$$

$$\frac{\partial F(\bar{\alpha}_{\ell}, \bar{\beta}_{\ell}, \bar{\lambda}_{\ell})}{\partial \bar{\beta}_{\ell}} = 2\bar{\beta}_{\ell} var(x_{\ell}^{(2)}) + 2\bar{\alpha}_{\ell} cov(x_{\ell}^{(1)}, x_{\ell}^{(2)}) + \bar{\lambda}_{\ell} = 0, \quad (3.37)$$

$$\frac{\partial F(\bar{\alpha}_{\ell}, \bar{\beta}_{\ell}, \bar{\lambda}_{\ell})}{\partial \bar{\lambda}_{\ell}} = \bar{\alpha}_{\ell} + \bar{\beta}_{\ell} - \frac{2}{(\ell_{max} - 1)} = 0. \quad (3.38)$$

This set of equations is solved by equations:

$$\alpha_\ell = 2 \frac{\text{var}(x_\ell^{(2)}) - \text{cov}(x_\ell^{(1)}, x_\ell^{(2)})}{\text{var}(x_\ell^{(1)}) + \text{var}(x_\ell^{(2)}) - 2\text{cov}(x_\ell^{(1)}, x_\ell^{(2)})}, \quad (3.39)$$

$$\beta_\ell = 2 \frac{\text{var}(x_\ell^{(1)}) - \text{cov}(x_\ell^{(1)}, x_\ell^{(2)})}{\text{var}(x_\ell^{(1)}) + \text{var}(x_\ell^{(2)}) - 2\text{cov}(x_\ell^{(1)}, x_\ell^{(2)})}, \quad (3.40)$$

$$\lambda_\ell = -2 \left(\text{cov}(x_\ell^{(1)}, x_\ell^{(2)}) + \frac{\text{var}(x_\ell^{(1)})\text{var}(x_\ell^{(2)}) - \text{cov}(x_\ell^{(1)}, x_\ell^{(2)}) (\text{var}(x_\ell^{(1)}) + \text{var}(x_\ell^{(2)}))}{\text{var}(x_\ell^{(1)}) + \text{var}(x_\ell^{(2)}) - 2\text{cov}(x_\ell^{(1)}, x_\ell^{(2)})} \right), \quad (3.41)$$

where we return to α_ℓ , β_ℓ and λ_ℓ by multiplying the barred quantities to $(\ell_{max} - 1)$ factor.

These coefficients, namely α_ℓ and β_ℓ as defined in Eqs.(3.39 and (3.40), will be actually used to build the \tilde{P} estimator. Note that as done for P , \tilde{P} , which depends on ℓ_{max} , has been normalised such that $\langle \tilde{P} \rangle = 2$ for any value of ℓ_{max} . Note also, that \tilde{P} can be employed up to $\ell_{max} = 30$ both for Planck and LiteBIRD-like simulated data: what changes between the two cases is the set of the coefficients α_ℓ and β_ℓ , or, in other words, the relative contribution of the temperature and polarisation data.

3.3 Dataset and simulations

We use the public Planck 2015² data release (PR2).³ In temperature we consider the Planck 2015 Commander map with its standard mask ($f_{sky}^T = 93.6$) entering the temperature sector of the low- ℓ PLANCK, whereas in polarisation we employ a noise-weighted combination of WMAP9 and PLANCK data as done in [90]. This allows to gain some signal-to-noise ratio and to deal with a larger sky fraction in polarisation ($f_{sky}^P = 73.9$). Temperature and polarisation maps are sampled at HEALPix⁴ [91] resolution $N_{side} = 16$. For sake of simplicity we will refer to this data set as the PLANCK-WMAP low- ℓ data set.

In order to build the estimators P and \tilde{P} , as defined in equations (3.27) and (3.30), we estimate the six CMB APS from 10000 simulated CMB-plus-noise maps over the observed sky fraction, with the optimal angular power

²<http://www.cosmos.esa.int/web/planck/pla>.

³At the moment of this analysis the corresponding Planck 2018 (PR3) likelihood code and corresponding data set was not publicly available.

⁴<http://healpix.sourceforge.net/>.

spectrum estimator *BolPol* [92]. The signal is extracted from the PLANCK fiducial Λ CDM model defined by the following parameters

$$\begin{aligned}\Omega_b h^2 &= 0.02224 \\ \Omega_c h^2 &= 0.1187 \\ 100 \theta &= 1.04101 \\ \tau &= 0.065 \\ \log[10^{10} A_s] &= 3.060 \\ n_s &= 0.9673\end{aligned}$$

being Ω_b the baryon density parameter, Ω_c the cold dark matter density parameter, θ the angle subtended by the sound horizon at recombination, τ the re-ionization optical depth, A_s the amplitude and n_s the spectral index of primordial scalar perturbation power spectrum. This set of parameters is obtained confronting data and models through the likelihood function defined as the sum of the three following likelihoods (see [93, 90] for further details):

- a pixel based low- ℓ likelihood, $2 \leq \ell \leq 29$, where the Planck 2015 Commander map enters the temperature sector and a noise-weighted combination of WMAP9 and PLANCK data enters the polarisation sector of this likelihood⁵;
- a high- ℓ Planck TT likelihood based on APS of Planck data in the range $30 \leq \ell \leq 2500$;
- the Planck lensing likelihood, based on the range $40 \leq \ell \leq 400$ of the four-point correlation function of the temperature anisotropies.

The noise of the simulated maps is generated through Cholesky decomposition of the total noise covariance matrix, i.e. \mathbb{N} , defined over the observed pixels. In particular, it is possible to generate a noise map, m_n , statistically compatible with \mathbb{N} , through the following expression:

$$m_n = \mathbb{L}y, \quad (3.42)$$

where \mathbb{L} is the lower triangular matrix of the Cholesky decomposition [94] such that:

$$\mathbb{N} = \mathbb{L}\mathbb{L}^t, \quad (3.43)$$

⁵Note that the low- ℓ data-set used to perform the analysis is exactly the same as the one entering the low- ℓ likelihood. This makes the whole investigation self-consistent.

and y is a vector with the same dimension as m_n and whose entries are randomly extracted from a normal distribution. In this way m_n turns out to be statistically compatible with \mathbb{N} since:

$$\langle (m_n)(m_n)^t \rangle = \langle (\mathbb{L}y)(\mathbb{L}y)^t \rangle = \mathbb{L}\langle yy^t \rangle \mathbb{L}^t = \mathbb{L}\mathbb{I}\mathbb{L}^t = \mathbb{N}, \quad (3.44)$$

where \mathbb{I} is the identity matrix and $\langle \dots \rangle$ stands for ensemble average.

Monte Carlo simulations for the PLANCK-WMAP low- ℓ data set are validated in Figure 3.1, where the average of the NAPS ($x_\ell^{(1)}$, $x_\ell^{(2)}$ and $x_\ell^{(3)}$) are shown respectively in the upper, middle and lower panels along with their uncertainties of the means (σ_μ). Each panel displays also a lower box where for each ℓ it is shown the distance of mean in units of standard deviation of the mean itself. Figure 3.2 shows the low- ℓ estimates of $x_\ell^{(1)}$, $x_\ell^{(2)}$ and $x_\ell^{(3)}$ of the PLANCK-WMAP low- ℓ data set (red dots), with the contours at one, two and three σ as estimated from simulations (blue regions).

The choice of the ℓ_{max} parameter, which enters the definition of P , see Eq.(3.27), is dictated by the signal-to-noise ratio of $x_\ell^{(2)}$ since $x_\ell^{(1)}$ is always signal dominated in the whole range considered. The total signal-to-noise ratio $(S/N)^2$ contained in $x_\ell^{(1)}$ or $x_\ell^{(2)}$ up to a maximum harmonic scale ℓ_{max} , is defined by summing up $(S/N)_l^2$ over the multipoles ℓ from 2 to ℓ_{max} as:

$$\left(\frac{S}{N}\right)^2 = \sum_{l=2}^{\ell_{max}} \left(\frac{S}{N}\right)_l^2 \quad (3.45)$$

where

$$\left(\frac{S}{N}\right)_l^2 = \frac{\langle x_\ell^{(i)} \rangle^2}{\langle (x_\ell^{(i)} - \langle x_\ell^{(i)} \rangle)^2 \rangle} = \frac{1}{\langle (x_\ell^{(i)} - 1)^2 \rangle}, \quad (3.46)$$

since $\langle x_\ell^{(i)} \rangle = 1$, for $i = 1, 2$. In Figure 3.3 we display the signal-to-noise ratio of the NAPS for the PLANCK-WMAP low- ℓ data set (see solid lines). While for $x_\ell^{(1)}$ such a ratio grows monotonically (red line), for $x_\ell^{(2)}$ (solid blue line) it saturates around $\ell_{max} \sim 6$. Consequently we will employ the estimator P with $\ell_{max} = 6$ for the PLANCK-WMAP low- ℓ data set.

Simulations for a LiteBIRD-like noise level [95] are obtained following the same procedure as described above but dividing the polarisation part of the noise covariance matrix by a factor of 100. The signal-to-noise ratio of $x_\ell^{(2)}$ for the LiteBIRD-like noise level is instead shown in Figure 3.3 as a dashed blue line. Since such a ratio grows monotonically, in this case we can choose the maximum ℓ_{max} available in our simulations, i.e. $\ell_{max} = 30$.

Note that this limitation in the choice of ℓ_{max} does not apply to \tilde{P} . In this case the coefficients α_ℓ and β_ℓ adjust themselves automatically (depending on the signal-to-noise ratio) such that noise-dominated multipoles do not contribute to the estimator, see also Section 3.2.1 and 3.4.2.

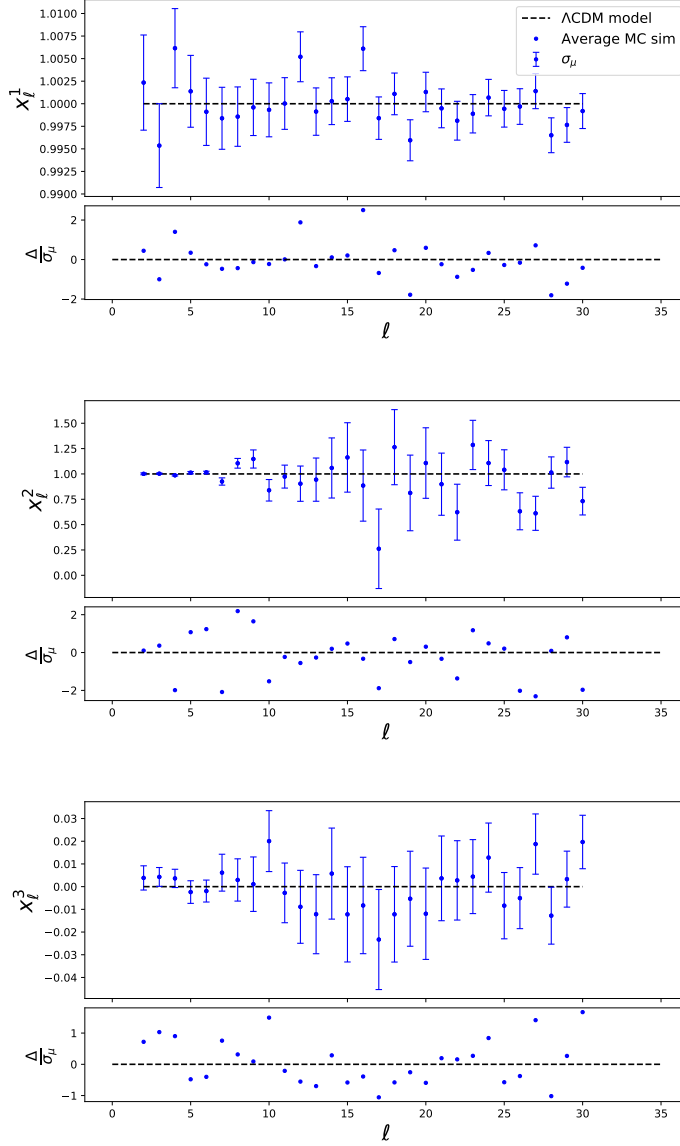


Figure 3.1: Averages of $x_\ell^{(1)}$ (upper panel), $x_\ell^{(2)}$ (middle panel) and $x_\ell^{(3)}$ (lower panel) as a function of ℓ obtained from Monte Carlo simulations corresponding to the PLANCK-WMAP low- ℓ data. Error bars represent the uncertainties associated to the averages. Each panel displays also a lower box where for each ℓ it is shown the distance of mean in units of standard deviation of the mean itself. Dashed horizontal lines represent what theoretically expected for the averages of $x_\ell^{(1)}$, $x_\ell^{(2)}$ and $x_\ell^{(3)}$, see equations (3.18),(3.19) and (3.20). Figure taken from:[22]

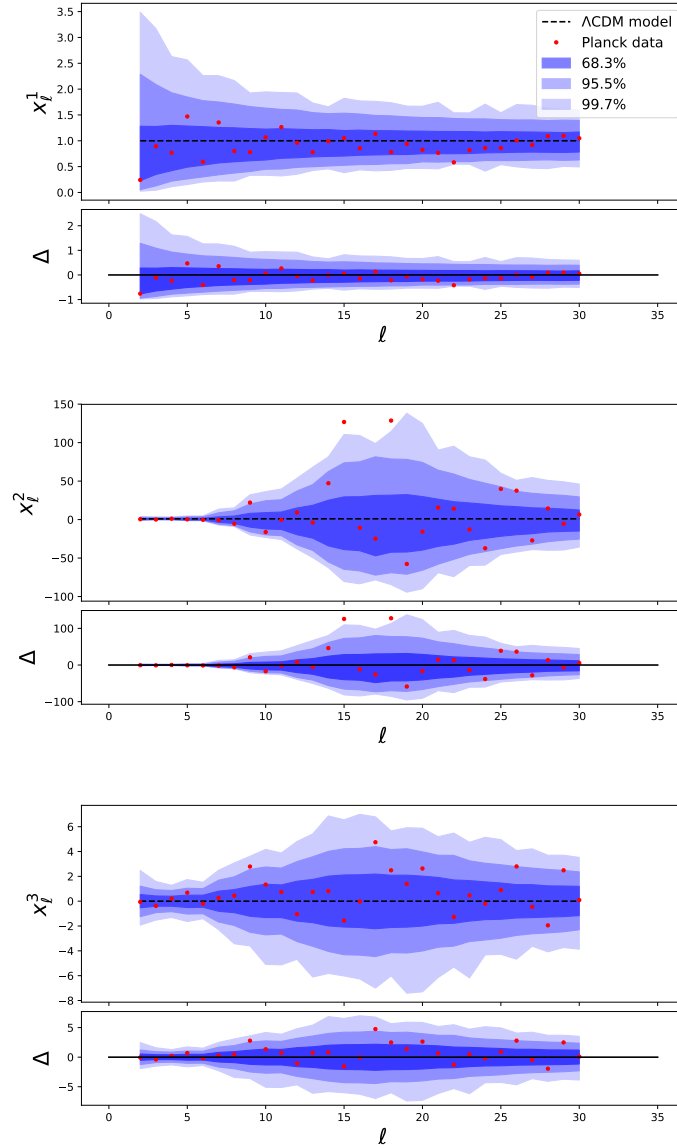


Figure 3.2: Red dots represent $x_\ell^{(1)}$ (upper panel), $x_\ell^{(2)}$ (middle panel) and $x_\ell^{(3)}$ (lower panel) as a function of ℓ obtained from the PLANCK-WMAP low- ℓ data set. Error bars (blue regions) represent the uncertainties associated to the estimates. Dashed horizontal lines represent what theoretically expected for the averages of $x_\ell^{(1)}$, $x_\ell^{(2)}$ and $x_\ell^{(3)}$, see equations (3.18), (3.19) and (3.20). Each panel displays also a lower box where for each ℓ it is shown the distance of the estimates in units of standard deviation of the estimate itself. Figure taken from: [22]

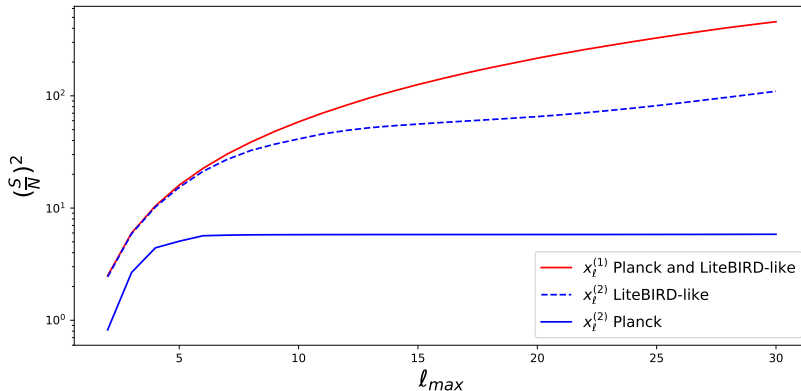


Figure 3.3: Signal-to-noise ratio of $x_\ell^{(1)}$ (red curve) and $x_\ell^{(2)}$ as a function of ℓ_{max} for the PLANCK-WMAP low- ℓ data set (solid blue line) and for the LiteBIRD-like noise level (dashed blue line). While the signal contained in $x_\ell^{(1)}$ grows monotonically in the considered range, $x_\ell^{(2)}$ saturates at $\ell_{max} \sim 6$ for the PLANCK-WMAP. Instead the signal-to-noise ratio of $x_\ell^{(2)}$ for the LiteBIRD-like noise level grows monotonically, and therefore, in this case, we can choose the maximum ℓ_{max} available in our simulations, i.e. $\ell_{max} = 30$. Figure taken from:[22]

3.4 Results of the analyses

3.4.1 Results for P

In Figure 3.4 we plot the empirical distribution expected in Λ CDM model for P with $\ell_{max} = 6$ considering the PLANCK-WMAP low- ℓ characteristics. The red vertical line stands for the observed value of the PLANCK-WMAP low- ℓ data set. The lower-tail probability (LTP) of the observed value of P is 3.63%. Such a value is smaller than the corresponding LTP of P when, still with $\ell_{max} = 6$, we neglect the contribution of $x_\ell^{(2)}$ in eq. (3.27). In that case the LTP we obtain is 17.63%. Similarly for the same maximum multipole, when we neglect the contribution of $x_\ell^{(1)}$ in P , we get a LTP of 6.71%. In short, the combination of temperature and polarisation data provides a LTP smaller than what obtained with only temperature or only polarisation, although our findings cannot be considered as statistically anomalous.

In Figure 3.5 we plot the empirical distribution of P expected in Λ CDM model with $\ell_{max} = 30$ for the PLANCK-WMAP low- ℓ data set and for the LiteBIRD-like noise level. In order to evaluate the improvement of the latter with respect to the former, we build the ratios between the widths of the empirical distributions of P , corresponding to the level of 68.3%, for the LiteBIRD-like noise level (σ_{LB}) and for the PLANCK-WMAP low- ℓ noise

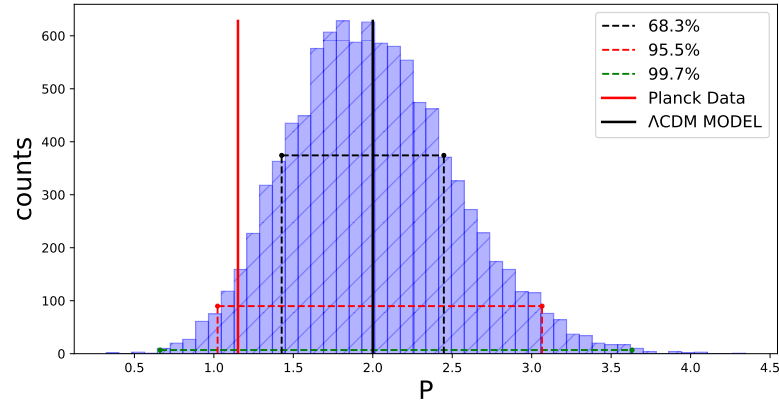


Figure 3.4: Empirical distribution of the P estimator, see eq. (3.27), for $\ell_{max} = 6$. The red and the black vertical lines represent the values of the Planck data and of the Λ CDM model respectively. The black, red and green dashed lines indicate the boundaries of the 68.3%, 95.5% and 99.7% confidence regions respectively. Figure taken from:[22]

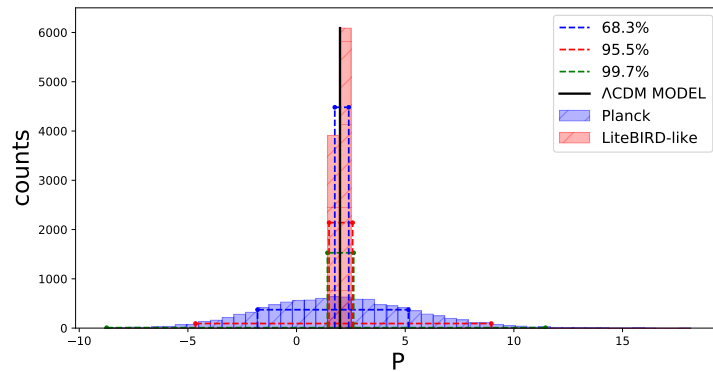


Figure 3.5: Empirical distribution of the P estimator, see eq. (3.27), for $\ell_{max} = 30$. Blue histogram refers to the PLANCK-WMAP low- ℓ data set, while the red one is for the case of the LiteBIRD-like noise level. Figure taken from:[22]

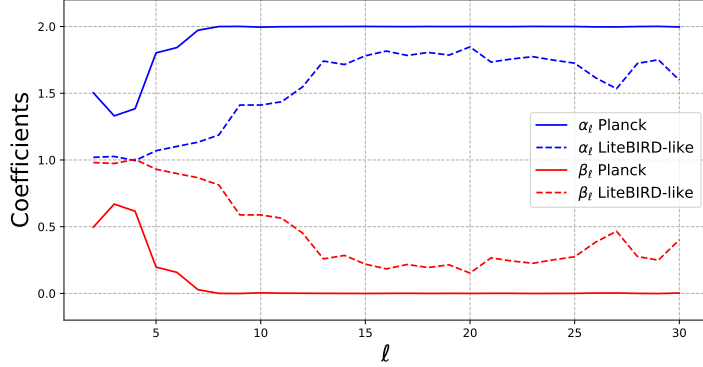


Figure 3.6: The behaviour of the coefficients α_ℓ (blue line) and β_ℓ (red line), see Eqs. (3.30),(3.39) and (3.40) for their definitions, as a function of ℓ for the PLANCK-WMAP low- ℓ data set (solid lines) and for the LiteBIRD-like noise level (dashed lines). Figure taken from:[22]

level (σ_{Planck}).

We find that the width of the estimator P in the LiteBIRD case can be even 30 times smaller with respect to what obtained in the PLANCK-WMAP low- ℓ case, if $\ell_{max} \gtrsim 20$.

3.4.2 Results for \tilde{P}

In Figure 3.6 we plot α_ℓ and β_ℓ (see equations (3.39) and (3.40)) as a function of ℓ for the PLANCK-WMAP low- ℓ data set (solid lines). Note how β_ℓ for $\ell > 7$ go to zero (and consequently $\alpha_\ell \rightarrow 2$ for same multipoles) because of the noise level in polarisation. For $\ell_{max} = 6$, even though the distribution of \tilde{P} is $\sim 32\%$ narrower with respect to P shown in Figure 3.4, PLANCK-WMAP low- ℓ data shift a little so that the LTP is increased to 8.33%. However \tilde{P} , as already mentioned, is not limited in the choice of ℓ_{max} and still for the PLANCK-WMAP low- ℓ data at $\ell_{max} = 30$ we obtain a LTP at the level of 3.68%. In Figure 3.7 we give the LTP for \tilde{P} at each ℓ_{max} , displayed in black, compared to a naive estimator defined only with temperature data as

$$P_T = \frac{1}{(\ell_{max} - 1)} \sum_{\ell=2}^{\ell_{max}} x_\ell^{(1)},$$

shown in blue. It is interesting to note how the inclusion of the subdominant polarisation part impacts on the analysis making the LTP of \tilde{P} smaller than P_T for the whole ℓ -range considered. In particular for P_T at $\ell_{max} = 30$ we obtain that the LTP is 7.22%.

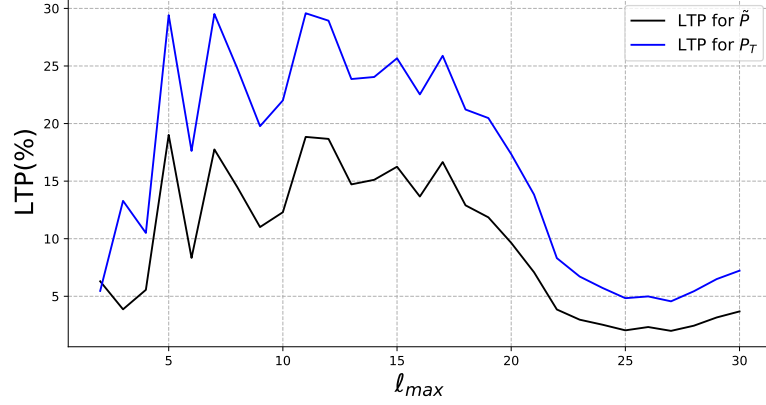


Figure 3.7: LTP of \tilde{P} (in black) and of P_T (in blue) as a function of ℓ_{max} for the PLANCK-WMAP low- ℓ data. Figure taken from:[22]

Still in Figure 3.6 we plot α_ℓ and β_ℓ as a function of ℓ for the LiteBIRD-like noise level (see dashed lines). Note that for this case none of the β_ℓ go to zero and therefore polarisation data provide a contribution for each of the multipoles considered at large scale. Correspondently temperature data will not saturate the information entering \tilde{P} for any considered multipoles.

In order to evaluate the impact of polarisation and temperature data on \tilde{P} we define the following weights

$$w_{x(1)}(\ell_{max}) = \frac{1}{2(\ell_{max} - 1)} \sum_{\ell=2}^{\ell_{max}} \alpha_\ell, \quad (3.47)$$

$$w_{x(2)}(\ell_{max}) = \frac{1}{2(\ell_{max} - 1)} \sum_{\ell=2}^{\ell_{max}} \beta_\ell, \quad (3.48)$$

such that $w_{x(1)}(\ell_{max}) + w_{x(2)}(\ell_{max}) = 1$ for every ℓ_{max} . For $\ell_{max} = 6$ we find that polarised PLANCK-WMAP low- ℓ data contribute at the level of 21.4% to the building of \tilde{P} . This value increases to 47.9% for future LiteBIRD-like polarised data at the same maximum multipole. At $\ell_{max} = 30$ we forecast that future LiteBIRD-like polarised data will weight as the 23.1% compared to the 3.8% obtained with PLANCK-WMAP low- ℓ data, therefore providing an increasing factor ~ 6 . The behaviour of $w_{x(1)}$ and $w_{x(2)}$ for each ℓ_{max} is given in Figure 3.8.

We end this Section showing in Figure 3.9 how the standard deviation σ of \tilde{P} shrinks for each ℓ_{max} from current PLANCK data (solid blue) to future LiteBIRD-like data (dashed blue). We compute that at low- ℓ future data

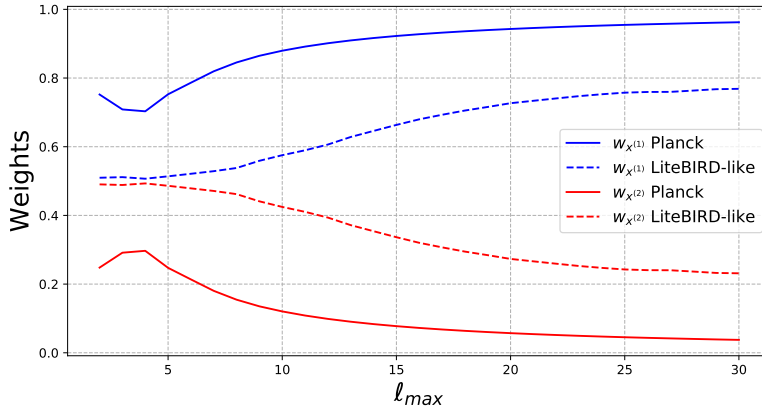


Figure 3.8: $w_{x(1)}$ (in blue) and $w_{x(2)}$ (in red) as a function of ℓ_{max} for the PLANCK-WMAP low- ℓ data set (solid line) and the LiteBIRD-like case (dashed line). Figure taken from:[22]

will allow to build \tilde{P} with a statistical uncertainty that will be around 20% smaller with respect to current PLANCK data.

3.5 Conclusions

In this chapter we studied how to analyse the power deficit anomaly present at large angular scale of the CMB anisotropies pattern considering both temperature and polarisation data. We have proposed a new one-dimensional estimator, i.e. P and its optimised version \tilde{P} , see equations (3.27) and (3.30), which is able to jointly test the lack of power in TT, TE and EE. The main outcomes of this analysis are listed below.

1. Considering PLANCK-WMAP low- ℓ data it is interesting to note that the inclusion of polarisation information through our new one-dimensional estimator, either P or \tilde{P} , provides estimates which are less likely accepted in a Λ CDM model than the corresponding only-temperature version of the same estimator. In other words, polarisation though subdominant in terms of signal-to-noise ratio with respect to temperature, plays a non-negligible role in the evaluation of the compatibility between data and the standard model. See for instance Figure 3.7: even though the weight of polarisation data is only around 4% of the total information budget, the LTP probability of \tilde{P} is always smaller than its corresponding temperature-only version P_T . In particular, at the maximum multipole considered, i.e. $\ell_{max} = 30$, we find that the

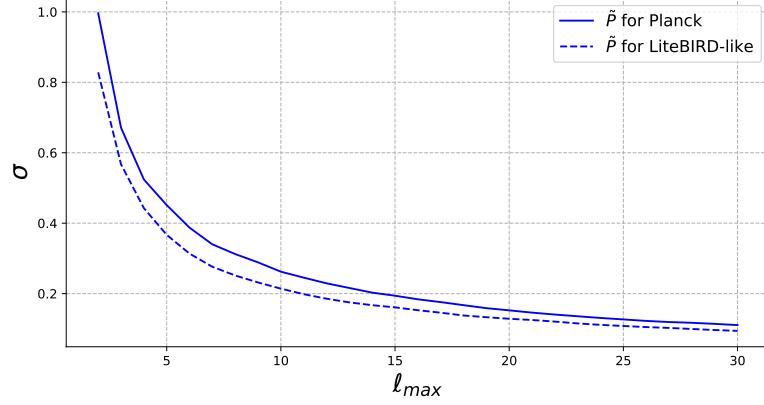


Figure 3.9: Upper panel: Standard deviation σ of \tilde{P} versus ℓ_{max} for PLANCK-WMAP low- ℓ data set (solid line) and the LiteBIRD-like case (dashed line). Figure taken from:[22]

probability that a random Λ CDM realisation is statistically accepted decreases by a factor of two when the polarisation is taken into account. However the LTP values obtained are at the level of few per cent and therefore still compatible with a statistical fluke.

2. E-modes at large angular scale still contain information which might be capable to probe new physics beyond the standard cosmological model.
 - We forecast that future CMB polarised measurements à la LiteBIRD can tight the empirical distribution of P up to a factor of ~ 30 , as displayed in Fig. 3.5.
 - Considering the optimised version of the proposed estimator, i.e. \tilde{P} , we evaluate that future LiteBIRD-like measurements can shrink the statistical uncertainty by 23 – 17% (see Fig 3.9) and at the same time increasing the contribution of the polarisation part by a factor ranging from ~ 2 to ~ 6 (see Fig 3.8).

Future all-sky CMB experiments aimed at detecting primordial B-modes (which in turn are related to the energy scale of inflation) are designed to observe CMB polarisation with exquisite accuracy and precision. In order to make this possible, residual systematic effects both of instrumental and astrophysical origin have to be carefully measured or, at least, kept under control. In this chapter we supposed that this is the case and that the statistical noise is the dominant source of uncertainty. Under these circumstances,

E-modes will be in practice known at the cosmic variance limit at large angular scales. This is a great opportunity, since E-mode polarisation might contain important information about the lack of power anomaly currently observed only in the temperature map, which could be tracing new physical phenomena beyond the standard cosmological model in the early universe.

3.6 Outlooks

3.6.1 Application to PR3 and PR4 data set

A natural outlook for this work is the employment of the above mentioned estimators, i.e. P (Eq. 3.27) and its optimised version \tilde{P} (Eq. 3.30), to the last Planck data, both PR3 and PR4 datasets, which were respectively released in 2018 and 2020. Up to now lack of power has never been studied with PR4 dataset. More in general, [75] and [85] are the only studies which investigate the CMB anomalies with the PR3 dataset.

In order to develop this project a new collaboration with the Observational Cosmology and Instrumentation group⁶ at the Instituto de Fisica de Cantabria (IFCA)⁷, Santander (Spain) started. The members of the IFCA group will provide guidance in the use of the PR3 and PR4 data set for this application. As described in [5], compared to the previous release, the PR3 but in particular the PR4 data better describe the polarisation component of CMB: in fact PR3 and PR4 show reduced levels of noise and systematics at all angular scales and an improved consistency across frequencies, particularly in polarisation. For this reason, we expect to obtain stricter constraints than in the analyses carried out with the (PR2) datasets.

3.6.2 Lack of correlation anomaly with the NAPS

Another interesting use of the NAPS, Eq (3.24) and (3.25), can be done to study the lack of correlation anomaly, an interestingly feature that seems to be correlated with the lack of power described in the previous sections. This signature, observed in the temperature CMB anisotropies pattern firstly by COBE [83] and then confirmed by WMAP [64] and Planck [13], consists of a suppression of the CMB two-point correlation function at large angular scales larger than 60 degrees with respect to what expected in the Λ CDM model. Fig. 3.10 shows the two-point correlation function as observed with Planck [13].

⁶<https://ifca.unican.es/en-us/research/observational-cosmology-and-instrumentation>

⁷<https://ifca.unican.es/en-us>

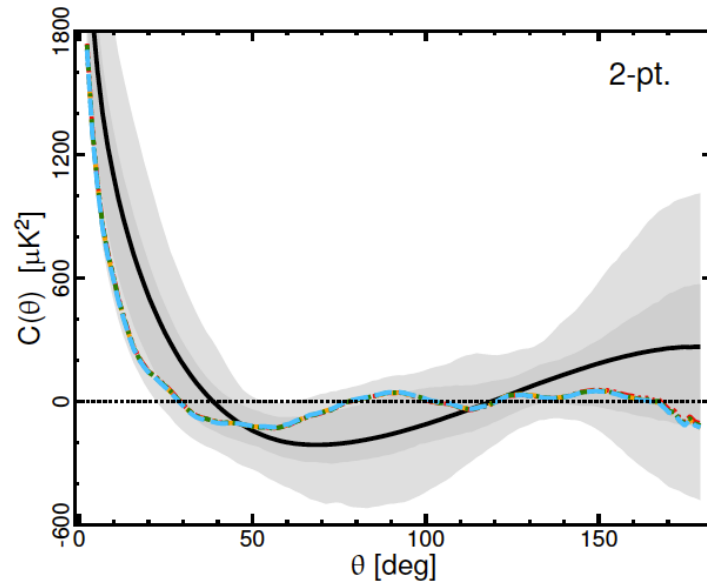


Figure 3.10: Angular two-point correlation function as observed by Planck [13]. The full black line and the shaded regions are the expectation from 1000 SMICA simulations based on the Λ CDM model and the 68% and 95% confidence regions. The plot also shows four colored lines that fall on top of each other and represent the results of the Planck analysis of the Commander, SEVEM, NILC and SMICA maps at resolution $N_{side} = 64$. While the measured two-point correlation is never outside the 95% confidence region, the surprising feature is that we observe essentially no correlations at $70^\circ < \theta < 170^\circ$ and a significant lack of correlations at $\theta > 60^\circ$. Figure taken from:[77].

In this section we will show briefly the formalism of a possible one-dimensional estimator able to constrain this feature, taking jointly into account the information in the TT, EE and TE CMB power spectra. We leave for future works its validation and application to real data.

Starting from Eq. (3.24) and (3.25) we define a scalar field in the harmonic space with the form:

$$X_\ell = \alpha_\ell x_\ell^{(1)} + \beta_\ell x_\ell^{(2)}, \quad (3.49)$$

where α_ℓ Eq. (3.39) and β_ℓ (Eq. 3.40) minimise the variance of X_ℓ for each ℓ . The field X_ℓ can be interpreted as a dimensionless normalised power and its expectation value is $\langle X_\ell \rangle = 2$ for any value of ℓ .

In pixel space the fluctuations of the field X_ℓ , i.e. δ_x , can be expanded on the sky through the spherical harmonic functions on a sphere $Y_{\ell m}(\hat{n})$:

$$\delta_x = \sum_{\ell m} a_{\ell m}^x Y_{\ell m}(\hat{n}) \quad (3.50)$$

with the unit-vector (\hat{n}) representing the direction of observation. The 2-point correlation function of the field X_ℓ will be:

$$\begin{aligned} C_2^{X_\ell}(\phi) &= \langle \delta_x(\hat{n}) \delta_x(\hat{n}') \rangle = \\ &= \sum_{\ell m} \sum_{\ell' m'} \langle a_{\ell m}^x (a_{\ell' m'}^x)^* \rangle Y_{\ell m}(\hat{n}) Y_{\ell' m'}^*(\hat{n}') = \\ &= \sum_{\ell} \frac{2\ell + 1}{4\pi} X_\ell P_\ell(\hat{n} \cdot \hat{n}'), \end{aligned} \quad (3.51)$$

where $\hat{n} \cdot \hat{n}' = \cos \phi$.

In order to evaluate the lack of correlation we focus on an estimator originally suggested by the WMAP team, called $S_{1/2}$ [96]. The idea is to measure the distance between the correlation function and zero over a chosen range of angles [97]. We formally define the $S_{1/2}$ statistic for the X_ℓ field in this way:

$$S_{1/2}^{X_\ell} = \int_{\cos\phi_2}^{\cos\phi_1} [C_2^{X_\ell}(\phi)]^2 d\cos(\phi). \quad (3.52)$$

In theory, such as estimator for $\cos\phi_1 = 1/2$ and $\cos\phi_2 = -1$ could be used to quantify the lack of correlation at scales larger than 60 degrees. The advantage of using X_ℓ , instead of the standard APS, comes directly from the nature of the NAPS. The latter, as we have shown, are dimensionless and similar amplitude numbers which can be easily combined to define a scalar field in harmonic space, which depends on temperature, E-mode polarisation and their cross-correlation.

Chapter 4

Cosmic Birefringence

Cosmic Birefringence (CB) is a tracer for new parity-violating physics beyond the standard model of particle physics [23]. Different models for dark matter and dark energy introduce scalar fields ϕ , which can couple to the photons through a Chern-Simons term, adding new parity violating terms to the Lagrangian of standard electromagnetism. The breaking of this symmetry produces an in-vacuum rotation of the linear polarisation plane of photons during propagation, i.e. the Cosmic Birefringence effect [24]. Such a rotation, naturally measured with an angle α , might signal the presence of new interactions beyond the standard electrodynamics and provide constraints on different theoretical models for dark energy, dark matter, axions and axion-like particles.

Several astrophysical sources of linearly polarised photons can be used to investigate this phenomenon [24, 25, 26, 27, 28, 29, 30]. Among these sources, in this Thesis we focus on the oldest and farthest one of the Universe, i.e. the CMB radiation, which is linearly polarised because of Thomson scattering (as described in detail in section 2.3.1) and therefore it represents a good candidate to perform these investigations. This rotation mixes the Q and U Stokes parameters and consequently the E- and B-modes polarisation, producing spurious B-modes which can screen the primordial signal. Therefore, for a robust detection of these primary B-modes, which is fundamental to probe primordial gravitational waves and other properties of inflation, in addition to an exquisite control of systematics (both of astrophysical and instrumental origin), one needs to exclude other possible new mechanisms able to create B-modes just as the birefringence effect [98].

Cosmic Birefringence is dubbed isotropic if $\alpha(\hat{n}) = \alpha_0$, with α_0 being a constant, which means that the rotation angle does not depend on the direction of observation \hat{n} . Cosmic Birefringence is instead called anisotropic if the rotation $\alpha(\hat{n})$ is a function of the direction of observations. The isotropic CB

is expected when the scalar field ϕ , that sources CB, is spatially independent, instead a spatially-varying ϕ produces the anisotropic effect. When expanded in spherical harmonics, the isotropic angle is mapped into the monopole term, i.e. $L = 0$, while the anisotropic angle can in principle be described through all the other multipoles, i.e. $L > 0$ [99, 100]¹.

Current estimates for both isotropic and anisotropic birefringence, see e.g. [101] and [34] whose main results are summarised in section 4.1, are compatible with null effect. However, very interestingly, recent analyses on Planck 2018 data [102] and on Planck 2020 data [103, 104], which employ the technique presented in [105], provide a hint of detection for the isotropic birefringence at the level of 2.4σ and 2.7σ respectively. Future CMB experiments, designed to detect the primary B-mode component, i.e. the signature that primordial gravitational waves have left on the CMB polarisation anisotropy pattern, will certainly constrain Cosmic Birefringence with a sensitivity which will be from one to few orders of magnitude better with respect to present measurements [106, 107].

In this chapter, after having recovered the main equations relating the birefringence effect to the observed CMB angular, we focus on evaluating the birefringence power spectrum. In literature there are several methods used to constrain this effect:

- The Mode Coupling approach [100, 108], where the map of $\alpha(\hat{n})$ is built exploiting the fact that, when expanded in spherical harmonics, each of its multipole-modes is coupled to all the CMB multipoles. Note that this is the same property which is used to evaluate/reconstruct the weak-lensing effect from CMB maps [109].
- The localisation of estimators aimed at isotropic birefringence, where the building of the map of $\alpha(\hat{n})$ is possible applying estimators for isotropic birefringence to patches of the sky. This was performed with the Stacking approach [33] and the so-called D-estimators [34].
- The Likelihood approach [110], where the anisotropic birefringence spectra are treated as additional parameters whose statistical distributions are sampled over through Monte Carlo Markov Chain (MCMC) techniques, once the relation between the CMB observed spectra and the phenomenon under investigation is inserted in the CMB likelihood function. See also [98, 111, 112] where a χ^2 -approach has been employed only on the BB observed spectrum.

¹By convention, we use capital letter (L, L_1, L_2, \dots) to indicate multipoles of the spherical harmonics transform of birefringence anisotropies.

In our analysis we develop and apply to Planck 2018 data two different and complementary methodologies. The first approach [35], developed in collaboration with the Cosmology group of the University of Ferrara, employs the localisation of the so-called D-estimators to build maps of the birefringence angle evaluating CB spectrum on angular scales larger than ~ 7 degrees. In the second approach [31], we develop a novel class of linear and quadratic fully harmonic-based estimators which are able to directly evaluate the power spectrum of Cosmic Birefringence rotation angle starting from the EE, BB and EB observed angular power spectra of the CMB anisotropies. As it will be discussed in more detail below, the algebra of the quadratic estimators is similar to the one of the Quadratic Maximum Likelihood (QML) technique for the APS of CMB anisotropies [113], with the difference that the new estimator takes the CMB spectra as an input instead of the CMB maps (in pixel space).

The chapter is organised as follows. In section 4.1 we introduce in detail the Cosmic Birefringence effect and recover the algebraic equations which relate the observed CMB spectra with isotropic and anisotropic birefringence effect writing down explicitly also the primordial parity conserving spectra (namely EB and TB), which were not previously reported in literature but are needed here to build the new quadratic estimators. In section 4.2 we introduce the formalism of the so called D-estimators [114, 115], i.e. two linear combinations of the observed CMB spectra, and of the new linear and quadratic estimators, along with a description of their main features and properties. In section 4.3 we describe the Planck 2018 Release (PR3). In sections 4.4 we apply the localisation approach on Planck data and in section 4.5, after having shown the validation of linear and quadratic estimators considering "vanilla" (i.e. systematics-free) simulations, we employ them on Planck data. Finally, in section 4.6 we draw our conclusions on these results.

4.1 Introduction

4.1.1 Physical origin of Cosmic Birefringence

Linearly polarised light can be written as the superposition of a right-handed and left-handed circular polarisation state. Parity-violating effect induces a difference between the effective refractive indexes for the right-handed and left-handed circular polarisation states of light. As result we have a change in phase during propagation of light, which produces an in-vacuum rotation in the linear polarisation angle. This phenomenon is known as CB. In order to investigate the latter, one needs linearly polarised sources for which the orientation of the polarisation plane at the emission is known and can therefore be compared with the one observed on earth, making it possible to check if it has been changed during its path.

Several astrophysical polarised sources, such as Pulsars, Supernovae, Radio Galaxies, Quasars and also the Crab Nebula (see e.g. [24, 25, 26, 27, 28, 29, 30]), have been used to investigate this phenomenon. In this Thesis we focused on CMB observations, since approximately 10% of the CMB photons are linearly polarised due to Thomson scattering (see Section 2.3.1). CB effect, naturally parametrised by an angle, results in a mixing between Q and U Stokes parameters that produces non-null CMB cross correlations between T and B-mode polarisation, and between E- and B-mode polarisation, which are expected to be null under the parity conserving assumption (that is beneath the standard cosmological model).

Physically, this rotation is a consequence of the coupling of a scalar field ϕ to the electromagnetic Chern-Simons term such that the CB angle α is proportional to the total change $\Delta\phi$ along the photon's path. The CMB is the first light emitted in the Universe, which means the farthest one, therefore it represents the ideal candidate to investigate the CB. Different models for dark matter and dark energy introduce scalar fields ϕ , such as the axion [116], which can couple to the photons through a Chern-Simons term. An example of such a scalar field is the Pseudo-Nambu-Goldstone-Boson field (PNGB), which is a natural candidate for quintessence, since it can drive the evolution of the Universe through epochs of accelerated expansion [24]. Models with a weakly broken global $U(1)$ symmetry provide a natural mechanism for producing a shallow potential for the PNGB field. The parity-violating extension of the standard electromagnetism Lagrangian can be written as:

$$\mathcal{L} = -\frac{1}{4}F_{\mu\nu}\tilde{F}_{\mu\nu} - \frac{\beta}{2M}\phi F_{\mu\nu}\tilde{F}_{\mu\nu}, \quad (4.1)$$

where $F_{\mu\nu}$ is the electromagnetic field tensor and $\tilde{F}_{\mu\nu} = \frac{1}{2}\epsilon^{\mu\nu\delta\gamma}F_{\delta\gamma}$ is its dual,

(with $\epsilon^{\mu\nu\delta\gamma}$ the Levi-Civita tensor), β is a dimensionless coupling constant and M is a parameter with dimensions of mass. It is possible to compute that the new parity-violating term in the extended Lagrangian, Eq. (4.1), produces the different effective refractive indexes for the left-handed and right-handed photon polarisations [23]. Therefore the direction of polarisation plane is rotated by an amount [98]:

$$\begin{aligned}\alpha(\hat{n}) &= \frac{\beta}{M} \int d\tau \left(\frac{\partial}{\partial\tau} + \hat{n} \cdot \nabla \right) \phi(\tau, \hat{n}) \\ &= \frac{\beta}{M} \Delta\phi(\hat{n}).\end{aligned}\tag{4.2}$$

with τ the conformal time and the unit-vector \hat{n} the direction of observation. Here the integration is along the space-time path of the photon and $\Delta\phi$ represents the variation of the scalar field along that trajectory. Due to the value of the mass M which can be of the order of the Planck mass, the CB effect is expected to be very small. In order for the angle α to be measurable, the variation $\Delta\phi$ must also be large and this might happen at cosmological scales. This is the reason to use cosmological observations to search for this phenomenon.

The birefringence angle $\alpha(\hat{n})$, which is a function of the direction of the observation, can be separated in an isotropic α_0 and in an anisotropic term $\delta\alpha(\hat{n})$ as:

$$\alpha(\hat{n}) = \alpha_0 + \delta\alpha(\hat{n}),\tag{4.3}$$

where:

$$\langle \delta\alpha(\hat{n}) \rangle = 0.\tag{4.4}$$

The monopole term α_0 is obtained taken the average of $\langle \alpha(\hat{n}) \rangle$ such that Eq. (4.4) is got by construction.

The isotropic CB is characterised by a rotation uniform across the sky, i.e. $\alpha(\hat{n}) = \alpha_0$. This phenomenon is expected when the scalar field ϕ , that sources CB, does not depend on space. Instead a spatially-varying ϕ produces the anisotropic effect and the rotation $\alpha(\hat{n})$ becomes a function of the direction of observations. The fluctuations $\delta\alpha(\hat{n})$ can be expanded on the sky through the spherical harmonics $Y_{\ell m}(\hat{n})$ [99]:

$$\delta\alpha(\hat{n}) = \sum_{LM} a_{\alpha,LM} Y_{LM}(\hat{n}),\tag{4.5}$$

and the expression for the harmonic coefficients is:

$$a_{\alpha,LM} = \int d\Omega \delta\alpha(\hat{n}) Y_{LM}^*(\hat{n}).\tag{4.6}$$

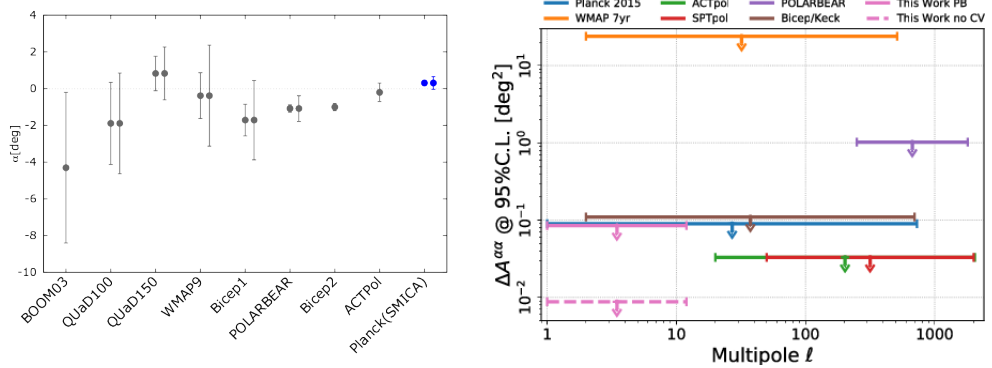


Figure 4.1: Constraints on Cosmic Birefringence re-printed from [101, 34]. The left panel shows the constraints on isotropic CB coming from several CMB experiment (grey points) as reviewed in [118] compared with the Planck 2016 Intermediate Results (in blue) [101]. For each experiment the left error bars are the 68% C.L., while right error bars (when displayed) are obtained by summing linearly the statistical and systematic uncertainties. The error bar of BOOM03 already contains a contribution from systematic effects. The right panel shows the scale invariant spectrum of the anisotropic birefringence angle from several CMB experiments with uncertainty at 95% C.L.[34].

Assuming statistical isotropy of $a_{\alpha,LM}$, we define the angular power spectrum of the birefringence angle:

$$\langle a_{\alpha,LM} a_{\alpha,L_1M_1} \rangle_{\alpha} = C_L^{\alpha} \delta_{LL_1} \delta_{MM_1}. \quad (4.7)$$

with $\langle \rangle_{\alpha}$ being the ensemble average of the fluctuations of the CB angle². For a scalar field ϕ which does not obtain a mass during the inflationary epoch, the power spectrum of this fluctuation at large scale, typically $L < 100$, will be scale invariant and it can be expressed in term of a constant amplitude K^{α} [117]:

$$K^{\alpha} = C_L^{\alpha} \frac{[L(L+1)]}{2\pi}. \quad (4.8)$$

Note however that the aim of this work is to derive a model-independent constraint on the angular power spectra of CB without restricting our self to any particular physical model.

Many CMB experiments have already constrained both isotropic and anisotropic birefringence. Figure 4.1 (taken from [101] and [34]) shows the current measurements of the CB rotation angle. For the isotropic CB the best

²By convention in section 4.1, we use the symbol $\langle \rangle$ without subscript to indicate the ensemble average of the CMB fluctuations, the symbol $\langle \rangle_{\alpha}$ to indicate the one of CB angle fluctuation and the symbol $\langle \rangle_{CMB,\alpha}$ to indicate the case where both are considered.

constraint on α_0 comes from the Planck experiment whose 68% confidence limit is $\alpha_0 = 0.31^\circ \pm 0.05^\circ(\text{stat}) \pm 0.28^\circ(\text{syst})$ [101]. Instead, for the anisotropic CB, a recent ACTPol analysis finds $K^\alpha < 0.033 \text{ deg}^2$ at a 95% confidence level (C.L.) [119]. These estimates for both isotropic and anisotropic CB are compatible with a null effect. However, it is important to mention that exists a degeneracy between the instrument polarisation angle and the isotropic CB angle that limits the evaluation of the latter. Note that in the Planck CB constraint the value of α_0 is dominated by the systematic uncertainties introduced by the instrument polarisation angle.

Interestingly, recent re-analyses of the Planck 2018 data (PR3) [102] and of the Planck 2020 data (PR4) [103, 104], which employ the technique presented in [105], provide a hint of detection for the isotropic birefringence at the level of 2.4σ and larger than 2.7σ respectively. According to the theory, the CB effect is proportional to the distance travelled by photons. In these analysis the authors consider the astrophysical foreground near enough to assume that the physical effect is not relevant. Therefore, using the information of the foregrounds, it is possible to disentangle a primordial rotation from the one induced by the instrument polarisation angle. Moreover, in [103, 104] is deeply investigated the impact of the foreground polarisation, considering different models which describe it [103], and employing a frequency-dependent analysis [104].

Future CMB experiments, designed to detect the signature that primordial gravitational waves have left on the CMB polarisation anisotropy pattern, i.e. the primordial B-modes component, as a byproduct will constrain also Cosmic Birefringence with a sensitivity which will be from one to few orders of magnitude better with respect to present measurements [106, 107].

4.1.2 CB impact on CMB

The effects of the Cosmic Birefringence on the CMB angular power spectra are predicted to be small, therefore they can be treated perturbatively. As we have seen in sections 2.2, 2.3, the temperature and polarisation CMB anisotropies can be expanded in spin-weighted spherical harmonic functions $Y_{\ell m}(\hat{n})$ and $Y_{\pm 2, \ell m}(\hat{n})$:

$$T(\hat{n}) = \sum_{\ell m} a_{T, \ell m} Y_{\ell m}(\hat{n}), \quad (4.9)$$

$$(Q + iU)(\hat{n}) = \sum_{\ell m} a_{\pm 2, \ell m} Y_{\pm 2, \ell m}(\hat{n}), \quad (4.10)$$

where T , Q and U are the primordial Stokes parameters and the unit-vector \hat{n} represents the direction of observation. Inverting Eqs. (4.9) and (4.10) we

find the expressions for the harmonic coefficients:

$$a_{T,\ell m} = \int d\Omega Y_{\ell m}^*(\hat{n}) T(\hat{n}), \quad (4.11)$$

$$a_{\pm 2,\ell m} = \int d\Omega Y_{\pm 2,\ell m}^*(\hat{n}) (Q + iU)(\hat{n}), \quad (4.12)$$

In presence of CB, the polarisation field acquires a phase factor which depends on \hat{n} while the temperature field is not modified:

$$T^{obs}(\hat{n}) = T(\hat{n}), \quad (4.13)$$

$$(Q + iU)^{obs}(\hat{n}) = e^{\pm 2i\alpha(\hat{n})} (Q + iU)(\hat{n}). \quad (4.14)$$

where the label *obs* at the left-hand side stands for observed, while the Stokes parameters T , Q and U in the right-hand side are the primordial quantities, i.e. those that are observed when CB is absent. Hence, the Chern-Simons term, which appears in the modified electromagnetism Lagrangian, Eq. (4.1), produces a rotation of the polarisation component given by the factor $e^{\pm 2i\alpha(\hat{n})}$. Thus, the expressions for the observed harmonic coefficients become:

$$a_{T,\ell m}^{obs} = \int d\Omega Y_{\ell m}^*(\hat{n}) T^{obs}(\hat{n}), \quad (4.15)$$

$$a_{\pm 2,\ell m}^{obs} = \int d\Omega Y_{\pm 2,\ell m}^*(\hat{n}) (Q + iU)^{obs}(\hat{n}). \quad (4.16)$$

Replacing Eqs. (4.14) and (4.3) in Eq. (4.16), we find [99]:

$$\begin{aligned} a_{\pm 2,\ell m}^{obs} &= \int d\Omega Y_{\pm 2,\ell m}^*(\hat{n}) (Q + iU)(\hat{n}) e^{\pm 2i\alpha(\hat{n})} \\ &= e^{\pm 2i\alpha_0} \sum_{\ell_1 m_1} a_{\pm 2,\ell_1 m_1} \int d\Omega Y_{\pm 2,\ell m}^*(\hat{n}) e^{\pm 2i\delta\alpha(\hat{n})} Y_{\pm 2,\ell_1 m_1}(\hat{n}), \end{aligned} \quad (4.17)$$

and defining the object $F_{\ell m \ell_1 m_1}^{\pm}$ as:

$$F_{\ell m \ell_1 m_1}^{\pm} = \int d\Omega Y_{\pm 2,\ell m}^*(\hat{n}) e^{\pm 2i\delta\alpha(\hat{n})} Y_{\pm 2,\ell_1 m_1}(\hat{n}), \quad (4.18)$$

we find that the expression for the harmonic coefficients of spin 2 and -2 is:

$$a_{\pm 2,\ell m}^{obs} = e^{\pm 2i\alpha_0} \sum_{\ell_1 m_1} a_{\pm 2,\ell_1 m_1} F_{\ell m \ell_1 m_1}^{\pm}. \quad (4.19)$$

Considering the definition of the E- and B-mode harmonic coefficients, see Eqs. (2.60) and (2.60) in section 2.3, the observed quantities are:

$$a_{E,\ell m}^{obs} = -\frac{1}{2} (a_{2,\ell m}^{obs} + a_{-2,\ell m}^{obs}), \quad (4.20)$$

$$a_{B,\ell m}^{obs} = +\frac{i}{2} (a_{2,\ell m}^{obs} - a_{-2,\ell m}^{obs}), \quad (4.21)$$

and replacing Eq. (4.19) in Eqs. (4.20) and (4.21):

$$a_{E,\ell m}^{obs} = -\frac{1}{2} \left(e^{2i\alpha_0} \sum_{\ell_1 m_1} a_{2,\ell_1 m_1} F_{\ell m \ell_1 m_1}^+ + e^{-2i\alpha_0} \sum_{\ell_1 m_1} a_{-2,\ell_1 m_1} F_{\ell m \ell_1 m_1}^- \right), \quad (4.22)$$

$$a_{B,\ell m}^{obs} = \frac{i}{2} \left(e^{2i\alpha_0} \sum_{\ell_1 m_1} a_{2,\ell_1 m_1} F_{\ell m \ell_1 m_1}^+ - e^{-2i\alpha_0} \sum_{\ell_1 m_1} a_{-2,\ell_1 m_1} F_{\ell m \ell_1 m_1}^- \right). \quad (4.23)$$

Now we define the following G-functions as:

$$G_{\ell m \ell_1 m_1}^{(1)} = e^{2i\alpha_0} F_{\ell m \ell_1 m_1}^+ + e^{-2i\alpha_0} F_{\ell m \ell_1 m_1}^-, \quad (4.24)$$

$$G_{\ell m \ell_1 m_1}^{(2)} = e^{2i\alpha_0} F_{\ell m \ell_1 m_1}^+ - e^{-2i\alpha_0} F_{\ell m \ell_1 m_1}^-, \quad (4.25)$$

and replacing in Eqs. (4.22),(4.23), we finally get the observed harmonic coefficients for the T, E and B CMB fields:

$$a_{T,\ell m}^{obs} = a_{T,\ell m}, \quad (4.26)$$

$$a_{E,\ell m}^{obs} = \frac{1}{2} \sum_{\ell_1 m_1} \left(G_{\ell m \ell_1 m_1}^{(1)} a_{E,\ell_1 m_1} + i G_{\ell m \ell_1 m_1}^{(2)} a_{B,\ell_1 m_1} \right), \quad (4.27)$$

$$a_{B,\ell m}^{obs} = \frac{1}{2} \sum_{\ell_1 m_1} \left(-i G_{\ell m \ell_1 m_1}^{(2)} a_{E,\ell_1 m_1} + G_{\ell m \ell_1 m_1}^{(1)} a_{B,\ell_1 m_1} \right), \quad (4.28)$$

in agreement with [99].

Now, starting from the definition of the angular power spectra, given in sections 2.2 and 2.3, and considering Eqs. (4.26), (4.27) and (4.28) we compute all the six observed CMB spectra when the CB effect is present. We do that by taking into account the following two hypotheses:

- primordial CMB anisotropies do not correlate with α ,
- $\delta\alpha$ is small (we keep these terms up to second order, which is the leading one).

Our computation extends the work done in [99] since we do not set to zero the primordial EB and TB CMB power spectra. As it was already clear from Eqs. (4.13) and (4.26), the CB does not impact on the CMB temperature

power spectrum:

$$\begin{aligned}
\langle C_\ell^{TT,obs} \rangle &= \frac{1}{2\ell+1} \sum_{m=-\ell}^{+\ell} \langle a_{T,\ell m}^{obs} (a_{T,\ell m}^{obs})^* \rangle \\
&= \frac{1}{2\ell+1} \sum_{m=-\ell}^{+\ell} \langle a_{T,\ell m} (a_{T,\ell m})^* \rangle \\
&= C_\ell^{TT}.
\end{aligned} \tag{4.29}$$

Now we calculate the observed correlation between the temperature and the polarisation, i.e. $C_\ell^{TE,obs}$ and $C_\ell^{TB,obs}$. Therefore:

$$\begin{aligned}
\langle C_\ell^{TE,obs} \rangle_{CMB,\alpha} &= \frac{1}{2\ell+1} \sum_{m=-\ell}^{+\ell} \langle a_{T,\ell m}^{obs} (a_{E,\ell m}^{obs})^* \rangle_{CMB,\alpha} \\
&= \frac{1}{2} \frac{1}{2\ell+1} \sum_m \sum_{\ell_1 m_1} \langle a_{T,\ell m} \left[\left(e^{2i\alpha_0} F_{\ell m \ell_1 m_1}^+ + e^{-2i\alpha_0} F_{\ell m \ell_1 m_1}^- \right)^* \right. \\
&\quad \left. (a_{E,\ell_1 m_1})^* + (i)^* \left(e^{2i\alpha_0} F_{\ell m \ell_1 m_1}^+ - e^{-2i\alpha_0} F_{\ell m \ell_1 m_1}^- \right)^* \right. \\
&\quad \left. (a_{B,\ell_1 m_1})^* \right] \rangle_{CMB,\alpha}.
\end{aligned} \tag{4.30}$$

Since primordial CMB anisotropies do not correlate with α , we have:

$$\begin{aligned}
\langle C_\ell^{TE,obs} \rangle_{CMB,\alpha} &= \frac{1}{2} \frac{1}{2\ell+1} \sum_m \sum_{\ell_1 m_1} \left[\langle a_{T,\ell m} (a_{E,\ell_1 m_1})^* \rangle \left(e^{2i\alpha_0} \langle F_{\ell m \ell_1 m_1}^+ \rangle_\alpha + \right. \right. \\
&\quad \left. \left. + e^{-2i\alpha_0} \langle F_{\ell m \ell_1 m_1}^- \rangle_\alpha \right)^* + (i)^* \langle a_{T,\ell m} (a_{B,\ell_1 m_1})^* \rangle \right. \\
&\quad \left. \left(e^{2i\alpha_0} \langle F_{\ell m \ell_1 m_1}^+ \rangle_\alpha - e^{-2i\alpha_0} \langle F_{\ell m \ell_1 m_1}^- \rangle_\alpha \right)^* \right].
\end{aligned} \tag{4.31}$$

Hence we need to calculate the following two quantities $\langle F_{\ell m \ell_1 m_1}^\pm \rangle_\alpha$. Up to the quadratic order of $\delta\alpha$, we have:

$$\begin{aligned}
\langle F_{\ell m \ell_1 m_1}^\pm \rangle_\alpha &= \int d\Omega Y_{\pm 2, \ell m}^*(\hat{n}) Y_{\pm 2, \ell_1 m_1}(\hat{n}) \langle e^{\pm 2i\delta\alpha(\hat{n})} \rangle_\alpha \\
&= \int d\Omega Y_{\pm 2, \ell m}^*(\hat{n}) Y_{\pm 2, \ell_1 m_1}(\hat{n}) \langle 1 \pm 2i\delta\alpha(\hat{n}) - 2\delta\alpha^2 \rangle_\alpha
\end{aligned} \tag{4.32}$$

The term $\langle \delta\alpha^2 \rangle_\alpha$ turns out not be dependent on the direction and it represents the variance of α , i.e. V_α :

$$\begin{aligned}
\langle \delta\alpha^2 \rangle_\alpha &= \langle \delta\alpha(\hat{n}) \delta\alpha(\hat{n}) \rangle_\alpha \\
&= \sum_L \frac{2L+1}{4\pi} P_L(\hat{n} \cdot \hat{n}) C_L^\alpha \\
&= \sum_L \frac{2L+1}{4\pi} C_L^\alpha = V_\alpha.
\end{aligned} \tag{4.33}$$

By construction $\langle \delta\alpha(\hat{n}) \rangle_\alpha = 0$, see Eq. (4.4), and therefore:

$$\begin{aligned} \langle F_{\ell m \ell_1 m_1}^\pm \rangle_\alpha &= \langle 1 - 2\delta\alpha^2 \rangle_\alpha \int d\Omega Y_{\pm 2, \ell m}^*(\hat{n}) Y_{\pm 2, \ell_1 m_1}(\hat{n}) \\ &= (1 - 2\langle \delta\alpha^2 \rangle_\alpha) \delta_{\ell \ell_1} \delta_{m m_1}. \end{aligned} \quad (4.34)$$

Replacing Eq. (4.34) in Eq. (4.31) we finally get:

$$C_\ell^{TE, obs} = (1 - 2\langle \delta\alpha^2 \rangle_\alpha) [C_\ell^{TE} \cos(2\alpha_0) - C_\ell^{TB} \sin(2\alpha_0)]. \quad (4.35)$$

In analogous way we obtain the TB observed power spectrum:

$$C_\ell^{TB, obs} = (1 - 2\langle \delta\alpha^2 \rangle_\alpha) [C_\ell^{TE} \sin(2\alpha_0) + C_\ell^{TB} \cos(2\alpha_0)]. \quad (4.36)$$

We now derive the expression for the observed EE, BB, EB. Let us starting with $C_\ell^{EB, obs}$:

$$\begin{aligned} \langle C_\ell^{EB, obs} \rangle_{CMB, \alpha} &= \frac{1}{2\ell + 1} \sum_{m=-\ell}^{+\ell} \langle a_{E\ell m}^{obs} (a_{B, \ell m}^{obs})^* \rangle_{CMB, \alpha} \\ &= \frac{1}{4} \frac{1}{2\ell + 1} \sum_m \sum_{\ell_1 m_1} \langle [(e^{2i\alpha_0} F_{\ell m \ell_1 m_1}^+ + e^{-2i\alpha_0} F_{\ell m \ell_1 m_1}^-) \\ &\quad a_{E, \ell_1 m_1} + i (e^{2i\alpha_0} F_{\ell m \ell_1 m_1}^+ - e^{-2i\alpha_0} F_{\ell m \ell_1 m_1}^-) \\ &\quad a_{B, \ell_1 m_1}] [(-i)^* (e^{2i\alpha_0} F_{\ell m \ell_1 m_1}^+ - e^{2i\alpha_0} F_{\ell m \ell_1 m_1}^-)]^* \\ &\quad (a_{E, \ell_1 m_1})^* + (e^{2i\alpha_0} F_{\ell m \ell_1 m_1}^+ + e^{-2i\alpha_0} F_{\ell m \ell_1 m_1}^-)^* \\ &\quad (a_{B, \ell_1 m_1})^*] \rangle_{CMB, \alpha}. \end{aligned} \quad (4.37)$$

Thus we need to calculate the four correlations: $\sum_{\ell_1 m_1} C_{\ell_1}^{XY} \langle F_{\ell m \ell_1 m_1}^\pm F_{\ell m \ell_1 m_1}^{\pm*} \rangle_\alpha$ and $\sum_{\ell_1 m_1} C_{\ell_1}^{XY} \langle F_{\ell m \ell_1 m_1}^\pm F_{\ell m \ell_1 m_1}^{\mp*} \rangle_\alpha$. Up to the second order in $\delta\alpha$, we get:

$$\begin{aligned} \sum_{\ell_1 m_1} C_{\ell_1}^{XY} \langle F_{\ell m \ell_1 m_1}^+ F_{\ell m \ell_1 m_1}^{+*} \rangle_\alpha &= \sum_{\ell_1 m_1} C_{\ell_1}^{XY} \langle \int d\Omega d\Omega' Y_{+2, \ell m}^*(\hat{n}) Y_{+2, \ell_1 m_1}(\hat{n}) e^{2i\delta\alpha(\hat{n})} \\ &\quad Y_{+2, \ell m}(\hat{n}') Y_{+2, \ell_1 m_1}^*(\hat{n}') e^{2i\delta\alpha(\hat{n}')} \rangle_\alpha \\ &= (1 - 4\langle \delta\alpha^2 \rangle_\alpha) C_{\ell_1}^{XY} + 4 \sum_{\ell_1 m_1} \sum_{L, M} C_{\ell_1}^{XY} C_L^\alpha \int d\Omega d\Omega' Y_{+2, \ell m}^*(\hat{n}) Y_{+2, \ell_1 m_1}(\hat{n}) \\ &\quad Y_{+2, \ell m}(\hat{n}') Y_{+2, \ell_1 m_1}^*(\hat{n}') Y_{+2, LM}^*(\hat{n}') Y_{+2, LM}(\hat{n}). \end{aligned} \quad (4.38)$$

Using the Wigner 3j symbol (see e.g. [120]), the last term can be expressed as:

$$\begin{aligned} &\sum_{\ell_1 m_1} \sum_{L, M} C_{\ell_1}^{XY} C_L^\alpha \int d\Omega d\Omega' Y_{+2, \ell m}^*(\hat{n}) Y_{+2, \ell_1 m_1}(\hat{n}) Y_{+2, \ell m}(\hat{n}') \\ &\quad Y_{+2, \ell_1 m_1}^*(\hat{n}') Y_{+2, LM}^*(\hat{n}') Y_{+2, LM}(\hat{n}) \\ &= \sum_{\ell_1 L} C_{\ell_1}^{XY} C_L^\alpha \frac{(2\ell_1 + 1)(2L + 1)}{\pi} \begin{pmatrix} \ell & \ell_1 & L \\ 2 & -2 & 0 \end{pmatrix}^2, \end{aligned} \quad (4.39)$$

thus:

$$\begin{aligned} \sum_{\ell_1 m_1} C_{\ell_1}^{XY} \langle F_{\ell m \ell_1 m_1}^+ F_{\ell m \ell_1 m_1}^{+*} \rangle_\alpha &= (1 - 4\langle \delta\alpha^2 \rangle_\alpha) C_\ell^{XY} + \\ &+ \sum_{\ell_1 L} C_{\ell_1}^{XY} C_L^\alpha \frac{(2\ell_1 + 1)(2L + 1)}{\pi} \begin{pmatrix} \ell & \ell_1 & L \\ 2 & -2 & 0 \end{pmatrix}^2. \end{aligned} \quad (4.40)$$

Similarly, it is possible to compute that:

$$\sum_{\ell_1 m_1} C_{\ell_1}^{XY} \langle F_{\ell m \ell_1 m_1}^+ F_{\ell m \ell_1 m_1}^{+*} \rangle_\alpha = \sum_{\ell_1 m_1} C_{\ell_1}^{XY} \langle F_{\ell m \ell_1 m_1}^- F_{\ell m \ell_1 m_1}^{-*} \rangle_\alpha, \quad (4.41)$$

and:

$$\begin{aligned} \sum_{\ell_1 m_1} C_{\ell_1}^{XY} \langle F_{\ell m \ell_1 m_1}^+ F_{\ell m \ell_1 m_1}^{-*} \rangle_\alpha &= \sum_{\ell_1 m_1} C_{\ell_1}^{XY} \langle F_{\ell m \ell_1 m_1}^+ F_{\ell m \ell_1 m_1}^{-*} \rangle_\alpha = \\ &= (1 - 4\langle \delta\alpha^2 \rangle_\alpha) C_\ell^{XY} + \sum_{\ell_1 L} (-1)^{\lambda+1} C_{\ell_1}^{XY} C_L^\alpha \frac{(2\ell_1 + 1)(2L + 1)}{\pi} \begin{pmatrix} \ell & \ell_1 & L \\ 2 & -2 & 0 \end{pmatrix}^2 \end{aligned} \quad (4.42)$$

with $\lambda = \ell + \ell_1 + L$. By replacing Eqs. (4.40)-(4.42) in Eq. (4.37) we get:

$$\begin{aligned} C_\ell^{EB,obs} &= (1 - 4\langle \delta\alpha^2 \rangle_\alpha) \left[\frac{1}{2} (C_\ell^{EE} - C_\ell^{BB}) \sin(4\alpha_0) + C_\ell^{EB} \cos(4\alpha_0) \right] + \\ &+ \sum_{\ell_1 L} \left[\frac{1}{2} (C_{\ell_1}^{EE} - C_{\ell_1}^{BB}) \sin(4\alpha_0) + C_{\ell_1}^{EB} \cos(4\alpha_0) \right] \\ &+ (-1)^{\lambda+1} C_L^\alpha \frac{(2\ell_1 + 1)(2L + 1)}{\pi} \begin{pmatrix} \ell & \ell_1 & L \\ 2 & -2 & 0 \end{pmatrix}^2 \end{aligned} \quad (4.43)$$

In analogous way we find the expressions for EE and BB observed power spectrum:

$$\begin{aligned} C_\ell^{EE,obs} &= (1 - 4\langle \delta\alpha^2 \rangle_\alpha) \left[C_\ell^{EE} \cos^2(2\alpha_0) + C_\ell^{BB} \sin^2(2\alpha_0) - C_\ell^{EB} \sin(4\alpha_0) \right] +, \\ &+ \frac{1}{2} \sum_{\ell_1 L} \left[C_{\ell_1}^{EE} (1 - (-1)^\lambda \cos(4\alpha_0)) + C_{\ell_1}^{BB} (1 + (-1)^\lambda \cos(4\alpha_0)) + \right. \\ &\left. - 2 C_{\ell_1}^{EB} (-1)^{\lambda+1} \sin(4\alpha_0) \right] C_L^\alpha \frac{(2\ell_1 + 1)(2L + 1)}{\pi} \begin{pmatrix} \ell & \ell_1 & L \\ 2 & -2 & 0 \end{pmatrix}^2 \end{aligned} \quad (4.44)$$

$$\begin{aligned} C_\ell^{BB,obs} &= (1 - 4\langle \delta\alpha^2 \rangle_\alpha) \left[C_\ell^{EE} \sin^2(2\alpha_0) + C_\ell^{BB} \cos^2(2\alpha_0) + C_\ell^{EB} \sin(4\alpha_0) \right] +, \\ &+ \frac{1}{2} \sum_{\ell_1 L} \left[C_{\ell_1}^{EE} (1 + (-1)^\lambda \cos(4\alpha_0)) + C_{\ell_1}^{BB} (1 - (-1)^\lambda \cos(4\alpha_0)) + \right. \\ &\left. + 2 C_{\ell_1}^{EB} (-1)^{\lambda+1} \sin(4\alpha_0) \right] C_L^\alpha \frac{(2\ell_1 + 1)(2L + 1)}{\pi} \begin{pmatrix} \ell & \ell_1 & L \\ 2 & -2 & 0 \end{pmatrix}^2 \end{aligned} \quad (4.45)$$

All the six CMB observed power spectra we have computed are reported here dropping out the operator $\langle \rangle_{CMB,\alpha}$ for sake of simplicity:

$$C_\ell^{TT,obs} = C_\ell^{TT} \quad (4.46)$$

$$C_\ell^{TE,obs} = (1 - 2V_\alpha) \left[C_\ell^{TE} \cos(2\alpha_0) - C_\ell^{TB} \sin(2\alpha_0) \right], \quad (4.47)$$

$$C_\ell^{TB,obs} = (1 - 2V_\alpha) \left[C_\ell^{TE} \sin(2\alpha_0) + C_\ell^{TB} \cos(2\alpha_0) \right], \quad (4.48)$$

$$\begin{aligned} C_\ell^{EE,obs} = & (1 - 4V_\alpha) \left[C_\ell^{EE} \cos^2(2\alpha_0) + C_\ell^{BB} \sin^2(2\alpha_0) - C_\ell^{EB} \sin(4\alpha_0) \right] +, \\ & + \frac{1}{2} \sum_{\ell_1 L} \left[C_{\ell_1}^{EE} \left(1 - (-1)^\lambda \cos(4\alpha_0) \right) + C_{\ell_1}^{BB} \left(1 + (-1)^\lambda \cos(4\alpha_0) \right) + \right. \\ & \left. - 2 C_{\ell_1}^{EB} (-1)^{\lambda+1} \sin(4\alpha_0) \right] M_{\ell\ell_1}^L C_L^\alpha, \end{aligned} \quad (4.49)$$

$$\begin{aligned} C_\ell^{BB,obs} = & (1 - 4V_\alpha) \left[C_\ell^{EE} \sin^2(2\alpha_0) + C_\ell^{BB} \cos^2(2\alpha_0) + C_\ell^{EB} \sin(4\alpha_0) \right] +, \\ & + \frac{1}{2} \sum_{\ell_1 L} \left[C_{\ell_1}^{EE} \left(1 + (-1)^\lambda \cos(4\alpha_0) \right) + C_{\ell_1}^{BB} \left(1 - (-1)^\lambda \cos(4\alpha_0) \right) + \right. \\ & \left. + 2 C_{\ell_1}^{EB} (-1)^{\lambda+1} \sin(4\alpha_0) \right] M_{\ell\ell_1}^L C_L^\alpha, \end{aligned} \quad (4.50)$$

$$\begin{aligned} C_\ell^{EB,obs} = & (1 - 4V_\alpha) \left[\frac{1}{2} \left(C_\ell^{EE} - C_\ell^{BB} \right) \sin(4\alpha_0) + C_\ell^{EB} \cos(4\alpha_0) \right] + \\ & + \sum_{\ell_1 L} \left[\frac{1}{2} \left(C_{\ell_1}^{EE} - C_{\ell_1}^{BB} \right) \sin(4\alpha_0) + C_{\ell_1}^{EB} \cos(4\alpha_0) \right] (-1)^{\lambda+1} M_{\ell\ell_1}^L C_L^\alpha, \end{aligned} \quad (4.51)$$

where the matrix with three indexes, $M_{\ell\ell_1}^L$, is defined as:

$$M_{\ell\ell_1}^L = \frac{(2\ell_1 + 1)(2L + 1)}{\pi} \begin{pmatrix} \ell & \ell_1 & L \\ 2 & -2 & 0 \end{pmatrix}^2. \quad (4.52)$$

Eqs. (4.46)-(4.51) recover the findings of [99] when the primordial parity-sensitive spectra are set to zero, i.e. $C_\ell^{TB} = C_\ell^{EB} = 0$. As it will be more clear in Section 4.2, the primordial EB power spectrum is needed here in order to build the quadratic estimator for C_L^α based on the observed EB spectrum (in which enters the covariance of primordial EB). In fact in for the Λ CDM model the C_ℓ^{EB} possesses a null mean value but a covariance different from zero.

It interesting to note that the spectra which involve the CMB temperature field, i.e. $C_\ell^{TE,obs}$ and $C_\ell^{TB,obs}$, are modified by an anisotropic birefringence effect just with a factor in front, proportional to the variance of the birefringence effect, see Eqs. (4.47), (4.48). Instead, the pure polarised CMB spectra, i.e. $C_\ell^{EE,obs}$, $C_\ell^{BB,obs}$ and $C_\ell^{EB,obs}$, in addition to the effect just described for

$C_\ell^{TE,obs}$ and $C_\ell^{TB,obs}$, get modified also through the terms which involve the matrix $M_{\ell\ell_1}^L$, coupling different multipoles, see Eqs. (4.49), (4.50) and (4.51).

When we switch-off the anisotropic contribution in Eqs. (4.46)-(4.51), we find the expressions of the CMB power spectra modified only by the isotropic CB (see e.g. [30], [121]):

$$C_\ell^{TT,obs} = C_\ell^{TT} \quad (4.53)$$

$$C_\ell^{TE,obs} = C_\ell^{TE} \cos(2\alpha_0) - C_\ell^{TB} \sin(2\alpha_0), \quad (4.54)$$

$$C_\ell^{TB,obs} = C_\ell^{TE} \sin(2\alpha_0) + C_\ell^{TB} \cos(2\alpha_0), \quad (4.55)$$

$$C_\ell^{EE,obs} = C_\ell^{EE} \cos^2(2\alpha_0) + C_\ell^{BB} \sin^2(2\alpha_0) - C_\ell^{EB} \sin(4\alpha_0), \quad (4.56)$$

$$C_\ell^{BB,obs} = C_\ell^{EE} \sin^2(2\alpha_0) + C_\ell^{BB} \cos^2(2\alpha_0) + C_\ell^{EB} \sin(4\alpha_0), \quad (4.57)$$

$$C_\ell^{EB,obs} = \frac{1}{2} (C_\ell^{EE} - C_\ell^{BB}) \sin(4\alpha_0) + C_\ell^{EB} \cos(4\alpha_0). \quad (4.58)$$

4.2 Formalism for the estimators

In our analysis we develop and perform two different and complementary methodologies to study in details the anisotropic birefringence effect. The first one is based on the localisation of the so-called D-estimators, a class of harmonic estimators for the isotropic birefringence. In section 4.2.1 we recall the formalism of the D-estimators and in section 4.2.2 we describe the employment of their localisation. The idea is to apply the D-estimators to patches of the sky in order to build maps of the birefringence angle, evaluating the CB spectrum on angular scales larger than ~ 7 degrees. This analysis [35] extends the paper [34] providing constraints for the CB spectrum on a wider multipoles range. Finally in section 4.2.3, we develop a novel class of linear and quadratic fully harmonic-based estimators which are able to directly evaluate the power spectrum of CB rotation angle starting from the EE, BB and EB observed angular power spectra of the CMB anisotropies [31].

4.2.1 D-estimators

The so-called D-estimators are harmonic-based estimators able to evaluate the isotropic birefringence angle, namely α_0 . They are defined through a linear combination of the CMB spectra by the following equations [114, 115]:

$$D_\ell^{TB,obs}(\beta) = C_\ell^{TB,obs} \cos(2\beta) - C_\ell^{TE,obs} \sin(2\beta), \quad (4.59)$$

$$D_\ell^{EB,obs}(\beta) = C_\ell^{EB,obs} \cos(4\beta) - \frac{1}{2} (C_\ell^{EE,obs} - C_\ell^{BB,obs}) \sin(4\beta), \quad (4.60)$$

where β is the estimator for the isotropic angle, α_0 . One of their most important features is that they depend explicitly on the multipole ℓ . This

makes them also suitable to search for scale dependence of the isotropic birefringence effect.

Replacing Eqs. (4.54)-(4.58) in the ensemble average of Eqs. (4.59) and (4.60) we find:

$$\langle D_\ell^{TB,obs}(\beta) \rangle = \sin(2(\alpha_0 - \beta)) C_\ell^{TE} + \cos(2(\alpha_0 - \beta)) C_\ell^{TB}, \quad (4.61)$$

$$\begin{aligned} \langle D_\ell^{EB,obs}(\beta) \rangle &= \sin(4(\alpha_0 - \beta)) \frac{1}{2} (C_\ell^{EE} - C_\ell^{BB}) + \\ &+ \cos(4(\alpha_0 - \beta)) C_\ell^{EB}, \end{aligned} \quad (4.62)$$

which are formally equal to Eq. (4.55) and Eq. (4.58) respectively with the replacement: $\alpha_0 \rightarrow \alpha_0 - \beta$. Moreover, for $\beta = \alpha_0$ we obtain

$$\langle D_\ell^{TB,obs}(\beta = \alpha_0) \rangle = C_\ell^{TB}, \quad (4.63)$$

$$\langle D_\ell^{EB,obs}(\beta = \alpha_0) \rangle = C_\ell^{EB}. \quad (4.64)$$

Eq. (4.63) and Eq. (4.64) tell us that if the primordial parity sensitive spectra are zero, i.e. $C_\ell^{TB} = C_\ell^{EB} = 0$, then the D-estimators vanish for $\beta = \alpha_0$,

$$\langle D_\ell^{TB,obs}(\beta = \alpha_0) \rangle = 0, \quad (4.65)$$

$$\langle D_\ell^{EB,obs}(\beta = \alpha_0) \rangle = 0, \quad (4.66)$$

whatever the value of α_0 is. Therefore, looking for β that nulls the expectation values of the D-estimators is equivalent to looking for the birefringence angle α that has rotated the primordial CMB spectra. Such an estimate of β can be obtained with a standard χ^2 -technique by minimising the following quantity:

$$\chi_{XY}^2 = \sum_{\ell, \ell'} D_\ell^{XY,obs} \left(C_{\ell\ell'}^{XY} \right)^{-1} D_{\ell'}^{XY,obs}, \quad (4.67)$$

where XY stands for TB or EB, $D_\ell^{XY,obs}$ is the respective D-estimator and $\left(C_{\ell\ell'}^{XY} \right)^{-1}$ is the inverse of the matrix $C_{\ell\ell'}^{XY} = \langle D_\ell^{XY,obs} D_{\ell'}^{XY,obs} \rangle$. In the present work we employ the D-estimators following a frequentist approach: a specific model is chosen and the matrices $C_{\ell\ell'}^{XY}$ are built for a reference model in which $\alpha = 0$, therefore the object $C_{\ell\ell'}^{XY}$ simply reduces to the XY covariance matrix. The idea is then to test whether the observed value of α is compatible with the null effect.

One can also minimise the combination [115]:

$$\chi_{(TB+EB)}^2 = \sum_{\ell, \ell'} \left(D_\ell^{TB,obs}, D_\ell^{EB,obs} \right) M_{\ell\ell'} \left(D_\ell^{TB,obs}, D_\ell^{EB,obs} \right), \quad (4.68)$$

where:

$$(M_{\ell\ell'})^{-1} = \begin{pmatrix} \langle D_{\ell}^{TB,obs} D_{\ell'}^{TB,obs} \rangle & \langle D_{\ell}^{TB,obs} D_{\ell'}^{EB,obs} \rangle \\ \langle D_{\ell}^{EB,obs} D_{\ell'}^{TB,obs} \rangle & \langle D_{\ell}^{EB,obs} D_{\ell'}^{EB,obs} \rangle \end{pmatrix}. \quad (4.69)$$

In Section 4.2.2 we will show the localisation approach of the D_{ℓ}^{EB} estimator to build maps of birefringence angle. Moreover, in Chapter 5, we employ the D_{ℓ}^{EB} estimator to investigate the impact of HWP non-idealities in measuring the isotropic CB angle.

4.2.1.1 D-estimators and anisotropic CB

It is possible to show that the formalism and the properties of the D-estimators continue to hold even in the more general framework which involves both isotropic and anisotropic CB. An useful relation for the computation of the D -estimators can be obtained by taking the half difference between Eq. (4.49) and (4.50):

$$\begin{aligned} \frac{1}{2} (C_{\ell}^{EE,obs} - C_{\ell}^{BB,obs}) &= (1 - 4V_{\alpha}) \left[\frac{1}{2} (C_{\ell}^{EE} - C_{\ell}^{BB}) \cos(4\alpha_0) + \right. \\ &\quad \left. - C_{\ell}^{EB} \sin(4\alpha_0) \right] + \sum_{\ell_1 L} \left[\frac{1}{2} (C_{\ell_1}^{EE} - C_{\ell_1}^{BB}) \cos(4\alpha_0) + \right. \\ &\quad \left. - C_{\ell_1}^{EB} \sin(4\alpha_0) \right] (-1)^{\lambda+1} M_{\ell\ell_1}^L C_L^{\alpha}. \end{aligned} \quad (4.70)$$

Therefore replacing Eqs. (4.47), (4.48) in Eq. (4.59) and Eqs. (4.51), (4.70) in Eq. (4.51) we obtain:

$$\begin{aligned} D_{\ell}^{TB,obs}(\beta) &= (1 - 2V_{\alpha}) \left[\sin(2(\alpha_0 - \beta)) C_{\ell}^{TE} + \cos(2(\alpha_0 - \beta)) C_{\ell}^{TB} \right], \quad (4.71) \\ D_{\ell}^{EB,obs}(\beta) &= (1 - 4V_{\alpha}) \left[\sin(4(\alpha_0 - \beta)) \frac{1}{2} (C_{\ell}^{EE} - C_{\ell}^{BB}) + \cos(4(\alpha_0 - \beta)) C_{\ell}^{EB} \right] + \\ &\quad + \sum_{\ell_1 L} \left[\sin(4(\alpha_0 - \beta)) \frac{1}{2} (C_{\ell_1}^{EE} - C_{\ell_1}^{BB}) + \cos(4(\alpha_0 - \beta)) C_{\ell_1}^{EB} \right] \cdot \\ &\quad \cdot (-1)^{\lambda+1} M_{\ell\ell_1}^L C_L^{\alpha}, \end{aligned} \quad (4.72)$$

which are formally equal to Eq. (4.48) and Eq. (4.51) respectively with the replacement: $\alpha_0 \rightarrow \alpha_0 - \beta$. Analogously to the isotropic case, for $\beta = \alpha_0$ we find:

$$D_{\ell}^{TB,obs}(\beta = \alpha_0) = (1 - 2V_{\alpha}) C_{\ell}^{TB}, \quad (4.73)$$

$$D_{\ell}^{EB,obs}(\beta = \alpha_0) = (1 - 4V_{\alpha}) C_{\ell}^{EB} + \sum_{\ell_1 L} C_{\ell_1}^{EB} (-1)^{\lambda+1} M_{\ell\ell_1}^L C_L^{\alpha}. \quad (4.74)$$

Eq. (4.73) and Eq. (4.74) tell us that the main property of the D-estimators still holds also when birefringence anisotropies are present: if the primordial parity sensitive spectra are zero, i.e. $C_\ell^{TB} = C_\ell^{EB} = 0$, then the D-estimators are null for $\beta = \alpha_0$, whatever the value of α_0 is. In other words the D-estimators are suitable to search for the isotropic birefringence angle even when an anisotropic effect is present.

4.2.2 Localisation approach with the D-estimators

This approach follows the methodology described in [34]. From the CMB T, Q and U maps at high resolution we build maps of the birefringence angle $\alpha(\hat{n})$ at low resolution, which allow us to evaluate the CB spectrum on angular scales larger than ~ 7 degrees. We divided the CMB sky in small regions of equal area, henceforth “patches”, following the Healpy³ [91] pixelization scheme at $N_{side} = 8$. The sky fraction covered by one single patch is $f_{sky,patch} = 0.13\%$ and the total number of patches is 768.

In each of these regions we have applied the D-estimators to extract the birefringence angle, which is assumed constant in that given region. Finally, from the values of the CB angle in each patch, the CB auto-correlation spectrum is evaluated through the use of a Quadratic Maximum Likelihood (QML) method. In [35] are also provided the cross-correlation of the CB spectrum with the T, E and B CMB fields.

The D-estimator based on the EB CMB spectra, Eq. (4.60), has more constraining power than the one based on TB spectrum, since the latter has a lower signal to noise ratio for the dataset we consider. Therefore we decide to estimate α in each patch only through the minimisation of the χ_{EB}^2 :

$$\chi_{EB}^2 = \sum_{\ell,\ell'} D_\ell^{EB,obs} \left(C_{\ell\ell'}^{EB} \right)^{-1} D_{\ell'}^{EB,obs}, \quad (4.75)$$

where $D_\ell^{EB,obs}$ is the D-estimator obtained with the CMB spectra extracted in that specific patch and $\left(C_{\ell\ell'}^{EB} \right)^{-1}$ is the inverse of $C_{\ell\ell'}^{EB} = \langle D_{\ell'}^{EB,obs} D_\ell^{EB,obs} \rangle$. Since we employ this minimisation following a frequentist approach with the specific model in which $\alpha_0 = 0$, the object $C_{\ell\ell'}^{EB}$ simply reduces to the EB covariance matrix computed for each patch.

At the end of this process we have a map for the CB angles, from which using a QML estimator [122], we evaluate the CB spectrum C_L^α .

³<http://healpix.sourceforge.net>

4.2.3 C_L^α estimators

In this section we assume that the monopole of CB is null, and we focus on deriving estimators able to constrain anisotropic birefringence from CMB observed power spectra. This choice is consistent with all the current estimates of α . However, in case the monopole is different from zero, it is always possible to de-rotate the CMB spectra and remove the contribution of this term, for example by applying the D-estimators (see section 4.2.1).

We are going to use Eq. (4.49), Eq. (4.50) and Eq. (4.51) with $\alpha_0 = 0$ to develop five estimators which can be divided in two classes, the first one is linear and the second one is quadratic in the CMB spectra. It is useful rewrite these equations in a slightly more compact form. We start considering Eq. 4.49, that can be re-written as:

$$C_\ell^{EE,obs} = (1 - 4V_\alpha)C_\ell^{EE} + \sum_{L'} \left[H_{\ell\ell',odd}^L C_{\ell'}^{EE} + H_{\ell\ell',ev}^L C_{\ell'}^{BB} \right] C_L^\alpha, \quad (4.76)$$

where the matrix $H_{\ell\ell',odd}^L$ is defined as:

$$\begin{aligned} H_{\ell\ell',odd}^L &= \frac{1 - (-1)^\lambda}{2} M_{\ell\ell'}^L \\ &= \begin{cases} \frac{(2\ell'+1)(2L+1)}{\pi} \begin{pmatrix} \ell & \ell' & L \\ 2 & -2 & 0 \end{pmatrix}^2 & (\lambda \text{ odd}) \\ 0 & (\lambda \text{ even}) \end{cases} \end{aligned} \quad (4.77)$$

and the matrix $H_{\ell\ell',ev}^L$ as:

$$\begin{aligned} H_{\ell\ell',ev}^L &= \frac{1 + (-1)^\lambda}{2} M_{\ell\ell'}^L = \\ &= \begin{cases} \frac{(2\ell'+1)(2L+1)}{\pi} \begin{pmatrix} \ell & \ell' & L \\ 2 & -2 & 0 \end{pmatrix}^2 & (\lambda \text{ even}) \\ 0 & (\lambda \text{ odd}) \end{cases} \end{aligned} \quad (4.78)$$

Replacing the definition of V_α , i.e.

$$V_\alpha = \sum_L \frac{2L+1}{4\pi} C_L^\alpha, \quad (4.79)$$

we obtain:

$$\begin{aligned} C_\ell^{EE,obs} &= C_\ell^{EE} + \sum_{L'} \left[(-1)^{\frac{2L+1}{\pi}} C_{\ell'}^{EE} \delta_{\ell\ell'} + H_{\ell\ell',odd}^L C_{\ell'}^{EE} + H_{\ell\ell',ev}^L C_{\ell'}^{BB} \right] C_L^\alpha \\ &= C_\ell^{EE} + \sum_{L'} \left[\tilde{H}_{\ell\ell'}^L C_{\ell'}^{EE} + H_{\ell\ell',ev}^L C_{\ell'}^{BB} \right] C_L^\alpha, \end{aligned} \quad (4.80)$$

where the matrix $\tilde{H}_{\ell\ell'}^L$ is:

$$\tilde{H}_{\ell\ell'}^L = H_{\ell\ell',\text{odd}}^L - \frac{2L+1}{\pi} \delta_{\ell\ell'}. \quad (4.81)$$

Thus, its final form becomes:

$$C_{\ell}^{EE,obs} = C_{\ell}^{EE} + [\tilde{H}_{\ell\ell'}^L C_{\ell'}^{EE} + H_{\ell\ell',ev}^L C_{\ell'}^{BB}] C_L^{\alpha}, \quad (4.82)$$

where the sum over repeated indexes is understood. In an analogous way, starting from Eq. (4.50) and Eq. (4.51), we obtain respectively:

$$C_{\ell}^{BB,obs} = C_{\ell}^{BB} + [\tilde{H}_{\ell\ell'}^L C_{\ell'}^{BB} + H_{\ell\ell',ev}^L C_{\ell'}^{EE}] C_L^{\alpha}, \quad (4.83)$$

$$C_{\ell}^{EB,obs} = C_{\ell}^{EB} + \tilde{K}_{\ell\ell'}^L C_{\ell'}^{EB} C_L^{\alpha}, \quad (4.84)$$

where the $\tilde{K}_{\ell\ell'}^L$ matrix is defined as:

$$\tilde{K}_{\ell\ell'}^L = (-1)^{\lambda+1} M_{\ell\ell'}^L - \frac{2L+1}{\pi} \delta_{\ell\ell'}. \quad (4.85)$$

Eqs.(4.82), (4.83) and (4.84) represent the starting point from which we derive the estimators for C_L^{α} . In the following section we build two linear estimators based on EE and BB CMB power spectra, and three quadratic estimator based on EE, BB and EB CMB power spectra. It is not possible to develop a linear estimator based on Eq.(4.84) because $C_{\ell}^{EB,obs}$ vanishes in absence of isotropic CB under the hypothesis of a null primordial EB spectrum (as expected in the standard Λ CDM cosmological model). In order to find expressions involving the $C_{\ell}^{EB,obs}$ which are sensitive to anisotropic birefringence we have to consider higher-order statistics. In particular, we are going to build an estimator which is quadratic in $C_{\ell}^{EB,obs}$.

4.2.3.1 Linear estimators

The idea is to look for estimators E^L linear in the CMB observed spectra:

$$E^L = E_{\ell}^L C_{\ell}^{obs}, \quad (4.86)$$

where the sum over repeated indexes is understood, such that their expectation value is the spectrum of birefringence

$$\langle E^L \rangle = C_L^{\alpha}. \quad (4.87)$$

Hence the goal is to find the two-indices object E_{ℓ}^L which satisfies the condition given by Eq. (4.87) and that it is also minimum variance.

Due to the (symmetry and) similarity between the EE and BB CMB observed power spectra, see Eqs. (4.82) and (4.83), the development of estimators based on these spectra follows the same algebraic steps. Therefore we show in detail the building of the linear estimator based on the EE CMB power spectra and just provide the result from the one based on BB.

EE-based estimator

Replacing Eq. (4.82) in Eq. (4.86) and neglecting terms beyond the linear order in C_L^α , we find:

$$\begin{aligned} E_{(EE)}^L &= E_\ell^L C_\ell^{EE,obs} \\ &= E_\ell^L C_\ell^{EE} + E_\ell^L \left[\tilde{H}_{\ell\ell'}^{L'} C_{\ell'}^{EE} + H_{\ell\ell',ev}^{L'} C_{\ell'}^{BB} \right] C_{L'}^\alpha. \end{aligned} \quad (4.88)$$

We take now the ensemble average of Eq. (4.88) over the CMB realisations:

$$\langle E_{(EE)}^L \rangle = E_\ell^L \langle C_\ell^{EE} \rangle + E_\ell^L W_\ell^{L'} C_{L'}^\alpha, \quad (4.89)$$

where $W_\ell^{L'}$ is defined as:

$$W_\ell^{L'} = \left[\tilde{H}_{\ell\ell'}^{L'} \langle C_{\ell'}^{EE} \rangle + H_{\ell\ell',ev}^{L'} \langle C_{\ell'}^{BB} \rangle \right]. \quad (4.90)$$

We note that $\langle E_{(EE)}^L \rangle$ in Eq. (4.89) is different from zero even if we switch off the anisotropic birefringence effect. But, of course, we wish to build an estimator whose expectation value is different from zero *only if* a birefringence effect is in action. Therefore we redefine $E_{(EE)}^L$ as:

$$E_{(EE)}^L \rightarrow E_{(EE)}^L - E_\ell^L \langle C_\ell^{EE} \rangle, \quad (4.91)$$

such that the estimator becomes:

$$E_{(EE)}^L = E_\ell^L C_\ell^{EE,obs} - E_\ell^L \langle C_\ell^{EE} \rangle, \quad (4.92)$$

and its expectation value reads:

$$\langle E_{(EE)}^L \rangle = E_\ell^L W_\ell^{L'} C_{L'}^\alpha, \quad (4.93)$$

which, as desired, is now different from zero only if there is anisotropic CB in action. Note that the term $E_\ell^L \langle C_\ell^{EE} \rangle$ represents the contribution we have in the standard Λ CDM model. For this reason in the following we call it Λ CDM-noise. It is now natural to require that:

$$E_\ell^L W_\ell^{L'} = \delta^{LL'}, \quad (4.94)$$

in order to have:

$$\langle E_{(EE)}^L \rangle = C_L^\alpha. \quad (4.95)$$

This equation is exactly our initial goal, i.e. Eq. (4.87).

We now require that the estimator is not only unbiased, as given by Eq. (4.94), but also minimum variance. Hence we apply the method of the

Lagrange multipliers for a given L , and minimise the Lagrange function, \mathcal{L} , defined as:

$$\mathcal{L}(E_\ell^L, \kappa) = V^{LL} - \kappa (E_\ell^L W_\ell^L - 1), \quad (4.96)$$

where κ is a constant, called Lagrange multiplier, which multiplies the constraint given by Eq. (4.94) for $L = L'$ and V^{LL} is the variance of the estimator $E_{(EE)}^L$, i.e.

$$V^{LL'} = \langle (E^L - \langle E^L \rangle) (E^{L'} - \langle E^{L'} \rangle) \rangle, \quad (4.97)$$

computed for $L = L'$. No sum over L is understood in Eq. (4.96).

Replacing Eq. (4.92) in Eq. (4.97) and using the Wick theorem, under the approximation that $C_\ell^{EE,obs}$ statistically behaves as a Gaussian distribution⁴, it is possible to compute the covariance of the estimator, i.e. $V^{LL'}$:

$$V^{LL'} = E_\ell^L C_{\ell\ell'}^{EE,obs} E_{\ell'}^{L'}, \quad (4.98)$$

where the sum over ℓ is understood and $C_{\ell\ell'}^{EE,obs}$ is the covariance matrix of the rotated power spectra⁵, i.e.

$$C_{\ell\ell'}^{EE,obs} = \langle (C_\ell^{EE,obs} - \langle C_\ell^{EE,obs} \rangle) (C_{\ell'}^{EE,obs} - \langle C_{\ell'}^{EE,obs} \rangle) \rangle. \quad (4.99)$$

The minimisation of Eq. (4.96) is performed through the computation of the following derivatives:

$$\frac{\partial \mathcal{L}(E_\ell^L, \kappa)}{\partial E_\ell^L} = 0, \quad (4.100)$$

$$\frac{\partial \mathcal{L}(E_\ell^L, \kappa)}{\partial \kappa} = 0, \quad (4.101)$$

which can be rewritten as:

$$2 E_{\ell'}^L C_{\ell\ell'}^{EE,obs} = \kappa W_\ell^L, \quad (4.102)$$

$$E_\ell^L W_\ell^L = 1. \quad (4.103)$$

No sum over L is understood. The solution of Eqs. (4.102) and (4.103) reads

$$E_\ell^L = \frac{\kappa}{2} W_{\ell'}^L (C_{\ell'\ell}^{EE,obs})^{-1}, \quad (4.104)$$

⁴This is not true of course, but we will see that in practice this is a fairly good approximation.

⁵Note that, when the label *obs* is applied on the covariance matrix it means that such matrix contains the birefringence effect.

where the constant, κ , is given by

$$\kappa = \frac{2}{W_{\ell'}^L (C_{\ell'\ell}^{EE,obs})^{-1} W_{\ell}^L}. \quad (4.105)$$

Now we can find the explicit expression for the estimator. Replacing Eq. (4.104) in Eq. (4.92), we obtain:

$$E_{(EE)}^L = \frac{\kappa}{2} W_{\ell'}^L (C_{\ell'\ell}^{EE,obs})^{-1} [C_{\ell}^{EE,obs} - \langle C_{\ell}^{EE} \rangle], \quad (4.106)$$

and taking the ensemble average of Eq. (4.106) we compute:

$$\begin{aligned} \langle E_{(EE)}^L \rangle &= \frac{\kappa}{2} W_{\ell'}^L (C_{\ell'\ell}^{EE,obs})^{-1} [\langle C_{\ell}^{EE,obs} \rangle - \langle C_{\ell}^{EE} \rangle] \\ &= \frac{\kappa}{2} W_{\ell'}^L (C_{\ell'\ell}^{EE,obs})^{-1} [\langle C_{\ell}^{EE} \rangle + W_{\ell}^{L'} C_{L'}^{\alpha} - \langle C_{\ell}^{EE} \rangle] \\ &= \frac{\kappa}{2} W_{\ell'}^L (C_{\ell'\ell}^{EE,obs})^{-1} W_{\ell}^{L'} C_{L'}^{\alpha} \\ &= F^{LL'} C_{L'}^{\alpha}, \end{aligned} \quad (4.107)$$

where:

$$F^{LL'} = \frac{\kappa}{2} W_{\ell'}^L (C_{\ell'\ell}^{EE,obs})^{-1} W_{\ell}^{L'}. \quad (4.108)$$

We find the expectation value of Eq. (4.95) only for $L = L'$ and neglecting all the off-diagonal terms⁶. However we wish to find Eq. (4.95) even when all the off-diagonal terms of $F^{LL'}$ are present. Hence, we define a new estimator, i.e. \hat{E}^L , as:

$$\hat{E}_{(EE)}^L = (F^{LL'})^{-1} E_{(EE)}^{L'}, \quad (4.109)$$

such that:

$$\hat{E}_{(EE)}^L = (F^{LL'})^{-1} [E_{\ell}^{L'} C_{\ell}^{EE,obs} - E_{\ell}^{L'} \langle C_{\ell}^{EE} \rangle], \quad (4.110)$$

and its expectation value reads:

$$\langle \hat{E}_{(EE)}^L \rangle = C_L^{\alpha}. \quad (4.111)$$

Eq. (4.110) represents the final algebraic expression of the linear EE-based estimator for anisotropic birefringence.

⁶This should not appear as a surprise since we have obtained our solution right under the condition $L = L'$.

Note that κ drops out in Eq. (4.110). This means that we have the freedom to choose the value of κ we like more. It is possible to show that by replacing Eq. (4.110) in Eq. (4.97), the covariance of the estimates is:

$$\begin{aligned} V^{LL'} &= \langle (\hat{E}^L - \langle \hat{E}^L \rangle) (\hat{E}^{L'} - \langle \hat{E}^{L'} \rangle) \rangle \\ &= \left[W_{\ell'}^L (C_{\ell'\ell}^{EE,obs})^{-1} W_{\ell}^{L'} \right]^{-1}. \end{aligned} \quad (4.112)$$

Therefore it is natural to set $\kappa = 2$ so that the inverse of the F matrix represents the covariance of the estimates:

$$(F^{LL'})^{-1} = V^{LL'}. \quad (4.113)$$

It will be shown in Section 4.5 that the implementation of Eq. (4.110) satisfies with a good approximation Eq. (4.113), therefore the inverse of F matrix can be used to make forecast for future CMB experiments without the need of producing a large set of CMB simulations.

Under the assumptions made above, the final expressions ⁷ of the objects used to build the estimator become:

$$E_{\ell}^L = W_{\ell'}^L (C_{\ell'\ell}^{EE,obs})^{-1}, \quad (4.114)$$

$$F^{LL'} = W_{\ell'}^L (C_{\ell'\ell}^{EE,obs})^{-1} W_{\ell}^{L'}, \quad (4.115)$$

$$W_{\ell}^{L'} = \left[\tilde{H}_{\ell\ell'}^{L'} \langle C_{\ell'\ell}^{EE} \rangle + H_{\ell\ell',ev}^{L'} \langle C_{\ell'\ell}^{BB} \rangle \right]. \quad (4.116)$$

It is possible to show that the expectation value of the estimator, Eq. (4.111), does not depend on the model used to build $C_{\ell'\ell}^{EE,obs}$. In other words, the estimator is still unbiased, i.e. Eq. (4.111), whatever the choice of $C_{\ell'\ell}^{EE,obs}$ used to compute the E_{ℓ}^L and $F^{LL'}$ in Eqs (4.115) and 4.116. Obviously, the latter have the statistical and physical meaning described above only if $C_{\ell'\ell}^{EE,obs}$ is a description of the statistical behaviour of the simulations and data which enter in Eq.(4.110).

BB-based estimator

Replacing Eq. (4.83) in Eq. (4.86) and following similar steps as done in the previous section, we can build an estimator which is linear in the $C_{\ell}^{BB,obs}$ power spectrum:

$$\hat{E}_{(BB)}^L = (F^{LL'})^{-1} \left[E_{\ell}^{L'} C_{\ell}^{BB,obs} - E_{\ell}^{L'} \langle C_{\ell}^{BB} \rangle \right], \quad (4.117)$$

⁷We report here for completeness also the expression for the object W_{ℓ}^L , see Eq. (4.90), even if it does not depend on the κ parameter

and its expectation value reads:

$$\langle \hat{E}_{(BB)}^L \rangle = C_L^\alpha. \quad (4.118)$$

The statistical objects that enter in this second estimator (Eq 4.117), under the choice of $\kappa = 2$, are

$$E_\ell^L = W_{\ell'}^L \left(C_{\ell'\ell}^{BB,obs} \right)^{-1}, \quad (4.119)$$

$$F^{LL'} = W_{\ell'}^L \left(C_{\ell'\ell}^{BB,obs} \right)^{-1} W_\ell^{L'}, \quad (4.120)$$

$$W_\ell^{L'} = \left[\tilde{H}_{\ell\ell'}^{L'} \langle C_{\ell'\ell}^{BB} \rangle + H_{\ell\ell',ev}^{L'} \langle C_{\ell'\ell}^{EE} \rangle \right]. \quad (4.121)$$

Also for the BB-based estimator:

- we re-find the useful relation Eq. (4.113) between the inverse of the F matrix and the covariance of the estimates;
- its expectation value does not depend on the choice of covariance matrix $C_{\ell'\ell}^{BB,obs}$ which enters in Eqs (4.120) and 4.121.

Summarising, starting from the expressions of the EE and BB observed CMB power spectra, see Eqs. (4.82) and (4.83), we have developed two new unbiased and nearly-minimum variance⁸ estimators for the birefringence spectrum under the assumption that we can write their covariance as given in Eq. (4.112).

4.2.3.2 Quadratic estimators

Now we search for estimators E^L quadratic in the CMB observed spectra:

$$E^L = C_{\ell_1}^{obs} E_{\ell_1 \ell_2}^L C_{\ell_2}^{obs}, \quad (4.122)$$

where the sum over repeated indexes is understood, whose expectation value is the spectrum of birefringence:

$$\langle E^L \rangle = C_L^\alpha. \quad (4.123)$$

As done for the linear estimators, we wish to compute the expression of the three-indices object $E_{\ell_1 \ell_2}^L$ that satisfies the condition given by Eq. (4.123) and is also minimum variance.

⁸The estimators are minimum variance as long as C_ℓ^{EE} and C_ℓ^{BB} statistically behave as Gaussian distributions: the APS are χ^2 -distributed, but for $\ell \gg 1$ their distributions tend to be Gaussian.

The EE,BB and EB CMB observed power spectra, (Eqs. 4.82,4.83 and 4.84), have an analogous functional form, so also in this case the development of estimators based on these spectra follow the same algebraic steps. As done for the linear estimators, we are going to show in detail the building of the quadratic estimator based on the EE CMB power spectra, while we will give only the results for the other ones.

EE-based estimator

Replacing Eq. (4.82) in Eq. (4.122) and neglecting terms beyond the linear order in C_L^α , we find:

$$\begin{aligned} E_{(EE^2)}^L &= C_{\ell_1}^{EE,obs} E_{\ell_1\ell_2}^L C_{\ell_2}^{EE,obs} \\ &= C_{\ell_1}^{EE} E_{\ell_1\ell_2}^L C_{\ell_2}^{EE} + E_{\ell_1\ell_2}^L \left[\tilde{H}_{\ell_2\ell_2}^{L'} C_{\ell_2'}^{EE} C_{\ell_1}^{EE} + H_{\ell_2\ell_2, ev}^{L'} C_{\ell_2'}^{BB} C_{\ell_1}^{EE} \right. \\ &\quad \left. + \tilde{H}_{\ell_1\ell_1}^{L'} C_{\ell_1'}^{EE} C_{\ell_2}^{EE} + H_{\ell_1\ell_1, ev}^{L'} C_{\ell_1'}^{BB} C_{\ell_2}^{EE} \right] C_{L'}^\alpha. \end{aligned} \quad (4.124)$$

The ensemble average of Eq. (4.124) over the CMB realisations reads:

$$\begin{aligned} \langle E_{(EE^2)}^L \rangle &= E_{\ell_1\ell_2}^L C_{\ell_2\ell_1}^{EE,EE} + E_{\ell_1\ell_2}^L \left[\tilde{H}_{\ell_2\ell_2}^{L'} C_{\ell_2'\ell_1}^{EE,EE} + H_{\ell_2\ell_2, ev}^{L'} C_{\ell_2'\ell_1}^{BB,EE} \right. \\ &\quad \left. + \tilde{H}_{\ell_1\ell_1}^{L'} C_{\ell_1'\ell_2}^{EE,EE} + H_{\ell_1\ell_1, ev}^{L'} C_{\ell_1'\ell_2}^{BB,EE} \right] C_{L'}^\alpha, \end{aligned} \quad (4.125)$$

where we have set $C_{\ell_1\ell_2}^{EE,EE} = \langle C_{\ell_1}^{EE} C_{\ell_2}^{EE} \rangle$ and $C_{\ell_1\ell_2}^{BB,EE} = \langle C_{\ell_1}^{BB} C_{\ell_2}^{EE} \rangle$ ⁹. Defining the symmetric statistical object $W_{\ell_1\ell_2}^{L1}$ as:

$$\begin{aligned} W_{\ell_1\ell_2}^{L'} &= \left[\tilde{H}_{\ell_2\ell_2}^{L'} C_{\ell_2'\ell_1}^{EE,EE} + H_{\ell_2\ell_2, ev}^{L'} C_{\ell_2'\ell_1}^{BB,EE} + \right. \\ &\quad \left. + \tilde{H}_{\ell_1\ell_1}^{L'} C_{\ell_1'\ell_2}^{EE,EE} + H_{\ell_1\ell_1, ev}^{L'} C_{\ell_1'\ell_2}^{BB,EE} \right], \end{aligned} \quad (4.126)$$

we can rewrite Eq. (4.125) in a slightly more compact form:

$$\langle E_{(EE^2)}^L \rangle = Tr \left[E^L C^{EE,EE} \right] + Tr \left[E^L W^{L'} \right] C_{L'}^\alpha \quad (4.127)$$

where the trace operator, $Tr[\dots]$, is acting on the CMB multipoles, which are therefore omitted. Note that in the linear estimator, at fixed L , the objects E_ℓ^L and W_ℓ^L are vectors in the CMB multipoles, while in the quadratic formalism they become symmetric matrices. In fact $E_{\ell_1\ell_2}^L$ is symmetric when exchanging of the lower indexes, i.e. the CMB multipoles, by construction

⁹By convention, to indicate the covariance of the spectra of the $C_{\ell_1}^{XX}$ we use the symbol $C_{\ell_1\ell_2}^{XX} = \langle C_{\ell_1}^{XX} C_{\ell_2}^{XX} \rangle - \langle C_{\ell_1}^{XX} \rangle \langle C_{\ell_2}^{XX} \rangle$, meanwhile the symbol $C_{\ell_1\ell_2}^{XX,XX}$ reads $C_{\ell_1\ell_2}^{XX,XX} = \langle C_{\ell_1}^{XX} C_{\ell_2}^{XX} \rangle$

and consistently in Eq. (4.127) it is contracted only with symmetric objects in the same lower indexes, as $C_{\ell_1\ell_2}^{EE,EE}$ and $W_{\ell_1\ell_2}^{L'}$.

As done for the linear estimator, in order to build an estimator whose expectation value is different from zero *only if* a birefringence effect is in action, we redefine $E_{(EE^2)}^L$ as:

$$E_{(EE^2)}^L \rightarrow E_{(EE^2)}^L - Tr \left[E^L C^{EE,EE} \right]. \quad (4.128)$$

Hence the estimator becomes:

$$E_{(EE^2)}^L = C_{\ell_1}^{EE,obs} E_{\ell_1\ell_2}^L C_{\ell_2}^{EE,obs} - Tr \left[E^L C^{EE,EE} \right], \quad (4.129)$$

and its expectation value reads

$$\langle E_{(EE^2)}^L \rangle = Tr \left[E^L W^{L'} \right] C_{L'}^\alpha, \quad (4.130)$$

which, as desired, is non-null *only if* there is a birefringence effect. We require that:

$$Tr \left[E^L W^{L'} \right] = \delta_{LL'} \quad (4.131)$$

such that the expectation value becomes exactly the birefringence power spectrum, Eq. (4.123), and therefore the estimator is unbiased.

As done before with the linear estimators, we now require that the estimator is also minimum variance, hence we apply the method of the Lagrange multipliers for a given L , and minimise the Lagrange function, \mathcal{L} , defined as:

$$\mathcal{L}(E^L, \kappa) = V^{LL} - 2\kappa Tr \left[E^L W^L - 1 \right], \quad (4.132)$$

where the constant κ is the Lagrange multiplier which multiplies the constraint given by Eq. (4.131) for $L = L'$ and V^{LL} is the variance of the estimator $E_{(EE^2)}^L$. No sum over L is understood in Eq. (4.132).

Replacing Eq. (4.129) in Eq. (4.97) and using the Wick theorem, under the approximation that $C_{\ell}^{EE,obs}$ statistically behaves as a Gaussian distribution¹⁰, it is possible to compute the covariance of the estimator, i.e. $V^{LL'}$:

$$V^{LL'} = 2Tr \left[E^L D^{E,E} E^{L'} D^{E,E} \right], \quad (4.133)$$

where we have set $D^{E,E} \equiv C_{\ell_1\ell_2}^{EE,EE,obs} = \langle C_{\ell_1}^{EE,obs} C_{\ell_2}^{EE,obs} \rangle$ to make the notation lighter.

¹⁰This is not true of course, but we will see that in practice this is a fairly good approximation.

Through the computation of the following derivatives we minimise Eq. (4.132):

$$\frac{\partial \mathcal{L}(E^L, \kappa)}{\partial E^L} = \text{Tr} \left[2(D^{E,E} E^L D^{E,E}) - \kappa W^L \right] = 0, \quad (4.134)$$

$$\frac{\partial \mathcal{L}(E^L, \kappa)}{\partial \kappa} = \text{Tr} \left[E^L W^L - 1 \right] = 0. \quad (4.135)$$

The solution of Eqs. (4.134) and (4.135) reads

$$E^L = \frac{\kappa}{2} \left(D_{\ell_1 \ell'_1}^{E,E} \right)^{-1} W_{\ell'_1 \ell'_2}^L \left(D_{\ell'_2 \ell_2}^{E,E} \right)^{-1}, \quad (4.136)$$

with the constant κ :

$$\kappa = \frac{1}{\text{Tr} \left[(D^{E,E})^{-1} W^L (D^{E,E})^{-1} W^L \right]}. \quad (4.137)$$

Therefore replacing Eq. (4.136) in Eq. (4.129) gives:

$$E_{(EE^2)}^L = \frac{\kappa}{2} \left[C_{\ell_1}^{EE,obs} \left(D_{\ell_1 \ell'_1}^{E,E} \right)^{-1} W_{\ell'_1 \ell'_2}^L \left(D_{\ell'_2 \ell_2}^{E,E} \right)^{-1} C_{\ell_2}^{EE,obs} - \text{Tr} \left[(D^{E,E})^{-1} W^L (D^{E,E})^{-1} C^{EE,EE} \right] \right]. \quad (4.138)$$

The ensemble average of Eq. (4.138) reads:

$$\langle E_{(EE^2)}^L \rangle = \frac{\kappa}{2} \text{Tr} \left[(D^{E,E})^{-1} W^L (D^{E,E})^{-1} (D^{E,E} - C^{EE,EE}) \right]. \quad (4.139)$$

Since it is possible to show that:

$$D_{\ell_2 \ell_1}^{E,E} = C_{\ell_2 \ell_1}^{EE,EE} + W_{\ell_2 \ell_1}^{L'} C_{L'}^\alpha, \quad (4.140)$$

we get:

$$\begin{aligned} \langle E_{(EE^2)}^L \rangle &= \frac{\kappa}{2} \text{Tr} \left[(D^{E,E})^{-1} W^L (D^{E,E})^{-1} W^{L'} \right] C_{L'}^\alpha \\ &= F^{LL'} C_{L'}^\alpha, \end{aligned} \quad (4.141)$$

where the matrix $F^{LL'}$ is defined as:

$$F^{LL'} = \frac{\kappa}{2} \text{Tr} \left[(D^{E,E})^{-1} W^L (D^{E,E})^{-1} W^{L'} \right]. \quad (4.142)$$

In order to find Eq. (4.123) when all the off-diagonal terms of $F^{LL'}$ are considered, we define a new estimator, $\hat{E}_{(EE^2)}^L$, as:

$$\hat{E}_{(EE^2)}^L = \left(F^{LL'} \right)^{-1} E_{(EE^2)}^{L'}, \quad (4.143)$$

such that:

$$\hat{E}_{(EE^2)}^L = \left(F^{LL'}\right)^{-1} \left[C_{\ell_1}^{EE,obs} E_{\ell_1\ell_2}^L C_{\ell_2}^{EE,obs} - Tr \left[E^L C^{EE,EE} \right] \right], \quad (4.144)$$

and its expectation value reads as Eq. (4.123):

$$\langle \hat{E}_{(EE^2)}^L \rangle = C_L^\alpha. \quad (4.145)$$

Replacing Eq. (4.144) in Eq. (4.97) it is possible to compute the covariance of the estimates:

$$V_{(EE^2)}^{LL'} = \left(\frac{1}{2} Tr \left[\left(D^{E,E} \right)^{-1} W^L \left(D^{E,E} \right)^{-1} W^{L'} \right] \right)^{-1}. \quad (4.146)$$

Eq. (4.144) represents the final algebraic expression of the EE -based quadratic estimator for anisotropic birefringence. The analogy with the QML for the angular power spectrum of CMB anisotropies, as presented in [113], is striking: in practice they are formally the same with $W_{\ell_1\ell_2}^L$, as defined in Eq. (4.126), playing the role of the Legendre polynomials, $P_\ell(i \cdot j)$ of the standard QML method [113], with the additional difference that the $P_\ell(i \cdot j)$ are matrices labeled by ℓ and defined in pixel space whereas here the $W_{\ell_1\ell_2}^L$ are matrices labeled by L and defined in the (CMB) harmonic space.

Note that, as for linear case, since κ drops out in the final expression of the estimator (Eq. 4.144), it is possible to choose the value of κ we like more. Since Eq. (4.146) is properly the inverse of the F matrix with $\kappa = 1$:

$$\left(F^{LL'}\right)^{-1} |_{\kappa=1} = V^{LL'}, \quad (4.147)$$

it is convenient to make this choice. The final expressions ¹¹ of the objects used to build the estimator choosing $\kappa = 1$ are:

$$E^L = \frac{1}{2} \left(D_{\ell_1\ell_1}^{E,E} \right)^{-1} W_{\ell_1\ell_2}^L \left(D_{\ell_2\ell_2}^{E,E} \right)^{-1}, \quad (4.148)$$

$$F^{LL'} = \frac{1}{2} Tr \left[\left(D^{E,E} \right)^{-1} W^L \left(D^{E,E} \right)^{-1} W^{L'} \right], \quad (4.149)$$

$$W_{\ell_1\ell_2}^{L'} = \left[\tilde{H}_{\ell_2\ell_2}^{L'} C_{\ell_2\ell_1}^{EE,EE} + H_{\ell_2\ell_2,ev}^{L'} C_{\ell_2\ell_1}^{BB,EE} + \tilde{H}_{\ell_1\ell_1}^{L'} C_{\ell_1\ell_2}^{EE,EE} + H_{\ell_1\ell_1,ev}^{L'} C_{\ell_1\ell_2}^{BB,EE} \right]. \quad (4.150)$$

¹¹We report here for completeness also the expression for the object $W_{\ell_1\ell_2}^L$ (Eq. 4.126) even if it does not depend on the κ parameter

BB-based estimator

Replacing Eq. (4.83) in Eq. (4.122) and following similar steps as done for the EE -based, we can build an estimator which is quadratic in the $C_\ell^{BB,obs}$ power spectrum:

$$\hat{E}_{(BB^2)}^L = \left(F^{LL'}\right)^{-1} \left[C_{\ell_1}^{BB,obs} E_{\ell_1 \ell_2}^L C_{\ell_2}^{BB,obs} - Tr \left[E^L C^{BB,BB} \right] \right], \quad (4.151)$$

such that its expectation reads:

$$\langle \hat{E}_{(BB^2)}^L \rangle = C_L^\alpha, \quad (4.152)$$

and the covariance of the estimates is:

$$V_{(BB^2)}^{LL'} = \left(F^{LL'}\right)^{-1}. \quad (4.153)$$

The objects that enter in this estimator, Eq. (4.151), under the choice of $\kappa = 1$, are:

$$E^L = \frac{1}{2} \left(D_{\ell_1 \ell_1}^{B,B}\right)^{-1} W_{\ell_1' \ell_2'}^L \left(D_{\ell_2' \ell_2}^{B,B}\right)^{-1}, \quad (4.154)$$

$$F^{LL'} = \frac{1}{2} Tr \left[\left(D^{B,B}\right)^{-1} W^L \left(D^{B,B}\right)^{-1} W^{L'} \right], \quad (4.155)$$

$$W_{\ell_1 \ell_2}^{L'} = \left[\tilde{H}_{\ell_2' \ell_2}^{L'} C_{\ell_2' \ell_1}^{BB,BB} + H_{\ell_2 \ell_2', ev}^{L'} C_{\ell_2' \ell_1}^{EE,BB} + \tilde{H}_{\ell_1 \ell_1'}^{L'} C_{\ell_1' \ell_2}^{BB,BB} + H_{\ell_1 \ell_1', ev}^{L'} C_{\ell_1' \ell_2}^{EE,BB} \right]. \quad (4.156)$$

EB-based estimator

Following similar steps as done in the previous section, we can build an estimator which is quadratic in $C_\ell^{EB,obs}$, Eq.(4.84):

$$\hat{E}_{(EB^2)}^L = \left(F^{LL'}\right)^{-1} \left[C_{\ell_1}^{EB,obs} E_{\ell_1 \ell_2}^L C_{\ell_2}^{EB,obs} - Tr \left[E^L C^{EB,EB} \right] \right], \quad (4.157)$$

such that expectation value reads:

$$\langle \hat{E}_{(EB^2)}^L \rangle = C_L^\alpha, \quad (4.158)$$

and the covariance of the estimates is:

$$V_{(EB^2)}^{LL'} = \left(\frac{1}{2} Tr \left[\left(D^{EB}\right)^{-1} W^L \left(D^{EB}\right)^{-1} W^{L'} \right] \right)^{-1}, \quad (4.159)$$

where:

$$D_{\ell_1 \ell_2}^{EB} = \langle C_{\ell_1}^{EB,obs} C_{\ell_2}^{EB,obs} \rangle, \quad (4.160)$$

$$C_{\ell_1 \ell_2}^{EB,EB} = \langle C_{\ell_1}^{EB} C_{\ell_2}^{EB} \rangle. \quad (4.161)$$

Note that in this case, since the primordial EB spectrum is null, Eq. (4.161) coincides with the covariance matrix of the $C_\ell^{(EB)}$ spectrum.

Moreover, under the choice of $\kappa = 1$:

$$E^L = \frac{1}{2} \left(D_{\ell_1 \ell'_1}^{EB} \right)^{-1} W_{\ell'_1 \ell'_2}^L \left(D_{\ell'_2 \ell_2}^{EB} \right)^{-1}, \quad (4.162)$$

$$F^{LL'} = \frac{1}{2} \text{Tr} \left[\left(D^{EB} \right)^{-1} W^L \left(D^{EB} \right)^{-1} W^{L'} \right], \quad (4.163)$$

$$W_{\ell_1 \ell_2}^{L'} = \left[\tilde{K}_{\ell_1 \ell'_1}^{L'} C_{\ell'_1 \ell'_2}^{EB, EB} + \tilde{K}_{\ell_2 \ell'_2}^{L'} C_{\ell'_2 \ell_1}^{EB, EB} \right]. \quad (4.164)$$

It is important to note that, also for this estimator the following relation holds:

$$\left(F^{LL'} \right)^{-1} = V_{(EB^2)}^{LL'}. \quad (4.165)$$

Analogously to the linear estimators, it is possible to show that the expectation values of the quadratic estimators, Eqs (4.145), (4.152) and (4.158), do not depend on the choice of matrix $D_{\ell_1 \ell_2}^{X, Y}$ ¹² used to compute the respective E^L and $F^{LL'}$ objects. Obviously, the latter have the statistical meaning described above only if $D_{\ell_1 \ell_2}^{X, Y}$ is a description of the statistical behaviour of the spectra on which the estimators are applied.

4.3 Planck 2018 dataset (PR3)

In this Thesis we make use of the CMB-cleaned maps provided by the four component separation algorithms employed in PLANCK, namely **commander**, **nilc**, **smica** and **sevem** [32]. These maps, available from the Planck Legacy Archive¹³ (PLA), are provided at HEALPix¹⁴ [91] resolution $N_{side} = 2048$, with a Gaussian beam with FWHM = 5'.

In addition, we employ Monte Carlo (MC) simulations, also publicly available from the PLA, which are an updated version of the full focal plane simulations described in [123], referred as FFP10, see e.g. [75]. The FFP10 set contains the most realistic simulations the PLANCK collaboration provides to characterise its 2018 data. They consist of 1000 CMB maps extracted from the current Λ CDM best-fit model (see section 4.5.2), which are beam smeared and contain residuals of beam leakage [123]. These maps are complemented by 300 instrumental noise simulations for the full mission and

¹²where (X, Y) stand for (E, E) , (B, B) and (EB) in the EE-based, BB-based and EB-based estimator, respectively.

¹³This thesis is based on observations obtained with Planck (<http://www.esa.int/Planck>), an ESA science mission with instruments and contributions directly funded by ESA Member States, NASA, and Canada.

¹⁴<http://healpix.sourceforge.net>

for each of the two half-mission (HM) data splits. These noise simulations, which are provided for each frequency channel, also include residual systematic effects as beam leakage again, ADC non linearities, thermal fluctuations (dubbed 4K fluctuations), band-pass mismatch and others [124]. The latter are processed through the component separation algorithms assuming the same weights adopted for the data.

4.4 Data analysis: localisation approach with PR3

In this section we show the CB spectrum obtained by applying the methodologies described in section 4.2.2 to the Planck 2018 data for all the four component separation algorithms employed in PLANCK. For this analysis we use the half-mission (HM) version for both data and FFP10 simulations describe in section 4.3. We have combined the first 300 CMB realisations with the two different HM splits of 300 noise maps so to effectively have two MC set of 300 signal and noise simulations which do contain also residuals of known systematic effects. For each of these two MC dataset we divided the CMB maps in the 768 patches following the Healpy¹⁵ [91] pixelization scheme at $N_{side} = 8$. Anyway, we decided to analyse only those patches which have at least 50% pixels left un-maxed by the the PR3 polarisation mask shown in Figure 4.2. Figure 4.3 shows the 571 active patches on which we perform our analysis.

As first step, in each of these regions we evaluate the EE, BB and EB CMB power spectra in the harmonic range $\ell \in [2 - 1500]$ with a binning of $\Delta\ell = 60$ in the multipoles. To do that we use NaMaster¹⁶, cross-correlating the two split maps for the data maps and for each pair of simulation maps. Such approach is preferable for the auto-spectra since it reduces residuals of systematic effects and noise mismatches. Figure 4.4 shows the EE, BB and EB power spectra evaluated in three patches for commander pipeline. The three patches, with indices 1 (blue), 207 (orange) and 542 (green) in the Healpix RING ordering scheme, have 100%, 74.5% and 51.1% of active pixels, respectively. The dots represent the average of the MC simulations with the error bars the σ of the mean of the MC distribution. In the upper panels the mean values from the MC are compared with the fiducial power spectrum (black solid line)¹⁷. The middle plots shows the fluctuation of the

¹⁵<http://healpix.sourceforge.net>

¹⁶<https://github.com/LSSTDESC/NaMaster>

¹⁷Note that we extract the CMB power spectra not de-convolving for the beam, and

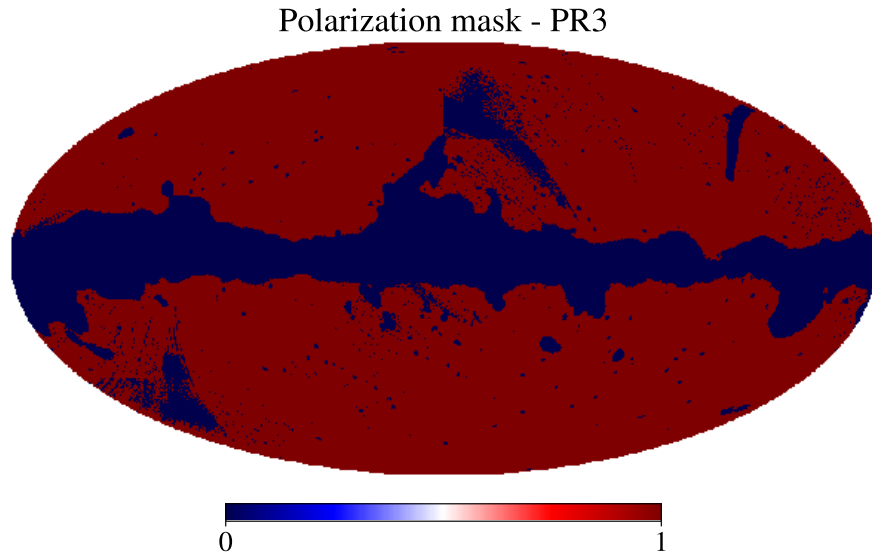


Figure 4.2: PR3 polarisation masks used to select the patches.

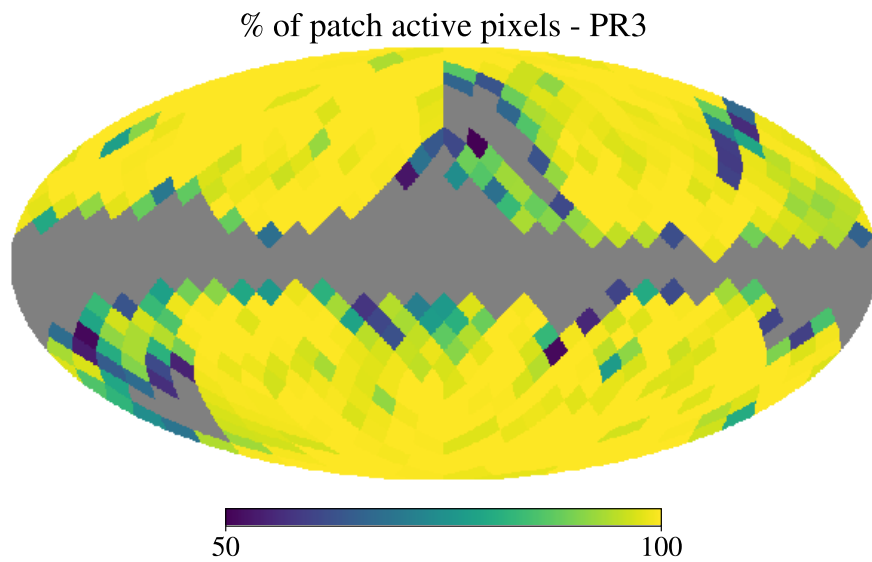


Figure 4.3: Percentage of active pixels in each patch. The grey patches are not used in the analysis.

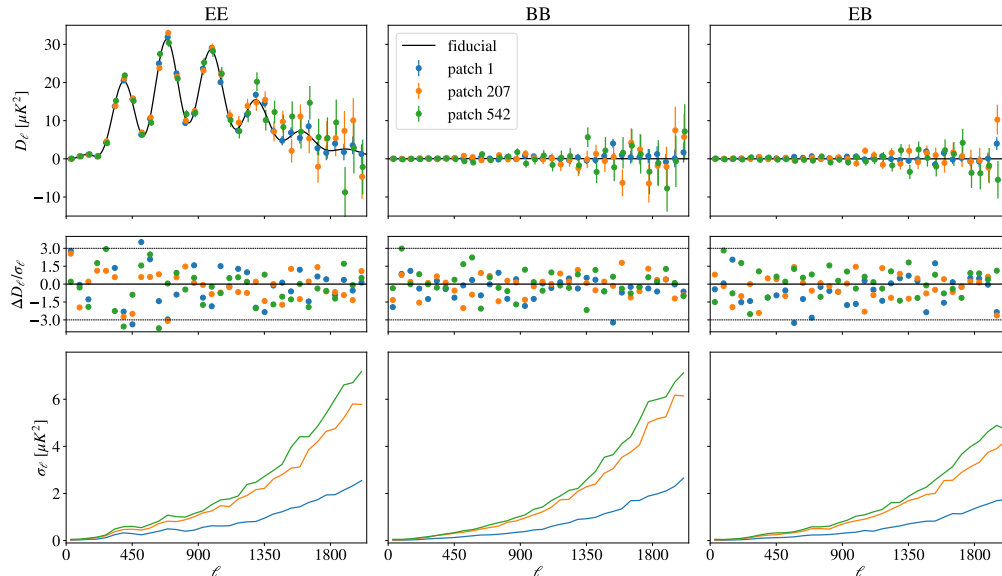


Figure 4.4: Upper panels: EE, BB and EB power spectra evaluated in three patches for `commander` pipeline. The three patches, with indices 1 (blue), 207 (orange) and 542 (green) in the Healpix RING ordering scheme, have 100%, 74.5% and 51.1% of active pixels, respectively. The dots points stands for the average of the MC with the error bars the standard deviation of the mean. The average of the MC are compared with the fiducial power spectrum (black solid line). Middle plots: the fluctuation of the mean with respect to the expected value. Lower panels: standard deviation of the MC.

mean with respect to the expected value: we can see how the impact of the residuals of systematics on the FFP10 MC does not impact significantly for the setup adopted. The lower panels show the standard deviation of the MC.

With the CMB spectra in hands we can apply in each patch the D-estimators based on the EB CMB spectra, Eq. (4.60). By minimising the χ^2_{EB} in Eq. 4.75 we estimate the CB isotropic angle α_0 in each patch, for the MC simulations and data. Note that, given the low number of simulations, to compute the covariance matrix $C_{\ell\ell'}^{EB}$ used in the χ^2_{EB} -minimisation, we employed a `NaMaster`¹⁸[125] routine to estimate the gaussian covariance matrix for the EB CMB power spectra. Figure 4.5 shows in the left column the CB angle maps obtained from the PR3 data and the right column the maps of standard deviation obtained from the FFP10 MC for the four PLANCK component separation methods. From this figure it is evident how the structures

therefore here we convolve the fiducial power spectrum for the beam.

¹⁸<https://github.com/LSSTDESC/NaMaster>

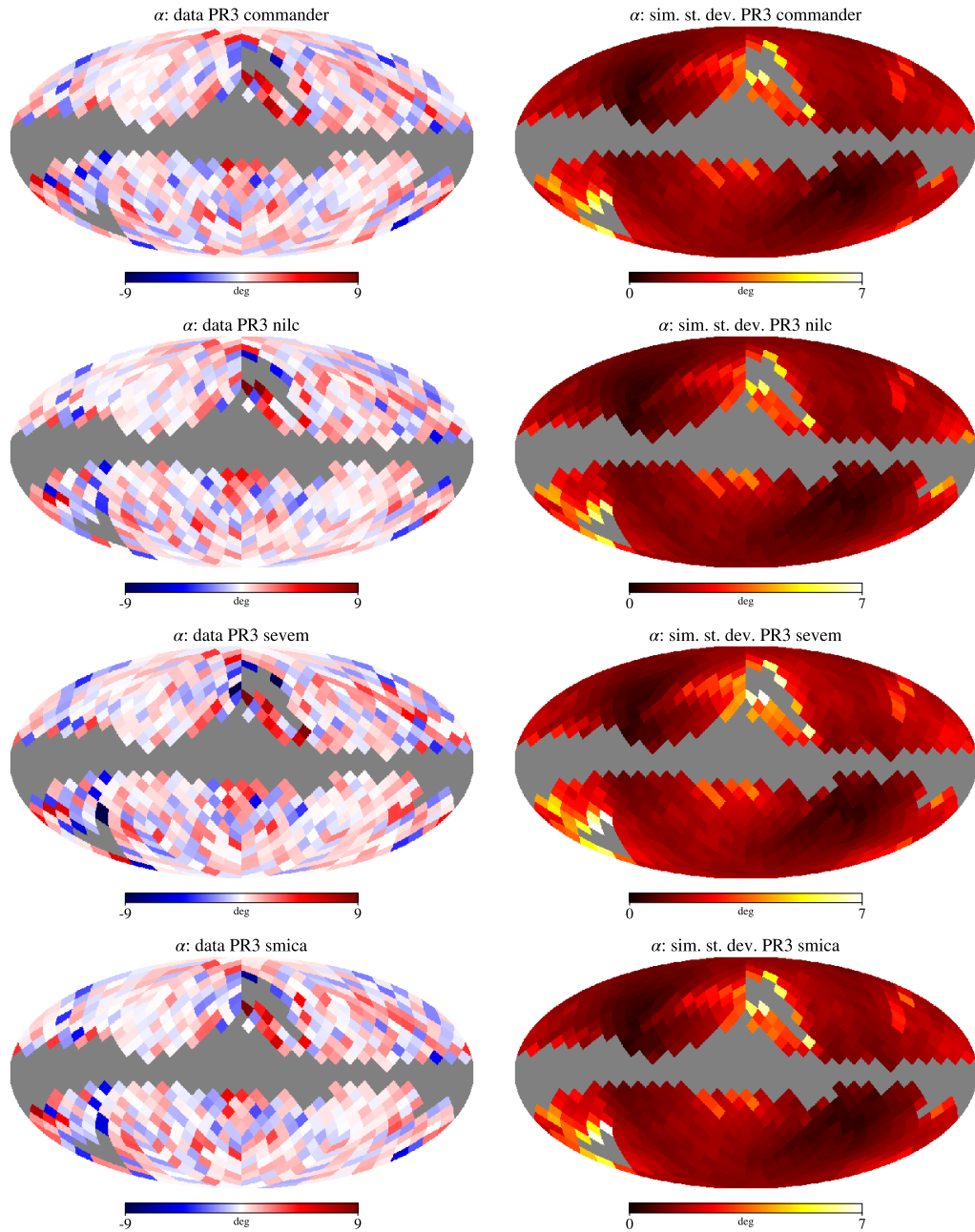


Figure 4.5: Left column: CB isotropic angle maps obtained from the PR3 2018 data for the **commander**, **nilc**, **sevem** and **smica** component separation algorithm (from the upper to the lower panel). Right column: maps of the standard deviation obtained from the FFP10 MC.

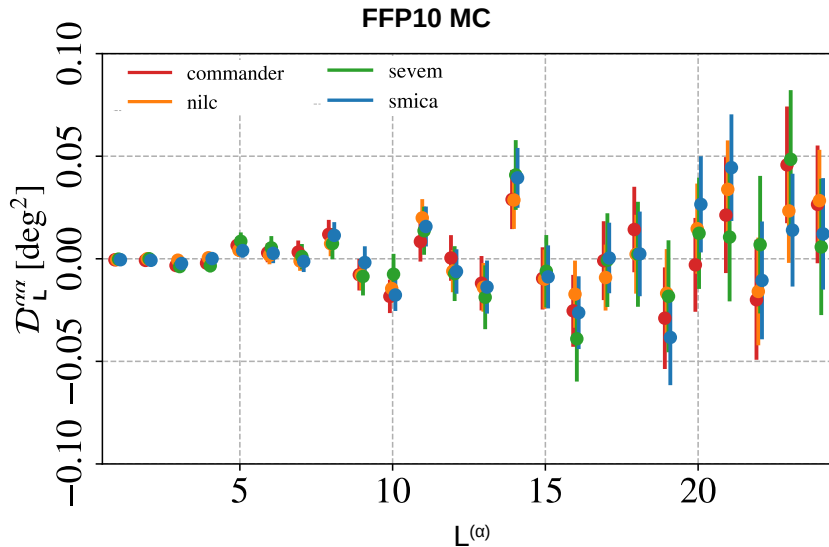


Figure 4.6: CB spectrum expressed in term of band power, i.e. $D_L^\alpha = C_L^\alpha \frac{L(L+1)}{2\pi}$ in the harmonic range $L \in [1 - 24]$ obtained from the FFP10 MC for the four PLANCK pipeline. Error bars represents the standard deviation of the mean.

present in the maps are similar for all the 4 component separation methods, meaning that the impact of the foregrounds is negligible.

Finally, from the CB angle maps we extract the auto-correlation spectra C_L^α using a Quadratic Maximum Likelihood (QML) estimator, described in [122]. In [35] are also provide the cross-spectra between the CB and CMB temperature and polarisation power spectra, considering also the PR4 dataset. With the aim of reduce the foreground contamination, we use only $f_{\text{sky}} \approx 74\%$ of the sky, masking the the CB angles maps with a combination of the mask in Figure 4.2, used at the beginning to exclude the patches with less than 50% of active pixels, and the Planck temperature mask reduced from $N_{\text{side}} = 2048$ to $N_{\text{side}} = 8$. Since the in the FFP10 MC the expected signal is null, we consider a diagonal matrix obtained by the variance of the simulations in the right column of Figure 4.5 to describe the covariance of the CB angle maps in the QML-methods. Note that we have also marginalised on the monopole to avoid spurious effect due to leaks induces by the mask.

The mean values of CB power spectrum in the harmonic range $L \in [1 - 24]$ obtained from the FFP10 MC for the four PLANCK pipeline are shown in Figure 4.6. Here the CB spectrum is expressed in term of band power, i.e. $D_L^\alpha = C_L^\alpha \frac{L(L+1)}{2\pi}$ ¹⁹. From this figures it is possible to note the FFP10 MC are

¹⁹We decide to show the band power also to have a direct comparison for the first 12

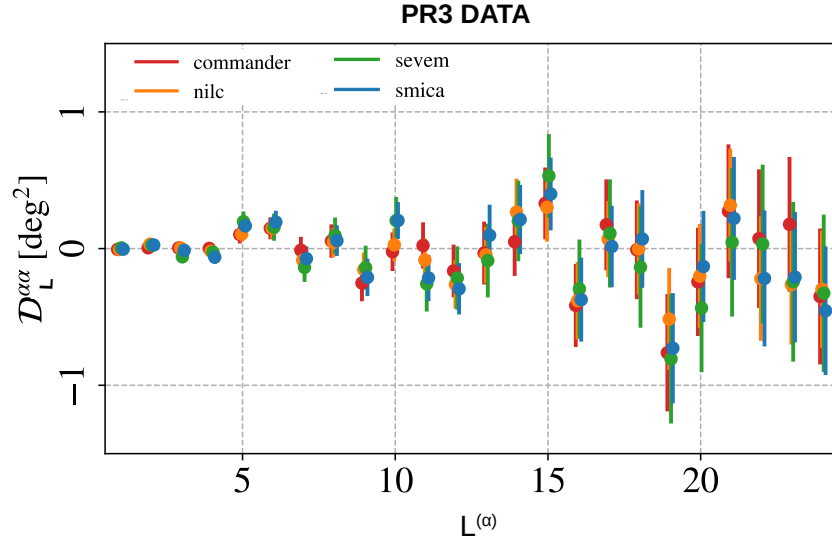


Figure 4.7: CB data spectrum expressed in term of band power, i.e. $D_L^\alpha = C_L^\alpha \frac{L(L+1)}{2\pi}$ in the harmonic range $L \in [1 - 24]$ for the four PLANCK pipeline. Error bars represents the standard deviation the MC distribution.

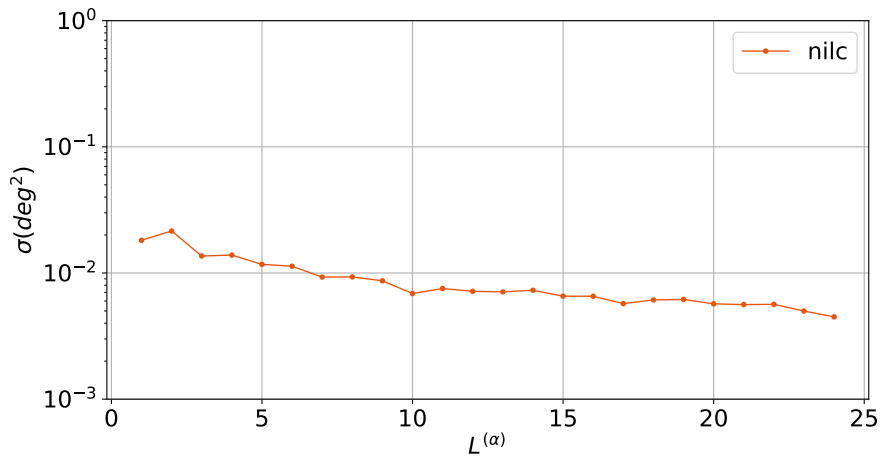


Figure 4.8: Solid line represents the standard deviation of CB spectrum as function of the CB multipoles obtained from the FFP10 MC for the nilc pipeline.

compatible within 3σ C.L. with the null effect, meaning that the impact of the residual contained in the MC is negligible.

Figure 4.7 represents the main result of this section: the CB spectrum obtained from PR3 data, expressed in term of band power in the harmonic range $L \in [1 - 24]$ for the four PLANCK pipeline. From this figure we can note that:

- the four PLANCK component separation algorithm provide well-compatible results;
- we extend the previous work [34] evaluating the CB spectrum until the multipole 12;
- we find a compatibility with the null effect better than $0.01deg^2$ on the whole harmonic range considered. In particular, from Figure 4.8, which displays the standard deviation of CB spectrum as function of the CB multipoles obtained from the FFP10 MC for the `nilc` pipeline, we can see that the level of uncertainties goes from 0.01 to $0.004deg^2$.

4.5 Data analysis: C_ℓ^α estimators

4.5.1 Implemented formalism

The final expressions of the linear and quadratic estimators, given in Eqs. (4.110), (4.117), (4.144), (4.151) and (4.157), were obtained starting from primordial and observed CMB power spectra at single- ℓ and without applying any binning on the birefringence spectrum. However, an implementation of such expressions would be computationally too heavy and could produce numerically unstable results. Moreover, to reduce the errors and the correlations between the power spectrum at different multipoles induced by the cut-sky, the CMB observed spectra are typically provided with a binning on the multipoles. In order to make easier the application of such estimators on real data sets and to have a solid implementation some changes need to be made. In particular, we have chosen:

- to use the band power instead of the CMB power spectra;
- to bin both CMB and CB multipoles.

We opportunely modified the expressions of the observed CMB power spectra Eqs.(4.82), (4.83) and (4.84) and then used the modified versions of the latter to re-compute the expressions of the estimators.

multipoles with the results shown in [34]

The introduction of the band power in Eqs.(4.82), (4.83) and (4.84) can be taken into account with the following transformations:

$$C_\ell^{(prim/obs)} \rightarrow C_\ell^{(prim/obs)} \left(\frac{\ell(\ell+1)}{2\pi} \right), \quad (4.166)$$

$$\tilde{H}_{\ell\ell'}^L \rightarrow \tilde{H}_{\ell\ell'}^L \left(\frac{\ell(\ell+1)}{\ell'(\ell'+1)} \right), \quad (4.167)$$

$$H_{\ell\ell',ev}^L \rightarrow H_{\ell\ell',ev}^L \left(\frac{\ell(\ell+1)}{\ell'(\ell'+1)} \right), \quad (4.168)$$

$$\tilde{K}_{\ell\ell'}^L \rightarrow \tilde{K}_{\ell\ell'}^L \left(\frac{\ell(\ell+1)}{\ell'(\ell'+1)} \right). \quad (4.169)$$

No sum over ℓ and ℓ' is understood in Eqs. (4.167),(4.168) and (4.169).

We use two operators, P and Q [126], to bin the CMB band power and the CB power spectra in Eqs.(4.82), (4.83), (4.84). For a set of n_{bins} bins, indexed by b , with respective boundaries $\ell_{low}^{(b)} < \ell_{high}^{(b)} < \ell_{low}^{(b+1)}$, one can define the binning operator P as follows:

$$P_{b\ell} = \begin{cases} \frac{1}{\ell_{low}^{(b+1)} - \ell_{low}^{(b)}}, & (if \ell_{min} \leq \ell_{low}^{(b)} \leq \ell < \ell_{low}^{(b+1)}) \\ 0, & (otherwise) \end{cases} \quad (4.170)$$

and the reciprocal operator Q reads:

$$Q_{\ell b} = \begin{cases} 1, & (if \ell_{min} \leq \ell_{low}^{(b)} \leq \ell < \ell_{low}^{(b+1)}) \\ 0, & (otherwise) \end{cases} \quad (4.171)$$

where ℓ_{min} stands for the minimum multipole considered, for the CMB it is typically $\ell_{min} = 2$ while for the CB it is $L_{min} = 1$. Given the different structure of the linear and the quadratic estimators, it is convenient to apply a different binning scheme on the CMB multipoles. In the follow we use the label b to indicate the bins on the CMB multipoles and B the ones on the CB multipoles.

4.5.1.1 Linear estimators binned

For the linear estimator we apply the operator $P_{b\ell}$ on the CMB multipoles and the the operator QP , namely the row-by-column product between the Q and the P operators, on the CB spectrum:

$$C_b^{EE,obs} = C_b^{EE} + P_{b\ell} \left[\tilde{H}_{\ell\ell'}^L C_{\ell'}^{EE} + H_{\ell\ell',ev}^L C_{\ell'}^{BB} \right] Q^{LB} P^{BL'} C_L^\alpha \quad (4.172)$$

$$C_b^{BB,obs} = C_b^{BB} + P_{b\ell} \left[\tilde{H}_{\ell\ell'}^L C_{\ell'}^{BB} + H_{\ell\ell',ev}^L C_{\ell'}^{EE} \right] Q^{LB} P^{BL'} C_L^\alpha \quad (4.173)$$

where the sum over the indices are understood and the band powers $C_b^{(prim/obs)}$ are obtained as $C_b^{(prim/obs)} = P_{b\ell} C_\ell^{(prim/obs)}$. Replacing Eq. (4.172) and (4.173) in Eq. (4.86) and following similar steps as done in the previous section, we can build the binning version of the two estimators Eq. (4.110) and Eq. (4.117). Thus:

$$\hat{E}_{(EE)}^B = (F^{BB'})^{-1} \left[E_b^{B'} C_b^{EE,obs} - E_b^{B'} \langle C_b^{EE} \rangle \right], \quad (4.174)$$

$$\hat{E}_{(BB)}^B = (F^{BB'})^{-1} \left[E_b^{B'} C_b^{BB,obs} - E_b^{B'} \langle C_b^{BB} \rangle \right], \quad (4.175)$$

and their expectation values read:

$$\langle \hat{E}_{(EE)}^B \rangle = C_B^\alpha, \quad (4.176)$$

$$\langle \hat{E}_{(BB)}^B \rangle = C_B^\alpha, \quad (4.177)$$

where $C_B^\alpha = P^{BL'} C_{L'}^\alpha$ is the binned CB spectrum.

We can interpret $C_b^{EE,obs}$ and $C_b^{BB,obs}$ in Eqs. (4.174) and Eqs. (4.175) as the CMB band power recovered by a CMB experiment under realistic circumstances, i.e. including noise residuals, incomplete sky fraction, finite angular resolution and also residuals of systematic effects. Once the model is chosen, i.e. once the spectra C_b^{EE} and C_b^{BB} are fixed, for example to Λ CDM model, one can employ the estimators Eqs. (4.174) and Eqs. (4.175) to compute the C_B^α for the observations and/or for the corresponding realistic simulations.

For these two estimators the covariance of the estimates are:

$$V^{BB'} = (F^{BB'})^{-1}. \quad (4.178)$$

The expressions of their statistical objects, under the choice of $\kappa = 2$, will be:

$$E_b^B = W_{b'}^B (C_{b'b}^{XX,obs})^{-1}, \quad (4.179)$$

$$F^{BB'} = W_{b'}^B (C_{b'b}^{XX,obs})^{-1} W_b^{B'}, \quad (4.180)$$

where for the EE-based estimator:

$$C_{b'b}^{XX,obs} = P_{b'\ell'} C_{\ell'\ell}^{EE,obs} (P_{\ell b})_T, \quad (4.181)$$

$$\begin{aligned} W_b^{B'} &= P_{b\ell} \left[\tilde{H}_{\ell\ell'}^{L'} \langle C_{\ell'}^{EE} \rangle + H_{\ell\ell',ev}^{L'} \langle C_{\ell'}^{BB} \rangle \right] Q^{L'B'} = \\ &= P_{b\ell} \left[W_\ell^{L'} \right] Q^{L'B'}, \end{aligned} \quad (4.182)$$

with the symbol $()_T$ representing the transpose of the matrix. While for the BB-based estimator we have:

$$C_{b'b}^{XX,obs} = P_{b'\ell'} C_{\ell'\ell}^{BB,obs} (P_{\ell b})_T, \quad (4.183)$$

$$\begin{aligned} W_b^{B'} &= P_{b\ell} \left[\tilde{H}_{\ell\ell'}^{L'} \langle C_{\ell'\ell}^{BB} \rangle + H_{\ell\ell',ev}^{L'} \langle C_{\ell'\ell}^{EE} \rangle \right] Q^{L'B'} \\ &= P_{b\ell} \left[W_{\ell}^{L'} \right] Q^{L'B'}. \end{aligned} \quad (4.184)$$

4.5.1.2 Quadratic estimators binned

In the quadratic estimators it is more suitable to introduce the binning, using the QP operator, also for the CMB dummy indexes of $\tilde{H}_{\ell\ell'}^L$, $H_{\ell\ell',ev}^L$ and $\tilde{K}_{\ell\ell'}^L$ in Eqs.(4.82), (4.83), (4.84). In this way we can use the binned covariance matrix to compute the $W_{bb'}^B$ object:

$$\begin{aligned} C_b^{EE,obs} &= C_b^{EE} + P_{b\ell} \left[\tilde{H}_{\ell\ell'}^L Q_{\ell'b'} P_{b'\ell''} C_{\ell''}^{EE} + \right. \\ &\quad \left. + H_{\ell\ell',ev}^L Q_{\ell'b'} P_{b'\ell''} C_{\ell''}^{BB} \right] Q^{LB} P^{BL'} C_{L'}^{\alpha}, \end{aligned} \quad (4.185)$$

$$\begin{aligned} C_b^{BB,obs} &= C_b^{BB} + P_{b\ell} \left[\tilde{H}_{\ell\ell'}^L Q_{\ell'b'} P_{b'\ell''} C_{\ell''}^{BB} + \right. \\ &\quad \left. + H_{\ell\ell',ev}^L Q_{\ell'b'} P_{b'\ell''} C_{\ell''}^{EE} \right] Q^{LB} P^{BL'} C_{L'}^{\alpha}, \end{aligned} \quad (4.186)$$

$$C_b^{EB,obs} = C_b^{EB} + P_{b\ell} \left[\tilde{K}_{\ell\ell'}^L Q_{\ell'b'} P_{b'\ell''} C_{\ell''}^{EB} \right] Q^{LB} P^{BL'} C_{L'}^{\alpha}. \quad (4.187)$$

Now replacing Eq. (4.185),(4.186) and (4.187) in Eq. (4.122) and following similar steps as done in the previous section, we build the binning version of the three quadratic estimators Eq. (4.144), (4.151) and (4.157):

$$\hat{E}_{(EE^2)}^B = \left(F^{BB'} \right)^{-1} \left[C_{b_1}^{EE,obs} E_{b_1 b_2}^B C_{b_2}^{EE,obs} - Tr \left[E^B C^{EE,EE} \right] \right], \quad (4.188)$$

$$\hat{E}_{(BB^2)}^B = \left(F^{BB'} \right)^{-1} \left[C_{b_1}^{BB,obs} E_{b_1 b_2}^B C_{b_2}^{BB,obs} - Tr \left[E^B C^{BB,BB} \right] \right], \quad (4.189)$$

$$\hat{E}_{(EB^2)}^B = \left(F^{BB'} \right)^{-1} \left[C_{b_1}^{EB,obs} E_{b_1 b_2}^B C_{b_2}^{EB,obs} - Tr \left[E^B C^{EB,EB} \right] \right], \quad (4.190)$$

such that their expectation values read:

$$\langle \hat{E}_{(EE^2)}^B \rangle = C_B^{\alpha}, \quad (4.191)$$

$$\langle \hat{E}_{(BB^2)}^B \rangle = C_B^{\alpha}, \quad (4.192)$$

$$\langle \hat{E}_{(EB^2)}^B \rangle = C_B^{\alpha}, \quad (4.193)$$

and the covariance of the estimates is:

$$V^{BB'} = \left(F^{BB'} \right)^{-1}. \quad (4.194)$$

As in the linear case, we can interpret $C_b^{EE,obs}$, $C_b^{BB,obs}$ and $C_b^{EB,obs}$ in Eqs. (4.188), (4.189) and (4.190) as the CMB band power recovered by a CMB experiment under realistic circumstances. Once the model is chosen, one can compute the matrices $C^{EE,EE}$, $C^{BB,BB}$ and $C^{EB,EB}$ and employ the quadratic estimators, Eqs. (4.188), (4.189) and (4.190), to evaluate the C_b^α for the observations and/or for the corresponding realistic simulations.

The objects that enter in these estimators, under the choice of $\kappa = 1$, are:

$$E_{b_1 b_2}^B = \frac{1}{2} \left(D_{b_1 b_1}^{X,X} \right)^{-1} W_{b_1' b_2'}^B \left(D_{b_2' b_2'}^{X,X} \right)^{-1}, \quad (4.195)$$

$$F^{BB'} = \frac{1}{2} \text{Tr} \left[\left(D^{X,X} \right)^{-1} W^B \left(D^{X,X} \right)^{-1} W^{B'} \right]. \quad (4.196)$$

Note that in Eq. (4.196) $D^{X,X}$ and W^B are binned in the CMB indexes. For the EE-based estimator $D^{X,X} = \langle C_{b_1}^{EE,obs} C_{b_2}^{EE,obs} \rangle$ and:

$$\begin{aligned} W_{b_1 b_2}^{B'} &= \left[P_{b_2 \ell_2} \tilde{H}_{\ell_2 \ell_2'}^{L'} Q_{\ell_2' b_2'} P_{b_2' \ell_2'} C_{\ell_2'' \ell_1}^{EE,EE} (P_{\ell_1 b_1})_T + \right. \\ &\quad + P_{b_2 \ell_2} H_{\ell_2 \ell_2', ev}^{L'} Q_{\ell_2' b_2'} P_{b_2' \ell_2'} C_{\ell_2'' \ell_1}^{BB,EE} (P_{\ell_1 b_1})_T + \\ &\quad + P_{b_1 \ell_1} \tilde{H}_{\ell_1 \ell_1'}^{L'} Q_{\ell_1' b_1'} P_{b_1' \ell_1'} C_{\ell_1'' \ell_2}^{EE,EE} (P_{\ell_2 b_2})_T + \\ &\quad \left. + P_{b_1 \ell_1} H_{\ell_1 \ell_1', ev}^{L'} Q_{\ell_1' b_1'} P_{b_1' \ell_1'} C_{\ell_1'' \ell_2}^{BB,EE} (P_{\ell_2 b_2})_T \right] Q^{L'B'} = \\ &= \left[\tilde{H}_{b_2 b_2'}^{B'} C_{b_2' b_1}^{EE,EE} + H_{b_2 b_2', ev}^{B'} C_{b_2' b_1}^{BB,EE} + \right. \\ &\quad \left. + \tilde{H}_{b_1 b_1'}^{B'} C_{b_1' b_2}^{EE,EE} + H_{b_1 b_1', ev}^{B'} C_{b_1' b_2}^{BB,EE} \right]. \quad (4.197) \end{aligned}$$

For the BB-based estimator $D^{X,X} = \langle C_{b_1}^{BB,obs} C_{b_2}^{BB,obs} \rangle$ and:

$$\begin{aligned} W_{b_1 b_2}^{B'} &= \left[P_{b_2 \ell_2} \tilde{H}_{\ell_2 \ell_2'}^{L'} Q_{\ell_2' b_2'} P_{b_2' \ell_2'} C_{\ell_2'' \ell_1}^{BB,BB} (P_{\ell_1 b_1})_T + \right. \\ &\quad + P_{b_2 \ell_2} H_{\ell_2 \ell_2', ev}^{L'} Q_{\ell_2' b_2'} P_{b_2' \ell_2'} C_{\ell_2'' \ell_1}^{EE,BB} (P_{\ell_1 b_1})_T + \\ &\quad + P_{b_1 \ell_1} \tilde{H}_{\ell_1 \ell_1'}^{L'} Q_{\ell_1' b_1'} P_{b_1' \ell_1'} C_{\ell_1'' \ell_2}^{BB,BB} (P_{\ell_2 b_2})_T + \\ &\quad \left. + P_{b_1 \ell_1} H_{\ell_1 \ell_1', ev}^{L'} Q_{\ell_1' b_1'} P_{b_1' \ell_1'} C_{\ell_1'' \ell_2}^{EE,BB} (P_{\ell_2 b_2})_T \right] Q^{L'B'} = \\ &= \left[\tilde{H}_{b_2 b_2'}^{B'} C_{b_2' b_1}^{BB,BB} + H_{b_2 b_2', ev}^{B'} C_{b_2' b_1}^{EE,BB} + \right. \\ &\quad \left. + \tilde{H}_{b_1 b_1'}^{B'} C_{b_1' b_2}^{BB,BB} + H_{b_1 b_1', ev}^{B'} C_{b_1' b_2}^{EE,BB} \right]. \quad (4.198) \end{aligned}$$

Analogously, for the EB-based estimator $D^{X,X} = \langle C_{b_1}^{EB,obs} C_{b_2}^{EB,obs} \rangle$ and:

$$\begin{aligned} W_{b_1 b_2}^{B'} &= \left[P_{b_1 \ell_1} \tilde{K}_{\ell_1 \ell_1'}^{L'} Q_{\ell_1' b_1'} P_{b_1' \ell_1'} C_{\ell_1'' \ell_2}^{EB,EB} (P_{\ell_2 b_2})_T + \right. \\ &\quad \left. + P_{b_2 \ell_2} \tilde{K}_{\ell_2 \ell_2'}^{L'} Q_{\ell_2' b_2'} P_{b_2' \ell_2'} C_{\ell_2'' \ell_1}^{EB,EB} (P_{\ell_1 b_1})_T \right] Q^{L'B'} = \\ &= \left[\tilde{K}_{b_1 b_1'}^{B'} C_{b_1' b_2}^{EB,EB} + \tilde{K}_{b_2 b_2'}^{B'} C_{b_2' b_1}^{EB,EB} \right]. \quad (4.199) \end{aligned}$$

Note that:

- in our implementation we evaluate the C_L^α spectrum considering different binning in the CMB multipoles checking that its impact in evaluating the CB spectrum is reasonable negligible, as expected from the formalism of estimators;
- we find a relation between the binning in the ℓ -multipoles and the one in the L-multipoles: the latter must be more aggressive than the first one, i.e. $\Delta L > \Delta \ell$, otherwise the objects W , E and F would lose their properties becoming numerically unstable objects.

4.5.2 Validation in a nearly-ideal case

We have implemented Eqs. (4.174), (4.175), (4.188), (4.189) and (4.190) in a `Python` code. They have been validated with 1000 Monte Carlo simulations, generated at $N_{side} = 2048$, where N_{side} is an `HEALPix`²⁰ parameter which is related to the total number of pixels, N_{pix} , through $N_{pix} = 12 N_{side}^2$. We produced two different sets of 1000 simulated maps, given by:

$$\begin{aligned} \text{set}_1 &= S + N_1, \\ \text{set}_2 &= S + N_2, \end{aligned} \tag{4.200}$$

where S stands for 1000 CMB signal maps and N_1, N_2 are two different sets of 1000 white noise maps with variance in temperature and polarisation maps respectively given by

$$\sigma_T = 1.00 \mu\text{Karcmin}, \tag{4.201}$$

$$\sigma_P = 1.41 \mu\text{Karcmin}. \tag{4.202}$$

The 1000 CMB signal maps were extracted from the Planck 2018 fiducial spectrum [75], defined by the following parameters

$$\Omega_b h^2 = 0.022166$$

$$\Omega_c h^2 = 0.12029$$

$$\Omega_\nu h^2 = 0.000645$$

$$\Omega_\Lambda = 0.68139$$

$$h = 0.67019$$

$$\tau = 0.06018$$

$$A_s = 2.1196 \cdot 10^{-9}$$

$$n_s = 0.96369$$

²⁰<https://healpix.sourceforge.io>

where $h = H_0/100 \text{ km s}^{-1} \text{ Mpc}^{-1}$. We estimated 1000 realisations of the six CMB angular power spectra without any binning in multipole space in the harmonic range $\ell \in [2, 4000]$ employing `NaMaster`²¹[125] in cross-mode on these two sets of maps. Such approach allows us to remove the noise bias for the auto-spectra. Hence, the obtained CMB spectra have been validated. Since these spectra do not contain any residual of systematics we also refer to them as “vanilla” simulations. Note that this set of simulations do not contain any birefringence affect.

In Figures 4.9 and 4.10 we show the validation of the linear and quadratic estimators from $L = 1$ to $L = 3000$, with a binning of $\Delta L = 100$, obtained considering the CMB band power estimated in the multipole range $\ell \in [2, 4000]$ with a binning of $\Delta \ell = 5$. In the five plots, given in Figures 4.9 and 4.10, one for each estimator, the upper panel displays the mean of the C_B^α with the error bar of the mean. The error bar of the mean, σ_μ , is computed as $\sigma_\mu = \sigma_{MC}/\sqrt{N_{sims}}$ where σ_{MC} is the standard deviation of the MC simulations. Note that the scale on the y-axis is not equal for all the plots. The lower panel shows the fluctuations from the expected signal (null in this case) of the mean in units of σ_μ . Since the lower panels of Figures 4.9 and 4.10 provide fluctuations well within 3σ C.L. we conclude that the code is validated.

Figure 4.11 shows the comparison in terms of the statistical uncertainties at level of $1\sigma_{MC}$ C.L. as a function of CB multipoles, for all the estimators. From this figure it is possible to note that:

- i. the linear and quadratic estimators which are based on the same spectra have nearly the same statistical uncertainties on the whole considered harmonic range;
- ii. for each estimator the level of uncertainties on the CB spectrum decreases when decreases when the birefringence multipoles L increase;
- iii. the BB-based linear, Eq. (4.175), and quadratic, Eq. (4.189), estimators are those which perform better: on the harmonic range $L \in [1 - 3000]$ the $1\sigma_{MC}$ C.L. goes from $\sim 4 \cdot 10^{-5} \text{ deg}^2$ to $\sim 4 \cdot 10^{-7} \text{ deg}^2$. While the quadratic EB-based estimator, Eq. (4.190), is the one with the largest uncertainties, reaching a difference of few order of magnitude from the others.

Finally, in Figure 4.12 we verify that the uncertainties given by inverse of the F matrix, i.e. $\sqrt{(F^{BB})^{-1}}$, are in agreement with what obtained from

²¹<https://github.com/LSSTDESC/NaMaster>

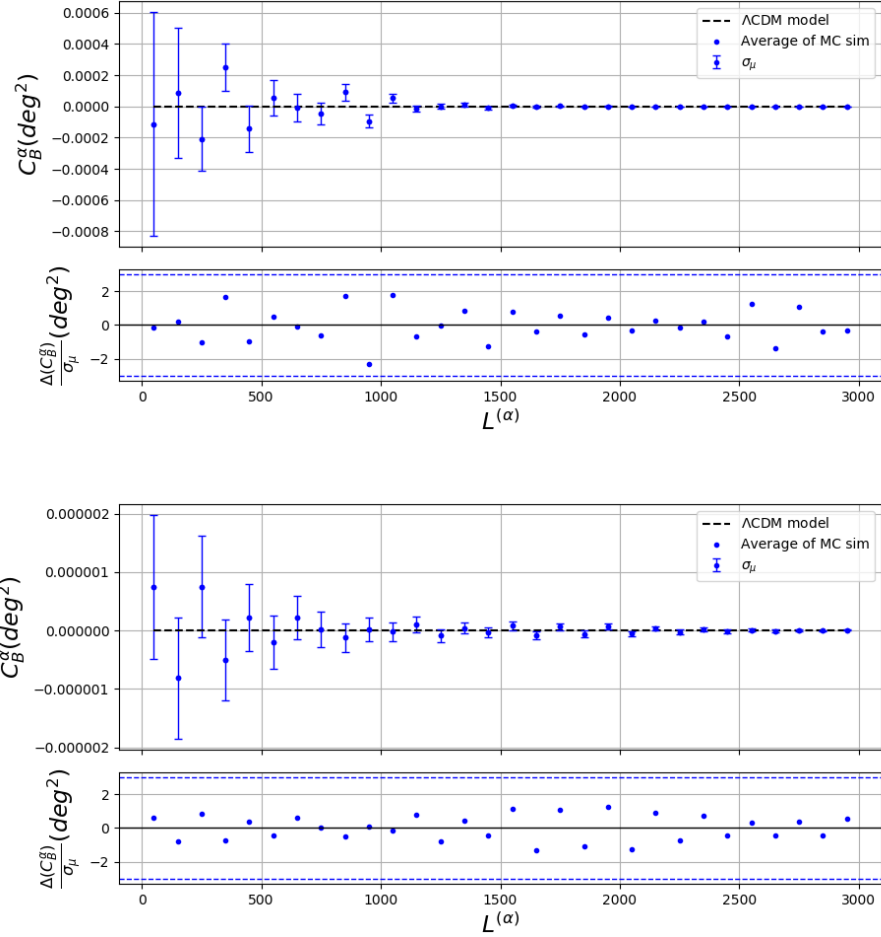


Figure 4.9: Averages of $\hat{E}_{(EE)}^B$ (upper panel) and $\hat{E}_{(BB)}^B$ (lower panel) as a function of CB multipoles, obtained from “vanilla” Monte Carlo simulations. Error bars represent the uncertainties associated to the averages. Each panel displays also a lower box where it is shown the distance of mean in units of standard deviation of the mean itself. Dashed horizontal lines represent what theoretically expected for the averages of $\hat{E}_{(EE)}^B$ and $\hat{E}_{(BB)}^B$ which are zero since in the “vanilla” Monte Carlo simulations the CB effect is absent by construction. Note that the y-scale of upper boxes are different for each panel.

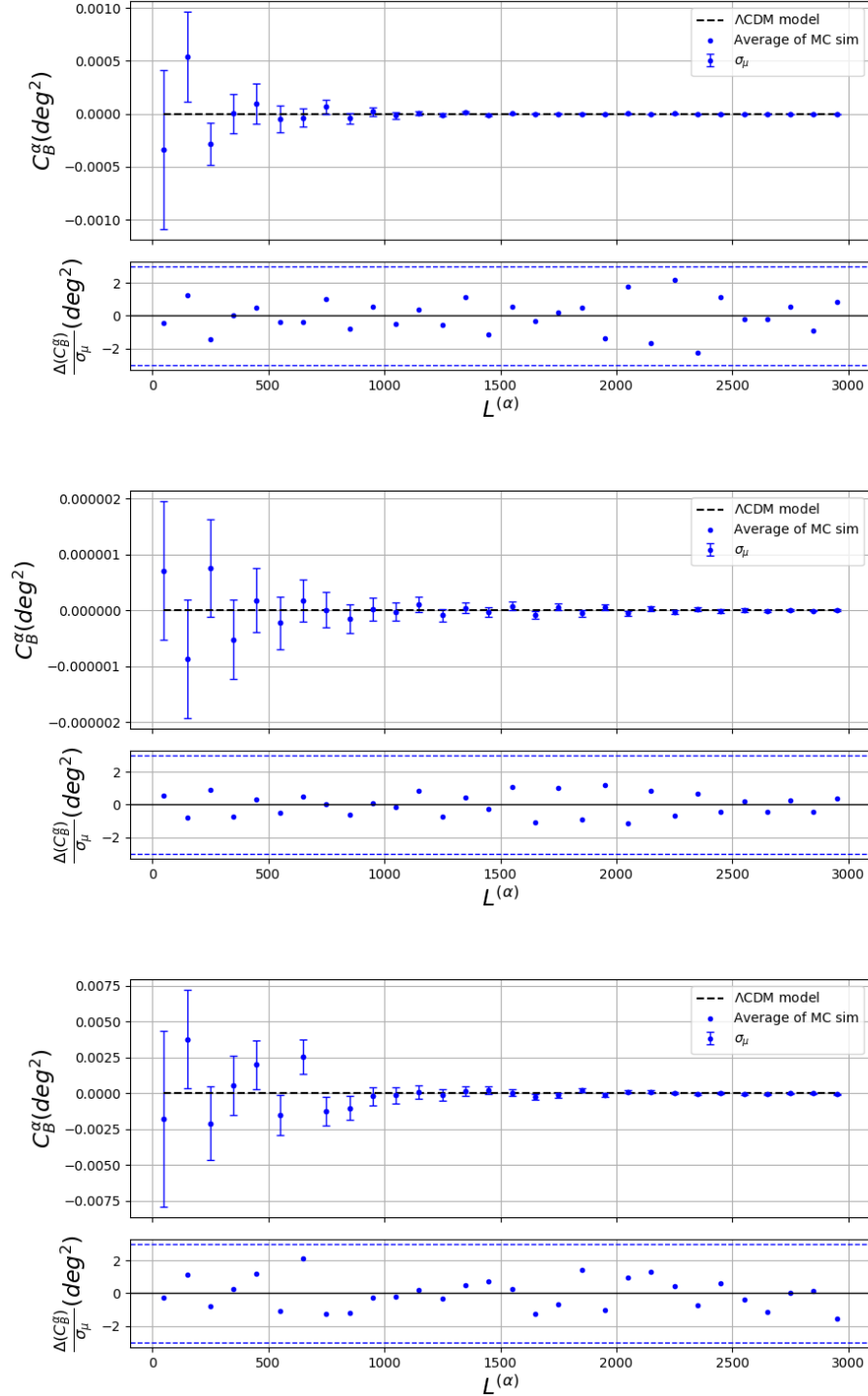


Figure 4.10: The same of Figure 4.9 but for the quadratic estimators $\hat{E}_{(EE^2)}^B$ (upper panel), $\hat{E}_{(BB^2)}^B$ (middle panel) and $\hat{E}_{(EB^2)}^B$ (lower panel)

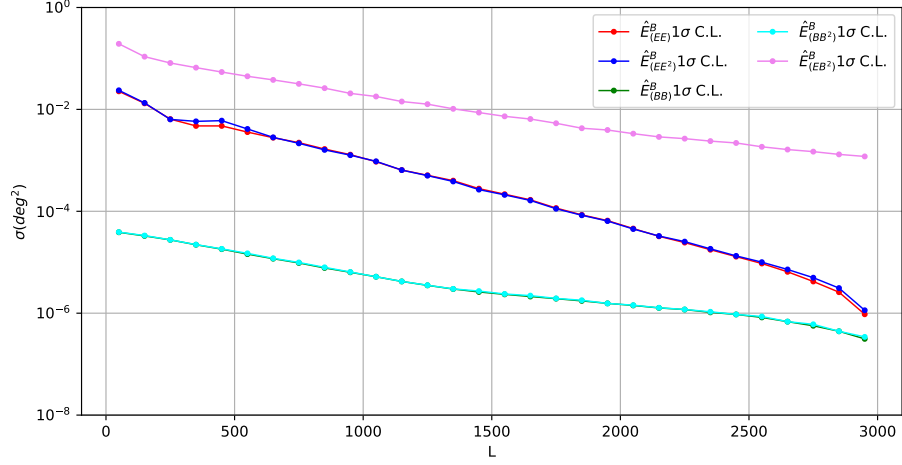


Figure 4.11: Solid lines represent the level at $1\sigma_{MC}$ C.L., i.e. the standard deviation of the MC simulations, as a function of CB multipoles, obtained for all the estimators $\hat{E}_{(EE)}^B$, $\hat{E}_{(BB)}^B$, $\hat{E}_{(EE^2)}^B$, $\hat{E}_{(BB^2)}^B$ and $\hat{E}_{(EB^2)}^B$.

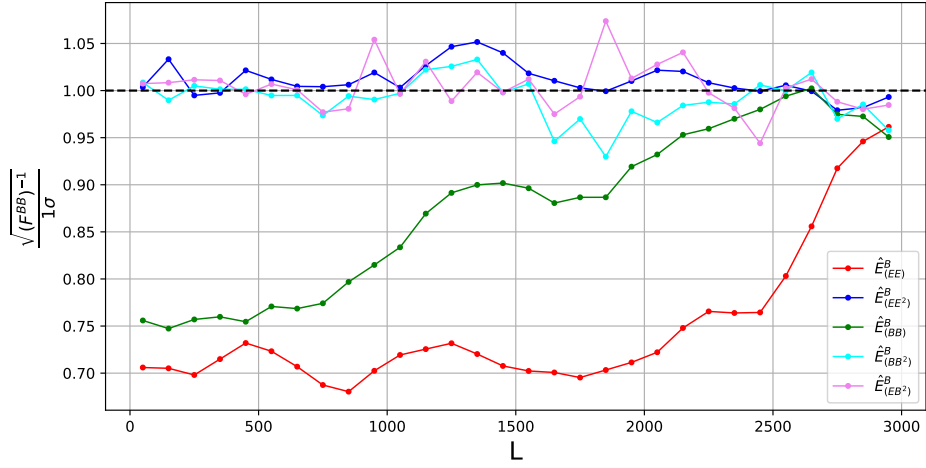


Figure 4.12: Solid lines represent the ratio between the standard deviation of the MC simulations and $\sqrt{(F^{BB})^{-1}}$ as a function of CB multipoles. The variance of quadratic estimators is well approximated by the inverse of the F matrix, while for the linear estimator it tends to underestimate the MC variance.

Monte Carlo simulations. In other words we check the relation:

$$\left(F^{LL}\right)^{-1} = V^{LL}, \quad (4.203)$$

which ultimately provides a justification of the approximation made upon the statistical behaviour of C_ℓ^{EE} , C_ℓ^{BB} and C_ℓ^{EB} . For the quadratic estimators Eq. 4.203 holds with a very good approximation. While for the linear estimators the inverse of the F matrix tends to underestimate the variance of MC simulations. In particular, in the harmonic range $L < 2000$ for the EE-based estimator $\sqrt{(F^{BB})^{-1}}$ is $\sim 20 - 25\%$ smaller than the standard deviation and for the BB-based estimator only after $L > 1000$ Eq. (4.203) is satisfied with a fairly-good approximation ($\sim 10\%$).

4.5.2.1 Correlation effect in the validation plots

The lower boxes of the validation plots for the estimators $\hat{E}_{(EE)}^B$, $\hat{E}_{(BB)}^B$, $\hat{E}_{(EE^2)}^B$, $\hat{E}_{(BB^2)}^B$ point out a correlation effects which characterised the fluctuations from the expected signal. It is possible to find an explanation for this behaviour displaying the covariance matrix of the estimate $V^{BB'}$ built with the MC simulations and the inverse of the F matrix, i.e. $(F^{BB'})^{-1}$.

Now, for simplicity, let us just take the BB-based linear estimator as an example²². Figure 4.13 shows the elements of the covariance matrix $V^{BB'}$ (upper panel) and the elements of $(F^{BB'})^{-1}$ (lower panel) for the BB-based linear estimator encoded with a color-map. From this figure we can note:

- the covariance of the estimate $V^{BB'}$ exhibits a checkerboard pattern of positive and negative elements which is the responsible for the correlation effect in the fluctuations from the expected signal, displayed in the lower boxes of the validation plots in Figures 4.9;
- that $(F^{BB'})^{-1}$ matrix maps very well the pattern of the covariance of estimates even if the amplitudes of the elements could be different (see Figure 4.12, in particular only 52 elements over 900 (less than 6%) differ in terms of sign. Therefore Eq. (4.178) still holds also in this regime and $(F^{BB'})^{-1}$ well describes the covariance of the estimate, or in other words, the statistical behaviour of the estimator. Note that such a matrix is obtained by inverting the $F^{BB'}$ matrix shown in Figure 4.14²³.

²²The $\hat{E}_{(EE)}^B$, $\hat{E}_{(BB)}^B$, $\hat{E}_{(EE^2)}^B$, $\hat{E}_{(BB^2)}^B$ estimators show the same behaviour, see appendix A.1 for more details.

²³We have checked that the inversion of the F matrix is numerically stable for each estimator and for each setup used.

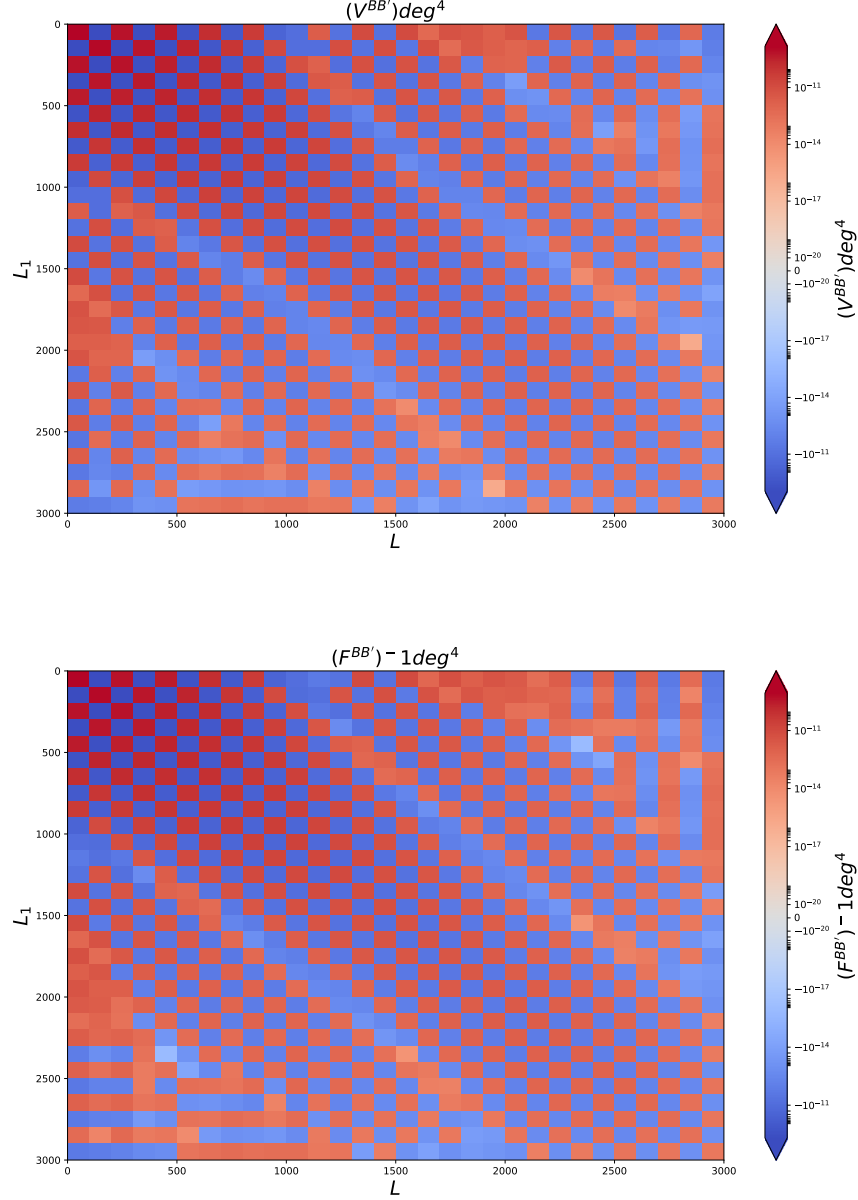


Figure 4.13: Upper panel: elements of the covariance matrix built with the simulations for the BB-based linear estimator encoded with a color-map. The checkerboard pattern of positive and negative elements produces the correlation effect we see in the fluctuations from the expected signal (displayed in the lower boxes of the validation plots in Figures 4.9 and 4.10). Lower Panel: elements of the $(F^{BB'})^{-1}$ matrix of the BB-based linear estimator encoded with the same color-map. Note that the $(F^{BB'})^{-1}$ matrix maps very well the pattern of the covariance of estimates even if the amplitudes of the elements could differ (see Figure 4.12, which displays the ratio between the main-diagonal elements of the covariance matrix and the ones of the $(F^{BB'})^{-1}$ matrix).

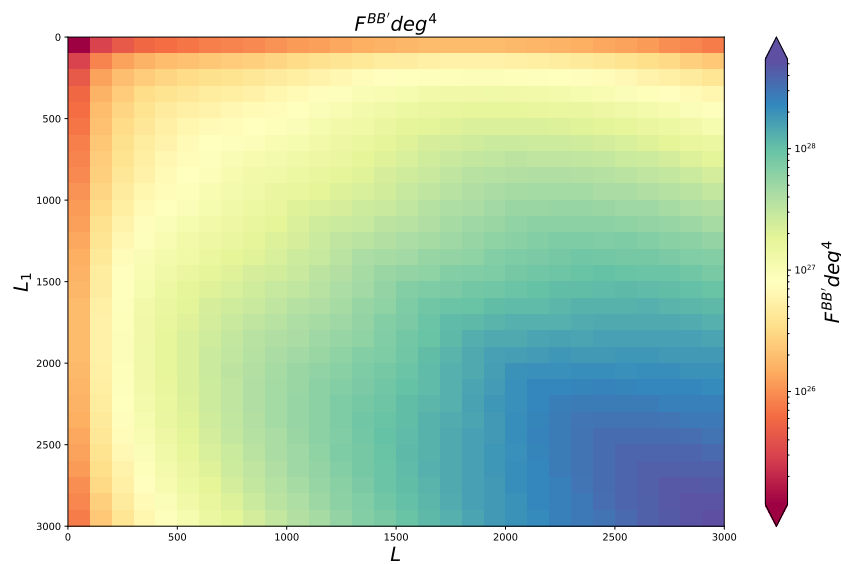


Figure 4.14: elements of the $F^{BB'}$ matrix of the BB-based linear estimator encoded with a color-map. Note that value of elements increases almost monotonically along any row from the left to the right and along any column from the top to the bottom.

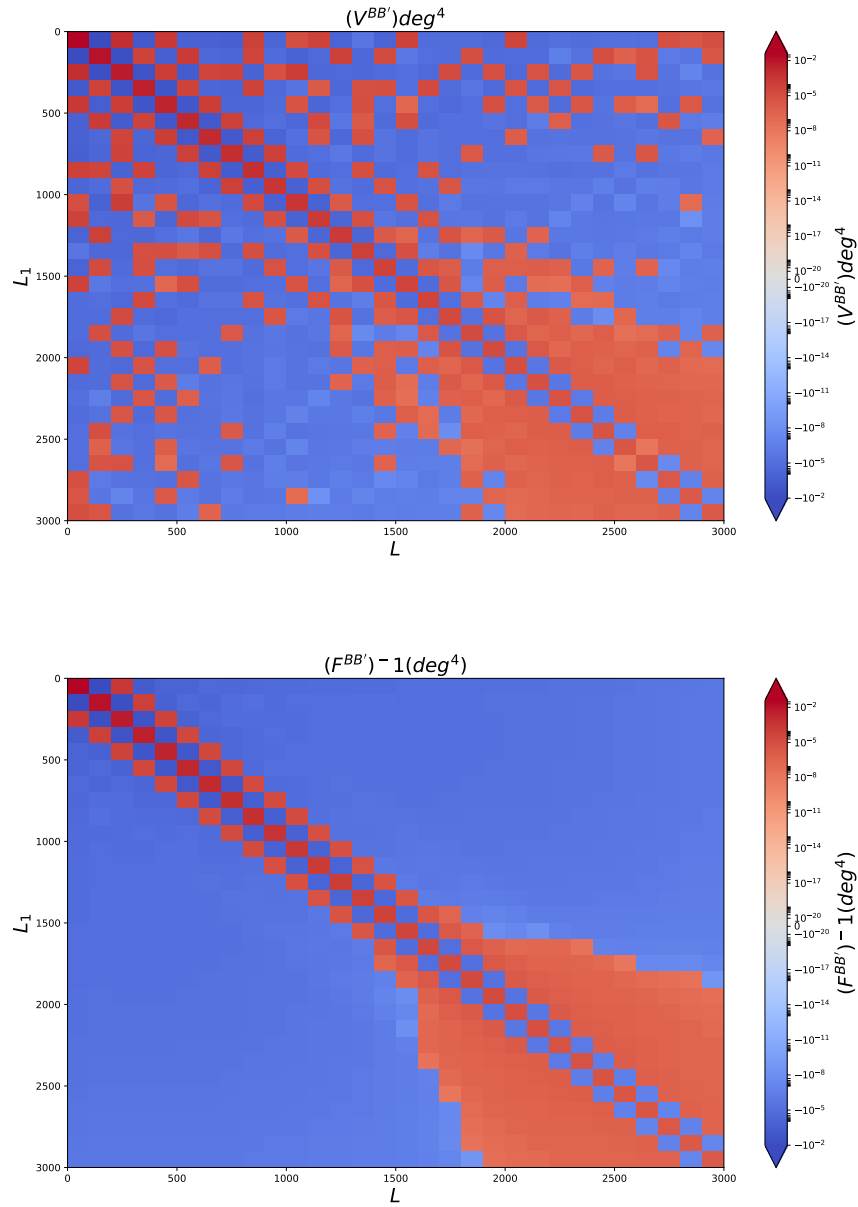


Figure 4.15: The same of Figure 4.13 but for the EB-based estimator. Note that here the matrices exhibit a much lower correlation pattern than in the case with the BB-based linear estimator.

Instead the $\hat{E}_{(EB^2)}^B$ estimator exhibits a much lower correlation pattern in the fluctuations from the expected signal than the other estimators, see the lower panel of Figure 4.10. We re-find this behaviour in the elements of the covariance matrix $V^{BB'}$ (upper panel) and the one of the $(F^{BB'})^{-1}$ matrix (lower panel) shown in Figure 4.15. Note that while the amplitude of the $V^{BB'}$ and $(F^{BB'})^{-1}$ elements is pretty the same (see Figure 4.12 in which it is compared the square root of the elements of the main diagonal), these two matrices have 180 elements over 900 (20%) with an opposite sign. Anyway the pattern of the covariance of the estimates is still well recognisable also in $(F^{BB'})^{-1}$, and therefore we can consider that Eq. (4.178) still holds with a good approximation.

We can try to explain the correlation pattern which characterised the EE-based and BB-based estimators (both linear and quadratic) by invoking the fact that the latter are built starting from $\tilde{H}_{\ell\ell'}^L$ and $H_{\ell\ell',ev}^L$, which are objects with a checkerboard pattern of null and non-null elements for a fixed L , while the EB-based estimator is computed from the $\tilde{K}_{\ell\ell'}^L$ matrix, which for a fixed L has a full pattern.

In appendix A.1 are reported, for completeness, the covariance matrix $V^{BB'}$ and $(F^{BB'})^{-1}$ for all the other estimators.

4.5.2.2 Dependence on the the maximum CMB multipole considered

We conclude the characterisation of our estimators checking what happens when we change the maximum CMB multipole considered to compute the CB spectrum. As done in the previous section, let us just take the BB-based linear estimator as an example. We computed C_B^α from $L = 1$ to $L = 2000$, with a binning of $\Delta L = 100$, considering four different CMB harmonic ranges: $[2 - 2500]$, $[2 - 3000]$, $[2 - 3500]$ and $[2 - 4000]$. Upper panel of Figure 4.16 shows the 1σ uncertainties as a function of the CB multipoles considering the four different cases mentioned above. Note that if we consider only the first 2500 multipoles in CMB to evaluate the CB in the harmonic range $L \in [1, 2000]$ we lose information. In fact, from the lower panel of Figure 4.16 we can see that the uncertainties on CB increase by a factor ~ 1.5 . The reason of this behaviour is given in Figure 4.17, which displays W_b^B as function of the CMB multipoles from $B = 0$ (corresponding to $L = 1 - 100$) to $B = 20$ (corresponding to $L = 1991 - 2000$). We can interpret the objects W_b^B as a sort of window function which selects the contribute of the different CMB multipoles to the birefringence multipoles. From Figure 4.17 it is clear that if we want to evaluate C_B^α from $L = 1$ to $L = 2000$, in CMB we need to go beyond the $\ell \sim 2500$ otherwise we cut off

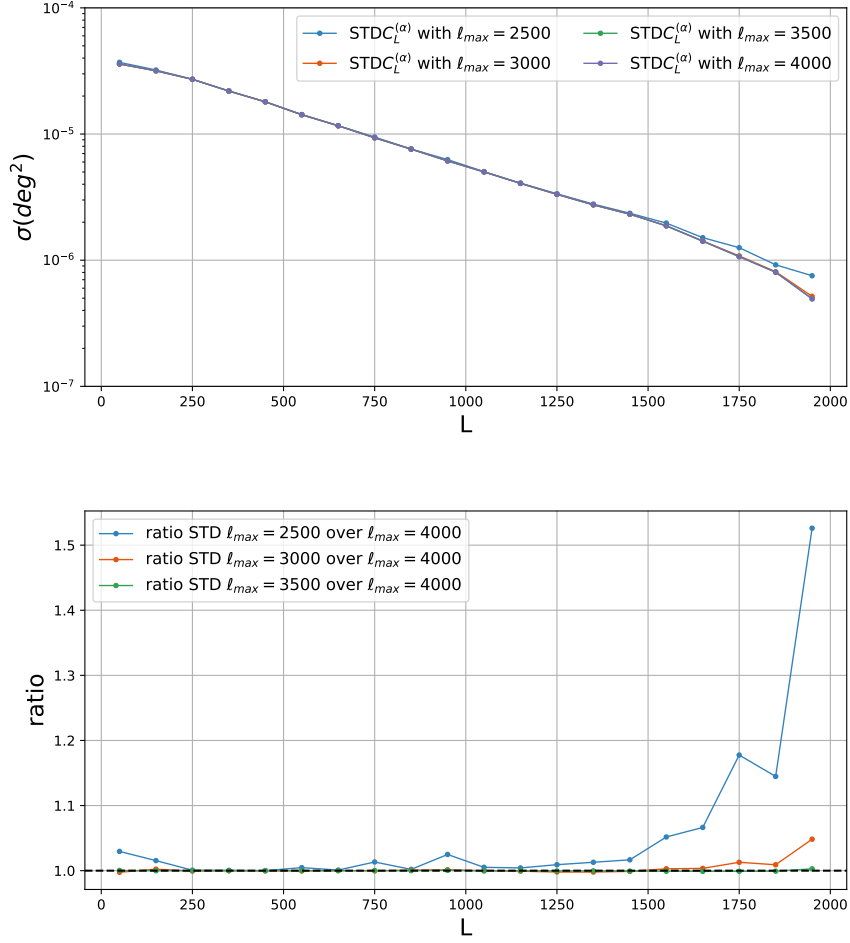


Figure 4.16: In the upper panel it is shown the comparison of the 1σ C.L. of C_B^α from $L = 1$ to $L = 2000$, obtained considering four different CMB harmonic ranges: $[2 - 2500]$ (blue line), $[2 - 3000]$ (orange line), $[2 - 3500]$ (green line) and $[2 - 4000]$ (violet line). In the lower panel it is displayed the ratio with respect to the best one, i.e. the $[2 - 4000]$ case.

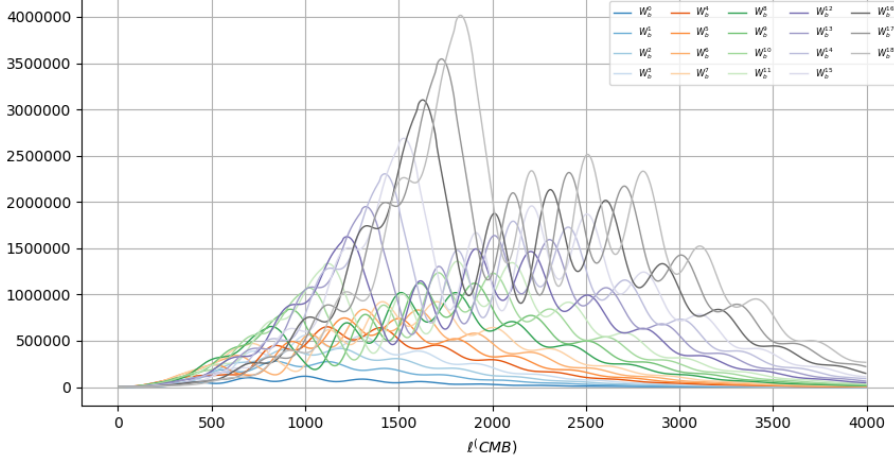


Figure 4.17: W_b^B for the BB-based linear estimator as a function of CMB multipoles, computed from $B = 0$ (corresponding to $L = 1 - 100$) to $B = 20$ (corresponding to $L = 1991 - 2000$). Note that, for a fixed multipole in CMB, the slopes of W_b^B increase along the y-axis at the increasing of the CB multipole considered

a relevant contribute to curve of W_b^B with $B > 10$.

4.5.3 Application to Planck Data

As in the analysis performed with the localisation approach, we use the half-mission (HM) version for both data and FFP10 simulations released with PR3 dataset and describe in section 4.3. Combining the first 300 CMB realisations with the two different HM splits of 300 noise maps we build two MC set of 300 signal and noise simulations which do contain also residuals of known systematic effects. From these maps we estimate the six CMB spectra in cross-mode, at the aim of reducing the residuals of systematic effects and noise mismatches in the auto-spectra. This is done for the four component separation methods, namely `commander`, `nilc`, `smica` and `sevem`. To test the robustness of our analysis we perform our estimators, see Eqs. (4.174), Eq. (4.175), Eq. (4.188), Eq. (4.189) and Eq. (4.190), on each Planck pipeline obtaining well compatible results.

4.5.3.1 Impact of residual of systematics

As described above, the CMB signal component in the HM simulations dataset also contains residuals of known instrumental, beam related, non-

idealities. However, PLA does not provide a version of such systematic component tailored to the HM splits, but only the one computed assuming the full mission (FM) set. As a consequence the cross-mode APS estimation cannot reduce these systematic residuals in the simulations as, instead, it would expect to happen for real data. This issue might lead to an over-estimation of residuals in the simulations with respect to data. In particular, we note that for the C_ℓ^{EE} and C_ℓ^{BB} the more significant impact of systematic effects is at large angular scales, around for $\ell < 100$.

The FFP10 simulations do not contain any birefringence effect therefore the average of the C_B^α obtained from this MC set should be compatible with zero. If this does not happen then there are some residuals of systematic effects in the FFP10 simulations which dominate the evaluation CB power spectrum. In order to estimate the impact of these systematics, we take into account the distance of the average of the MC with respect to the expected signal and compared it with the statistical uncertainties in term of percentage. If that percentage is larger than a certain threshold, which is around the 20%²⁴, than the systematic effects in the FFP10 simulations dominate and the mean values of C_B^α of the MC are not compatible with the null effect. We find that to minimise the systematic effects in the FFP10 simulations we have to exclude from the analysis the first CMB multipoles, in this way the systematic uncertainties decrease under the threshold and the MC average fall in the $3\sigma_\mu$ confidence region.

As done in the previous section, let us just take the BB-based linear estimator as an example. Considering the `commander` pipeline, we compute C_B^α from $L = 1$ to $L = 1000$, with a binning of $\Delta L = 100$, taking the CMB band power in the multipole range $\ell \in [2, 1500]$ with a binning of $\Delta\ell = 5$. The upper panel of Figure 4.18 shows a plot analogous to the ones of Figure 4.9. The upper box displays the mean of C_B^α with $\sigma_\mu = \sigma_{MC}/\sqrt{N_{sims}}$ as error bar of the mean, while the lower box shows the fluctuations from the expected signal of the mean in units of σ_μ . For this configuration we get that, in the first half of the considered CB harmonic range, the FFP10 simulations are not compatible with the null effect. We can visualise that also from the lower panel of Figure 4.18, which shows how the systematic error on C_B^α in terms of percentage of the $1\sigma_{MC}$ uncertainties as a function of the CB multipoles exceeds the 20% threshold for $L < 500$. Now if we re-computed C_B^α taking the CMB spectra in the multipole range $\ell \in [102, 1500]$, i.e. excluding the

²⁴This percentage depends on the number of the simulations considered. We are asking that: $\frac{|\mu|}{\sigma_\mu} < 3$, where $|\mu|$ is the distance of the average of the MC with respect to the expected signal and σ_{MC} is the standard deviation of the mean. This is equivalent to ask that: $\frac{|\mu|}{\sigma_{MC}} < 3\sqrt{N_{sims}}$. Since $N_{sims} = 300$, we get that the threshold is around ~ 0.2 (or in percentage $\sim 20\%$).

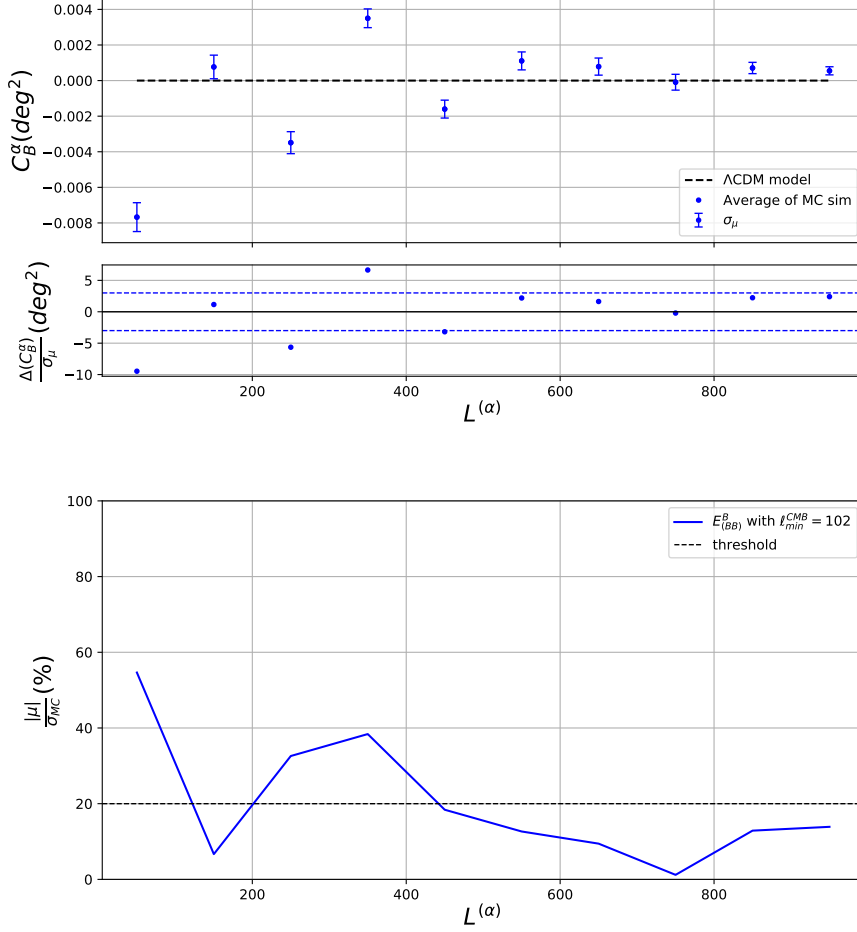


Figure 4.18: C_B^α from $L = 1$ to $L = 1000$, with a binning of $\Delta L = 100$. We apply the BB-based linear estimator, $\hat{E}_{(BB)}^B$, on the `commander` FFP10 simulations, considering the CMB spectra estimated in the range $\ell \in [2, 1500]$ with a binning of $\Delta\ell = 5$. Upper panel shows the averages of C_B^α as a function of CB multipoles. Error bars represent the uncertainties associated to the averages. Upper panel displays also a lower box where for each bin of the CB multipoles it is shown the distance of mean in units of standard deviation of the mean itself. Dashed horizontal lines represent the expected value for the averages of C_B^α , which are zero since in the FFP10 MC simulations the CB effect is absent by construction. In the lower panel it is displayed the distance of the average of the MC from zero and compared it with the $1\sigma_{MC}$ uncertainties in terms of percentage.

Estimator	$\ell_{min}^{(CMB)}$	$\ell_{max}^{(CMB)}$	$\Delta\ell^{(CMB)}$	$L_{min}^{(\alpha)}$	$L_{max}^{(\alpha)}$	$\Delta L^{(\alpha)}$
$\hat{E}_{(EE)}^B$	152	1500	5	1	1000	100
$\hat{E}_{(BB)}^B$	102	1500	5	1	1000	100

Table 4.1: Setup adopted for the analyses on the FFP10 simulations and data presented in section 4.5.3.2. C_B^α is evaluated from $L = 1$ to $L = 1000$, with a binning of $\Delta L = 100$. We apply the EE- and BB-based linear estimators taking the CMB spectra with a binning of $\Delta\ell = 5$ in the range $\ell \in [152, 1500]$ and $\ell \in [102, 1500]$, respectively.

first 100 multipoles, we reduce the impact of systematic effects and the MC simulations become compatible with the expected signal, see Figure 4.19.

Therefore we test different configurations, varying the minimum CMB multipole considered in the analysis, in order to find the best setup which minimises the systematic effects and makes the FFP10 simulations compatible with the null effect.

4.5.3.2 CB spectrum with Linear Estimator

In this section we show and discuss the CB power spectrum obtained employing the EE- and the BB-based linear estimators, see Eqs. (4.174) and (4.175), on the FFP10 dataset, both simulations and data, adopting the configurations reported in table 4.1. Figures 4.20 and 4.21, one for each estimator, characterise the distributions of C_B^α obtained by applying $\hat{E}_{(EE)}^B$ and $\hat{E}_{(BB)}^B$ on the four PLANCK pipelines of the FFP10 MC. In the upper panels of these figures, the upper box shows the mean of C_B^α with $\sigma_\mu = \sigma_{MC}/\sqrt{N_{sims}}$ as error bar of the mean, while the lower box displays the fluctuations from the expected signal of the mean in units of σ_μ . In the lower panels it is shown the statistical uncertainties at level of 1σ C.L. as a function of CB multipoles. See appendix A.2 for the ratio between $\sqrt{(F^{BB})^{-1}}$ and the standard deviations. From these figures it is possible to note that:

- adopting the configuration and in particular taking into account the CMB band power from the minimum multipoles shown in table 4.1, the impact of the residual of systematics in FFP10 is kept under control in the evaluation of C_B^α ;
- the BB-based linear estimator, Eq. (4.175), is the one which performs better: on the harmonic range $L \in [1 - 1000]$ the $1\sigma_{MC}$ C.L. goes from $\sim 1 \cdot 10^{-2} \text{deg}^2$ to $\sim 4 \cdot 10^{-3} \text{deg}^2$, reaching also a difference of one order of magnitude from the EE-based estimators, see Figure 4.22

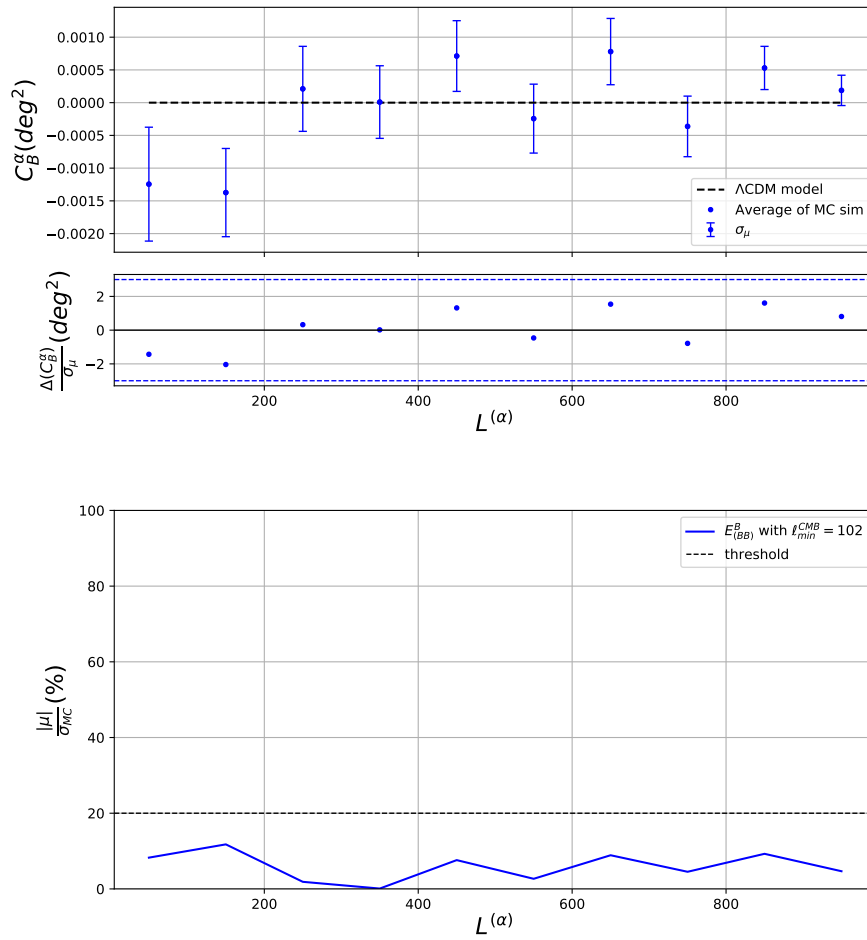


Figure 4.19: The same of Figure 4.18 but here $\hat{E}_{(BB)}^B$ is applied considering the CMB spectra estimated in the range $\ell \in [102, 1500]$, i.e. excluding the first 100 multipoles.

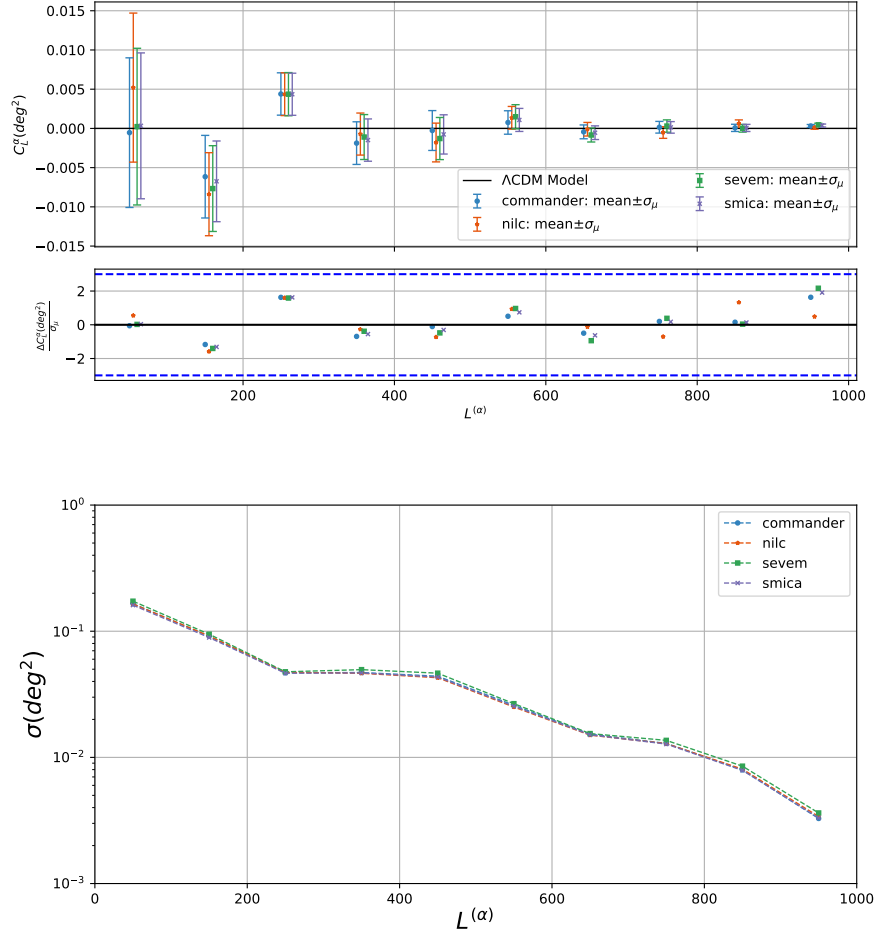


Figure 4.20: CB power spectrum estimates obtained by applying the $\hat{E}_{(EE)}^B$ estimator, Eq. (4.174), on the FFP10 simulations with the configuration shown in table 4.1. Upper panel shows the averages of C_B^α as a function of CB multipoles. Error bars represent the uncertainties associated to the mean. Upper panel displays also a lower box where for each B it is shown the distance of mean in units of standard deviation of the mean itself. Dashed lines represent what theoretically expected for the averages of C_B^α . In the lower panel it is displayed the 1σ uncertainties for the four pipelines as function of the CB multipoles.

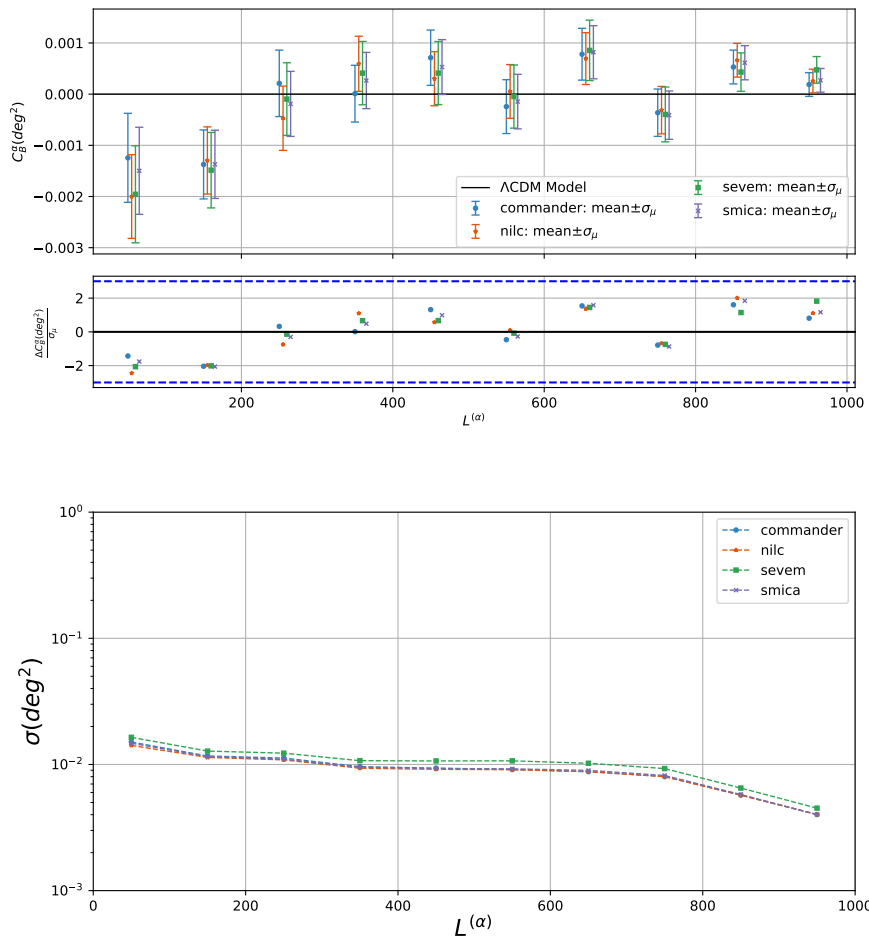


Figure 4.21: The same of Figure 4.20 but for the $\hat{E}_{(BB)}^B$ estimator, Eq. (4.175), applied to on the FFP10 simulations considering the setup in table 4.1.

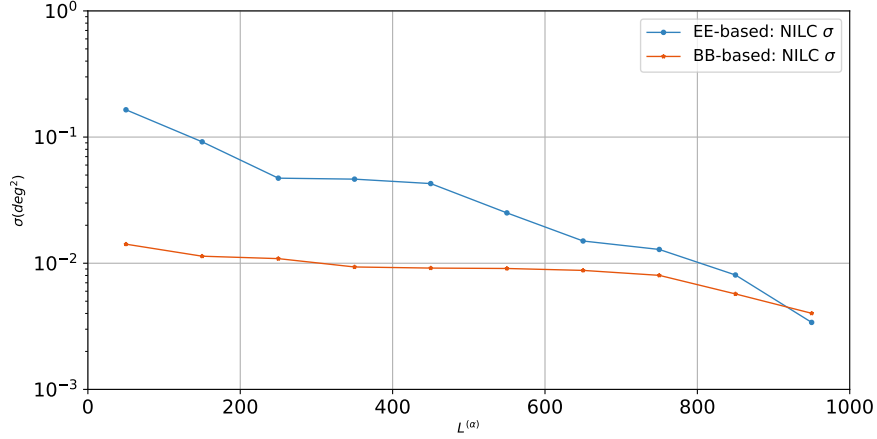


Figure 4.22: Comparisons between the $\hat{E}_{(BB)}^B$ (orange line) and $\hat{E}_{(EE)}^B$ (blue line) estimators applied to the FFP10 Planck 2018 for the `nilc` pipeline in terms of 1σ C.L. as a function of CB multipoles.

which displays the 1σ uncertainties as a function of CB multipoles for EE-based (blue solid line) and for the BB-based (orange solid line) estimator applied on the `nilc` pipeline²⁵.

Note that in this analysis, we did not apply any de-lensing procedure on the FFP10 dataset, therefore we expect that subtracting the contribute of the weak lensing on the CMB power spectra the constraining power of the BB-based estimator will improve.

Finally Figure 4.23 shows the CB power spectrum obtained by applying $\hat{E}_{(EE)}^B$ and $\hat{E}_{(BB)}^B$ to the Planck 2018 data with the setup in table 4.1. It is important to note:

- considering the more constraining BB-based estimator we find a compatibility with the null effect better than 0.009 deg^2 for $L > 400$;
- the level of the uncertainties presented here is worse than previous analyses, but we have been able to explore a much wider harmonic range of C_B^g with Planck data [33]. The region from $L=700$ to $L=1000$ was not cover before;

²⁵Since the estimates of CB obtained with the four PLANCK pipelines are well-compatible, we can choose one pipeline to compare the uncertainties of these two estimators.

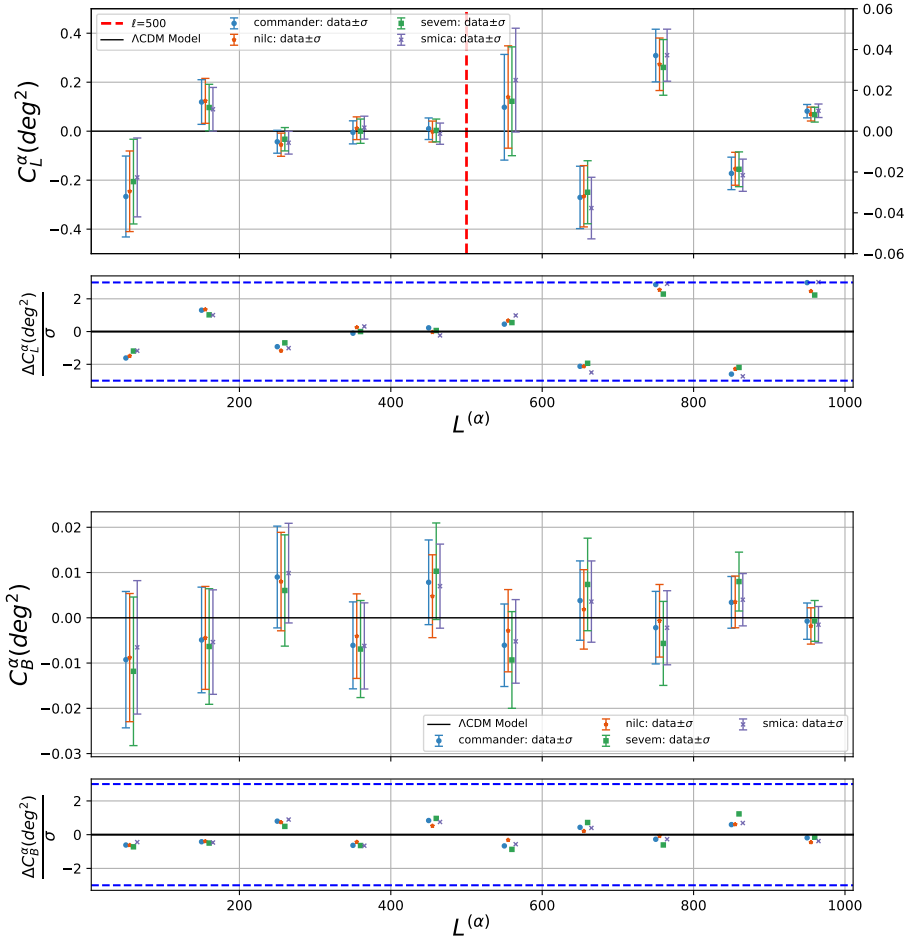


Figure 4.23: C_B^α estimates obtained by applying $\hat{E}_{(EE)}^B$ (upper panel) and $\hat{E}_{(BB)}^B$ (lower panel), see Eqs. 4.174 and 4.175, to the FFP10 Planck 2018 data considering the setup in table 4.1. For each panel, upper boxes show the averages of C_B^α as a function of CB multipoles. Error bars represent the standard deviation of the distribution. Note that in the upper panel the vertical dashed red line stands for a change in the y-scale: the points of the left-side of the red bar are referred to the scale on the left, while the points on the right-side are referred to the y-scale on the right. In the lower boxes for each binning in the CB multipoles it is shown the distance of data in units of standard deviation from zero which is the value theoretically expected in the Λ CDM standard model (dashed horizontal lines) for CB spectrum.

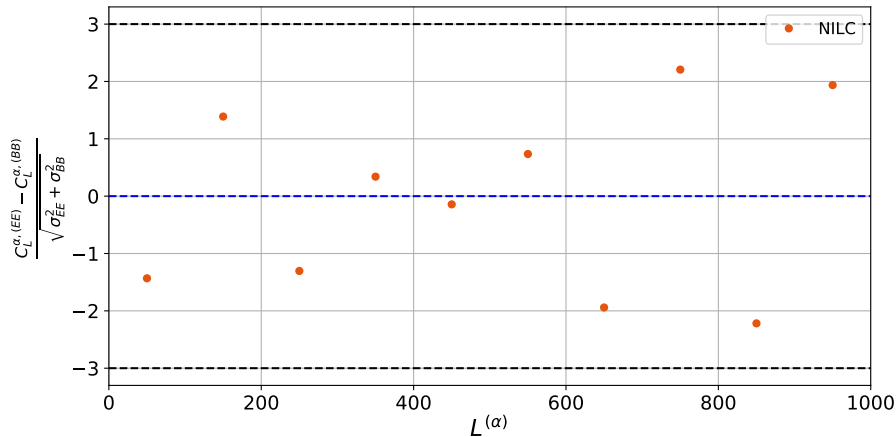


Figure 4.24: Compatibility between the CB spectrum evaluated by applying $\hat{E}_{(BB)}^B$ and $\hat{E}_{(EE)}^B$, see Eqs. (4.175) and (4.174), to the Planck FFP10 data for the `nilc` pipeline. Each point represents the difference between the estimates of C_B^α obtained with the two estimators in terms of sum of uncertainties.

- since the treatment of the foregrounds is different for each pipeline, their high-compatibility in terms of CB spectrum tells us that the impact of foreground residuals is negligible;
- the estimates of C_B^α obtained by applying $\hat{E}_{(EE)}^B$ and $\hat{E}_{(BB)}^B$ are very compatible between them. In Figure 4.24 it is shown the compatibility in units of the difference of the estimates over the sum of the square of 1σ C.L. for each binning in the CB multipoles.

4.5.3.3 CB spectrum with Quadratic Estimator

In this section we discuss the CB power spectrum obtained by applying the EE-, BB- and EB-based quadratic estimators, see Eqs. (4.188), (4.189) and (4.190), on the FFP10 dataset, both simulations and data, adopting the configurations reported in table 4.2. We kept these results separate from the outcomes of the analysis conducted in the previous section because in this case the minimisation of the systematics introduced by the CMB spectra turned out to be not completely stable yet. For the EB-based estimator there is no need to exclude any multipole of the CMB in the analysis. Instead, for the EE- and the BB-based quadratic estimators, the systematics become subdominant by excluding the first multipoles up to $\ell = 202$ for both the estimators, but contrary to what is expected, if further multipoles are

Estimator	$\ell_{min}^{(CMB)}$	$\ell_{max}^{(CMB)}$	$\Delta\ell^{(CMB)}$	$L_{min}^{(\alpha)}$	$L_{max}^{(\alpha)}$	$\Delta L^{(\alpha)}$
$\hat{E}_{(EE^2)}^B$	202	1500	5	1	1000	100
$\hat{E}_{(BB^2)}^B$	202	1500	5	1	1000	100
$\hat{E}_{(EB^2)}^B$	2	1500	5	1	1000	100

Table 4.2: Setup adopted for the analyses on the FFP10 simulations and data presented in section 4.5.3.3. C_B^α is evaluated from $L = 1$ to $L = 1000$, with a binning of $\Delta L = 100$. Note that for the EE- and BB-based estimators we exclude the first CMB multipoles until $\ell_{min}^{(CMB)} = 202$, while for the EB-based estimator, we consider the whole harmonic range, i.e. $\ell \in [2, 1500]$.

excluded, the systematics begin to impact on the estimation of the birefringence spectrum. In order to better understand this behaviour we need to produce a set of "vanilla" simulation, i.e. without systematic effects, with a Planck-like noise level and repeat the analysis. This analysis is left for future works.

Figures 4.25, 4.26 and 4.27, for the $\hat{E}_{(BB^2)}^B$, $\hat{E}_{(EE^2)}^B$ and $\hat{E}_{(EB^2)}^B$ respectively, are the analogues of Figures 4.20 and 4.21 shown in the previous section. In the upper panels of these figures, the upper box shows the mean of C_B^α with $\sigma_\mu = \sigma_{MC}/\sqrt{N_{sim}}$ as error bar of the mean, while the lower box displays the fluctuations from the expected signal of the mean in units of σ_μ . In the lower panels it is displayed the statistical uncertainties at level of 1σ C.L. as a function of CB multipoles. In the appendix A.2 it is displayed the ratio between $\sqrt{(F^{BB})^{-1}}$ and the standard deviations.

From these figures it is possible to note that the BB-based quadratic estimator, Eq. (4.189), is the one which performs better for the quadratic ones. Anyway the corresponding linear estimators are still more constraining. Figure 4.28 shows the comparison in terms of the 1σ C.L. as a function of CB multipoles for all the estimators considering the `nilc` pipeline. This plot says us that:

- unlike in the "Vanilla" case, see Figure 4.11, here the linear and quadratic estimators based on the same spectra do not have the same performance in terms of uncertainties of the CB spectrum, this because here the information does not saturate;
- the BB-based linear estimator remains the one with more constraining power on the whole harmonic range considered.

Figure 4.29 shows the CB power spectrum obtained by applying $\hat{E}_{(EE^2)}^B$, $\hat{E}_{(BB^2)}^B$ and $\hat{E}_{(EB^2)}^B$ to the Planck 2018 data with the setup in table 4.2. As

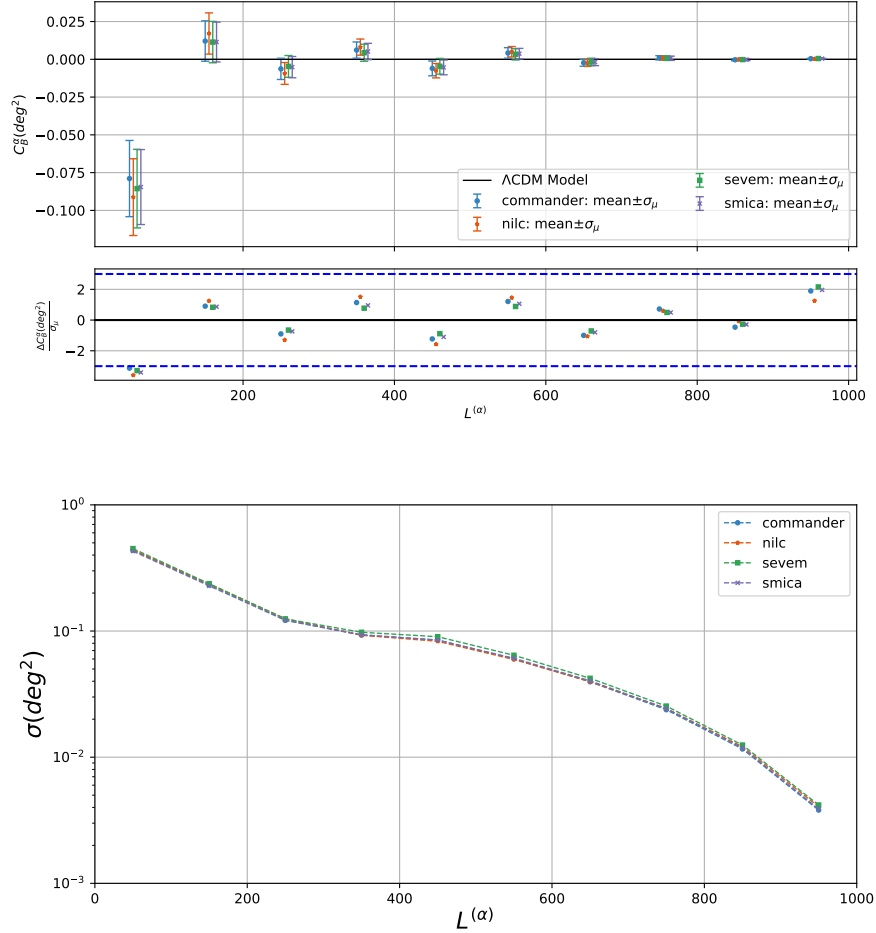


Figure 4.25: CB power spectrum estimates obtained by applying the $\hat{E}_{(EE^2)}^B$ estimator, Eq. (4.188), on the FFP10 simulations with the configuration shown in table 4.2. Upper panel shows the averages of C_B^α as a function of CB multipoles. Error bars represent the uncertainties associated to the mean. Upper panel displays also a lower box where for each B it is shown the distance of the mean in units of standard deviations of the mean itself. Dashed lines represent what theoretically expected for the averages of C_B^α . In the lower panel it is displayed the 1σ uncertainties for the four pipelines as a function of the CB multipoles.

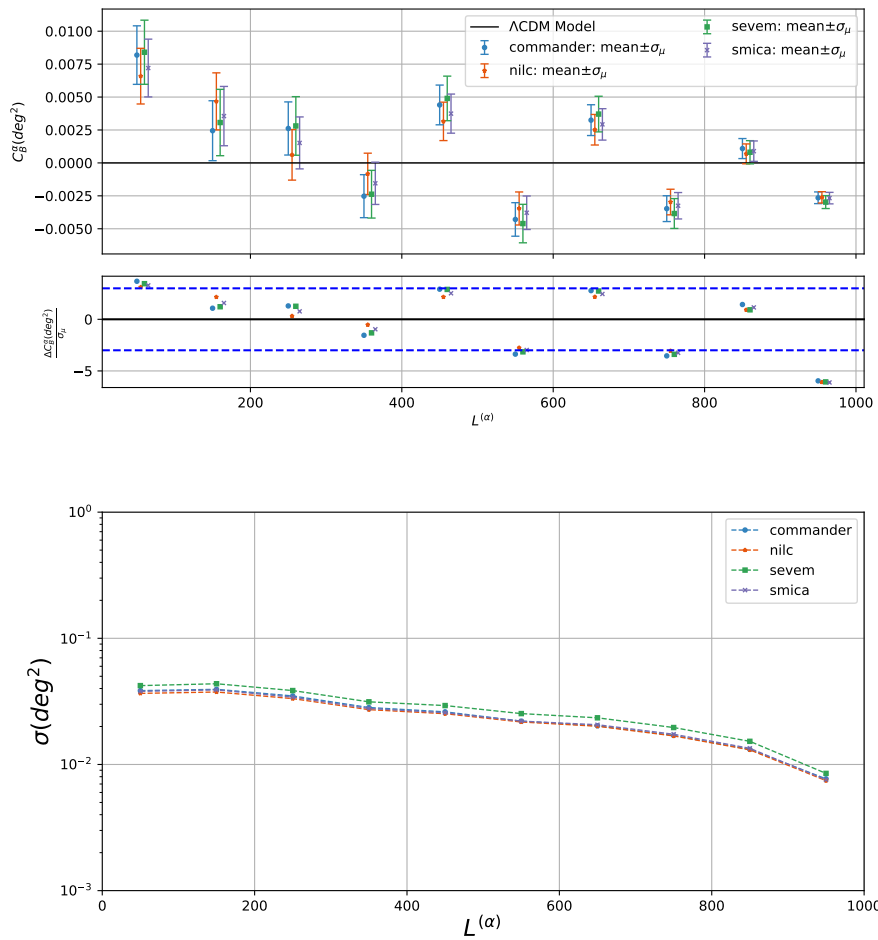


Figure 4.26: The same of Figure 4.25 but for the $\hat{E}_{(BB^2)}^B$ estimator, Eq. (4.189), employed on the FFP10 simulations considering the setup in table 4.2.

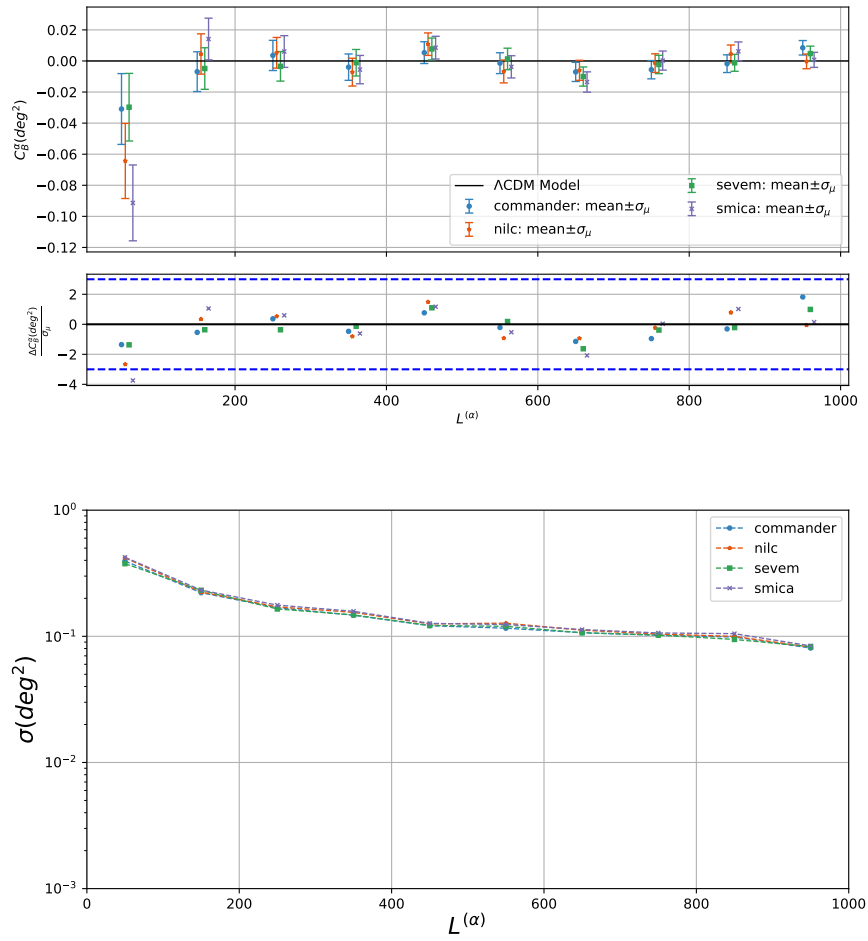


Figure 4.27: The same of Figure 4.25 but for the $\hat{E}_{(EB^2)}^B$ estimator, Eq. (4.190), employed on the FFP10 simulations considering the setup in table 4.2.

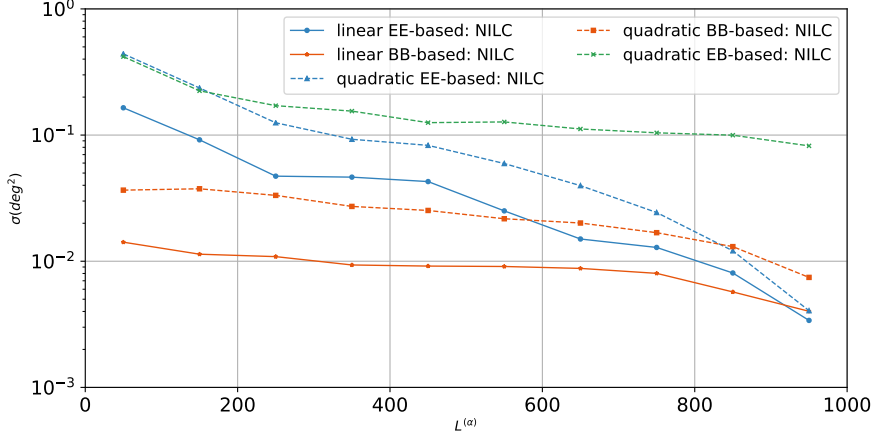


Figure 4.28: Here the comparison of the 1σ uncertainties as a function of CB multipoles for all the estimators developed in this analysis, namely $\hat{E}_{(BB)}^B$ (solid orange line), $\hat{E}_{(EE)}^B$ (solid blue line), $\hat{E}_{(BB^2)}^B$ (dashed orange line), $\hat{E}_{(EE^2)}^B$ (dashed blue line) and $\hat{E}_{(EB^2)}^B$ (dashed green line), see Eqs. (4.175), (4.174), (4.189), (4.188) and (4.190), when employed on the FFP10 dataset for the `nilc` pipeline.

for the estimates obtained with the linear estimators:

- we find a compatibility with null effect;
- the high-compatibility of the CB spectrum evaluated from different pipelines tells us that the impact of foreground residuals is negligible.

Note that, before to employ $\hat{E}_{(EB^2)}^B$ on the Planck 2018 data we have applied a de-rotation of the CMB EB data spectrum to remove the contribution of the monopole of CB. We consider an angle of $\alpha_0 = 0.27$ deg, which is the value of CB isotropic angle provided by the PR3 [75].

4.6 Conclusions

In this chapter we use CMB polarisation observations to constrain the anisotropic CB effect. We propose two complementary approaches aiming at evaluating the CB power spectrum.

1. In the first approach, based on the methodology described in [34], we use the localisation of the so-called D-estimators to built maps of the birefringence angle and thus constraining the CB spectrum on angular

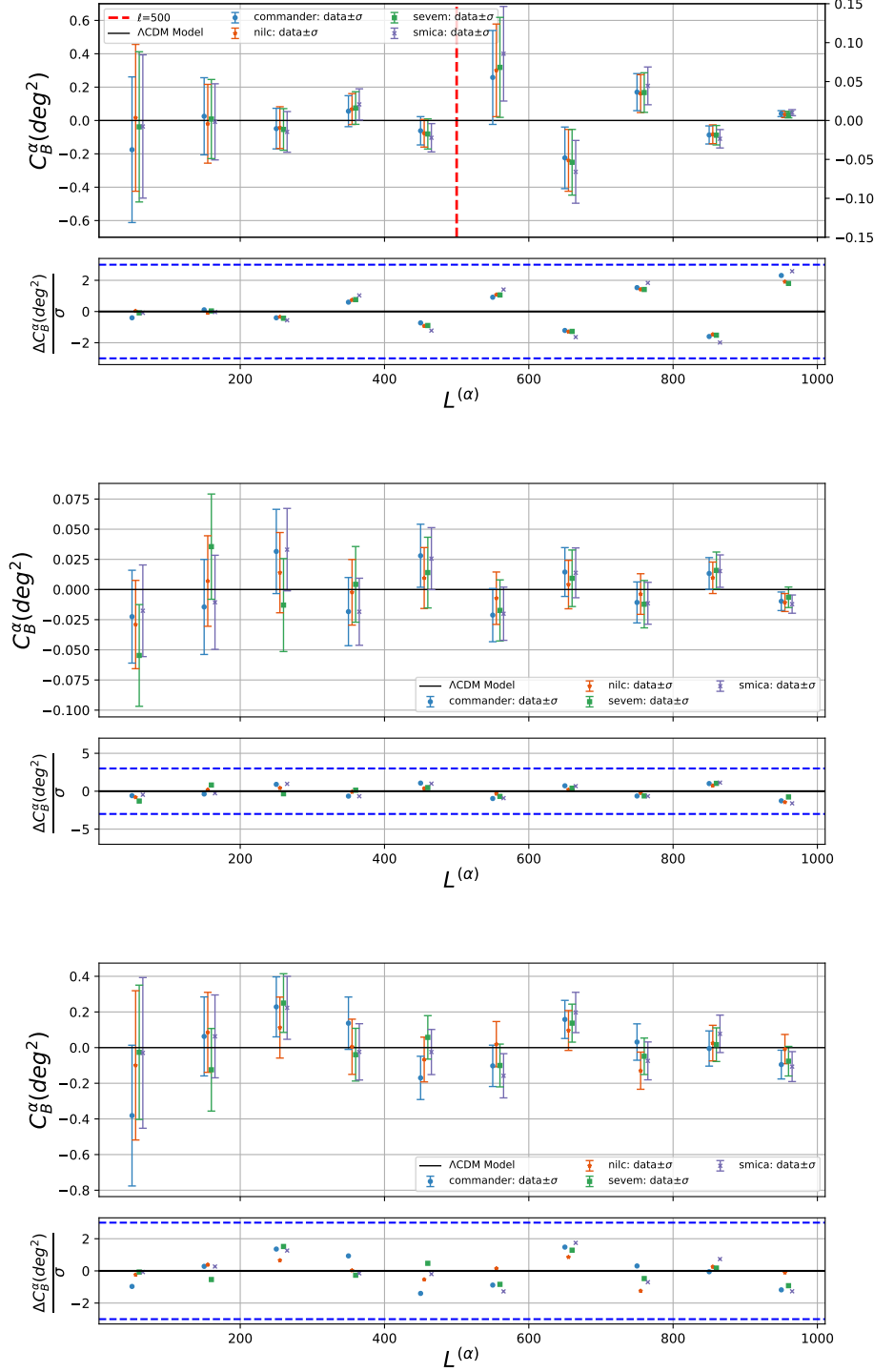


Figure 4.29: The same of Figure 4.23 but for the quadratic estimators: C_B^α estimates obtained by employing $\hat{E}_{(EE^2)}^B$ (upper panel) and $\hat{E}_{(BB^2)}^B$ (middle panel) and $\hat{E}_{(EB^2)}^B$ (lower panel), see Eqs. 4.174 and 4.175, on the FFP10 Planck 2018 data considering the setup in table 4.2. Note that the red dashed bar in the upper panel, as in Figure 4.23, stands for a change in the y-scale.

scales larger than ~ 7 degrees. Considering the Planck PR3 dataset (see section 4.3) we evaluate the CB spectrum for each multipole L in the harmonic range $L \in [1 - 24]$ (see Figure 4.7), obtaining a compatibility with the null effect with a precision better than 0.01 deg^2 (see Figure 4.8).

2. In the second approach we develop a novel class of linear and quadratic harmonic-based estimators which are able to directly evaluate the power spectrum of CB rotation angle starting from the EE, BB and EB observed angular power spectra of the CMB anisotropies.

- We use 1000 Monte Carlo 'vanilla' simulations to validate and assess the performances of the Python implementation of these estimators, see Eqs. (4.174), (4.175), (4.188), (4.189) and (4.190). We evaluate the CB effect in the harmonic range $L \in [1 - 3000]$ with a binning of $\Delta L = 100$ on the CB multipoles. We show that the BB-based linear and quadratic estimators are those which perform better: the standard deviations of the MC distribution spaces from $\sim 4 \cdot 10^{-5} \text{ deg}^2$ to $\sim 4 \cdot 10^{-7} \text{ deg}^2$ on the considered harmonic range (see Figure 4.11).
- We have employed these estimators on Planck 2018 Release (PR3) both data and FFP10 MC simulations. While for the EE- and BB-based linear estimator we found stable configurations (see table 4.1) to minimise the residuals of systematics contained in the FFP10 MC, for the quadratic estimators the configurations adopted (table 4.2) turned out to be not completely stable yet and they need further investigations. Considering the most constraining estimator, i.e. the linear one based on the BB power spectrum, we evaluate the CB spectrum of Planck 2018 data on the harmonic region $L \in [1 - 1000]$ with a binning of $\Delta L = 100$ (Figure 4.23). We find a compatibility with the null effect better than 0.009 deg^2 for $L > 400$: in particular the standard deviation of the distribution goes from $\sim 1 \cdot 10^{-2} \text{ deg}^2$ to $\sim 4 \cdot 10^{-3} \text{ deg}^2$ (4.21). Even if the level of the uncertainties presented here is worse than previous analyses, we have been able to explore a much wider harmonic range of C_B^α with Planck data [33], since the region from $L=700$ to $L=1000$ was not covered before. Anyway, a detailed comparison with other techniques is left for future works.

In this analysis, we have not applied any de-lensing procedure on both the FFP10 dataset and the 'vanilla' MC simulations (which are built

from the Planck fiducial). We expect that subtracting the contribute of the weak lensing on the CMB power spectra the constraining power of the BB-based estimators will improve.

Chapter 5

Half-wave plate non-idealities

5.1 Introduction

The CMB temperature observations have greatly contributed to build the Λ CDM cosmological model. With the Planck ESA mission, CMB temperature anisotropies have been observed at the cosmic variance limit, but polarisation remains to be further investigated: in particular, informations in the E-modes have not been fully extracted yet and the primordial B -mode, essential to detect the primordial gravitational waves [127, 73], have not been detected and only the upper limits are provided. The measure of CMB polarisation represents a technological challenge, since the polarised signal is much fainter than the signal in temperature. Future CMB experiments aimed at detecting primordial B -mode are designed to observe CMB polarisation with exquisite accuracy and precision. In order to make this possible, residual of instrumental systematics has to be carefully measured. Unfortunately, the lack of suitable astrophysical calibration sources in the microwave frequency band makes optical systematics, i.e. spurious signals due to imperfect telescopes, a concern for CMB polarisation observation.

An attractive approach to minimise spurious polarisation in order to measure the weak CMB polarisation, is the use of a half-wave plate (HWP). The latter is a birefringent optical element that shifts the polarisation angle of linearly polarised light that passes through. The shift depends on the orientation of the plate, which allows modulation of the polarised sky signal by rotation of the HWP. This class of modulators is currently used in various CMB experiments, such as MAXIPOL [37], POLARBEAR [38, 39], ABS [45], SPIDER [36], PILOT [128], BLAST [129], EBEX [130]. In addition, several upcoming B -mode experiments are planning to use HWPs; see e.g. the Simons Observatory small-aperture telescopes [42] and the proposed *LiteBIRD*

satellite [40, 41].

An ideal rotating HWP only modulates the linearly polarised sky signal and therefore allows one to cleanly separate this desired signal from unpolarised sky signal. Non-ideal HWPs impede perfectly controlled modulation and indirectly cause spurious polarised signal of their own. Consequently, there exists a rich body of literature describing the optical impact of HWPs, including descriptions of various HWP non-idealities [44, 45, 46, 43] and mitigation strategies [47, 48, 49, 50]. In order to efficiently modulate polarisation over a wide frequency range, necessary to separate astrophysical foregrounds from the CMB signal, an achromatic half-wave plate (AHWP) is likely required [39, 131]. The latter consist in a combinations of layers of birefringent materials that, unlike the single-layer HWPs, can behave in an almost achromatic manner. In fact, the modulation efficiency of single birefringent crystals is constant over a relatively small frequency range and the plate will cause loss in linear polarisation for signals outside that frequency range. AHWPs largely remove the frequency-dependent loss in polarisation modulation efficiency, but they can also rotate the polarisation angle of linearly polarised light by a frequency-dependent angle. This angle offset, which can be significant for certain AHWP configurations, is potentially troublesome. When present, an observer needs prior knowledge of the spatial and spectral energy distribution of various astrophysical sources in order to correctly interpret the modulated sky signal. For instance, a sky region dominated by polarised dust requires a different angle correction compared to the one dominated by the polarised CMB [47, 132].

In section 5.2 we study how different (A)HWP configurations, see table 5.1, optimised for detectors sensitive to both 95 and 150 GHz impact our ability to reconstruct primordial B-mode polarisation in the CMB, paying particular attention to possible biases arising from the interaction of frequency dependent HWP non-idealities with polarised Galactic dust emission and the interaction between the HWP and the instrumental beam. This analysis is the outcome of the collaboration with Dr A. J. Duivenvoorden, Dr A. E. Adler, Dr. N. Dachlythra, Dr J. E. Gudmundsson at the Stockholm University [51]. To produce these simulations, we extended the capabilities of the publicly available `beamconv`¹ code, first described in [52]. To our knowledge, we produced the first time-domain simulations that include both HWP non-idealities and realistic full-sky beam convolution. With the upgraded version of `beamconv`, we have been able to estimate the contamination of the BB power spectrum due to the interplay between dust modelling, beam and HWP non-idealities.

¹<https://github.com/AdriJD/beamconv>

We conclude the chapter presenting in section 5.3 a preliminary application of the realistic CMB simulations produced with `beamconv`. We use the latter to investigate instrumental contamination which could specifically bias the measure of the CB effect in view of future and present CMB missions.

5.2 HWPs systematics with `beamconv`

In this analysis, through the extended version of `beamconv` code, we simulate the interaction between the HWP non-idealities and a realistic polarised beam and point out the importance of this potential systematic. In section 5.2.1 we introduce the mathematical framework and the data model used for the simulations. After a brief introduction on the Mueller matrix description of an HWP (see e.g. [133, 134, 135, 136, 137]), we derive a data model for a typical CMB polarisation experiment (see section 5.2.1.2) which considers the effects of a non-ideal HWP combined with beam convolution on the time-ordered data (TOD). We generalize the one presented in [44] to the case of multi-layer HWPs and arbitrary shaped and non-trivially polarised beams. In section 5.2.2 the description of our fiducial instrument, the HWP properties, the proposed scanning strategy and the input sky models are presented. Results are given in section 5.2.3: we provide the residual power spectra obtained from the HWP configurations in table 5.1, considering firstly a symmetric gaussian beam and then realistic beam models with non-negligible cross-polarization and sidelobes. We show also how certain AHWP configurations produce significant systematic polarisation angle offsets that vary for sky components with different frequency dependence.

Throughout this section we make use of the Einstein summation convention: pairs of upper and lower indices are implicitly summed over. We use θ and ϕ to denote the polar and azimuthal angles of the standard spherical coordinate system. The metric of the sphere is given by $g_{ij} = \text{diag}(1, \sin^2 \theta)$ in these coordinates.

5.2.1 Mathematical Framework

In `beamconv` code [52] it is considered the case where the time-ordered data (TOD), i.e. the raw data, depends linearly on the sky signal in the pixel space, i.e. the map. In this approach it is possible to write a generic data model of a CMB experiment in matrix notation as:

$$\mathbf{d} = \mathbf{A} \mathbf{s} + \mathbf{n}, \quad (5.1)$$

where \mathbf{d} is the n -dimensional time-ordered data, \mathbf{s} is the sky signal, \mathbf{A} is the linear transformation which relates \mathbf{d} to \mathbf{s} and \mathbf{n} represents the additive noise in the time-domain. After the data \mathbf{d} are measured, in order to produce an estimate $\hat{\mathbf{s}}$ of the sky signal in the pixel space, one need to solve the inverse problem $\mathbf{d} \mapsto \hat{\mathbf{s}}$:

$$\hat{\mathbf{s}} = (\mathbf{A}^T \mathbf{N}^{-1} \mathbf{A})^{-1} \mathbf{A}^T \mathbf{N}^{-1} \mathbf{d}, \quad (5.2)$$

with \mathbf{N}^{-1} matrix stands for the inverse of the noise autocorrelation matrix in the time-domain. The process described in Eq. (5.2) is called map-making [138]. Without loss of generality, we can take a gaussian noise \mathbf{n} with zero mean, so the \mathbf{N}^{-1} matrix is $\mathbf{N} = \langle \mathbf{n} \mathbf{n}^T \rangle$. Under this assumption, the noise of the sky estimate $\hat{\mathbf{s}}$ is described as a mean zero random gaussian field with a noise covariance matrix \mathbf{C}_N in the pixel basis defined as:

$$\mathbf{C}_N = (\mathbf{A}^T \mathbf{N}^{-1} \mathbf{A})^{-1}. \quad (5.3)$$

Inside the matrix \mathbf{A} is encoded the modeling of the optics of the instrument which describes how the latter transforms the sky signal \mathbf{s} before it is absorbed by the detectors of the instrument. In map-making procedure optical systematics are then caused by an incomplete description of \mathbf{A} during the process. Uncertainties in optical calibration and numerical limitations generally force CMB analyses to employ rather crude descriptions of their instrument's optical response. Simplified versions of \mathbf{A} are thus generally used to calculate Eq. (5.2) and Eq. (5.3).

In order to evaluate the resulting bias in the sky signal and the derived power spectra, the approach employed in `beamconv` is to simulate the forward process $\mathbf{s} \mapsto \mathbf{d}$ as realistically as possible while using the standard simplified map-making techniques to perform $\mathbf{d} \mapsto \hat{\mathbf{s}}$. Therefore the aim becomes to find the more realistic model which describes the time-ordered data. In the updated version of `beamconv` code [51] the implemented data model considers the interaction between all-sky beam convolution with asymmetric beams and non-ideal HWPs.

5.2.1.1 Half-wave plate Mueller Matrix

We start by describing the polarised sky signal incident from direction $\hat{\mathbf{n}}$ and at frequency ν as a Stokes vector:

$$\mathbf{S}_{\text{sky}}(\hat{\mathbf{n}}, \nu) = \begin{pmatrix} I \\ Q \\ U \\ V \end{pmatrix}(\hat{\mathbf{n}}, \nu). \quad (5.4)$$

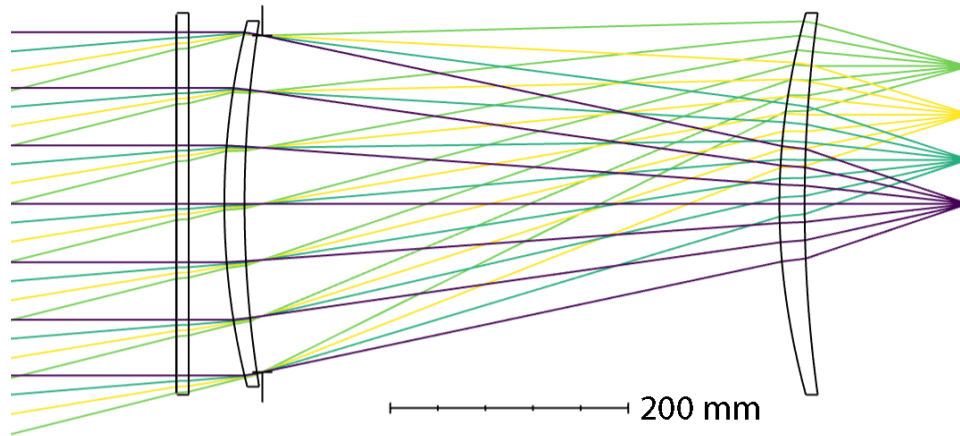


Figure 5.1: Sketch of the telescope model used for this study. Light coming in from the left interacts with an HWP before hitting the primary lens. Light from the primary lens then gets further focused by the secondary lens before hitting the focal plane (on the right). The edge pixel has a beam centroid of 14° relative to boresight (see ray-bundle emitted from top right corner). Figure taken from: [51]

Here, I represents the total intensity of the radiation, while Q and U describe the linearly polarised part of the radiation and V describes the circularly polarised component. Stokes vectors have real elements that obey

$$I \geq \sqrt{Q^2 + U^2 + V^2}. \quad (5.5)$$

The above inequality is saturated for completely polarised light, while the right hand side of the equality goes to zero for unpolarised light.

Mueller matrices describe the set of linear transformations that transform Stokes vectors to other valid Stokes vectors. Linear optical media such as HWPs are described by Mueller matrices. Multiplying a Stokes vector by such a Mueller matrix describes how the HWP alters the polarisation properties of the radiation described by the Stokes vector.

Half-wave plates are optical elements used to change the polarisation state of an incident wave, by inducing a predetermined phase difference between two perpendicular polarisation components. A traditional HWP design involves a single layer of birefringent crystal cut to a thickness such that the phase shift incurred from a particular wavelength at normal incidence is exactly half a period. In other words, incoming linear polarisation is decomposed into two orthogonal linear polarisations along the crystal axes of the sapphire, i.e. ordinary and extraordinary axes. These two waves travel at different speeds. The sapphire thickness is chosen to produce a π phase

shift between these two waves, which reflects the incoming polarisation along the extraordinary axis of the crystal. As a result, the polarisation rotates by an angle of $2\alpha_t$, where the angle between the fast axis and the incoming polarisation is α_t (see Figure 2 of [45]). Rotating the HWP thus results in a controlled modulation of the incoming linear polarisation. There are two different regimes of modulation speed: one that is much slower, i.e. stepped rotation, and the other much faster, i.e. continuous rotation.

In the Mueller formalism, an HWP comprised of a single layer of birefringent material and any number of layers of isotropic dielectric materials can be represented through a matrix characterized by four parameters:

$$\mathbf{M}_{\text{HWP}}(\nu) = \begin{pmatrix} T & \rho & 0 & 0 \\ \rho & T & 0 & 0 \\ 0 & 0 & c & -s \\ 0 & 0 & s & c \end{pmatrix}(\nu) \quad (\text{single layer}), \quad (5.6)$$

where T can be interpreted as the total transmission, ρ as the difference in transmission between the fast and the slow axes, c as the linear polarisation response and, s as the coupling to circular polarisation. The values of these parameters can be directly linked to the Fresnel coefficients for reflection and transmission. For an ideal HWP, we note that $T = 1 = -c$ and $\rho = s = 0$. For a real single-layer HWP these elements are instead variable and dependent on the frequency and the incidence angle of the incoming radiation. Figure 5.1 shows how the angle of incidence made by light hitting the HWP changes significantly as one moves across the focal plane. For wide field-of-view telescopes, this incidence angle can be as large as 17° [42].

In [139] it is shown that there exists combinations of layers of birefringent materials that, unlike the single-layer HWPs, can behave in an almost achromatic manner. The resulting achromatic half-wave plates (AHWPs) have a low frequency dependence in polarisation modulation efficiency across a broad frequency range. This is achieved by introducing a relative rotation angle for one or several of the birefringent layers such that not all of the fast optical axes are aligned. The setup is discussed in detail in [140]. A complication of AHWPs is their effective frequency-dependent rotation angle offset. We will come back to this issue in section 5.2.2.4.

The Mueller matrix of an AHP, being composed of more than one birefringent layer, cannot be adequately described by the four parameters in Eq. (5.6). Instead, the transfer matrix method (TMM) can be used to generate an appropriate Mueller matrix. The TMM formalism captures the response of materials that are composed of any collection of dielectric and birefringent media. For the work presented here, we use the publicly available

code described in [134] to calculate the Mueller matrices of the HWPs that we study.²

5.2.1.2 Data model

We model the TOD of a single incoherent detector of a CMB polarimeter as follows:

$$d_t = \int d\nu F(\nu) \int d\Omega(\hat{\mathbf{n}}) I_{\text{tot}}^{(t)}(\hat{\mathbf{n}}, \nu) + n_t. \quad (5.7)$$

Since a incoherent detector is only sensitive to total intensity, the signal incident on the detector $I_{\text{tot}}^{(t)}$ depends on the Stokes vector of the sky \mathbf{S}_{sky} , but it is a scalar quantity. The signal is time-varying, the index t runs over the number of recorded time samples. The frequency passband of the detector and the additive noise are denoted by $F(\nu)$ and n_t respectively.

To describe how the polarisation of the sky couples to the instrument, we express $I_{\text{tot}}^{(t)}$ in terms of the trace of the product of two density matrices: one that describes the polarisation state of the sky \mathbf{W}_{sky} and one time-varying density matrix $\mathbf{W}_{\text{instr}}^{(t)}$ that describes the instrumental response on the sky [141, 142, 143]:

$$I_{\text{tot}}^{(t)}(\hat{\mathbf{n}}, \nu) = 2 \text{Tr} \left(\mathbf{W}_{\text{instr}}^{(t)} \mathbf{W}_{\text{sky}} \right) (\hat{\mathbf{n}}, \nu). \quad (5.8)$$

The density matrices are rank 2 tensor fields defined on the sphere that contain the same polarisation state information as the Stokes vectors. In fact, it is possible to express a density matrix \mathbf{W} in terms of a Stokes vector $S^\mu = \{I, Q, U, V\}$ using

$$\mathbf{W}(\hat{\mathbf{n}}, \nu) = S^\mu(\hat{\mathbf{n}}, \nu) \boldsymbol{\sigma}_\mu(\hat{\mathbf{n}}), \quad (5.9)$$

where $\boldsymbol{\sigma}_\mu$ is given by the identity matrix and the (permuted) Pauli matrices defined on the sphere: $\boldsymbol{\sigma}_\mu = \{\boldsymbol{\sigma}_0, \boldsymbol{\sigma}_3, \boldsymbol{\sigma}_1, \boldsymbol{\sigma}_2\}$, with:

$$(\sigma_0)_{ij} = \begin{pmatrix} 1 & 0 \\ 0 & \sin^2 \theta \end{pmatrix}, \quad (5.10)$$

$$(\sigma_3)_{ij} = \begin{pmatrix} 1 & 0 \\ 0 & -\sin^2 \theta \end{pmatrix}, \quad (5.11)$$

$$(\sigma_1)_{ij} = \begin{pmatrix} 0 & \sin \theta \\ \sin \theta & 0 \end{pmatrix}, \quad (5.12)$$

$$(\sigma_2)_{ij} = \begin{pmatrix} 0 & -i \sin \theta \\ i \sin \theta & 0 \end{pmatrix}. \quad (5.13)$$

²https://github.com/tomessingerhileman/birefringent_transfer_matrix

The additional factors of $\sin \theta$ compared to the standard Pauli matrices are a consequence of the metric of the assumed spherical coordinates: $g_{ij} = \text{diag}(1, \sin^2 \theta)$. The tensor nature of the polarisation state is explicit in the density matrix formulation, it is implicit in the Stokes vector formulation. Using the standard spherical coordinate system, the elements of the sky density matrix are given by

$$\left(W_{\text{sky}}\right)_{ij}(\hat{\mathbf{n}}, \nu) = \frac{1}{2} \begin{pmatrix} I + Q & (U - iV) \sin \theta \\ (U + iV) \sin \theta & (I - Q) \sin^2 \theta \end{pmatrix}(\hat{\mathbf{n}}, \nu). \quad (5.14)$$

While the time-dependent instrumental density matrix is similarly expressed as

$$\begin{aligned} \left(W_{\text{instr}}^{(t)}\right)_{ij}(\hat{\mathbf{n}}, \nu) = \\ \frac{1}{2} \begin{pmatrix} \tilde{I}_i^{(t)} + \tilde{Q}_i^{(t)} & \left(\tilde{U}_i^{(t)} - i\tilde{V}_i^{(t)}\right) \sin \theta \\ \left(\tilde{U}_i^{(t)} + i\tilde{V}_i^{(t)}\right) \sin \theta & \left(\tilde{I}_i^{(t)} - \tilde{Q}_i^{(t)}\right) \sin^2 \theta \end{pmatrix}(\hat{\mathbf{n}}, \nu), \end{aligned} \quad (5.15)$$

where we have used a tilde to distinguish these Stokes parameters from those of the sky. The t and i indices denote that the parameters are time dependent and correspond to the instrument (i.e. the combination of beam and HWP), respectively.

Both density matrices in Eq. (5.8) are defined with respect to the same coordinate basis that is fixed relative to the sky. As a result, the instrumental density matrix $\mathbf{W}_{\text{instr}}^{(t)}$ is time dependent due to the continuous rotation of the instrument with respect to the sky (another time dependence is due to the HWP rotation, which is kept implicit for now). This time dependence can be factored out by considering the instrumental density matrix in a coordinate system fixed relative to the instrument. Let us denote the density matrix in the instrument frame by $\mathbf{W}_{\text{instr}}^{(0)}$. The two frames are connected by a 3D rotation \mathbf{R}_t that we define as the rotation that would align the instrument frame to the frame fixed relative to the sky. We can thus perform an active rotation of the $\mathbf{W}_{\text{instr}}^{(0)}$ tensor by \mathbf{R}_t to get back $\mathbf{W}_{\text{instr}}^{(t)}$:

$$\begin{aligned} \left(W_{\text{instr}}^{(0)}\right)_{ij}(\hat{\mathbf{n}}, \nu) &\mapsto \left(W_{\text{instr}}^{(t)}\right)_{ij}(\hat{\mathbf{n}}, \nu) \\ &= \Lambda_i^k(\mathbf{R}_t) \Lambda_j^l(\mathbf{R}_t) \left(W_{\text{instr}}^{(0)}\right)_{kl}(\mathbf{R}_t^{-1} \hat{\mathbf{n}}, \nu). \end{aligned} \quad (5.16)$$

The Λ matrices are matrix representations of the 3D rotation \mathbf{R}_t that rotates the vector $\hat{\mathbf{n}}$ from the instrument frame to the frame fixed on the sky [144].

The 3D rotation from the instrument frame to the sky frame can be parameterized using 3 time-dependent Euler angles:

$$\mathbf{R}_t = \mathbf{R}(\psi_t, \theta_t, \phi_t). \quad (5.17)$$

The ψ_t , θ_t , and ϕ_t angles quantify right-handed rotation around the three axes of 3D Cartesian coordinate frame, namely X, Y, and Z. Note that in such frame the Z axis point towards the centre of the instrumental response, i.e. the beam centre. The 3D rotation is then achieved by a sequence of 3 right-handed rotations.

Under the rotation \mathbf{R}_t the $\mathbf{W}_{\text{instr}}^{(0)}$ tensor transforms as Eq. (5.16). While it is possible to evaluate the transformation directly, we follow [144, 145] and perform it in the spherical harmonic domain instead. In order to derive the harmonic-domain version of the data model, we start expressing the data model in terms of the Stokes parameters of the instrument and the sky by inserting Eq. (5.8) in Eq. (5.7):

$$d_t = \int d\nu F(\nu) \int d\Omega(\hat{\mathbf{n}}) \left(I\tilde{I}_i^{(t)} + Q\tilde{Q}_i^{(t)} + U\tilde{U}_i^{(t)} + V\tilde{V}_i^{(t)} \right) (\hat{\mathbf{n}}, \nu). \quad (5.18)$$

Note that we omit the noise term for brevity. The instrumental Stokes parameters in the above equation are defined in a basis fixed to the sky and thus change continuously as the telescope scans over the sky. In this derivation we will however first express the data model in the harmonic domain before performing the transformation between sky and instrument coordinate frame is given by Eq. (5.16)

By working in the harmonic domain we can make use of the fact that a generic set of spin-weighted spherical harmonic (SWSH) coefficients $f_{\ell m}^{(0)}$ defined with respect to the coordinate basis fixed to the instrument transform as follows:

$$f_{\ell m}^{(0)} \mapsto f_{\ell m}^{(t)} = \sqrt{\frac{4\pi}{2\ell+1}} \sum_{s=-\ell}^{\ell} f_{\ell s}^{(0)} {}_s Y_{\ell-m}(\theta_t, \phi_t) e^{-is\psi_t}, \quad (5.19)$$

when we instead define the coefficients with respect to the coordinate frame fixed relative to the sky. Here ${}_s Y_{\ell m}$ is a spin- s spherical harmonic [146, 147].

In a manner similar to [148], we do not directly work with the Q and U Stokes parameters. We find it more convenient to work with the complex field $P \equiv Q + iU$ and its complex conjugate, as these quantities transform under the spin-weighted representations of the rotation group (see e.g. [73]).

To make use of Eq. (5.19) it is necessary to know the SWSH coefficients for each of the different Stokes parameters in Eq. (5.18). Using the transformation rule for the density matrix in Eq. (5.16), we may illustrate why $\tilde{I}_i^{(t)}$, and $\tilde{V}_i^{(t)}$ should be expanded into regular (spin-0) spherical harmonics and why

$$\tilde{P}_i^{(t)} = \tilde{Q}_i^{(t)} + i\tilde{U}_i^{(t)}, \quad (5.20)$$

ought to be expanded in spin-2 spherical harmonics. We note that the Λ matrices in Eq. (5.16) generally depend on the ψ_t , θ_t , and ϕ_t angles that describe \mathbf{R}_t but that in the case where \mathbf{R}_t describes a right-handed rotation around $\hat{\mathbf{n}}$ by an angle ψ_t the matrices are simply given by

$$\Lambda_i^j(\mathbf{R}_{\hat{\mathbf{n}}}(\psi_t)) = \begin{pmatrix} \cos \psi_t & \sin \psi_t \\ -\sin \psi_t & \cos \psi_t \end{pmatrix}. \quad (5.21)$$

It is straightforward to check that when this specific rotation is applied to $\mathbf{W}_{\text{instr}}^{(t)}$, the $\tilde{I}_i^{(t)}$ and $\tilde{V}_i^{(t)}$ elements remain invariant, while the elements of the symmetric trace-free part, $\tilde{Q}_i^{(t)}$ and $\tilde{U}_i^{(t)}$, transform as a spin-2 field:

$$\left(\tilde{Q}_i^{(t)} \pm i\tilde{U}_i^{(t)}\right)(\hat{\mathbf{n}}) \mapsto e^{\mp 2i\psi_t} \left(\tilde{Q}_i^{(t)} \pm i\tilde{U}_i^{(t)}\right)(\hat{\mathbf{n}}). \quad (5.22)$$

We now expand the instrumental Stokes parameters into the appropriate spin-weighted spherical harmonics:

$$\tilde{I}_i^{(t)}(\hat{\mathbf{n}}, \nu, \alpha_t) = \sum_{\ell=0}^{\ell_{\max}} \sum_{m=-\ell}^{\ell} b_{\ell m}^{\tilde{I}_i^{(t)}}(\nu, \alpha_t) Y_{\ell m}(\hat{\mathbf{n}}), \quad (5.23)$$

$$\tilde{P}_i^{(t)}(\hat{\mathbf{n}}, \nu, \alpha_t) = \sum_{\ell=2}^{\ell_{\max}} \sum_{m=-\ell}^{\ell} {}_2b_{\ell m}^{\tilde{P}_i^{(t)}}(\nu, \alpha_t) {}_2Y_{\ell m}(\hat{\mathbf{n}}), \quad (5.24)$$

$$\tilde{V}_i^{(t)}(\hat{\mathbf{n}}, \nu, \alpha_t) = \sum_{\ell=0}^{\ell_{\max}} \sum_{m=-\ell}^{\ell} b_{\ell m}^{\tilde{V}_i^{(t)}}(\nu, \alpha_t) Y_{\ell m}(\hat{\mathbf{n}}). \quad (5.25)$$

The Stokes parameters of the sky are expanded in a similar manner:

$$I(\hat{\mathbf{n}}, \nu) = \sum_{\ell=0}^{\ell_{\max}} \sum_{m=-\ell}^{\ell} a_{\ell m}^I(\nu) Y_{\ell m}(\hat{\mathbf{n}}), \quad (5.26)$$

$$P(\hat{\mathbf{n}}, \nu) = \sum_{\ell=2}^{\ell_{\max}} \sum_{m=-\ell}^{\ell} {}_2a_{\ell m}^P(\nu) {}_2Y_{\ell m}(\hat{\mathbf{n}}), \quad (5.27)$$

$$V(\hat{\mathbf{n}}, \nu) = \sum_{\ell=0}^{\ell_{\max}} \sum_{m=-\ell}^{\ell} a_{\ell m}^V(\nu) Y_{\ell m}(\hat{\mathbf{n}}), \quad (5.28)$$

The different b coefficients are spin-weighted spherical harmonic (SWSH) coefficients that describe $\mathbf{W}_{\text{instr}}^{(0)}$, while the different a SWSH coefficients correspond to \mathbf{W}_{sky} . The sum over ℓ runs from 0 to the harmonic band-limit of the beams: ℓ_{\max} , while the sums over m run from $-\ell$ to ℓ .

We insert Eqs. (5.23)-(5.28) into Eq. (5.18) to produce the following version of the data model:

$$d_t = \int d\nu F(\nu) \sum_{\ell=0}^{\ell_{\max}} \sum_{m=-\ell}^{\ell} \left\{ \left[b_{\ell m}^{\tilde{I}_i^{(t)}}(\nu, \alpha_t) \right]^* a_{\ell m}^I(\nu) \right. \\ \left. + \text{Re} \left(\left[{}_2b_{\ell m}^{\tilde{P}_i^{(t)}}(\nu, \alpha_t) \right]^* {}_2a_{\ell m}^P(\nu) \right) + \left[b_{\ell m}^{\tilde{V}_i^{(t)}}(\nu, \alpha_t) \right]^* a_{\ell m}^V(\nu) \right\}. \quad (5.29)$$

To obtain this expression, we have made use of the orthogonality of the spin-weighted spherical harmonics:

$$\int_{S^2} d\Omega(\hat{\mathbf{n}}) {}_s Y_{\ell m}(\hat{\mathbf{n}}) {}_s Y_{\ell' m'}^*(\hat{\mathbf{n}}) = \delta_{\ell, \ell'} \delta_{m, m'}. \quad (5.30)$$

Note that the $b_{\ell m}^{\tilde{I}_i^{(t)}}$, ${}_2 b_{\ell m}^{\tilde{P}_i^{(t)}}$, and $b_{\ell m}^{\tilde{V}_i^{(t)}}$ coefficients in Eq. (5.29) are still defined on the basis fixed to the sky, so they are time dependent (they change as the telescope scans over the sky). We may now use Eq. (5.19) to relate these time-varying coefficients to those defined with respect to the coordinate frame fixed to the instrument. Under the rotation \mathbf{R}_t the following relationships hold:

$$\begin{aligned} b_{\ell m}^{\tilde{I}_i^{(0)}}(\alpha_t) &\mapsto b_{\ell m}^{\tilde{I}_i^{(t)}}(\alpha_t) \\ &= q_\ell \sum_{s=-\ell}^{\ell} b_{\ell s}^{\tilde{I}_i^{(0)}}(\alpha_t) {}_s Y_{\ell-m}(\theta_t, \phi_t) e^{-is\psi_t}, \end{aligned} \quad (5.31)$$

$$\begin{aligned} {}_2 b_{\ell m}^{\tilde{P}_i^{(0)}}(\alpha_t) &\mapsto {}_2 b_{\ell m}^{\tilde{P}_i^{(t)}}(\alpha_t) \\ &= q_\ell \sum_{s=-\ell}^{\ell} {}_2 b_{\ell s}^{\tilde{P}_i^{(0)}}(\alpha_t) {}_s Y_{\ell-m}(\theta_t, \phi_t) e^{-is\psi_t}, \end{aligned} \quad (5.32)$$

$$\begin{aligned} b_{\ell m}^{\tilde{V}_i^{(0)}}(\alpha_t) &\mapsto b_{\ell m}^{\tilde{V}_i^{(t)}}(\alpha_t) \\ &= q_\ell \sum_{s=-\ell}^{\ell} b_{\ell s}^{\tilde{V}_i^{(0)}}(\alpha_t) {}_s Y_{\ell-m}(\theta_t, \phi_t) e^{-is\psi_t}, \end{aligned} \quad (5.33)$$

where we have defined the shorthand:

$$q_\ell \equiv \sqrt{\frac{4\pi}{2\ell+1}}. \quad (5.34)$$

Inserting the above equation into Eq. (5.29) yields the final expression for the data model in the harmonic domain:

$$\begin{aligned} d_t &= \int d\nu F(\nu) \sum_{\ell, m, s} \left\{ b_{\ell s}^{\tilde{I}_i^{(0)}}(\nu, \alpha_t) a_{\ell m}^I(\nu) + b_{\ell s}^{\tilde{V}_i^{(0)}}(\nu, \alpha_t) a_{\ell m}^V(\nu) \right. \\ &\quad \left. + \frac{1}{2} \left[-{}_2 b_{\ell s}^{\tilde{P}_i^{(0)}}(\nu, \alpha_t) {}_2 a_{\ell m}^P(\nu) + {}_2 b_{\ell s}^{\tilde{P}_i^{(0)}}(\nu, \alpha_t) {}_{-2} a_{\ell m}^P(\nu) \right] \right\} \\ &\quad \times \sqrt{\frac{4\pi}{2\ell+1}} e^{-is\psi_t} {}_s Y_{\ell m}(\theta_t, \phi_t) + n_t, \end{aligned} \quad (5.35)$$

where the sum over ℓ runs from 0 to the harmonic band-limit of the beams ℓ_{\max} , while the sums over m and s run from $-\ell$ to ℓ . It should be noted that

the sum over s can be truncated drastically for an approximately symmetric instrumental response. For perfectly symmetric beams only $s = 0$ and $s = \pm 2$ are needed for the $\tilde{I}_i^{(0)}$, $\tilde{V}_i^{(0)}$; and $\tilde{P}_i^{(0)}$ coefficients, respectively [144, 143]. The expression matches that of a general CMB polarimeter derived in [144], but is generalized to have an explicit dependency on frequency and on the HWP rotation angle α_t .

The b harmonic coefficients that describe the instrument in Eq. (5.35) are given by combinations of the Stokes parameters of the beam, denoted in the following with the subscript b , and the elements of the HWP Mueller matrix. To derive their expressions, we have assumed that the instrumental Stokes vector, which is related to $\mathbf{W}_{\text{instr}}^{(0)}$ by Eq. (5.9), can be factorised into a Stokes vector describing the beam and a Mueller matrix describing the skywards HWP:

$$\mathbf{S}_{\text{instr}}^{(0)\text{T}}(\hat{\mathbf{n}}, \nu, \alpha_t, \vartheta_{\text{inc}}) = \mathbf{S}_{\text{beam}}^{(0)\text{T}}(\hat{\mathbf{n}}, \nu) \mathbf{M}_{\text{HWP}}(\nu, \alpha_t, \vartheta_{\text{inc}}). \quad (5.36)$$

The Stokes vector describing the beam has an angular dependence that describes the finite resolution of the experiment, but it is constant with time. On the other hand, the Mueller matrix of the HWP depends on the time-varying HWP angle α_t but it is assumed to have no angular dependence. Note that the Mueller matrix varies between detectors based on their position on the focal plane (see Figure 5.1). This dependence on detector incidence angle is captured by the ϑ_{inc} parameter and it will be kept implicit in the following. The factorisation of the beam and HWP response in Eq. (5.36) is an approximation, valid when the radiation in between the HWP and the beam-forming optical elements is described by plane waves propagating along $\hat{\mathbf{n}}$. We expect that our approximation describes the interaction between the HWP and the beam sufficiently well for our aims.

We start by rewriting Eq. (5.36) as follows:

$$\mathbf{S}_{\text{instr}}^{(0)\text{T}}(\hat{\mathbf{n}}, \nu, \alpha_t) \mathbf{T}^\dagger = \mathbf{S}_{\text{beam}}^{(0)\text{T}}(\hat{\mathbf{n}}, \nu) \mathbf{T}^\dagger \mathbf{T} \mathbf{M}_{\text{HWP}}(\nu, \alpha_t) \mathbf{T}^\dagger, \quad (5.37)$$

where we have introduced the following complex transformation matrix:

$$\mathbf{T} = \begin{pmatrix} 1 & 0 & 0 & 0 \\ 0 & \frac{1}{\sqrt{2}} & \frac{i}{\sqrt{2}} & 0 \\ 0 & \frac{1}{\sqrt{2}} & \frac{-i}{\sqrt{2}} & 0 \\ 0 & 0 & 0 & 1 \end{pmatrix}, \quad (5.38)$$

that should be understood as transforming the real Stokes parameter basis to a complex basis spanned by I , $(Q + iU)/\sqrt{2}$, $(Q - iU)/\sqrt{2}$ and V . Note

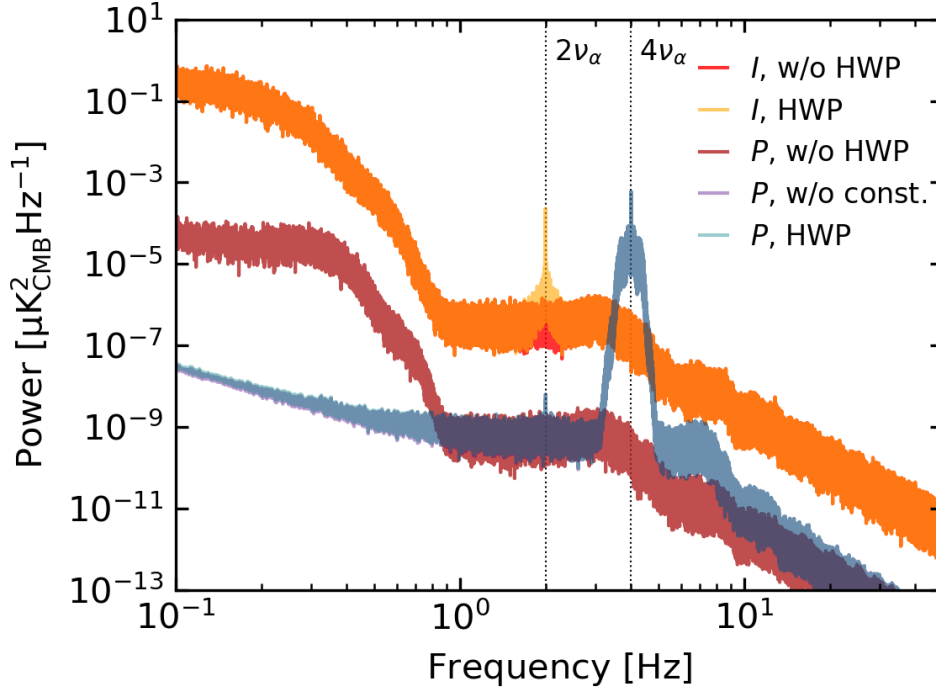


Figure 5.2: Power spectral densities (PSDs) corresponding to a typical two-hour segment of noiseless time-ordered data for a single detector. The curves labelled I (P) correspond to scans over an I -only ((Q, U) -only) simulated CMB sky. The curves labelled HWP include HWP modulation using the three-layer BR3 HWP configuration (to be discussed in section 5.2.2) spinning at a frequency ν_α of 1 Hz. The curve labelled P , w/o const. (overlapping with P , HWP but it slightly different below ~ 2 Hz) incorporates the same HWP modulation, but does not include the HWP systematic that is constant with HWP angle α , see Eq. (5.53). The curves labelled w/o HWP do not include HWP modulation. The simulated data are recorded at a monochromatic frequency of 90 GHz using a gaussian beam with a FWHM of $32.2'$. Each curve is the average of ten PSDs corresponding to successive two-hour scans. The scan strategy is described in section 5.2.2.1. Figure taken from: [51]

that \mathbf{T} is unitary, i.e. $\mathbf{T}^\dagger \mathbf{T} = \mathbf{T} \mathbf{T}^\dagger = \mathbf{1}$. Next, we factor the rotated HWP Mueller matrix into the unrotated matrix and two Mueller rotation matrices:

$$\mathbf{M}_{\text{HWP}}(\alpha) = \mathbf{M}_\alpha^\top \mathbf{M}_{\text{HWP}} \mathbf{M}_\alpha, \quad (5.39)$$

with:

$$\mathbf{M}_\alpha = \begin{pmatrix} 1 & 0 & 0 & 0 \\ 0 & \cos 2\alpha & \sin 2\alpha & 0 \\ 0 & -\sin 2\alpha & \cos 2\alpha & 0 \\ 0 & 0 & 0 & 1 \end{pmatrix}. \quad (5.40)$$

Note that the \mathbf{T} matrix diagonalizes the rotation matrix:

$$\mathbf{T} \mathbf{M}_\alpha \mathbf{T}^\dagger = \begin{pmatrix} 1 & 0 & 0 & 0 \\ 0 & e^{-2i\alpha} & 0 & 0 \\ 0 & 0 & e^{2i\alpha} & 0 \\ 0 & 0 & 0 & 1 \end{pmatrix}. \quad (5.41)$$

Putting everything together yields:

$$\mathbf{S}_{\text{instr}}^{(0)\top}(\hat{\mathbf{n}}, \nu, \alpha_t) \mathbf{T}^\dagger = \mathbf{S}_{\text{beam}}^{(0)\top}(\hat{\mathbf{n}}, \nu) \mathbf{T}^\dagger \mathbf{T} \mathbf{M}_\alpha^\top \mathbf{T}^\dagger \mathbf{T} \mathbf{M}_{\text{HWP}}(\nu) \mathbf{T}^\dagger \mathbf{T} \mathbf{M}_\alpha \mathbf{T}^\dagger. \quad (5.42)$$

Evaluating this expression provides us with the instrumental Stokes parameters in terms of the beam Stokes parameters and the HWP:

$$\begin{aligned} \tilde{I}_i^{(0)}(\hat{\mathbf{n}}, \alpha_t, \nu) &= \tilde{I}_b^{(0)}(\hat{\mathbf{n}}, \nu) C_{IV}(\nu) + \tilde{V}_b^{(0)}(\hat{\mathbf{n}}, \nu) C_{VV}(\nu) \\ &\quad + \sqrt{2} \text{Re} \left(\tilde{P}_b^{(0)}(\hat{\mathbf{n}}, \nu) C_{P^*V}(\nu) e^{-2i\alpha} \right), \end{aligned} \quad (5.43)$$

$$\begin{aligned} \tilde{P}_i^{(0)}(\hat{\mathbf{n}}, \alpha, \nu) &= \tilde{I}_b^{(0)}(\hat{\mathbf{n}}, \nu) C_{IP}(\nu) \sqrt{2} e^{-2i\alpha} \\ &\quad + \tilde{V}_b^{(0)}(\hat{\mathbf{n}}, \nu) C_{VP}(\nu) \sqrt{2} e^{-2i\alpha} \\ &\quad + \tilde{P}_b^{(0)}(\hat{\mathbf{n}}, \nu) C_{P^*P}(\nu) e^{-4i\alpha} \\ &\quad + \tilde{P}_b^{(0)*}(\hat{\mathbf{n}}, \nu) C_{PP}(\nu), \end{aligned} \quad (5.44)$$

$$\begin{aligned} \tilde{V}_i^{(0)}(\hat{\mathbf{n}}, \alpha, \nu) &= \tilde{I}_b^{(0)}(\hat{\mathbf{n}}, \nu) C_{IV}(\nu) + \tilde{V}_b^{(0)}(\hat{\mathbf{n}}, \nu) C_{VV}(\nu) \\ &\quad + \sqrt{2} \text{Re} \left(\tilde{P}_b^{(0)}(\hat{\mathbf{n}}, \nu) C_{P^*V}(\nu) e^{-2i\alpha} \right), \end{aligned} \quad (5.45)$$

where:

$$\tilde{P}_i^{(0)} = \tilde{Q}_i^{(0)} + i \tilde{U}_i^{(0)}, \quad (5.46)$$

Note that in Eqs. (5.43)-(5.45) we have used the following shorthand for the unrotated HWP Mueller matrix expressed in the complex basis:

$$\mathbf{C} = \mathbf{T}\mathbf{M}_{\text{HWP}}\mathbf{T}^\dagger, \quad (5.47)$$

that, in terms of the original HWP Mueller matrix elements, is given by:

$$\mathbf{C} = \begin{pmatrix} M_{II} & \frac{M_{IQ}-iM_{IU}}{\sqrt{2}} \\ \frac{M_{QI}+iM_{UI}}{\sqrt{2}} & \frac{M_{QQ}+M_{UU}-i(M_{QU}-M_{UQ})}{2} \\ \frac{M_{QI}-iM_{UI}}{\sqrt{2}} & \frac{M_{QQ}-M_{UU}-i(M_{QU}+M_{UQ})}{2} \\ M_{VI} & \frac{M_{VQ}-iM_{VU}}{\sqrt{2}} \\ \frac{M_{IQ}+iM_{IU}}{\sqrt{2}} & M_{IV} \\ \frac{M_{QQ}-M_{UU}+i(M_{QU}+M_{UQ})}{2} & \frac{M_{QV}+iM_{UV}}{\sqrt{2}} \\ \frac{M_{QQ}+M_{UU}+i(M_{QU}-M_{UQ})}{2} & \frac{M_{QV}-iM_{UV}}{\sqrt{2}} \\ \frac{(M_{VQ}+iM_{VU})}{\sqrt{2}} & M_{VV} \end{pmatrix}. \quad (5.48)$$

Finally, we plug the instrumental Stokes parameters in Eqs. (5.43)-(5.45) into the transformations below:

$$b_{\ell m}^{\tilde{I}_i^{(0)}}(\nu) = \int_{S^2} d\Omega(\hat{\mathbf{n}}) \tilde{I}_i^{(0)}(\hat{\mathbf{n}}, \alpha_t, \nu) Y_{\ell m}^*(\hat{\mathbf{n}}), \quad (5.49)$$

$${}_2b_{\ell m}^{\tilde{P}_i^{(0)}}(\nu) = \int_{S^2} d\Omega(\hat{\mathbf{n}}) \tilde{P}_i^{(0)}(\hat{\mathbf{n}}, \alpha_t, \nu) {}_2Y_{\ell m}^*(\hat{\mathbf{n}}), \quad (5.50)$$

$$b_{\ell m}^{\tilde{V}_i^{(0)}}(\nu) = \int_{S^2} d\Omega(\hat{\mathbf{n}}) \tilde{V}_i^{(0)}(\hat{\mathbf{n}}, \alpha_t, \nu) Y_{\ell m}^*, \quad (5.51)$$

to obtain the harmonic coefficients that describe the instrumental response in Eq. (5.35). We find that:

$$\begin{aligned} b_{\ell s}^{\tilde{I}_i^{(0)}}(\nu, \alpha) &= \int_{S^2} d\Omega(\hat{\mathbf{n}}) \left[\tilde{I}_b^{(0)}(\hat{\mathbf{n}}, \nu) C_{II}(\nu) \right. \\ &\quad \left. + \tilde{V}_b^{(0)}(\hat{\mathbf{n}}, \nu) C_{VI}(\nu) \right. \\ &\quad \left. + \sqrt{2} \operatorname{Re} \left(\tilde{P}_b^{(0)}(\hat{\mathbf{n}}, \nu) C_{P^*I}(\nu) e^{-2i\alpha} \right) \right] Y_{\ell s}^*(\hat{\mathbf{n}}), \end{aligned} \quad (5.52)$$

$$\begin{aligned} {}_2b_{\ell s}^{\tilde{P}_i^{(0)}}(\nu, \alpha) &= \int_{S^2} d\Omega(\hat{\mathbf{n}}) \left[\tilde{I}_b^{(0)}(\hat{\mathbf{n}}, \nu) C_{IP}(\nu) \sqrt{2} e^{-2i\alpha} \right. \\ &\quad \left. + \tilde{V}_b^{(0)}(\hat{\mathbf{n}}, \nu) C_{VP}(\nu) \sqrt{2} e^{-2i\alpha} \right. \\ &\quad \left. + \tilde{P}_b^{(0)}(\hat{\mathbf{n}}, \nu) C_{P^*P}(\nu) e^{-4i\alpha} \right. \\ &\quad \left. + \tilde{P}_b^{(0)*}(\hat{\mathbf{n}}, \nu) C_{PP}(\nu) \right] {}_2Y_{\ell s}^*(\hat{\mathbf{n}}), \end{aligned} \quad (5.53)$$

$$\begin{aligned}
b_{\ell s}^{\tilde{V}_i^{(0)}}(\nu, \alpha) &= \int_{S^2} d\Omega(\hat{\mathbf{n}}) \left[\tilde{I}_b^{(0)}(\hat{\mathbf{n}}, \nu) C_{IV}(\nu) \right. \\
&\quad + \tilde{V}_b^{(0)}(\hat{\mathbf{n}}, \nu) C_{VV}(\nu) \\
&\quad \left. + \sqrt{2} \operatorname{Re} \left(\tilde{P}_b^{(0)}(\hat{\mathbf{n}}, \nu) C_{P^*V}(\nu) e^{-2i\alpha} \right) \right] Y_{\ell s}^*(\hat{\mathbf{n}}).
\end{aligned} \tag{5.54}$$

The elements of the **C** HWP matrix are given in Eq. (5.48). Note that the ${}_{-2}b_{\ell s}$ coefficients can be obtained using the following symmetry relation:

$${}_{-2}b_{\ell s}^{\tilde{P}_i^{(0)}}(\alpha) = \left[{}_2b_{\ell -s}^{\tilde{P}_i^{(0)}}(\alpha) \right]^* (-1)^s. \tag{5.55}$$

The harmonic coefficients that represent the Stokes parameters of the sky in Eq. (5.35) are given by

$$a_{\ell m}^I(\nu) = \int_{S^2} d\Omega(\hat{\mathbf{n}}) I(\hat{\mathbf{n}}, \nu) Y_{\ell m}^*(\hat{\mathbf{n}}), \tag{5.56}$$

$$\pm 2a_{\ell m}^P(\nu) = \int_{S^2} d\Omega(\hat{\mathbf{n}}) (Q \pm iU)(\hat{\mathbf{n}}, \nu) \pm 2Y_{\ell m}^*(\hat{\mathbf{n}}), \tag{5.57}$$

$$a_{\ell m}^V(\nu) = \int_{S^2} d\Omega(\hat{\mathbf{n}}) V(\hat{\mathbf{n}}, \nu) Y_{\ell m}^*(\hat{\mathbf{n}}). \tag{5.58}$$

Figure 5.2 helps to qualify the rather verbose expressions for the above harmonic coefficients. It illustrates the effect of a non-ideal HWP on the time-ordered data by comparing the corresponding power spectrum densities for two cases: without an HWP and with a non-ideal HWP (see section 5.2.2.3). Recall that ideal HWP modulation will only modulate the Q and U sky signal, which it will do at a modulation frequency $4\nu_\alpha$, where ν_α is the HWP rotation frequency. It can be seen that the non-ideal HWP introduces an additional spurious $2\nu_\alpha$ modulation of the I sky (second line of Eq. (5.52)), a $2\nu_\alpha$ modulation of the Q and U skies (first and second lines of Eq. (5.53)) and a $2\nu_\alpha$ modulation of the V sky (second line of Eq. (5.54), not shown in the figure). Finally, the non-ideal HWP also introduces a spurious constant $0\nu_\alpha$ modulation of the Q and U skies (fourth line of Eq. (5.53)). Note that Figure 5.2 omits the case of an input V sky. The ν_α dependence of the V -input case will be the same, qualitatively, as the Stokes I -input case.

The dependence on HWP angle α of the different terms in the data model is relevant because this dependence is used by the subsequent map-making procedure to distinguish between I , Q , U , (and possibly V) sky signals. Leakage between the Stokes parameters will occur when the data model used by the map-maker does not capture the full α modulation of the time-ordered data. For the experimental configuration considered in this work, see section 5.2.2, we find that the $I \rightarrow (Q, U)$ leakage that is caused by ignoring

the $2\nu_\alpha$ terms during map-making is subdominant to the $Q \leftrightarrow U$ leakage that is caused by ignoring non-idealities in the $4\nu_\alpha$ term.

The data model described by Eqs. (5.35)-(5.58) is now implemented in the `beamconv` library. The frequency dependence of the model is handled by approximating the integral over the instrumental frequency band with a small number ($n_\nu = 7$ for the results in section 5.2.3) of monochromatic input skies, beams and HWP Mueller matrices. The memory costs and computational scaling of the algorithm have thus gained a linear scaling with n_ν compared to the algorithm in [52] but they are unchanged otherwise. The algorithm allows for efficient time-domain simulations that include all-sky beam convolution with asymmetric beams and non-ideal HWPs.

5.2.2 Simulation setup

We consider a telescope similar to the one described in [52], but with a HWP in front of the primary lens. Incoming radiation passes through the HWP followed by a pair of lenses before being absorbed by the detectors on the focal plane (see Figure 5.1). A beam profile for a typical 150-GHz detector used in this analysis is shown in Figure 5.3. We model 50 dichroic detectors sensitive to two 30-GHz-wide frequency windows centred at 95 and 150 GHz. The detectors are evenly distributed on a square grid of a focal plane fed by a 30-cm aperture telescope. The field of view of this square grid is only 7° compared to the 28° that can be supported by this telescope; the detectors therefore only cover a fraction of the focal plane. The spectral response of the detectors is assumed to be represented by a top-hat function within each band. In order to test frequency-dependent effects, we run simulations at 7 sub-frequencies within a band. These sub-frequencies are 80, 85, 90, 95, 100, 105, and 110 GHz for the 95-GHz band and 135, 140, 145, 150, 155, 160, and 165 GHz for the 150-GHz band (see hatched regions in Figure 5.4).

5.2.2.1 Simulated scanning

Using the updated version of `beamconv`, we simulate one year of satellite scanning for 50 detectors. We use a similar scan strategy as in [52], which is based on [150, 151]. The satellite spins around its principal axis with a period of 600 seconds. It precesses about the boresight axis with a period of 90 minutes. The two axes are separated by 50° . We set the HWP rotation frequency ν_α to 1 Hz (angular frequency of 2π rad/s) and sample the data at 12.01 Hz. Although the sampling frequency is likely an order of magnitude below that of a real experiment, we find that this rate suffices for our noiseless simulations. The resulting angular coverage is excellent and allows

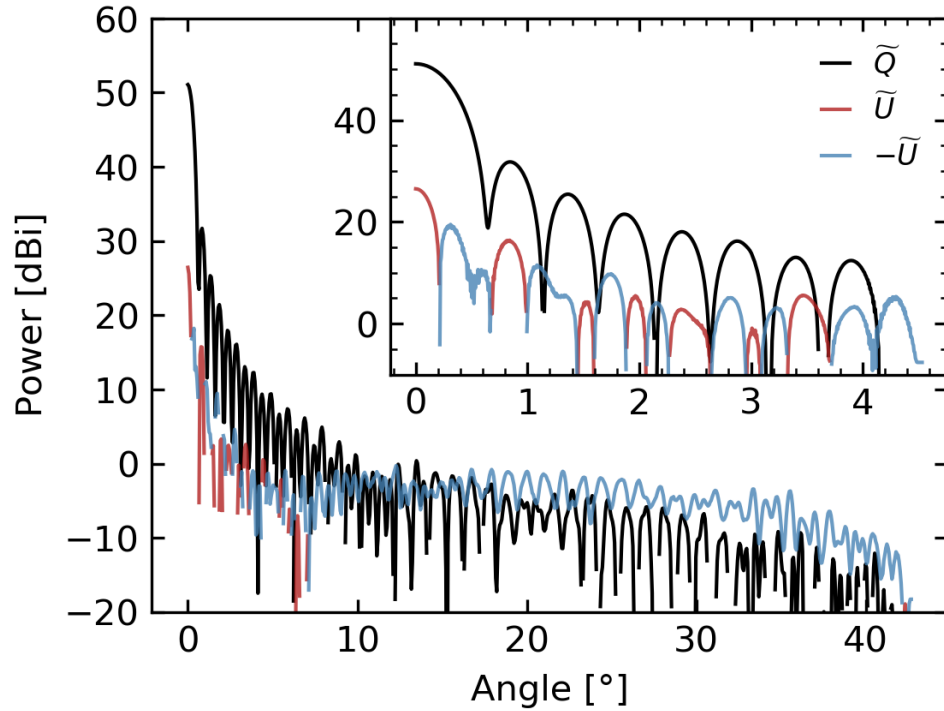


Figure 5.3: Azimuthally averaged beam profiles (dBi units) for a representative detector of one of the 50 used in this analysis. Shown are the Stokes \tilde{Q} and \tilde{U} beam components. For this figure, we have defined the Stokes parameters with respect to the Ludwig-3 basis [149]. This basis is approximately Cartesian around the beam centre and has been aligned with the polarised element of the detector. As a result, the $\pm\tilde{U}$ profile quantifies the amount of non-aligned (or “cross-polar”) polarised sensitivity of the beam. It can be seen that $|\tilde{U}|$ is subdominant close to the centre of the beam (see inset) while having a relatively large contribution at large opening angles. Figure taken from: [51]

for simultaneous per-pixel recovery of I , Q , and U over the full sky. Even without a continuously-spinning HWP, the average condition number of the per-pixel (I, Q, U) covariance matrix, which is inverted as part of the solution [52], is approximately 2.9 for a $N_{\text{side}} = 256$ map. In comparison, the condition number approaches 2.0 (the minimum value) for all pixels when the HWP is spun with a 1-Hz rotation frequency.

5.2.2.2 Input maps

We generate statistically isotropic random gaussian Stokes I , Q , and U CMB maps (with a vanishing B -mode component) using the `synfast` utility in `HEALPix`'s [91] Python implementation, `healpy`³⁴ and the best-fit 2018 *Planck* power spectra [59]. To probe how frequency-dependent HWP systematics interact with the different components of the microwave sky, we also simulate polarised Galactic dust using the Python Sky Model (`PySM`) code [152]. Other foreground sources, including synchrotron radiation, are subdominant in our 95 and 150 GHz frequency bands. `PySM` provides different templates for dust emission, all based on the high-frequency *Planck* data [153].⁵ We use six different `PySM` dust models: `d0` to `d5`. The first four models are directly based on a modified black body distribution. In units of CMB brightness temperature these models all follow the same parametrization:

$$\begin{pmatrix} Q \\ U \end{pmatrix}(\hat{\mathbf{n}}, \nu) = \begin{pmatrix} A_Q \\ A_U \end{pmatrix}(\hat{\mathbf{n}}) \times \left(\frac{\nu}{\nu_0}\right)^{\beta(\hat{\mathbf{n}})+1} \frac{e^{h\nu_0/k_B T(\hat{\mathbf{n}})} - 1}{e^{h\nu/k_B T(\hat{\mathbf{n}})} - 1}, \quad (5.59)$$

There are four parameters: the spectral index β , the dust temperature T and the $A_{Q/U}$ amplitudes at the reference frequency $\nu_0 = 353$ GHz. A brief description of each model follows, see [152] for more details.

- **d0 model** uses a fixed spectral index ($\beta = 1.54$), a fixed temperature ($T = 20$ K) and the `Commander` dust template from [154] for $A_{Q/U}$.
- **d1 model** extends the `d0` model with spatially varying spectral index and temperature that are both given by the `Commander` templates from [154].
- **d2 model** modifies the `d1` model with a spectra index that varies randomly on degree scales, following a gaussian distribution: $\beta \sim \mathcal{N}(\mu = 1.59, \sigma^2 = 0.04)$.

³<http://healpix.sf.net>

⁴<https://github.com/healpy/healpy>

⁵<https://pysm3.readthedocs.io/en/latest/>

Model	Orientation	Phase 95 GHz CMB/Dust	Phase 150 GHz CMB/Dust
BR1	0°	$0^\circ/0^\circ$	$0^\circ/0^\circ$
BR3	$\{0^\circ, 54^\circ, 0^\circ\}$	$30.75^\circ / 31.16^\circ$	$32.51^\circ / 32.30^\circ$
BR5	$\{22.9^\circ, -50^\circ, 0^\circ$ $50^\circ, -22.9^\circ\}$	$0^\circ/0^\circ$	$0^\circ/0^\circ$

Table 5.1: HWP configurations adopted for the analysis presented in this chapter. Orientation angles are those of the fast axis of the birefringent layers relative to the plane of incoming vertically polarised radiation. The rotation angle offset is given in each band following Eq. (5.60), for CMB and dust weights as defined in Eq. (5.61).

- **d3 model** is the same as **d2** except that $\beta \sim \mathcal{N}(\mu = 1.59, \sigma^2 = 0.09)$.
- **d4 model** models two dust populations as two modified black bodies with different but spatially constant spectral indices and two different spatially varying temperatures and dust amplitudes [155].
- **d5 model** is a more physically motivated model based on the physical properties of two populations of dust grains (silicate and carbonaceous) [156, 157].

The inclusion of these six models in our analysis serves to roughly bracket the current uncertainty in dust modelling. We note that the **d3** model is designed to match the largest variation in spectral index allowed by the *Planck* data. We study the interplay between the HWP non-idealities and these different foreground models in section 5.2.3.3.

5.2.2.3 Selection of HWPs

A wide range of HWP designs have been described and studied in the literature [38, 39, 130, 44, 131]. HWP design involves a complex optimization problem where absorptive and reflective losses from materials with high index of refraction need to be balanced against the desire for unity polarisation efficiency across a wide band. We choose to study three HWP configurations, which are loosely based on [44] as a model of a one layer HWP, [39] for the 3-layer HWP, and a 5-layer HWP model taken from [158]. Some key properties of these three HWP configurations, which we denote as BR1, BR3, and BR5, are shown in Table 5.1.

We adopt a fixed thickness, $d = 3.75$ mm, for the individual sapphire plate layers for all three polarisation modulators. This thickness was found

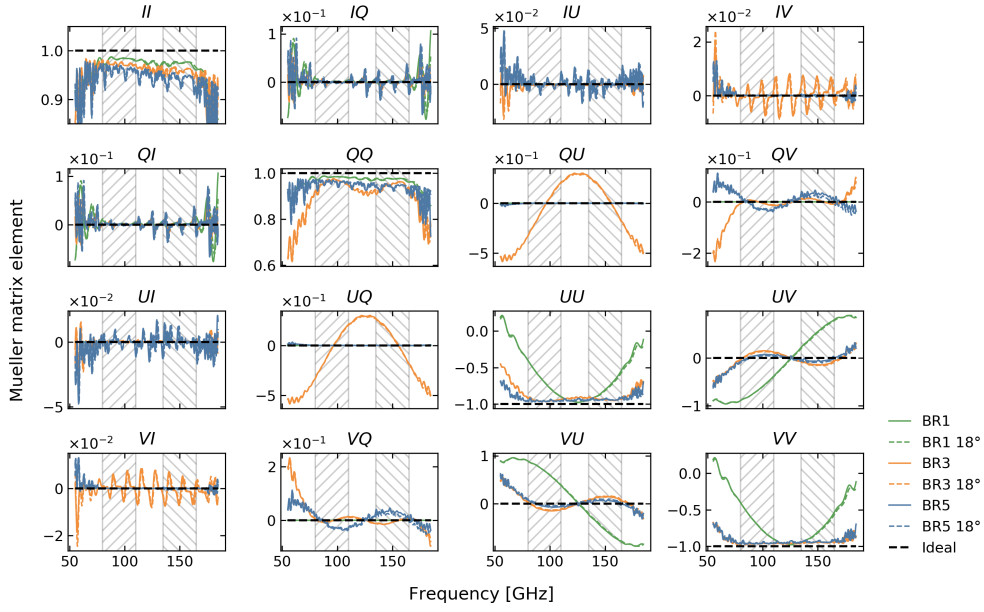


Figure 5.4: HWP Mueller matrix elements as a function of frequency in the normal incidence case (solid lines) and for an incidence angle ϑ_{inc} of 18° (dashed lines, virtually indistinguishable from solid lines) simulated using the transfer matrix method. The three HWP configurations described in Table 5.1 are shown. A 31.4° HWP rotation angle offset is applied to the 3-layer BR3 model. The black dashed line represents the ideal HWP ($T = -c = 1$, $\rho = s = 0$ in Eq. (5.6)). The grey hatched bands illustrate the two instrumental frequency bands used in this work. Figure taken from: [51]

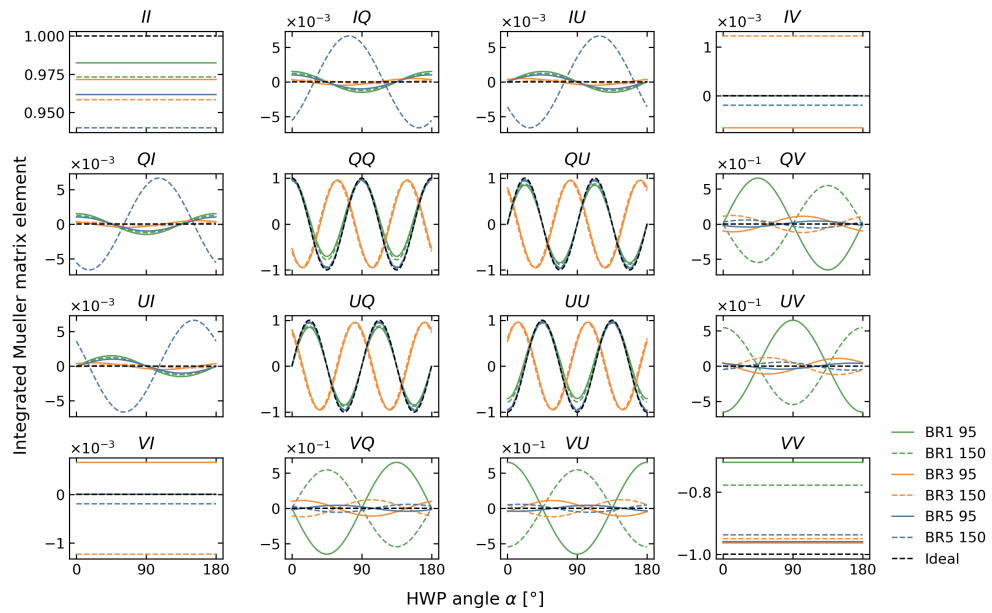


Figure 5.5: Mueller matrix elements for the three HWP models described in Table 5.1, integrated over the instrumental frequency bands (95: solid lines, 80 GHz to 110 GHz; 150: dashed lines, 135 GHz to 165 GHz) as a function of the HWP rotation angle. The dashed black lines represent the behaviour of the ideal HWP ($T = -c = 1$, $\rho = s = 0$ in Eq. (5.6)). It can be seen that the BR3 configuration (orange lines) is out of phase with the other HWP configurations. Figure taken from: [51]

using the traditional formula for half wave plates made of a single layer of birefringent material $d = c/[2\nu(n_e - n_o)]$, where n_o and n_e correspond to the index of refraction for the ordinary and extraordinary axes, respectively. The selected thickness is optimal for $\nu = 126$ GHz, near the average of our two band centres. We adopt an anti-reflection (AR) coating similar to the one described in [159] that is optimized for 75–170 GHz. We settle on three AR layers with thicknesses $d_{\text{AR}} = 0.5, 0.31, 0.257$ mm and individual indices $n_{\text{AR}} = (1.268, 1.979, 2.855)$. The above parameters are used as input to the TMM formalism to calculate the Mueller matrices of the HWPs. We produce a unique set of Mueller matrices for each unique HWP incidence angle ϑ_{inc} .

Figure 5.4 shows the Mueller matrix elements for our three HWP configurations as function of frequency. It can be seen that the additional layers of the BR3 and BR5 HWPs improve the frequency uniformity of the polarisation efficiency (see the UU elements) compared to the BR1 case. Describing the efficiency loss for the different Stokes parameters is a rather complicated task. Although the efficiency loss of Stokes I is easy to understand, as the II elements decrease in value with additional layers, the same is not true for the polarisation efficiency.⁶ Because of these complications, we do not directly use the HWP Mueller matrix elements to correct our results for the efficiency loss. As will be detailed in section 5.2.3, we settle for a more robust and simpler power-spectrum based calibration method. Such an approach will likely also be taken by a real experiment. Finally, we note that the Mueller matrix models that we use do not include systematic effects caused by non-ideal manufacturing or material non-uniformity, which are likely to exist at some non-negligible level even in next-generation experiments.

5.2.2.4 Determining the AHWP induced rotation offset

Achromatic HWPs, such as the three- and five-layer configurations discussed in this section, tend to have higher polarisation efficiency over a given frequency range compared to a single-layer HWP. However, they also introduce an undesirable frequency-dependent phase between the in-going and out-going electric field that manifests itself as a frequency-dependent HWP rotation angle offset. Figure 5.5 shows our HWP Mueller matrices, integrated over the two frequency bands, as a function of the half-wave plate angle α . From the inner two-by-two set of panels it is clear that the 3-layer HWP has

⁶The amplitude of incoming linear polarisation $\sqrt{Q^2 + U^2}$ will be changed based on the QQ , QU , UQ , UU submatrices. The change in amplitude will be bounded by the singular values of this matrix. Note that the amplitude change will generally be different per pixel and frequency. Furthermore, the input I and V signal will also alter the linear polarisation amplitude due to leakage caused by the QI , UI , QV and UV terms.

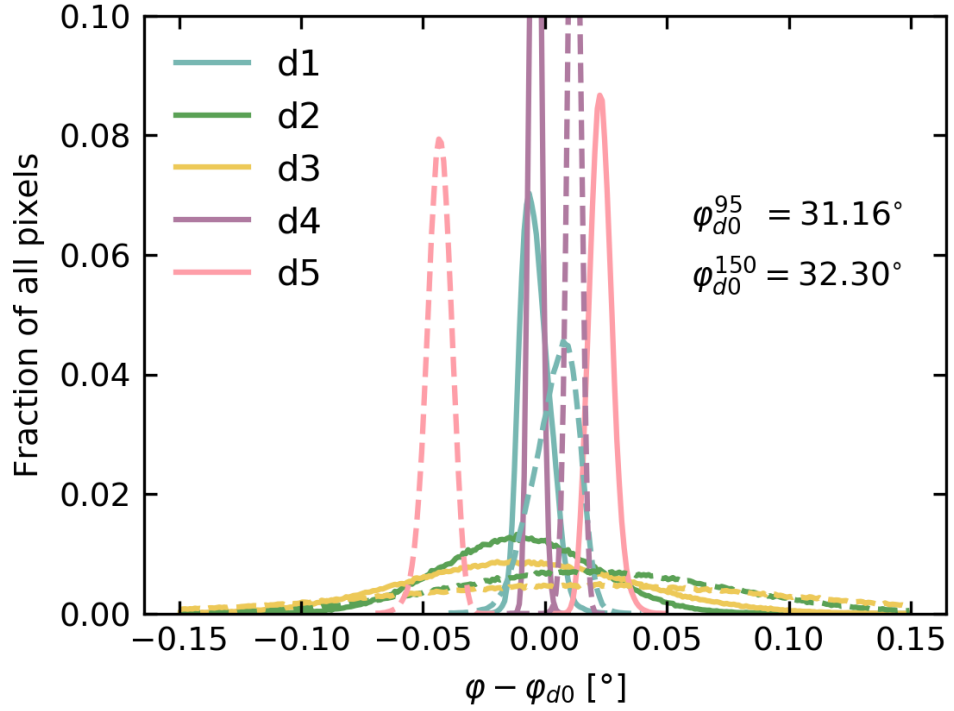


Figure 5.6: Distribution of optimal BR3 HWP rotation angle offset φ in the 95 (solid lines) and 150 GHz (dashed lines) bands for the PySM Galactic dust models based on their per-pixel spectral energy distribution at $N_{\text{side}} = 512$. The distributions are given for the 40 per cent sky mask used in our analysis. The abscissa is expressed as the difference between the rotation angle offset φ and the reference angle φ_{d0} corresponding to a modified blackbody with $T = 20$ K and $\beta = 1.54$ as in Table 5.1. Figure taken from: [51]

a relatively large rotation angle offset. It turns out that the offset angle of the 3-layer model also displays the largest variation with frequency. While the average value of this offset angle can be simply calibrated out, this large variation with frequency poses a difficulty: sky components with different frequency characteristics will require different offset angles after integration over the instrumental frequency band.

We can determine an optimal rotation angle offset for a specific sky component as the HWP rotation angle, α_{\min} , that minimises the difference between the QQ , QU , UQ , UU submatrices of the Mueller matrices of the HWP and the ideal HWP. The α_{\min} angle is found by minimising

$$R(\alpha) = \sum_{i,j \in \{Q,U\}} \left[\sum_{k=1}^{n_\nu} w(\nu_k) M_{\text{HWP},ij}(\nu_k) - D_{ij}(\alpha) \right]^2, \quad (5.60)$$

where $\mathbf{M}_{\text{HWP}}(\nu_k)$ is the same as in Eq. (5.36) with normally incident light and $\mathbf{D}(\alpha)$ is the Mueller matrix of the ideal HWP rotated by an angle α . The quantities ν_k are a set of sub-frequencies within the band, and $w(\nu_k)$ are weights applied to model the SED. Because we work in units of CMB brightness temperature, we use uniform weighting for the CMB. If we assume that Galactic dust follows a modified blackbody distribution with a fixed temperature and spectral index across the sky, the weights can be derived from Eq. (5.59):

$$w(\nu_k) = \left(\sum_{i=1}^{n_\nu} \frac{\nu_i^{\beta+1}}{e^{h\nu_i/k_B T} - 1} \right)^{-1} \frac{\nu_k^{\beta+1}}{e^{h\nu_k/k_B T} - 1}. \quad (5.61)$$

However, note that these assumptions about the dust SED are only valid for the d0 PySM model (with $T = 20$ K and $\beta = 1.54$). The optimal offset angles for the CMB and the above dust weights are given in Table 5.1. The 3-layer configuration shows a significantly different optimal offset angle for the CMB versus dust.

The optimal HWP rotation angle correction will vary across the sky for foregrounds models that include spatial SED variations. We can determine an optimal per-pixel correction for a given foreground component by applying Eq. (5.60) on a pixel-by-pixel basis. In Figure 5.6 we compare the distribution of the optimal HWP rotation offset angles for the d1-d5 PySM dust models to the d0 value given by Eq. (5.61). We only show results for BR3 in Figure 5.6. The BR1 and BR5 configurations have a near-constant rotation angle offset over the range of frequencies that we consider and show no appreciable deviation from an isotropic angle offset. Calculating the distributions in Figure 5.6 requires knowledge on the per-pixel SED weights

$w(\nu_k)$ in Eq. (5.60). Although we lack a closed-form expression for all of the SEDs of our dust models, we can make use of the `PySM` predictions at each subfrequency ν_k to determine the SED weights using

$$w(\hat{\mathbf{n}}, \nu_k) = \left(\sum_{j=1}^{n_\nu} |P(\hat{\mathbf{n}}, \nu_j)| \right)^{-1} |P(\hat{\mathbf{n}}, \nu_k)|, \quad (5.62)$$

where $|P(\hat{\mathbf{n}}, \nu_k)|$ is the amplitude of linear polarisation at subfrequency ν_k in direction $\hat{\mathbf{n}}$.

5.2.3 Analysis Results

To test the capabilities of the updated `beamconv` code, we run a number of simulations that probe the different HWP configurations, sky models and instrumental beams. Each simulation batch is based on seven sub-frequency maps per frequency band that are combined assuming a top-hat passband. Seven sub-frequencies represent the lowest adequate sampling of the frequency variation of the HWP Mueller matrices. The simulated time-ordered data are binned on the sphere using the standard map-making scheme that ignores the instrumental beam and assumes the following data model for each detector:

$$d_t = I(\hat{\mathbf{n}}_t) + Q(\hat{\mathbf{n}}_t) \cos[2(\psi_t + \gamma) + 4(\alpha_t + \varphi)] \\ + U(\hat{\mathbf{n}}_t) \sin[2(\psi_t + \gamma) + 4(\alpha_t + \varphi)] + n_t. \quad (5.63)$$

Here, $\hat{\mathbf{n}}_t$, ψ_t and α_t describe the instrumental pointing and HWP rotation angle at time-sample t while γ and φ describe the detector polarisation angle and HWP rotation angle offset, respectively. The map-maker solves for I , Q and U per pixel, uses uniform weighting of the time-ordered data and does not explicitly use detector pair differencing, see e.g. [52].

For every simulated systematic effect, the same simulation is performed using an ideal HWP ($T = -c = 1$, $\rho = s = 0$ in Eq. (5.6)). With ideal and non-ideal maps in hand, we can calculate difference maps that quantify signal residuals due to HWP-related systematics. The resulting difference maps cover the entire sky, but we use a 40 per cent sky mask (`gal040`) [154] before calculating power spectra using `PolSpice` [160].

5.2.3.1 Calibration

To correct for the non-ideal polarisation efficiency of each HWP model, we calibrate each map on a map obtained by scanning with an ideal HWP. This

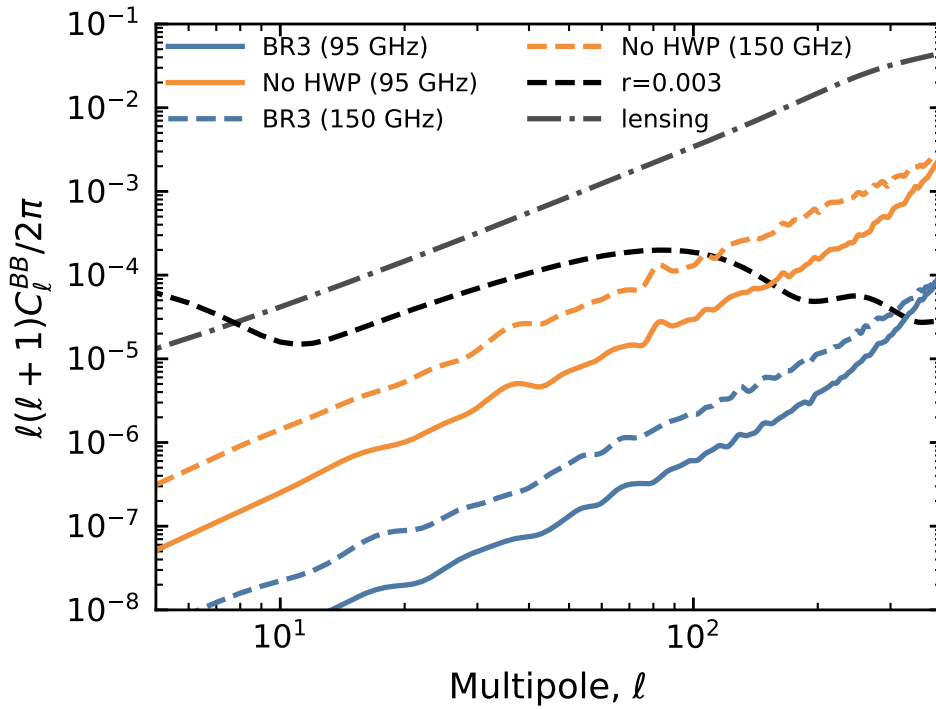


Figure 5.7: Residual B -mode power spectra obtained by observing the CMB with the BR3 configurations presented in Table 5.1 (including the rotation angle offset optimized for the CMB). The beams are gaussian. We omit the BR1 and BR5 HWP configurations since their residuals fall below the limits on the vertical axis. The no-HWP case is also shown (orange curves). Figure taken from: [51]

is performed using the EE angular power spectrum at degree angular scales, $50 \leq \ell \leq 200$. The choice of angular scales roughly coincides with the peak in the expected primordial gravitational wave power spectrum. Note that the calibration procedure could instead be performed using lab measurements or simulated HWP (and other optical component) material properties [161, 44, 133, 39]. The EE calibration approach uses the following factor:

$$g = \frac{1}{151} \sum_{\ell=50}^{200} \frac{C_{\ell}^{EE, \text{ideal}}}{C_{\ell}^{EE}}, \quad (5.64)$$

where the denominator (numerator) is the E -mode power spectrum estimated from the output maps created with a non-ideal (ideal) HWP. The final difference maps are formed by subtracting the calibrated output of the non-ideal simulation from the ideal output simulation :

$$\begin{pmatrix} Q \\ U \end{pmatrix}_{\text{diff}} = \begin{pmatrix} Q \\ U \end{pmatrix}_{\text{ideal}} - \sqrt{g} \begin{pmatrix} Q \\ U \end{pmatrix}. \quad (5.65)$$

The residual B -mode power spectrum caused by the non-ideal HWP is then estimated from these calibrated difference maps.

Finally, we divide out a beam window function to correct the power spectrum for the azimuthally symmetric part of the beam. This allows us to directly compare the residual to theory spectra. For each simulation we use a window function that corresponds to the averaged symmetric part of the input detector beams.

5.2.3.2 Scanning with an ideal gaussian beam

We start by exploring effects that are purely caused by non-ideal HWPs. This is achieved by choosing a co-polar polarised and azimuthally symmetric gaussian beam model, see e.g. [52]. Using this beam, we scan the CMB with the different HWP configurations; we summarize our results in Figure 5.7. We find that only the BR3 configuration shows an appreciable B -mode residual in this case. All three HWP configurations outperform the case without HWP modulation, which shows a relatively large white-noise spectrum caused by small conditioning problems in the map-making solution that are approximately uncorrelated between pixels. It is instructive to determine which terms of the data model in Eqs. (5.52)-(5.54) are causing the BR3 residual. It turns out that this spurious signal is due to $E \rightarrow B$ leakage from the $4\nu_{\alpha}$ terms, i.e. non-idealities in the inner two-by-two part of the HWP Mueller matrix. We have checked that the residual is not caused by $I \rightarrow (Q, U)$ leakage due to the $2\nu_{\alpha}$ term in Eq. (5.52) that couples the linearly polarised

beam to the I sky signal: we obtain virtually identical residuals when the input Stokes I signal is artificially set to zero. The insignificance of the $2\nu_\alpha$ term can be attributed to the smallness of the IQ and IU elements in the HWP Mueller matrices (see Figure 5.5), the lack of a strong atmospheric I signal and, most importantly, the rather good conditioning of the map-making solution. Even without modification, the map-maker corresponding to Eq. (5.63) accurately distinguishes between time-ordered signal that is modulated at $2\nu_\alpha$ and $4\nu_\alpha$.

Using the same setup, we then explore the addition of a foreground component. Specifically, we simulate what happens when a map-maker that uses an HWP angle offset φ (see Eq. (5.63)) that is optimized for the CMB encounters polarised signal from Galactic dust. Figure 5.8 shows the B -mode residual for this hypothetical situation as well as for the opposite case in which the CMB is observed with φ optimized for the SED of dust. We again only show the BR3 HWP configuration. The error in φ causes $E \rightarrow B$ leakage: the residual clearly traces the shape of the input E -mode spectrum. The effect is identical to that of a systematic polarisation angle calibration error. It can be seen that for both cases the residual is larger for 95 GHz than for 150 GHz. This is due to the fact that the optimal BR3 offset angle for dust in the 95 GHz band differs from the optimal angle offset for the CMB by about 0.4° while the difference at 150 GHz is only half that.

From this section it becomes clear that in the presence of multiple sky components a single HWP offset angle φ will not effectively reduce B -mode residual caused by HWP non-idealities. The remaining spurious signal for the BR3 HWP configuration is at a level that would be unacceptable for upcoming B -mode experiments. A correction angle per sky component seems to be necessary. We further explore this point in the next section.

5.2.3.3 Foreground dependence

To investigate how the HWP-induced systematics depend on foreground emission, we scan the different PySM Galactic dust models (d0-d5) with gaussian beams (using the same setup as in the previous section). Data from the *Planck* satellite have provided a wealth of information on Galactic dust emission, but there remains considerable uncertainty regarding both its frequency scaling and spatial variation [162]. It is therefore natural to ask whether this uncertainty is large enough to impact the modelling of HWP systematics. We are particularly interested in checking if spatial variation in the effective spectral index invalidates the use of a single HWP rotation angle offset. Recall that in Figure 5.6 the offset angles for the various PySM dust models are compared to the offset angle determined for the simplest modified black-body

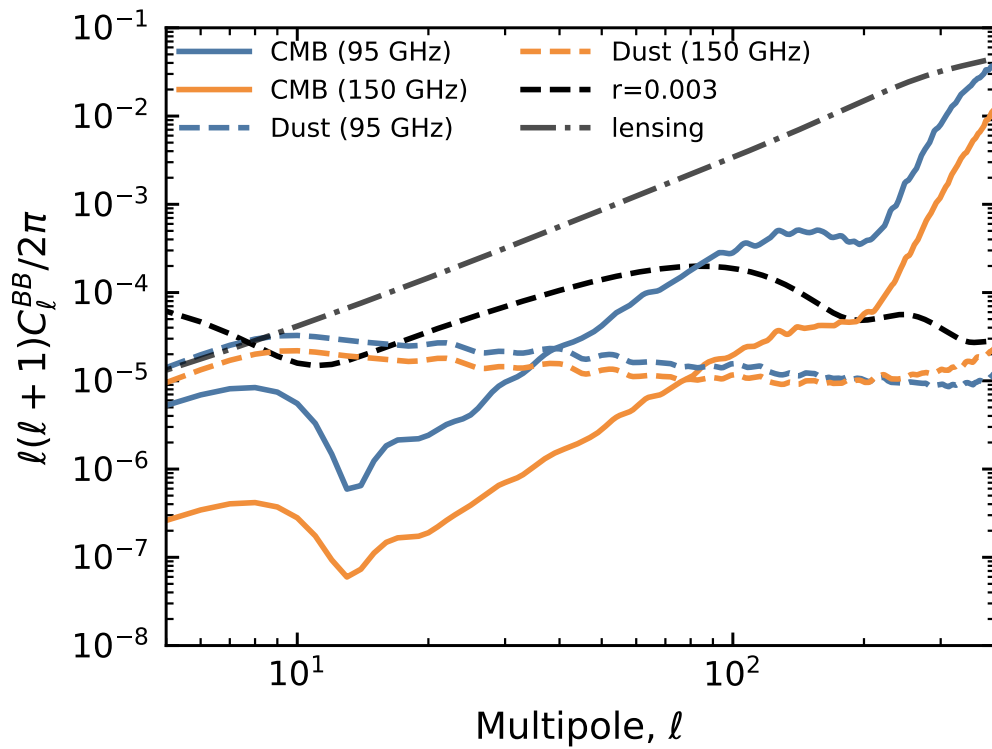


Figure 5.8: Residual B -mode power spectra generated when the CMB is observed using the BR3 HWP with a rotation angle offset optimized for the PySM Galactic dust model d1 (solid curves) and vice versa (dashed curves). Figure taken from: [51]

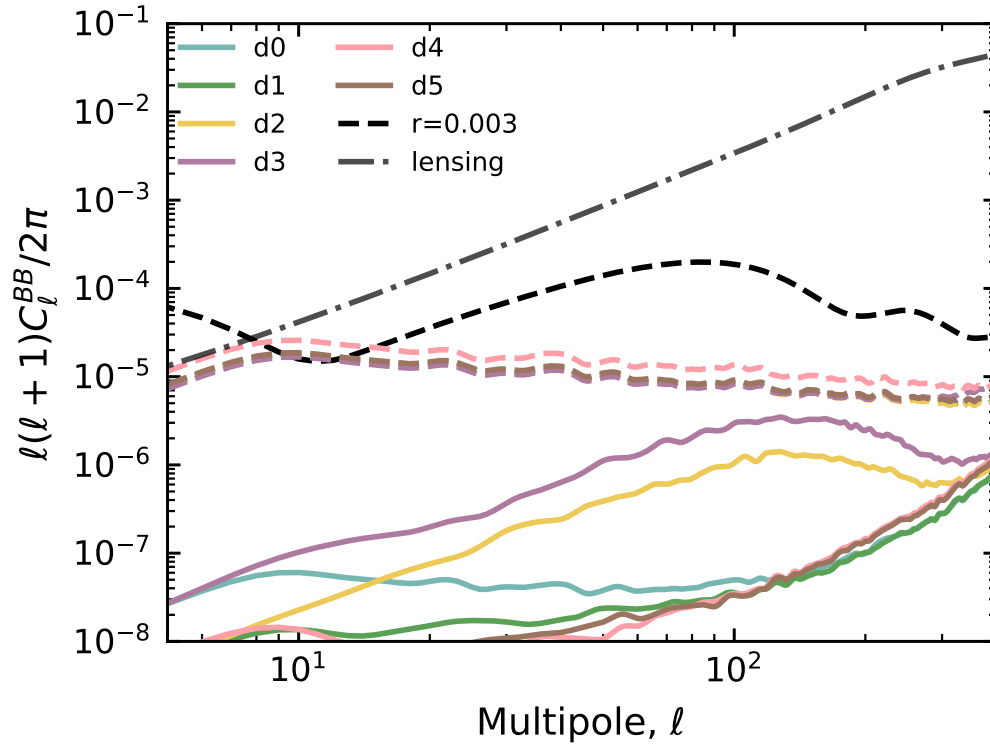


Figure 5.9: Residual B -mode power spectra for the different PySM Galactic dust models in the 150 GHz frequency band scanned using the BR3 HWP configuration. The solid lines use a value of the HWP angle offset that is tailored to each dust model (the median of the distributions shown in Figure 5.6). The dashed colored lines use the median of the rotation angle offsets calculated for the case of a SED given by the combination of CMB and dust. Figure taken from: [51]

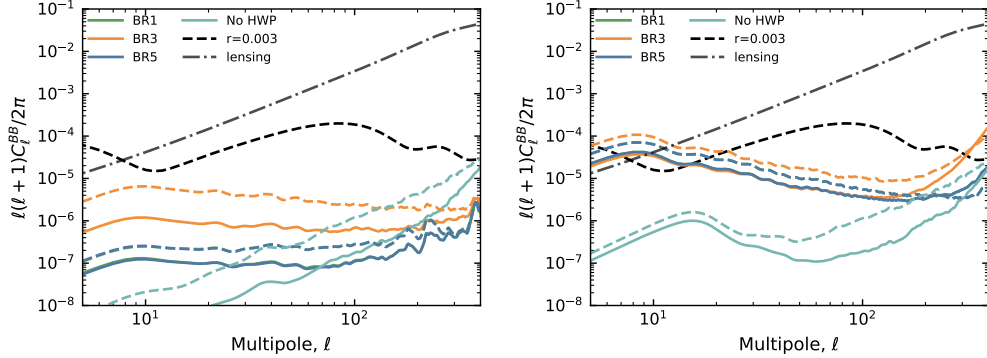


Figure 5.10: Left: Residual B -mode power spectra at 95 GHz (solid lines) and 150 GHz (dashed lines) derived from the band-averaged difference maps obtained by observing the PySM **d1** dust model using all of the HWP configurations presented in Table 5.1 for scans with a physical optics beam truncated at 3° . Right: The same, but when observing the sky with a physical optics beam that extends to 30° and therefore includes a higher contribution from sidelobes (see Figure 5.3). Note that the BR1 curves are almost completely hidden behind the BR5 curves. Figure taken from: [51]

model **d0**. The offset angle distributions of the more involved dust models are both biased from the **d0** value and show a dispersion. The model with the greatest dispersion (**d3**) predicts that a significant number of sky pixels will have an optimal offset angle that is more than 0.1° away from the mean value for the BR3 HWP configuration.

Figure 5.9 shows the effect of ignoring the spatial SED variations of the various PySM models. We scan the dust models using the BR3 HWP and correct for the HWP-induced rotation offset using an angle that corresponds to the mean of each distribution in Figure 5.6. As expected, we see that the **d2** and **d3** models, which both have a relatively large spread in spectral index over the sky, give the largest residuals. However, the amplitude of the spurious signal is still well below any detectable B -mode power spectrum amplitude. It thus seems that any realistic spatial variation in the dust SED can be safely ignored when determining the optimal HWP rotation angle correction for the dust component.

Similar to the previous section, we also explore the case in which a single angle calculated for the SED of the combination of CMB and dust is used to correct for the HWP-induced rotation angle. These residuals are given by the dashed lines in Figure 5.9. We again see that this choice of correction angle would produce significant residual and we see that this results is insensitive to the choice of dust model.

5.2.3.4 Scanning with a non-ideal beam

The simulation framework presented in this section enables studies of the complicated interplay between non-ideal HWPs and non-ideal beams. For this purpose, we can use physical optics (PO) simulations that include extended beam sidelobes with non-negligible cross-polar response; features that could be present in an optical configuration shown in Figure 5.1. The azimuthally averaged beam profiles for the Stokes Q and U beams of a representative beam used in this analysis are shown in Figure 5.3. We study two cases, one where we apodize the beam maps at 3° away from the beam centre (no far-sidelobes) and one where we extend our beam maps out to 30° (with far-sidelobes). In order to focus on effects from the interplay between the beam and the HWP, we calculate difference maps by subtracting a map generated using the same beam model but with an ideal HWP.

Figure 5.10 shows the resultant B -mode residuals; the input sky is the **d1** dust model, the amplitude of the curves should be compared to the solid **d1** curve in Figure 5.9. The effect of the more complex beam model is twofold. The increased solid angle of the beam, i.e. the sidelobe, brings in E -mode dust signal from behind the Galactic mask. Given that we use a correction for the HWP rotation angle offset φ that has been calculated for unmasked pixels, the correction that we apply is not quite appropriate for this extra signal. The result is $E \rightarrow B$ leakage close to the edges of the mask. The second, more significant, effect is due to the cross-polar beam. This is especially obvious in the right panel of Figure 5.10 that was made with the beam model that extends out to 30° and includes a relatively large cross-polar component. The impact of the cross-polar beam can be understood as an ℓ -dependent polarisation rotation that, given the shape of the cross-polar component in Figure 5.3, is larger at lower ℓ . One might wonder why the resulting $E \rightarrow B$ leakage is not cancelled in our setup when we subtract the ideal-HWP maps that were created using the same cross-polar beam. The reason is that the dominant HWP non-ideality couples directly to the cross-polar beam component: the two effects are not additive but multiplicative. This can be seen in the third line of Eq. (5.53): the dominant $4\nu_\alpha$ term of the data model contains a term proportional to $\tilde{U}_b^{(0)} C_{P^*P}$, i.e. the product of the cross-polar beam and the P^*P component of the HWP Mueller matrix in Eq. (5.48). Roughly speaking, the difference maps used to create the spectra in Figure (5.10) are thus proportional to the cross-polar beam times $(1 - C_{P^*P})$, the deviation from the ideal HWP Mueller element. The outcome is $E \rightarrow B$ leakage from the HWP non-ideality that is modulated by the cross-polar beam, resulting in the leaking of a redder version of the original E -mode dust spectrum to the B -mode spectrum, as can be observed in the right panel

of Figure (5.10).

5.2.3.5 Polarisation sensitivity

Given the results that we have discussed so far, there does not seem to be large differences between the BR1 and BR5 performances. Both outperform the BR3 HWP configuration in all the tests we presented and in Fig. 5.10 the BR1 and BR5 curves overlap almost perfectly. However, the calibration process that we described in section 5.2.3.1 masks the fact that the BR5 configuration has much greater polarisation modulation efficiency than the BR1 configuration. For example, in the case when we scan the CMB with a gaussian beam (see section 5.2.3.2, Fig. 5.7), we find that the calibration coefficients based on the E -mode power spectrum are 1.44, 1.10, 1.09, and 1.00 for the BR1, BR3, BR5, and no HWP configurations, respectively. In comparison, the calibration procedure that uses the temperature power spectrum gives 1.04, 1.05, 1.08, and 1.00, for the BR1, BR3, BR5, and no-HWP configurations, respectively. This shows that even though the BR5 configuration has lower optical efficiency because of the larger number of optical elements, and therefore a greater number of both loss and reflection mechanisms, its polarisation modulation efficiency, and therefore sensitivity, is approximately 15 per cent higher than that of the BR1 configuration when integrated over the 95-GHz band.

5.3 Impact of HWPs non-idealities on Cosmic Birefringence

An interesting study that can be performed with the realistic CMB simulations produced with `beamconv`, which do also contain beam convolution and HWP non-idealities, is to investigate instrumental contamination which could bias the measure of the CB effect in view of present and future CMB missions.

In this section we compute a first estimate of the impact of non-ideal HWPs on CB, both isotropic and anisotropic. We want to explore the effects that are purely caused by non-ideal HWPs, therefore we take into account the HWPs residual spectra produced with the setup described in Section 5.2.3.2. In particular we consider a co-polar polarised and azimuthally symmetric gaussian beam model and we observe only the CMB, without foreground, in the 150 GHz band. Figure 5.11 shows the residual BB (upper panel), EE (middle panel) and EB (lower panel) power spectra obtained by observing the CMB with the BR1, BR3 BR5 configurations presented in Table 5.1,

5.3. IMPACT OF HWPS NON-IDEALITIES ON COSMIC BIREFRINGENCE 163

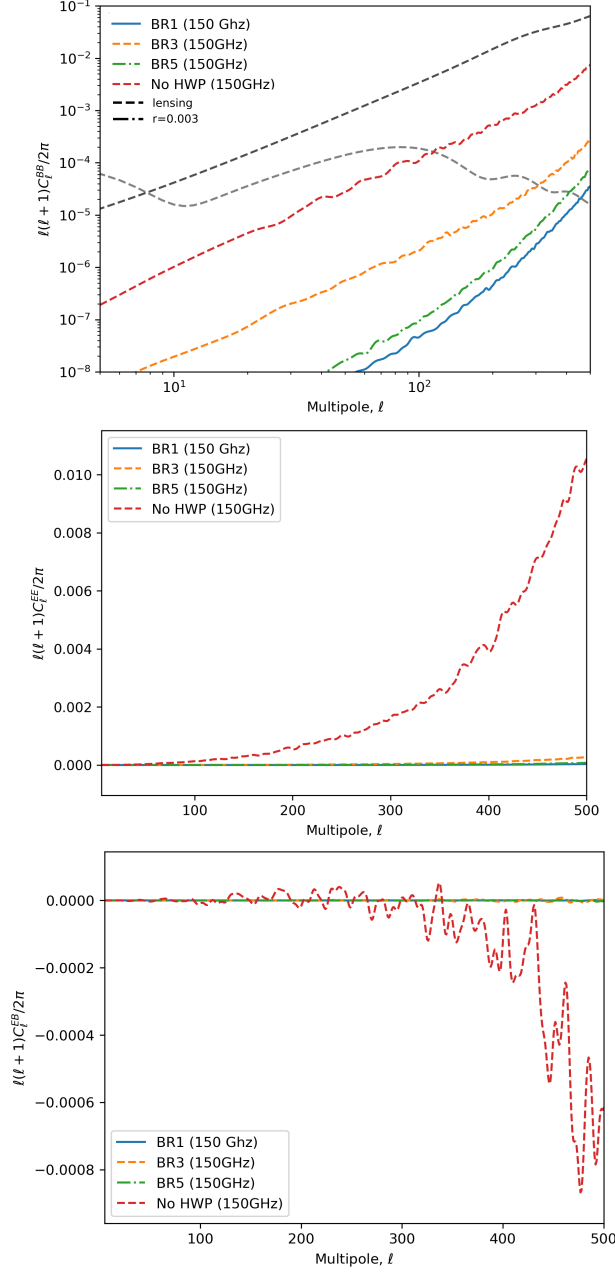


Figure 5.11: Residual BB (upper panel), EE (middle panel) and EB (lower panel) power spectra obtained by observing the CMB with the BR1, BR3 BR5 configurations presented in Table 5.1, including the rotation angle offset optimized for the CMB, and "No-HWP" in the harmonic range $l \in [5 - 500]$. The beams are gaussian.

including the rotation angle offset optimized for the CMB, and "No-HWP" in the harmonic range $\ell \in [5 - 500]$. All three HWP configurations, also for the EE and EB power spectra, outperform the case without HWP modulation, always because the small conditioning problems in the map-making solution, that are approximately uncorrelated between pixels, produce a relatively large white-noise spectrum.

In order to obtain the level of systematics that impact on the birefringence angle and spectra, we apply the statistical estimators for CB effect, described in Chapter 4, taking as an input the sum of the residual power spectra, shown in Figure 5.11, and the Planck 2018 fiducial spectrum [75]. Those level of systematics are then compared with the results obtained employing the same estimators on 1000 only-signal CMB simulated maps with the same characteristics of the input map used in the `beamconv` analysis. In particular the latter are been extracted from Planck 2018 fiducial spectrum [75], considering $N_{side} = 256$, where N_{side} is an `HEALPix`⁷ parameter which is related to the total number of pixels, N_{pix} , through $N_{pix} = 12 N_{side}^2$, and a symmetric gaussian beam with $FWHM = 18.85'$. Finally we mask the simulated maps with the Planck mask `gal040` (which leaves unmasked the 40% of the sky) and extract the power spectra using `NaMaster`⁸[125]. In this way we are able to evaluate an eventual bias in terms of σ_{MC} , i.e. the standard deviation of the Monte Carlo simulations.

5.3.1 Isotropic birefringence

Let us start considering the isotropic birefringence. The map-maker corresponding to Eq. 5.63 shows that the HWP rotation angle α_t , relative at time-sample t , and the HWP rotation angle offset φ enters in the expression of the map-maker in the same way of detector polarisation angle γ , which it is known to be degenerate with the isotropic CB angle α_0 . So we would expect some effects on constraining the CB angle by using HWP.

With the aim of evaluating a possible bias we apply in the harmonic range $\ell \in [5 - 500]$ the D -estimator based on the EB power spectra, i.e. $D_\ell^{EB,obs}$ Eq. (4.60), on the 1000 only-signal CMB simulations and on the residual power spectra plus the Planck fiducial⁹. In the latter case, looking for β that nulls the expectation values of the D -estimators, is equivalent to looking for a systematic angle that has rotated the observed CMB spectra and not for the

⁷<https://healpix.sourceforge.io>

⁸<https://github.com/LSSTDESC/NaMaster>

⁹Note that we consider the sum of the residual spectra with a CMB fiducial spectra, and not only the residual one, because we minimise the D -estimator using the covariance matrix of the MC simulation which does contain the CMB signal

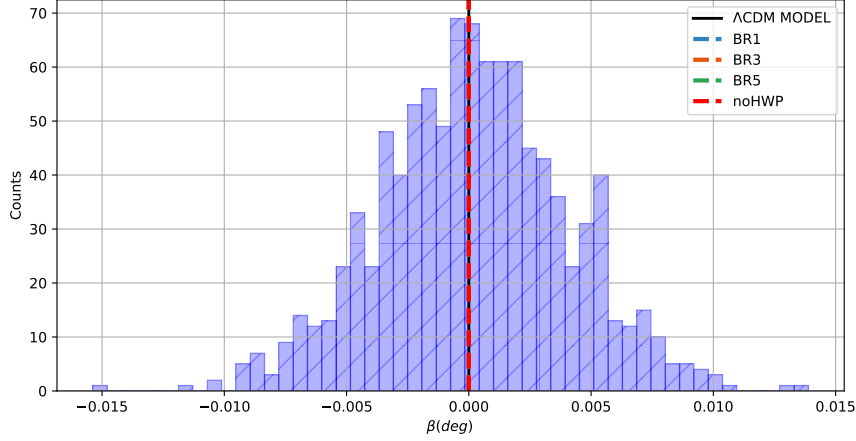


Figure 5.12: The histogram represents the distribution of the β angle, obtained with a standard χ^2 -technique by minimising $D_\ell^{EB,obs}$ Eq. (4.60) when applied on the 1000 only-signal CMB simulations. Vertical dashed lines, virtually indistinguishable from the zero, represent the β angles for the BR1, BR3 BR5 configurations presented in Table 5.1 and "No-HWP"

CB angle that has rotated the primordial CMB spectra. Such an estimate of β is obtained with a standard χ^2 -technique by minimising the quantity in Eq. (4.67), see section 4.2.1. Figure 5.12 shows the distribution of the β for the CMB simulations with the vertical lines representing the ones for the residual spectra. From this figure those lines are virtually indistinguishable from the zero value. Such analysis shows that the impacts of HWP configurations in Table 5.1, when it is considered a symmetric gaussian beam, does not impacts in a relevant way on the constraints for the CB angle. Anyway, it is important to note that here we are ignoring the complicated interplay between non-ideal HWPs and non-ideal beams, which as show in Figure 5.10 produce a significant impact on the the B-mode spectrum.

5.3.2 Anisotropic birefringence

In order to estimate whether the HWP modulation impacts on the evaluation of the anisotropic birefringence, we employ the BB-based linear estimator $\hat{E}_{(BB)}^B$ Eq. 4.175, which turned out to be the one with the best constraining power for estimating the CB spectrum, see section 4.5. We apply such estimator on the 1000 only-signal CMB simulated spectra and on the residual

Estimator	$\ell_{min}^{(CMB)}$	$\ell_{max}^{(CMB)}$	$\Delta\ell^{(CMB)}$	$L_{min}^{(\alpha)}$	$L_{max}^{(\alpha)}$	$\Delta L^{(\alpha)}$
$\hat{E}_{(BB)}^B$	5	500	1	1	400	50

Table 5.2: Setup adopted for the analyses on the 1000 only-signal CMB simulated spectra and on the residual power spectra obtained with BR1, BR3 BR5 configurations presented in Table 5.1 and "No-HWP". C_B^α is evaluated from $L = 1$ to $L = 400$, with a binning of $\Delta L = 50$.

power spectra plus the Planck fiducial¹⁰. In such analysis we consider the CMB harmonic range $\ell \in [2, 500]$ without any binning and the birefringence harmonic range $L \in [1, 400]$ with a binning of $\Delta L = 50$, see table 5.2. Note that when the estimator is applied on the residual spectra what we get is not an estimate of the birefringence spectrum but the level of bias produced by the HWP modulation that impacts on that bin.

Results are shown in Figure 5.13. The upper panel shows the level of bias produced by different HWP modulations for each bin. Error bars represent the standard deviation of the mean obtained applying the estimator on the MC simulations. The lower panel provides the fluctuations from the expected signal (null in this case) of this bias in units of σ_μ . In Figure 5.14 we plot the absolute value of the fluctuation in the lower panel of Figure 5.13 against the $1\sigma_{mu}$ C.L. obtained from the MC simulation as a function of CB multipoles. From Figures 5.13 and 5.14 we can see that all the HWP configurations considered do not produce any relevant bias in terms of CB power spectrum. However, it is important to note that here we have considered the residual spectra obtained neglecting some complications, as for instance the interplay between HWPs, PO beams and foreground components.

5.4 Conclusions

In this chapter we have presented the upgraded version of the beam convolution algorithm `beamcov` capable now to take into accounts also systematic effects produce by non-ideal HWPs [51]. The extended algorithm allows to produce time-domain simulations which include spurious signal from non-ideal HWPs and realistic full-sky beam convolution.

In the first part of the chapter we use `beamconv` code to simulate a CMB satellite experiment that employs a spinning HWP as polarisation modula-

¹⁰We sum a CMB fiducial spectra to the residual ones, because, by construction, the $\hat{E}_{(BB)}^B$ estimator subtracts the contribute due to the Λ CDM model. This subtraction makes the estimator unbiased when applied on CMB spectra but would produce a bias if the estimator would directly employed on the residual spectra.

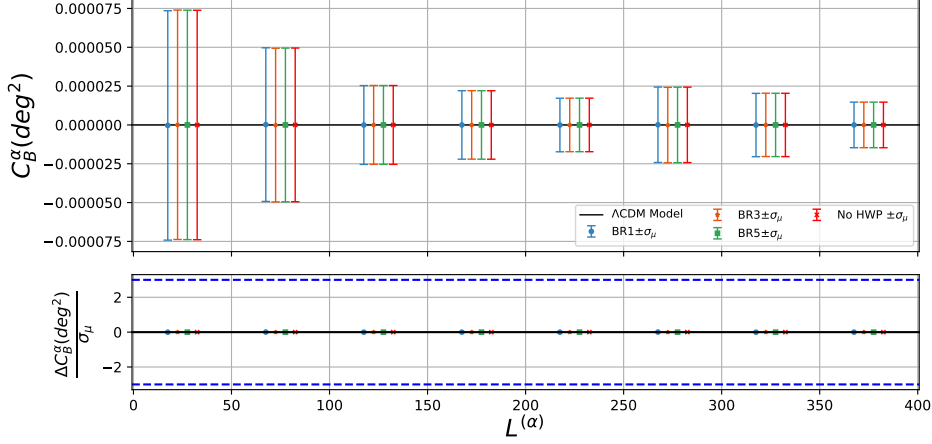


Figure 5.13: $\hat{E}_{(BB)}^B$, Eq. (4.175), employed on the residual power spectra plus Planck CMB fiducial for BR1, BR3, BR5 (table 5.1) and "No-HWP" configurations. For such analysis we consider the configuration in table 5.2. The upper panel shows the level of bias produced by different HWP modulations for each bin. Error bars represent the standard deviation of the mean obtained applying the estimator on 1000 only-signal CMB simulated spectra. The lower panel shows the fluctuations from the expected signal (null in this case) of this bias in units of σ_μ . We can note that all the configurations analysed are virtually indistinguishable from the zero.

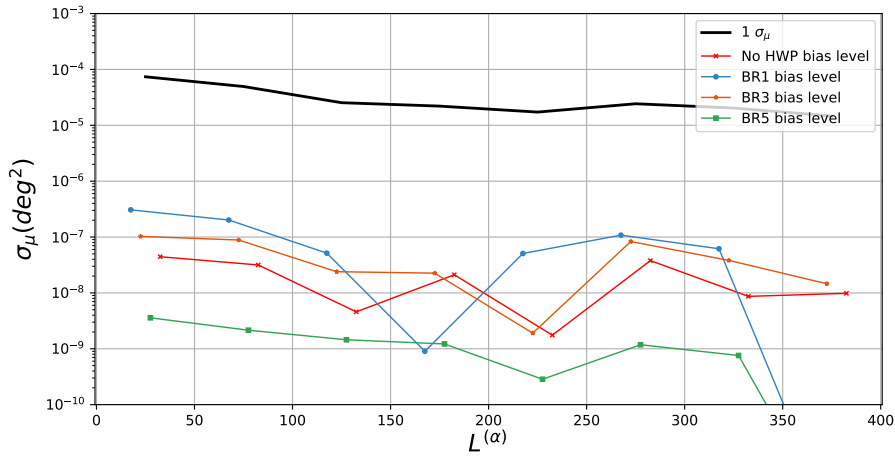


Figure 5.14: This figure shows the absolute value of the fluctuation in the lower panel of Figure 5.13 against the $1\sigma_\mu$ C.L. obtained from the MC simulation as a functions of CB multipoles. We can note that all the configuration analysed produce bias few order of magnitude lower than the level of $1\sigma_\mu$ C.L..

tor. We use those simulations to characterised the HWP systematics coming from three different HWP configurations: a 1-, 3-, and 5-layer model. We find that the choice of HWP configuration could significantly impacts our ability to reconstruct primordial B -mode. In particular, the 3-layer HWP exhibits a significant frequency dependent rotation angle offset, which, if not corrected for, produces E -mode to B -mode leakage which could screen primordial B signal obtained with a tensor-to-scalar ratio r to a level of $r < 0.003$, see Figure 5.8. In order to correct this rotation offset in necessary introduce an HWP angle offset φ , which depends on the SED of the observed signal. Such an angle φ changes significantly between the CMB signal and the Galactic foreground. This could represents a problem for the standard paradigm adopted in CMB data analysis. In fact the map-making process transforms the measured time-ordered data in sky maps losing the information relating to the contribution of each component of the sky to the TOD. As result, it is possible to evaluate a single φ angle, which it represents the combination of the optimal φ of each of the sky components, producing a bias in the sky map. A possible solution could be to introduce φ as a sky component parameter in the parametric component separation algorithms, which start from a prior on the SEDs of the various sky components. Since EB power spectrum for both dust and the CMB has not been observed yet [162], such methods might evaluate the optimal φ angles for each component of the sky comparing the observed value of EB signal with the expected null one. We also investigated if realistic spatial variation in the dust SED could impact on the the BB power spectrum. Considering six different models for galactic dust, we find that the amplitude of the spurious signal is still well below any detectable B -mode power spectrum amplitude, see Figure 5.9. In section 5.2.3.4 we explore the full potential of the upgraded version of `beamconv` code by simulating data using non-ideal HWPs and physical optics beams. We find that the interplay between the cross-polar component of the beam and HWP non-idealities produces significant B -mode residual for all three HWP configurations, see Figure 5.10, exploiting the importance of modelling HWP non-idealities in future CMB experiments.

Finally in section 5.3 we provide preliminary results on the impact of HWP modulation on constraining CB effect. Such an analysis explores the effects purely caused by non-ideal HWPs modulations showing that all the HWP configurations considered do not produce any relevant bias in terms of CB angle and power spectrum, see Figures 5.12 and 5.14. However, it is important to note that here we have considered the residual power spectra got observing the CMB signal considering a symmetric gaussian beam, and without foreground component. Considering the interest in CB effect and the recent push towards HWPs in CMB experiments, an extended analysis, which

takes into account a more complete characterisation of systematic effects, introducing for instance PO beams and foreground, is important and left for future investigations.

Chapter 6

Conclusions and outlook

This Thesis has been focusing on non-standard signatures from CMB polarisation, which might hint at the existence of new phenomena beyond the Λ CDM cosmological model and the standard model of particle physics. CMB polarisation data are important not only because they contribute to provide tighter constraints of cosmological parameters but also because they allow the investigation of physical processes that would be precluded if just the CMB temperature map were considered. We took polarisation data into account in Chapter 3 to assess the statistical significance of the anomalies currently observed only in the CMB temperature map and in Chapter 4 to constrain the Cosmic Birefringence (CB) effect, which is expected in parity-violating extensions of the standard electromagnetism. Unfortunately, the measure of CMB polarisation represents a technological challenge, since the polarised signal is much fainter than the signal in temperature, and to make accurate estimates in polarisation, one has to keep an exquisite control of the systematic effects. In order to study the impact of spurious signals in forthcoming CMB polarisation experiments, in Chapter 5 we have investigated the interplay between half-wave plates (HWP) non-idealities and the beams. In the following we summarise the main outcomes of our analysis.

1. **Lack of power anomaly:** in order to analyse this feature, observed at large angular scale in the CMB anisotropies pattern, we proposed a new one-dimensional estimator which is able to jointly test the lack of power in TT, TE and EE. Considering PLANCK-WMAP 2015 low- ℓ data in the harmonic range $2 \leq \ell \leq 30$ we have assessed that polarisation though subdominant in terms of signal-to-noise ratio with respect to temperature, can play a non-negligible role in the evaluation of compatibility between data and the standard model. Even though the weight of Planck polarisation data is only around 4% of the total

information budget, the probability that a random Λ CDM realisation is statistically accepted decreases by a factor of two when the polarisation is taken into account. In particular, at the maximum multipole considered, we found that the lower-tail-probability (LTP) value shifts downward from 7.22% to 3.68%, which however is still compatible with a statistical fluke. Moreover, we have forecasted that for future experiments, such as the LiteBIRD satellite, the polarisation contribution can increase by a factor of 6. Therefore we guess that E-modes at large angular scale still contain information which might be capable to probe new physics beyond the standard cosmological model. In this analysis we supposed that the statistical noise is the dominant source of uncertainty, leaving for future work the study of the impact of instrumental and astrophysical effects.

2. **Anisotropic CB:** we have developed and performed two complementary methods aiming at evaluating the CB power spectrum. By employing them on Planck 2018 Release (PR3) we provided new constraints on the CB spectrum with Planck data. In the first approach using the "localisation" of the so-called D -estimator, a class of harmonic estimators for the isotropic birefringence, we built maps of the birefringence angle, and evaluated the CB spectrum on angular scales larger than ~ 7 degrees. We found a compatibility with the null effect with a precision better than 0.01 deg^2 . In the second approach we developed a novel class of linear and quadratic harmonic-based estimators which are able to evaluate the power spectrum of CB angle from the EE, BB and EB observed angular power spectra of the CMB anisotropies. By employing these estimators on Planck 2018 Release (PR3), we evaluated the CB spectrum of Planck 2018 data on the harmonic region $L \in [1 - 1000]$ with a binning of $\Delta L = 100$. Considering the most constraining estimator, i.e. the linear one based on the BB power spectrum, we found a compatibility with the null effect better than 0.009 deg^2 for $L > 400$. Even if the level of the uncertainties presented here is worse than previous analyses, we have been able to explore this effect in a much wider harmonic range with Planck data, since the region from $L=700$ to $L=1000$ was not covered before. Anyway, a detailed comparison with other techniques is left for future work. Moreover, we have not investigated how a de-lensing procedure, prior to the application of our estimators, might improve the given constraints, especially for those based on BB. Also this is left for future investigations.
3. **HWPs non-idealities:** we have presented the upgraded version of the

beam convolution algorithm `beamcov` capable now to take into accounts also systematic effects produced by non-ideal HWPs. The extended algorithm allows one to produce time-domain simulations which include spurious signal from non-ideal HWPs and realistic full-sky beam convolution. We have used the `beamconv` code to simulate a CMB satellite experiment that employs a spinning HWP as polarisation modulator. Through those simulations we have characterised the HWP systematics coming from three different HWP configurations: a 1-, 3-, and 5-layer model. Our analysis has shown that certain HWP configurations, depending on the complexity of Galactic foregrounds and the beam models, significantly impact on the B-mode reconstruction fidelity and could limit the capabilities of next-generation CMB experiments. In particular, also considering a symmetric gaussian beam, the 3-layer HWP exhibits a significant frequency dependent rotation angle offset, which, if not corrected for, produces *E*-mode to *B*-mode leakage which could screen primordial B signal obtained with a tensor-to-scalar ratio r to a level of $r < 0.003$. Furthermore, we found that the interplay between the cross-polar component of the beam and HWP non-idealities produces significant *B*-mode residuals for all three HWP configurations, exploiting the importance of modelling HWP non-idealities in future CMB experiments. Finally we provided preliminary results on the impact of HWP modulation on constraining the CB effect. Such an analysis has explored the systematic effects purely caused by non-ideal HWPs modulations showing that all the HWP configurations do not produce any relevant bias in terms of CB angle and power spectrum. However, it is important to note that here we have take into account the residual power spectra got observing the CMB signal considering a symmetric gaussian beam and without foreground components. Considering the interest in CB effect and the recent push towards HWPs in CMB experiments, an extended analysis, which takes into account a more complete characterisation of systematic effects, introducing for instance Physical Optics beams and foreground, is important and left for future investigations.

Acknowledgements

First of all, I would like to thank my supervisor Dr Alessandro Gruppuso for all the teaching and the support he has provided me during my PhD. I would like to thank my co-supervisors Prof Lauro Moscardini and Prof Reno Mandolesi for their guidance and their willingness.

I also thank the CMB group of the University of Ferrara, and in particular Dr Marco Bortolami, for the splendid collaboration born in these years.

I would like to express my gratitude to Dr Jon Gudmundsson for inviting and hosting me at Stockholm University, and for making this trip to Stockholm a wonderful experience together with Dr Adri Duivenvoorden, Dr Alexandre Adler and Dr Nadia Dachlythra.

Further thanks to my PhD fellows, for making this journey fun and unforgettable. To all of you, and to all the other colleagues and collaborators not mentioned here, thank you for sharing your knowledge and experience with me over the years.

Finally I would like to thank my family. In particular my parents, Luciano and Nadia, for always supporting and encouraging me. Special thanks to Valentina who every day gives me her love and makes me happy. Last but not least, thanks to lifelong friends.

I acknowledge the use of the Planck Legacy Archive (PLA). This Thesis is based on observations obtained with Planck (<http://www.esa.int/Planck>), an ESA science mission with instruments and contributions directly funded by ESA Member States, NASA, and Canada. This research was supported by ASI through the Grant 2016-24-H.0 (COSMOS).

Bibliography

- [1] A. A. Penzias, R. W. Wilson, A Measurement of Excess Antenna Temperature at 4080 Mc/s., *The Astrophysical Journal* 142 (1965) 419–421. doi:10.1086/148307.
- [2] P. A. R. Ade, et al., Planck 2013 results. I. Overview of products and scientific results, *Astron. Astrophys.* 571 (2014) A1. arXiv:1303.5062, doi:10.1051/0004-6361/201321529.
- [3] R. Adam, et al., Planck 2015 results. I. Overview of products and scientific results, *Astron. Astrophys.* 594 (2016) A1. arXiv:1502.01582, doi:10.1051/0004-6361/201527101.
- [4] N. Aghanim, et al., Planck 2018 results. I. Overview and the cosmological legacy of Planck, *Astron. Astrophys.* 641 (2020) A1. arXiv:1807.06205, doi:10.1051/0004-6361/201833880.
- [5] Y. Akrami, et al., *Planck* intermediate results. LVII. Joint Planck LFI and HFI data processing, *Astron. Astrophys.* 643 (2020) A42. arXiv:2007.04997, doi:10.1051/0004-6361/202038073.
- [6] G. F. Smoot, COBE observations and results, in: L. Maiani, F. Melchiorri, N. Vittorio (Eds.), *3K cosmology*, Vol. 476 of American Institute of Physics Conference Series, 1999, pp. 1–10. arXiv:astro-ph/9902027, doi:10.1063/1.59326.
- [7] G. F. Smoot, C. L. Bennett, A. Kogut, E. L. Wright, J. Aymon, N. W. Boggess, E. S. Cheng, G. de Amici, S. Gulkis, M. G. Hauser, G. Hinshaw, P. D. Jackson, M. Janssen, E. Kaita, T. Kelsall, P. Keegstra, C. Lineweaver, K. Loewenstein, P. Lubin, J. Mather, S. S. Meyer, S. H. Moseley, T. Murdock, L. Rokke, R. F. Silverberg, L. Tenorio, R. Weiss, D. T. Wilkinson, Structure in the COBE Differential Microwave Radiometer First-Year Maps, *The Astrophysical Journal Letters* 396 (1992) L1. doi:10.1086/186504.

- [8] W. Hu, M. J. White, A CMB polarization primer, *New Astron.* 2 (1997) 323. [arXiv:astro-ph/9706147](#), [doi:10.1016/S1384-1076\(97\)00022-5](#).
- [9] C. Monteserin, R. B. B. Barreiro, P. Vielva, E. Martinez-Gonzalez, M. P. Hobson, A. N. Lasenby, A low CMB variance in the WMAP data, *Mon. Not. Roy. Astron. Soc.* 387 (2008) 209–219. [arXiv:0706.4289](#), [doi:10.1111/j.1365-2966.2008.13149.x](#).
- [10] M. Cruz, P. Vielva, E. Martinez-Gonzalez, R. B. Barreiro, Anomalous variance in the WMAP data and Galactic Foreground residuals, *Mon. Not. Roy. Astron. Soc.* 412 (2011) 2383. [arXiv:1005.1264](#), [doi:10.1111/j.1365-2966.2010.18067.x](#).
- [11] A. Gruppuso, P. Natoli, F. Paci, F. Finelli, D. Molinari, A. De Rosa, N. Mandolesi, Low Variance at large scales of WMAP 9 year data, *JCAP* 07 (2013) 047. [arXiv:1304.5493](#), [doi:10.1088/1475-7516/2013/07/047](#).
- [12] P. A. R. Ade, et al., Planck 2013 results. XXIII. Isotropy and statistics of the CMB, *Astron. Astrophys.* 571 (2014) A23. [arXiv:1303.5083](#), [doi:10.1051/0004-6361/201321534](#).
- [13] P. A. R. Ade, et al., Planck 2015 results. XVI. Isotropy and statistics of the CMB, *Astron. Astrophys.* 594 (2016) A16. [arXiv:1506.07135](#), [doi:10.1051/0004-6361/201526681](#).
- [14] C. R. Contaldi, M. Peloso, L. Kofman, A. D. Linde, Suppressing the lower multipoles in the CMB anisotropies, *JCAP* 07 (2003) 002. [arXiv:astro-ph/0303636](#), [doi:10.1088/1475-7516/2003/07/002](#).
- [15] J. M. Cline, P. Crotty, J. Lesgourgues, Does the small CMB quadrupole moment suggest new physics?, *JCAP* 09 (2003) 010. [arXiv:astro-ph/0304558](#), [doi:10.1088/1475-7516/2003/09/010](#).
- [16] C. Destri, H. J. de Vega, N. G. Sanchez, The pre-inflationary and inflationary fast-roll eras and their signatures in the low CMB multipoles, *Phys. Rev. D* 81 (2010) 063520. [arXiv:0912.2994](#), [doi:10.1103/PhysRevD.81.063520](#).
- [17] M. Cicoli, S. Downes, B. Dutta, Power Suppression at Large Scales in String Inflation, *JCAP* 12 (2013) 007. [arXiv:1309.3412](#), [doi:10.1088/1475-7516/2013/12/007](#).

- [18] E. Dudas, N. Kitazawa, S. P. Patil, A. Sagnotti, CMB Imprints of a Pre-Inflationary Climbing Phase, *JCAP* 05 (2012) 012. [arXiv:1202.6630](#), [doi:10.1088/1475-7516/2012/05/012](#).
- [19] A. Gruppuso, A. Sagnotti, Observational Hints of a Pre-Inflationary Scale?, *Int. J. Mod. Phys. D* 24 (12) (2015) 1544008. [arXiv:1506.08093](#), [doi:10.1142/S0218271815440083](#).
- [20] A. Gruppuso, N. Kitazawa, N. Mandolesi, P. Natoli, A. Sagnotti, Pre-Inflationary Relics in the CMB?, *Phys. Dark Univ.* 11 (2016) 68–73. [arXiv:1508.00411](#), [doi:10.1016/j.dark.2015.12.001](#).
- [21] A. Gruppuso, N. Kitazawa, M. Lattanzi, N. Mandolesi, P. Natoli, A. Sagnotti, The Evens and Odds of CMB Anomalies, *Phys. Dark Univ.* 20 (2018) 49–64. [arXiv:1712.03288](#), [doi:10.1016/j.dark.2018.03.002](#).
- [22] M. Billi, A. Gruppuso, N. Mandolesi, L. Moscardini, P. Natoli, Polarisation as a tracer of CMB anomalies: Planck results and future forecasts, *Phys. Dark Univ.* 26 (2019) 100327. [arXiv:1901.04762](#), [doi:10.1016/j.dark.2019.100327](#).
- [23] S. M. Carroll, G. B. Field, R. Jackiw, Limits on a Lorentz and Parity Violating Modification of Electrodynamics, *Phys. Rev. D* 41 (1990) 1231. [doi:10.1103/PhysRevD.41.1231](#).
- [24] S. M. Carroll, Quintessence and the rest of the world, *Phys. Rev. Lett.* 81 (1998) 3067–3070. [arXiv:astro-ph/9806099](#), [doi:10.1103/PhysRevLett.81.3067](#).
- [25] A. Cimatti, S. di Serego Alighieri, G. B. Field, R. A. E. Fosbury, Stellar and scattered light in a radio galaxy at $z = 2.63$, *Astrophys. J.* 422 (1994) 562. [doi:10.1086/173749](#).
- [26] A. Cimatti, S. d. S. Alighieri, R. A. E. Fosbury, M. Salvati, D. Taylor, Optical polarization in distant radio galaxies, *Monthly Notices of the Royal Astronomical Society* 264 (2) (1993) 421–438. [doi:10.1093/mnras/264.2.421](#).
- [27] J. F. C. Wardle, R. A. Perley, M. H. Cohen, Observational evidence against birefringence over cosmological distances, *Phys. Rev. Lett.* 79 (1997) 1801–1804. [arXiv:astro-ph/9705142](#), [doi:10.1103/PhysRevLett.79.1801](#).

- [28] S. di Serego Alighieri, F. Finelli, M. Galaverni, Limits on Cosmological Birefringence from the UV Polarization of Distant Radio Galaxies, *Astrophys. J.* 715 (2010) 33–38. [arXiv:1003.4823](#), [doi:10.1088/0004-637X/715/1/33](#).
- [29] A. Lue, L.-M. Wang, M. Kamionkowski, Cosmological signature of new parity violating interactions, *Phys. Rev. Lett.* 83 (1999) 1506–1509. [arXiv:astro-ph/9812088](#), [doi:10.1103/PhysRevLett.83.1506](#).
- [30] B. Feng, M. Li, J.-Q. Xia, X. Chen, X. Zhang, Searching for CPT Violation with Cosmic Microwave Background Data from WMAP and BOOMERANG, *Phys. Rev. Lett.* 96 (2006) 221302. [arXiv:astro-ph/0601095](#), [doi:10.1103/PhysRevLett.96.221302](#).
- [31] M. Billi, M. Bortolami, A. Gruppuso, P. Natoli, L. Pagano, New estimators for anisotropic birefringence from CMB observations: the formalism and the application to Planck 2018 data.
- [32] Y. Akrami, et al., Planck 2018 results. IV. Diffuse component separation, *Astron. Astrophys.* 641 (2020) A4. [arXiv:1807.06208](#), [doi:10.1051/0004-6361/201833881](#).
- [33] D. Contreras, P. Boubel, D. Scott, Constraints on direction-dependent cosmic birefringence from Planck polarization data, *JCAP* 12 (2017) 046. [arXiv:1705.06387](#), [doi:10.1088/1475-7516/2017/12/046](#).
- [34] A. Gruppuso, D. Molinari, P. Natoli, L. Pagano, Planck 2018 constraints on anisotropic birefringence and its cross-correlation with CMB anisotropy, *JCAP* 11 (2020) 066. [arXiv:2008.10334](#), [doi:10.1088/1475-7516/2020/11/066](#).
- [35] M. Bortolami, M. Billi, A. Gruppuso, P. Natoli, L. Pagano, Constraints on anisotropic birefringence and its cross-correlation with CMB temperature and polarization fields.
- [36] A. S. Rahlin, et al., Pre-flight integration and characterization of the SPIDER balloon-borne telescope, *Proc. SPIE Int. Soc. Opt. Eng.* 9153 (2014) 915313. [arXiv:1407.2906](#), [doi:10.1117/12.2055683](#).
- [37] B. R. Johnson, et al., MAXIPOL: Cosmic Microwave Background Polarimetry Using a Rotating Half-Wave Plate, *Astrophys. J.* 665 (2007) 42–54. [arXiv:astro-ph/0611394](#), [doi:10.1086/518105](#).

- [38] T. P. Collaboration, J. Errard, P. A. R. Ade, A. Anthony, K. Arnold, F. Aubin, D. Boettger, J. Borrill, C. Cantalupo, M. A. Dobbs, D. Flanagan, A. Ghribi, N. Halverson, M. Hazumi, W. L. Holzapfel, J. Howard, P. Hyland, A. Jaffe, B. Keating, T. Kisner, Z. Kermish, A. T. Lee, E. Linder, M. Lungu, T. Matsumura, N. Miller, X. Meng, M. Myers, H. Nishino, R. O'Brient, D. O'Dea, C. Reichardt, I. Schanning, A. Shimizu, C. Shimmin, M. Shimon, H. Spieler, B. Steinbach, R. Stompor, A. Suzuki, T. Tomaru, H. T. Tran, C. Tucker, E. Quealy, P. L. Richards, O. Zahn, The new generation cmb b-mode polarization experiment: Polarbear (2010). [arXiv:1011.0763](https://arxiv.org/abs/1011.0763).
- [39] C. A. Hill, et al., Design and development of an ambient-temperature continuously-rotating achromatic half-wave plate for CMB polarization modulation on the POLARBEAR-2 experiment, *Proc. SPIE Int. Soc. Opt. Eng.* 9914 (2016) 99142U. [arXiv:1607.07399](https://arxiv.org/abs/1607.07399), [doi:10.1117/12.2232280](https://doi.org/10.1117/12.2232280).
- [40] A. Suzuki, P. A. R. Ade, Y. Akiba, D. Alonso, K. Arnold, J. Aumont, C. Baccigalupi, D. Barron, S. Basak, S. Beckman, et al., The litebird satellite mission: Sub-kelvin instrument, *Journal of Low Temperature Physics* 193 (5-6) (2018) 1048–1056. [doi:10.1007/s10909-018-1947-7](https://doi.org/10.1007/s10909-018-1947-7).
URL <http://dx.doi.org/10.1007/s10909-018-1947-7>
- [41] H. Sugai, P. A. R. Ade, Y. Akiba, D. Alonso, K. Arnold, J. Aumont, J. Austermann, C. Baccigalupi, A. J. Banday, R. Banerji, et al., Updated design of the cmb polarization experiment satellite litebird, *Journal of Low Temperature Physics* 199 (3-4) (2020) 1107–1117. [doi:10.1007/s10909-019-02329-w](https://doi.org/10.1007/s10909-019-02329-w).
URL <http://dx.doi.org/10.1007/s10909-019-02329-w>
- [42] N. Galitzki, T. Baildon, D. Barron, J. Lashner, A. T. Lee, Y. Li, M. Limon, M. Lungu, F. Matsuda, P. D. Mauskopf, et al., The simons observatory: instrument overview, *Millimeter, Submillimeter, and Far-Infrared Detectors and Instrumentation for Astronomy IX* (Jul 2018). [doi:10.1117/12.2312985](https://doi.org/10.1117/12.2312985).
URL <http://dx.doi.org/10.1117/12.2312985>
- [43] M. H. Abitbol, Z. Ahmed, D. Barron, R. B. Thakur, A. N. Bender, B. A. Benson, C. A. Bischoff, S. A. Bryan, J. E. Carlstrom, C. L. Chang, D. T. Chuss, K. T. Crowley, A. Cukierman, T. de Haan, M. Dobbs, T. Essinger-Hileman, J. P. Filippini, K. Ganga, J. E. Gudmundsson,

- N. W. Halverson, S. Hanany, S. W. Henderson, C. A. Hill, S.-P. P. Ho, J. Hubmayr, K. Irwin, O. Jeong, B. R. Johnson, S. A. Kernasovskiy, J. M. Kovac, A. Kusaka, A. T. Lee, S. Maria, P. Mauskopf, J. J. McMahon, L. Moncelsi, A. W. Nadolski, J. M. Nagy, M. D. Niemack, R. C. O'Brient, S. Padin, S. C. Parshley, C. Pryke, N. A. Roe, K. Rostem, J. Ruhl, S. M. Simon, S. T. Staggs, A. Suzuki, E. R. Switzer, O. Tajima, K. L. Thompson, P. Timbie, G. S. Tucker, J. D. Vieira, A. G. Vieregg, B. Westbrook, E. J. Wollack, K. W. Yoon, K. S. Young, E. Y. Young, Cmb-s4 technology book, first edition (2017). [arXiv:1706.02464](https://arxiv.org/abs/1706.02464).
- [44] S. A. Bryan, P. A. R. Ade, M. Amiri, S. Benton, R. Bihary, J. J. Bock, J. R. Bond, J. A. Bonetti, H. C. Chiang, C. R. Contaldi, et al., Modeling and characterization of the spider half-wave plate, Millimeter, Submillimeter, and Far-Infrared Detectors and Instrumentation for Astronomy V (Jul 2010). [doi:10.1117/12.857837](https://doi.org/10.1117/12.857837).
URL <http://dx.doi.org/10.1117/12.857837>
- [45] A. Kusaka, et al., Modulation of cosmic microwave background polarization with a warm rapidly rotating half-wave plate on the Atacama B-Mode Search instrument, *Rev. Sci. Instrum.* 85 (2014) 024501. [arXiv:1310.3711](https://arxiv.org/abs/1310.3711), [doi:10.1063/1.4862058](https://doi.org/10.1063/1.4862058).
- [46] G. Pisano, B. Maffei, M. W. Ng, V. Haynes, M. Brown, F. Noviello, P. de Bernardis, S. Masi, F. Piacentini, L. Pagano, et al., Development of large radii half-wave plates for cmb satellite missions, Millimeter, Submillimeter, and Far-Infrared Detectors and Instrumentation for Astronomy VII (Jul 2014). [doi:10.1117/12.2056380](https://doi.org/10.1117/12.2056380).
URL <http://dx.doi.org/10.1117/12.2056380>
- [47] C. Bao, B. Gold, C. Baccigalupi, J. Didier, S. Hanany, A. Jaffe, B. R. Johnson, S. Leach, T. Matsumura, A. Miller, et al., The impact of the spectral response of an achromatic half-wave plate on the measurement of the cosmic microwave background polarization, *The Astrophysical Journal* 747 (2) (2012) 97. [doi:10.1088/0004-637x/747/2/97](https://doi.org/10.1088/0004-637x/747/2/97).
URL <http://dx.doi.org/10.1088/0004-637x/747/2/97>
- [48] T. Matsumura, Mitigation of the spectral dependent polarization angle response for achromatic half-wave plate (4 2014). [arXiv:1404.5795](https://arxiv.org/abs/1404.5795).
- [49] C. Bao, C. Baccigalupi, B. Gold, S. Hanany, A. Jaffe, R. Stompor, Maximum Likelihood Foreground Cleaning for Cosmic Microwave Background Polarimeters in the Presence of Systematic Effects, *The Astro-*

- physical Journal 819 (1) (2016) 12. doi:10.3847/0004-637X/819/1/12.
- [50] C. Vergès, J. Errard, R. Stompor, Framework for analysis of next generation, polarised CMB data sets in the presence of galactic foregrounds and systematic effects, ArXiv e-prints (Sep. 2020). arXiv:2009.07814.
- [51] A. J. Duivenvoorden, A. E. Adler, M. Billi, N. Dachlythra, J. E. Gudmundsson, Probing frequency-dependent half-wave plate systematics for CMB experiments with full-sky beam convolution simulations, Mon. Not. Roy. Astron. Soc. 502 (3) (2021) 4526–4539. arXiv:2012.10437, doi:10.1093/mnras/stab317.
- [52] A. J. Duivenvoorden, J. E. Gudmundsson, A. S. Rahlin, Full-Sky Beam Convolution for Cosmic Microwave Background Applications, Mon. Not. Roy. Astron. Soc. 486 (4) (2019) 5448–5467. arXiv:1809.05034, doi:10.1093/mnras/stz1143.
- [53] P. Coles, F. Lucchin, Cosmology: The Origin and evolution of cosmic structure, 1995.
- [54] S. Dodelson, Modern Cosmology, Academic Press, Amsterdam, 2003.
- [55] V. Mukhanov, Physical Foundations of Cosmology, Cambridge University Press, Oxford, 2005.
- [56] S. Weinberg, Cosmology, 2008.
- [57] P. Ntelis, et al., Exploring cosmic homogeneity with the BOSS DR12 galaxy sample, JCAP 06 (2017) 019. arXiv:1702.02159, doi:10.1088/1475-7516/2017/06/019.
- [58] N. Suzuki, D. Rubin, C. Lidman, G. Aldering, R. Amanullah, K. Barbary, L. F. Barrientos, J. Botyanszki, M. Brodwin, N. Connolly, K. S. Dawson, A. Dey, M. Doi, M. Donahue, S. Deustua, P. Eisenhardt, E. Ellingson, L. Faccioli, V. Fadeyev, H. K. Fakhouri, A. S. Fruchter, D. G. Gilbank, M. D. Gladders, G. Goldhaber, A. H. Gonzalez, A. Goobar, A. Gude, T. Hattori, H. Hoekstra, E. Hsiao, X. Huang, Y. Ihara, M. J. Jee, D. Johnston, N. Kashikawa, B. Koester, K. Konishi, M. Kowalski, E. V. Linder, L. Lubin, J. Melbourne, J. Meyers, T. Morokuma, F. Munshi, C. Mullis, T. Oda, N. Panagia, S. Perlmutter, M. Postman, T. Pritchard, J. Rhodes, P. Ripoche, P. Rosati, D. J. Schlegel, A. Spadafora, S. A. Stanford, V. Stanishev, D. Stern,

- M. Strovink, N. Takanashi, K. Tokita, M. Wagner, L. Wang, N. Yasuda, H. K. C. Yee, Thehubble space telescopecluster supernova survey. v. improving the dark-energy constraints above $z > 1$ and building an early-type-hosted supernova sample, *The Astrophysical Journal* 746 (1) (2012) 85. doi:10.1088/0004-637x/746/1/85.
URL <http://dx.doi.org/10.1088/0004-637x/746/1/85>
- [59] Planck Collaboration, Planck 2018 results. VI. Cosmological parameters, *Astron. Astrophys.* 641 (2020) A6. arXiv:1807.06209, doi:10.1051/0004-6361/201833910.
- [60] N. Bartolo, E. Komatsu, S. Matarrese, A. Riotto, Non-Gaussianity from inflation: Theory and observations, *Phys. Rept.* 402 (2004) 103–266. arXiv:astro-ph/0406398, doi:10.1016/j.physrep.2004.08.022.
- [61] A. Riotto, Inflation and the theory of cosmological perturbations, *ICTP Lect. Notes Ser.* 14 (2003) 317–413. arXiv:hep-ph/0210162.
- [62] Y. Akrami, et al., Planck 2018 results. X. Constraints on inflation, *Astron. Astrophys.* 641 (2020) A10. arXiv:1807.06211, doi:10.1051/0004-6361/201833887.
- [63] R. H. Dicke, P. J. E. Peebles, P. G. Roll, D. T. Wilkinson, Cosmic Black-Body Radiation., *The Astrophysical Journal* 142 (1965) 414–419. doi:10.1086/148306.
- [64] C. L. Bennett, et al., First year Wilkinson Microwave Anisotropy Probe (WMAP) observations: Preliminary maps and basic results, *Astrophys. J. Suppl.* 148 (2003) 1–27. arXiv:astro-ph/0302207, doi:10.1086/377253.
- [65] J. C. Mather, E. S. Cheng, D. A. Cottingham, J. Eplee, R. E., D. J. Fixsen, T. Hewagama, R. B. Isaacman, K. A. Jensen, S. S. Meyer, P. D. Noerdlinger, S. M. Read, L. P. Rosen, R. A. Shafer, E. L. Wright, C. L. Bennett, N. W. Boggess, M. G. Hauser, T. Kelsall, J. Moseley, S. H., R. F. Silverberg, G. F. Smoot, R. Weiss, D. T. Wilkinson, Measurement of the Cosmic Microwave Background Spectrum by the COBE FIRAS Instrument, *The Astrophysical Journal* 420 (1994) 439. doi:10.1086/173574.
- [66] N. Aghanim, et al., Planck 2018 results. VI. Cosmological parameters, *Astron. Astrophys.* 641 (2020) A6, [Erratum: *Astron. Astrophys.* 652, C4 (2021)]. arXiv:1807.06209, doi:10.1051/0004-6361/201833910.

- [67] Y. Akrami, et al., Planck 2018 results. IX. Constraints on primordial non-Gaussianity, *Astron. Astrophys.* 641 (2020) A9. [arXiv:1905.05697](#), [doi:10.1051/0004-6361/201935891](#).
- [68] R. K. Sachs, A. M. Wolfe, Perturbations of a Cosmological Model and Angular Variations of the Microwave Background, *The Astrophysical Journal* 147 (1967) 73. [doi:10.1086/148982](#).
- [69] R. A. Sunyaev, Y. B. Zeldovich, The Spectrum of Primordial Radiation, its Distortions and their Significance, *Comments on Astrophysics and Space Physics* 2 (1970) 66.
- [70] C. J. Copi, M. O'Dwyer, G. D. Starkman, The ISW effect and the lack of large-angle CMB temperature correlations, *Mon. Not. Roy. Astron. Soc.* 463 (3) (2016) 3305–3310. [arXiv:1605.09732](#), [doi:10.1093/mnras/stw2163](#).
- [71] A. Lewis, The full squeezed CMB bispectrum from inflation, *JCAP* 06 (2012) 023. [arXiv:1204.5018](#), [doi:10.1088/1475-7516/2012/06/023](#).
- [72] S. Chandrasekhar, *Radiative transfer*, 1960.
- [73] M. Zaldarriaga, U. Seljak, An all sky analysis of polarization in the microwave background, *Phys. Rev. D* 55 (1997) 1830–1840. [arXiv:astro-ph/9609170](#), [doi:10.1103/PhysRevD.55.1830](#).
- [74] D. Baumann, M. Jackson, P. Adshead, A. Amblard, A. Ashoorioon, N. Bartolo, R. Bean, M. Beltran, F. Bernardis, S. Bird, X. Chen, D. Chung, L. Colombo, A. Cooray, P. Creminelli, S. Dodelson, J. Dunkley, C. Dvorkin, R. Easther, K. Smith, Probing inflation with cmb polarization, *Vol. 1141*, 2009, pp. 10–120. [doi:10.1063/1.3160885](#).
- [75] Y. Akrami, et al., Planck 2018 results. VII. Isotropy and Statistics of the CMB, *Astron. Astrophys.* 641 (2020) A7. [arXiv:1906.02552](#), [doi:10.1051/0004-6361/201935201](#).
- [76] A. Suzuki, et al., The LiteBIRD Satellite Mission - Sub-Kelvin Instrument, *J. Low Temp. Phys.* 193 (5-6) (2018) 1048–1056. [arXiv:1801.06987](#), [doi:10.1007/s10909-018-1947-7](#).
- [77] D. J. Schwarz, C. J. Copi, D. Huterer, G. D. Starkman, CMB Anomalies after Planck, *Class. Quant. Grav.* 33 (18) (2016) 184001. [arXiv:1510.07929](#), [doi:10.1088/0264-9381/33/18/184001](#).

- [78] K. Land, J. Magueijo, Is the Universe odd?, *Phys. Rev. D* 72 (2005) 101302. [arXiv:astro-ph/0507289](#), [doi:10.1103/PhysRevD.72.101302](#).
- [79] H. K. Eriksen, F. K. Hansen, A. J. Banday, K. M. Gorski, P. B. Lilje, Asymmetries in the Cosmic Microwave Background anisotropy field, *Astrophys. J.* 605 (2004) 14–20, [Erratum: *Astrophys. J.* 609, 1198 (2004)]. [arXiv:astro-ph/0307507](#), [doi:10.1086/382267](#).
- [80] A. de Oliveira-Costa, M. Tegmark, M. Zaldarriaga, A. Hamilton, The Significance of the largest scale CMB fluctuations in WMAP, *Phys. Rev. D* 69 (2004) 063516. [arXiv:astro-ph/0307282](#), [doi:10.1103/PhysRevD.69.063516](#).
- [81] C. Copi, D. Huterer, D. Schwarz, G. Starkman, The Uncorrelated Universe: Statistical Anisotropy and the Vanishing Angular Correlation Function in WMAP Years 1-3, *Phys. Rev. D* 75 (2007) 023507. [arXiv:astro-ph/0605135](#), [doi:10.1103/PhysRevD.75.023507](#).
- [82] P. Vielva, E. Martinez-Gonzalez, R. B. Barreiro, J. L. Sanz, L. Cayon, Detection of non-Gaussianity in the WMAP 1 - year data using spherical wavelets, *Astrophys. J.* 609 (2004) 22–34. [arXiv:astro-ph/0310273](#), [doi:10.1086/421007](#).
- [83] G. Hinshaw, A. J. Banday, C. L. Bennett, K. M. Gorski, A. Kogut, C. H. Lineweaver, G. F. Smoot, E. L. Wright, 2-point correlations in the COBE DMR 4-year anisotropy maps, *Astrophys. J. Lett.* 464 (1996) L25–L28. [arXiv:astro-ph/9601061](#), [doi:10.1086/310076](#).
- [84] A. Gruppuso, Two-point correlation function of Wilkinson Microwave Anisotropy Probe 9-yr data, *Mon. Not. Roy. Astron. Soc.* 437 (3) (2014) 2076–2082. [arXiv:1310.2822](#), [doi:10.1093/mnras/stt1937](#).
- [85] C. Chiocchetta, A. Gruppuso, M. Lattanzi, P. Natoli, L. Pagano, Lack-of-correlation anomaly in CMB large scale polarisation maps, *JCAP* 08 (2021) 015. [arXiv:2012.00024](#), [doi:10.1088/1475-7516/2021/08/015](#).
- [86] A. Yoho, C. J. Copi, G. D. Starkman, A. Kosowsky, Probing Large-Angle Correlations with the Microwave Background Temperature and Lensing Cross Correlation, *Mon. Not. Roy. Astron. Soc.* 442 (3) (2014) 2392–2397. [arXiv:1310.7603](#), [doi:10.1093/mnras/stu942](#).

- [87] D. Contreras, J. P. Zibin, D. Scott, A. J. Banday, K. M. Górski, Testing physical models for dipolar asymmetry with CMB polarization, *Phys. Rev. D* 96 (12) (2017) 123522. [arXiv:1704.03143](#), doi:10.1103/PhysRevD.96.123522.
- [88] C. Gibelyou, D. Huterer, W. Fang, Detectability of large-scale power suppression in the galaxy distribution, *Phys. Rev. D* 82 (2010) 123009. [arXiv:1007.0757](#), doi:10.1103/PhysRevD.82.123009.
- [89] C. J. Copi, D. Huterer, D. J. Schwarz, G. D. Starkman, Large-Angle CMB Suppression and Polarization Predictions, *Mon. Not. Roy. Astron. Soc.* 434 (2013) 3590–3596. [arXiv:1303.4786](#), doi:10.1093/mnras/stt1287.
- [90] M. Lattanzi, C. Burigana, M. Gerbino, A. Gruppuso, N. Mandolesi, P. Natoli, G. Polenta, L. Salvati, T. Trombetti, On the impact of large angle CMB polarization data on cosmological parameters, *JCAP* 02 (2017) 041. [arXiv:1611.01123](#), doi:10.1088/1475-7516/2017/02/041.
- [91] K. M. Górski, E. Hivon, A. J. Banday, B. D. Wandelt, F. K. Hansen, M. Reinecke, M. Bartelman, HEALPix - A Framework for high resolution discretization, and fast analysis of data distributed on the sphere, *Astrophys. J.* 622 (2005) 759–771. [arXiv:astro-ph/0409513](#), doi:10.1086/427976.
- [92] A. Gruppuso, A. De Rosa, P. Cabella, F. Paci, F. Finelli, P. Natoli, G. de Gasperis, N. Mandolesi, New estimates of the CMB angular power spectra from the WMAP 5 yrs low resolution data, *Mon. Not. Roy. Astron. Soc.* 400 (2009) 463–469. [arXiv:0904.0789](#), doi:10.1111/j.1365-2966.2009.15469.x.
- [93] N. Aghanim, et al., Planck 2015 results. XI. CMB power spectra, likelihoods, and robustness of parameters, *Astron. Astrophys.* 594 (2016) A11. [arXiv:1507.02704](#), doi:10.1051/0004-6361/201526926.
- [94] W. H. Press, S. A. Teukolsky, W. T. Vetterling, B. P. Flannery, *Numerical Recipes 3rd Edition: The Art of Scientific Computing*, 3rd Edition, Cambridge University Press, 2007.
URL http://www.amazon.com/Numerical-Recipes-3rd-Scientific-Computing/dp/0521880688/ref=sr_1_1?ie=UTF8&s=books&qid=1280322496&sr=8-1

- [95] T. Matsumura, et al., Mission design of LiteBIRD, *J. Low Temp. Phys.* 176 (2014) 733. [arXiv:1311.2847](#), [doi:10.1007/s10909-013-0996-1](#).
- [96] D. N. Spergel, et al., First year Wilkinson Microwave Anisotropy Probe (WMAP) observations: Determination of cosmological parameters, *Astrophys. J. Suppl.* 148 (2003) 175–194. [arXiv:astro-ph/0302209](#), [doi:10.1086/377226](#).
- [97] C. J. Copi, D. Huterer, D. J. Schwarz, G. D. Starkman, No large-angle correlations on the non-Galactic microwave sky, *Mon. Not. Roy. Astron. Soc.* 399 (2009) 295–303. [arXiv:0808.3767](#), [doi:10.1111/j.1365-2966.2009.15270.x](#).
- [98] J. Williams, A. Rotti, R. Battye, Constraining cosmic polarization rotation and implications for primordial B-modes, *JCAP* 09 (2020) 006. [arXiv:2006.04899](#), [doi:10.1088/1475-7516/2020/09/006](#).
- [99] M. Li, X. Zhang, Cosmological CPT violating effect on CMB polarization, *Phys. Rev. D* 78 (2008) 103516. [arXiv:0810.0403](#), [doi:10.1103/PhysRevD.78.103516](#).
- [100] M. Kamionkowski, How to De-Rotate the Cosmic Microwave Background Polarization, *Phys. Rev. Lett.* 102 (2009) 111302. [arXiv:0810.1286](#), [doi:10.1103/PhysRevLett.102.111302](#).
- [101] N. Aghanim, et al., Planck intermediate results. XLIX. Parity-violation constraints from polarization data, *Astron. Astrophys.* 596 (2016) A110. [arXiv:1605.08633](#), [doi:10.1051/0004-6361/201629018](#).
- [102] Y. Minami, E. Komatsu, New Extraction of the Cosmic Birefringence from the Planck 2018 Polarization Data, *Phys. Rev. Lett.* 125 (22) (2020) 221301. [arXiv:2011.11254](#), [doi:10.1103/PhysRevLett.125.221301](#).
- [103] P. Diego-Palazuelos, et al., Cosmic Birefringence from Planck Data Release 4 (1 2022). [arXiv:2201.07682](#).
- [104] J. R. Eskilt, Frequency-Dependent Constraints on Cosmic Birefringence from the LFI and HFI Planck Data Release 4 (1 2022). [arXiv:2201.13347](#).
- [105] Y. Minami, E. Komatsu, Simultaneous determination of the cosmic birefringence and miscalibrated polarization angles II: Including

- cross frequency spectra, PTEP 2020 (10) (2020) 103E02. arXiv:2006.15982, doi:10.1093/ptep/ptaa130.
- [106] D. Molinari, A. Gruppuso, P. Natoli, Constraints on parity violation from ACTpol and forecasts for forthcoming CMB experiments, Phys. Dark Univ. 14 (2016) 65–72. arXiv:1605.01667, doi:10.1016/j.dark.2016.09.006.
- [107] L. Pogosian, M. Shimon, M. Mewes, B. Keating, Future CMB constraints on cosmic birefringence and implications for fundamental physics, Phys. Rev. D 100 (2) (2019) 023507. arXiv:1904.07855, doi:10.1103/PhysRevD.100.023507.
- [108] V. Gluscevic, M. Kamionkowski, A. Cooray, De-Rotation of the Cosmic Microwave Background Polarization: Full-Sky Formalism, Phys. Rev. D 80 (2009) 023510. arXiv:0905.1687, doi:10.1103/PhysRevD.80.023510.
- [109] W. Hu, T. Okamoto, Mass reconstruction with cmb polarization, Astrophys. J. 574 (2002) 566–574. arXiv:astro-ph/0111606, doi:10.1086/341110.
- [110] H. Zhai, S.-Y. Li, M. Li, X. Zhang, Joint constraint on primordial gravitational waves and polarization rotation angle with current CMB polarization data, Phys. Lett. B 802 (2020) 135240. arXiv:1910.02395, doi:10.1016/j.physletb.2020.135240.
- [111] G.-C. Liu, K.-W. Ng, Axion Dark Matter Induced Cosmic Microwave Background B -modes, Phys. Dark Univ. 16 (2017) 22–25. arXiv:1612.02104, doi:10.1016/j.dark.2017.02.004.
- [112] H.-H. Mei, W.-T. Ni, W.-P. Pan, L. Xu, S. di Serego Alighieri, New constraints on cosmic polarization rotation from the ACTPol cosmic microwave background B-Mode polarization observation and the BICEP2 constraint update, Astrophys. J. 805 (2) (2015) 107. arXiv:1412.8569, doi:10.1088/0004-637X/805/2/107.
- [113] M. Tegmark, How to measure CMB power spectra without losing information, Phys. Rev. D 55 (1997) 5895–5907. arXiv:astro-ph/9611174, doi:10.1103/PhysRevD.55.5895.
- [114] E. Y. S. Wu, et al., Parity Violation Constraints Using Cosmic Microwave Background Polarization Spectra from 2006 and 2007 Observations by the QUaD Polarimeter, Phys. Rev. Lett. 102 (2009) 161302. arXiv:0811.0618, doi:10.1103/PhysRevLett.102.161302.

- [115] A. Gruppuso, G. Maggio, D. Molinari, P. Natoli, A note on the birefringence angle estimation in CMB data analysis, *JCAP* 05 (2016) 020. [arXiv:1604.05202](#), [doi:10.1088/1475-7516/2016/05/020](#).
- [116] D. J. E. Marsh, Axion Cosmology, *Phys. Rept.* 643 (2016) 1–79. [arXiv:1510.07633](#), [doi:10.1016/j.physrep.2016.06.005](#).
- [117] R. R. Caldwell, V. Gluscevic, M. Kamionkowski, Cross-correlation of cosmological birefringence with cmb temperature, *Phys. Rev. D* 84 (2011) 043504. [doi:10.1103/PhysRevD.84.043504](#).
URL <https://link.aps.org/doi/10.1103/PhysRevD.84.043504>
- [118] J. P. Kaufman, B. G. Keating, B. R. Johnson, Precision Tests of Parity Violation over Cosmological Distances, *Mon. Not. Roy. Astron. Soc.* 455 (2) (2016) 1981–1988. [arXiv:1409.8242](#), [doi:10.1093/mnras/stv2348](#).
- [119] T. Namikawa, et al., Atacama Cosmology Telescope: Constraints on cosmic birefringence, *Phys. Rev. D* 101 (8) (2020) 083527. [arXiv:2001.10465](#), [doi:10.1103/PhysRevD.101.083527](#).
- [120] W. Hu, Weak lensing of the CMB: A harmonic approach, *Phys. Rev. D* 62 (2000) 043007. [arXiv:astro-ph/0001303](#), [doi:10.1103/PhysRevD.62.043007](#).
- [121] Y. Minami, H. Ochi, K. Ichiki, N. Katayama, E. Komatsu, T. Matsumura, Simultaneous determination of the cosmic birefringence and miscalibrated polarization angles from CMB experiments, *PTEP* 2019 (8) (2019) 083E02. [arXiv:1904.12440](#), [doi:10.1093/ptep/ptz079](#).
- [122] L. Pagano, J. M. Delouis, S. Mottet, J. L. Puget, L. Vibert, Reionization optical depth determination from Planck HFI data with ten percent accuracy, *Astron. Astrophys.* 635 (2020) A99. [arXiv:1908.09856](#), [doi:10.1051/0004-6361/201936630](#).
- [123] P. A. R. Ade, et al., Planck 2015 results. XII. Full Focal Plane simulations, *Astron. Astrophys.* 594 (2016) A12. [arXiv:1509.06348](#), [doi:10.1051/0004-6361/201527103](#).
- [124] N. Aghanim, et al., Planck 2018 results. III. High Frequency Instrument data processing and frequency maps, *Astron. Astrophys.* 641 (2020) A3. [arXiv:1807.06207](#), [doi:10.1051/0004-6361/201832909](#).

- [125] D. Alonso, J. Sanchez, A. Slosar, A unified pseudo- C_ℓ framework, *Mon. Not. Roy. Astron. Soc.* 484 (3) (2019) 4127–4151. [arXiv:1809.09603](#), [doi:10.1093/mnras/stz093](#).
- [126] E. Hivon, K. M. Gorski, C. B. Netterfield, B. P. Crill, S. Prunet, F. Hansen, Master of the cosmic microwave background anisotropy power spectrum: a fast method for statistical analysis of large and complex cosmic microwave background data sets, *Astrophys. J.* 567 (2002) 2. [arXiv:astro-ph/0105302](#), [doi:10.1086/338126](#).
- [127] M. Kamionkowski, A. Kosowsky, A. Stebbins, A Probe of primordial gravity waves and vorticity, *Phys. Rev. Lett.* 78 (1997) 2058–2061. [arXiv:astro-ph/9609132](#), [doi:10.1103/PhysRevLett.78.2058](#).
- [128] R. Misawa, J.-P. Bernard, P. Ade, Y. Andr  , P. de Bernardis, M. Bouzit, M. Charra, B. Crane, J. P. Dubois, C. Engel, et al., Pilot: a balloon-borne experiment to measure the polarized fir emission of dust grains in the interstellar medium, *Millimeter, Submillimeter, and Far-Infrared Detectors and Instrumentation for Astronomy VII* (Jul 2014). [doi:10.1117/12.2055506](#).
URL <http://dx.doi.org/10.1117/12.2055506>
- [129] N. Galitzki, P. Ade, F. E. Angil  , P. Ashton, J. Austermann, T. Billings, G. Che, H.-M. Cho, K. Davis, M. Devlin, et al., Instrumental performance and results from testing of the blast-tng receiver, submillimeter optics, and mkid detector arrays, *Millimeter, Submillimeter, and Far-Infrared Detectors and Instrumentation for Astronomy VIII* (Jul 2016). [doi:10.1117/12.2231167](#).
URL <http://dx.doi.org/10.1117/12.2231167>
- [130] A. M. Aboobaker, P. Ade, D. Araujo, F. Aubin, C. Baccigalupi, C. Bao, D. Chapman, J. Didier, M. Dobbs, et al., The ebex balloon-borne experiment-optics, receiver, and polarimetry, *The Astrophysical Journal Supplement Series* 239 (1) (2018) 7. [doi:10.3847/1538-4365/aee434](#).
URL <http://dx.doi.org/10.3847/1538-4365/aee434>
- [131] K. Komatsu, T. Matsumura, M. Hazumi, H. Imada, H. Ishino, N. Katayama, Y. Sakurai, H. Sugai, R. Takaku, Prototype design and evaluation of the nine-layer achromatic half-wave plate for the Lite-BIRD low frequency telescope, in: *Millimeter, Submillimeter, and Far-Infrared Detectors and Instrumentation for Astronomy IX*, Vol. 10708

- of Society of Photo-Optical Instrumentation Engineers (SPIE) Conference Series, 2018, p. 1070847. doi:10.1117/12.2312431.
- [132] M. H. Abitbol, et al., The Simons Observatory: gain, bandpass and polarization-angle calibration requirements for B-mode searches, *JCAP* 05 (2021) 032. arXiv:2011.02449, doi:10.1088/1475-7516/2021/05/032.
- [133] S. A. Bryan, T. E. Montroy, J. E. Ruhl, Modeling dielectric half-wave plates for cosmic microwave background polarimetry using a Mueller matrix formalism, *Applied Optics* 49 (2010) 6313. arXiv:1006.3359, doi:10.1364/AO.49.006313.
- [134] T. Essinger-Hileman, Transfer matrix for treating stratified media including birefringent crystals, *Applied Optics* 52 (2013) 212. arXiv:1301.6160, doi:10.1364/AO.52.000212.
- [135] L. Moncelsi, P. A. R. Ade, F. E. Angilè, S. J. Benton, M. J. Devlin, L. M. Fissel, N. N. Gandilo, J. O. Gundersen, T. G. Matthews, C. B. Netterfield, G. Novak, D. Nutter, E. Pascale, F. Poidevin, G. Savini, D. Scott, J. D. Soler, L. D. Spencer, M. D. P. Truch, G. S. Tucker, J. Zhang, Empirical modelling of the BLASTPol achromatic half-wave plate for precision submillimetre polarimetry, *MNRAS* 437 (2014) 2772–2789. arXiv:1208.4866, doi:10.1093/mnras/stt2090.
- [136] M. Salatino, P. de Bernardis, S. Masi, Modeling Transmission and Reflection Mueller Matrices of Dielectric Half-Wave Plates, *Journal of Infrared* 38 (2) (2017) 215–228. doi:10.1007/s10762-016-0320-7.
- [137] M. Salatino, J. Lashner, M. Gerbino, S. M. Simon, J. Didier, A. Ali, P. C. Ashton, S. Bryan, Y. Chinone, K. Coughlin, K. T. Crowley, G. Fabbian, N. Galitzki, N. Goeckner-Wald, J. E. Gudmundsson, C. A. Hill, B. Keating, A. Kusaka, A. T. Lee, J. McMahon, A. D. Miller, G. Puglisi, C. L. Reichardt, G. Teply, Z. Xu, N. Zhu, Studies of systematic uncertainties for Simons Observatory: polarization modulator related effects, in: *Millimeter, Submillimeter, and Far-Infrared Detectors and Instrumentation for Astronomy IX*, Vol. 10708 of Society of Photo-Optical Instrumentation Engineers (SPIE) Conference Series, 2018, p. 1070848. arXiv:1808.07442, doi:10.1117/12.2312993.
- [138] M. Tegmark, How to make maps from CMB data without losing information, *Astrophys. J. Lett.* 480 (1997) L87–L90. arXiv:astro-ph/9611130, doi:10.1086/310631.

- [139] S. Pancharatnam, Achromatic combinations of birefringent plates - part ii. an achromatic quarter-wave plate, *Proceedings of the Indian Academy of Sciences - Section A* 41 (1955) 137–144. doi:10.1007/BF03047098.
- [140] A. M. Title, Improvement of birefringent filters. 2: Achromatic wave-plates, *Applied Optics* 14 (1) (1975) 229–237. doi:10.1364/AO.14.000229.
- [141] W. Hu, M. M. Hedman, M. Zaldarriaga, Benchmark parameters for CMB polarization experiments, *Phys. Rev. D.* 67 (4) (2003) 043004. arXiv:astro-ph/0210096, doi:10.1103/PhysRevD.67.043004.
- [142] M. Kamionkowski, E. D. Kovetz, The Quest for B Modes from Inflationary Gravitational Waves, *Annual Review of Astronomy and Astrophysics* 54 (2016) 227–269. arXiv:1510.06042, doi:10.1146/annurev-astro-081915-023433.
- [143] E. Hivon, S. Mottet, N. Ponthieu, QuickPol: Fast calculation of effective beam matrices for CMB polarization, *Astronomy and Astrophysics* 598 (2017) A25. arXiv:1608.08833, doi:10.1051/0004-6361/201629626.
- [144] A. Challinor, P. Fosalba, D. Mortlock, M. Ashdown, B. Wandelt, K. Górski, All-sky convolution for polarimetry experiments, *Phys. Rev. D* 62 (12) (2000) 123002. arXiv:astro-ph/0008228, doi:10.1103/PhysRevD.62.123002.
- [145] B. D. Wandelt, K. M. Gorski, Fast convolution on the sphere, *Phys. Rev. D* 63 (2001) 123002. arXiv:astro-ph/0008227, doi:10.1103/PhysRevD.63.123002.
- [146] J. N. Goldberg, A. J. Macfarlane, E. T. Newman, F. Rohrlich, E. C. G. Sudarshan, Spin-s Spherical Harmonics and $\bar{\partial}$, *J. Math. Phys.* 8 (1967) 2155–2161. doi:10.1063/1.1705135.
- [147] E. T. Newman, R. Penrose, Note on the Bondi-Metzner-Sachs Group, *J. Math. Phys.* 7 (1966) 863–870. doi:10.1063/1.1931221.
- [148] D. O’Dea, A. Challinor, B. R. Johnson, Systematic errors in cosmic microwave background polarization measurements, *Monthly Notices of the Royal Astronomical Society* 376 (4) (2007) 1767–1783. arXiv:https://academic.oup.com/mnras/article-pdf/376/4/1767/18670856/mnras0376-1767.pdf,

doi:10.1111/j.1365-2966.2007.11558.x.

URL <https://doi.org/10.1111/j.1365-2966.2007.11558.x>

- [149] A. C. Ludwig, The definition of cross polarization., *IEEE Transactions on Antennas and Propagation* 21 (1973) 116–119. doi:10.1109/TAP.1973.1140406.
- [150] K. M. Gorski, presentation at “mitigating systematic errors in space-based cmb polarization measurements”, annapolis, maryland, usa, 28-30 july 2008, (accessed July 9, 2020) (2008).
URL http://cmbpol.uchicago.edu/workshops/systematic2008/depot/krzysztof-gorski_scanning.pdf
- [151] C. G. R. Wallis, M. L. Brown, R. A. Battye, J. Delabrouille, Optimal scan strategies for future CMB satellite experiments, *MNRAS* 466 (2017) 425–442. arXiv:1604.02290, doi:10.1093/mnras/stw2577.
- [152] B. Thorne, J. Dunkley, D. Alonso, S. Naess, The Python Sky Model: software for simulating the Galactic microwave sky, *Mon. Not. Roy. Astron. Soc.* 469 (3) (2017) 2821–2833. arXiv:1608.02841, doi:10.1093/mnras/stx949.
- [153] Planck Collaboration, Planck 2015 results. X. Diffuse component separation: Foreground maps, *Astron. Astrophys.* 594 (2016) A10. arXiv:1502.01588, doi:10.1051/0004-6361/201525967.
- [154] Planck Collaboration, Planck 2015 results. IX. Diffuse component separation: CMB maps, *Astron. Astrophys.* 594 (2016) A9. arXiv:1502.05956, doi:10.1051/0004-6361/201525936.
- [155] A. M. Meisner, D. P. Finkbeiner, Modeling Thermal Dust Emission with Two Components: Application to the Planck High Frequency Instrument Maps, *Astrophysical Journal* 798 (2) (2015) 88. arXiv:1410.7523, doi:10.1088/0004-637X/798/2/88.
- [156] B. Hensley, On the nature of interstellar grains, Ph.D. thesis, Princeton University, chapter 4 in particular (11 2015).
- [157] B. S. Hensley, P. Bull, Mitigating Complex Dust Foregrounds in Future Cosmic Microwave Background Polarization Experiments, *Astrophysical Journal* 853 (2) (2018) 127. arXiv:1709.07897, doi:10.3847/1538-4357/aaa489.

- [158] K. Komatsu, H. Ishino, N. Katayama, T. Matsumura, Y. Sakurai, R. Takaku, Design of the frequency independent optic axis of the Pancharatnam base achromatic half-wave plate for CMB polarization experiment, in: J. Zmuidzinas, J.-R. Gao (Eds.), *Millimeter, Submillimeter, and Far-Infrared Detectors and Instrumentation for Astronomy X*, Vol. 11453, International Society for Optics and Photonics, SPIE, 2020, pp. 750 – 760. doi:10.1117/12.2562092.
URL <https://doi.org/10.1117/12.2562092>
- [159] K. P. Coughlin, J. J. McMahon, K. T. Crowley, B. J. Koopman, K. H. Miller, S. M. Simon, E. J. Wollack, Pushing the Limits of Broadband and High-Frequency Metamaterial Silicon Antireflection Coatings, *Journal of Low Temperature Physics* 193 (5-6) (2018) 876–885. arXiv:1804.08368, doi:10.1007/s10909-018-1955-7.
- [160] A. Challinor, G. Chon, S. Colombi, E. Hivon, S. Prunet, I. Szapudi, PolSpice: Spatially Inhomogeneous Correlation Estimator for Temperature and Polarisation (Sep. 2011). arXiv:1109.005.
- [161] G. Pisano, G. Savini, P. A. R. Ade, V. Haynes, W. K. Gear, Achromatic half-wave plate for submillimeter instruments in cosmic microwave background astronomy: experimental characterization, *Applied Optics* 45 (27) (2006) 6982–6989. doi:10.1364/AO.45.006982.
- [162] Planck Collaboration, Planck 2018 results. XI. Polarized dust foregrounds, *Astron. Astrophys.* 641 (2020) A11. arXiv:1801.04945, doi:10.1051/0004-6361/201832618.

Appendix A

Appendix

A.1 Correlation between CB multipoles for the "vanilla" case

This appendix completes the section 4.5.2.1 reporting the covariance matrix $V^{BB'}$ built from the MC simulation and the $(F^{BB'})^{-1}$ matrix for the $\hat{E}_{(EE)}^B$, $\hat{E}_{(BB)}^B$, $\hat{E}_{(EE^2)}^B$, $\hat{E}_{(BB^2)}^B$ estimators when employed on the "vanilla" MC simulations. Figures A.1,A.2,A.3 show for each estimator the elements of the covariance matrix $V^{BB'}$ (upper panel) and the elements of $(F^{BB'})^{-1}$ (lower panel) encoded with a color-map. From these figures we can note:

- all the covariance matrices $V^{BB'}$ exhibit the same checkerboard pattern of positive and negative elements shown by the one the BB-based estimator discussed in section 4.5.2.1;
- that $(F^{BB'})^{-1}$ matrix maps very well the pattern of the covariance of estimates for each estimator even if the amplitudes of the elements could be different (see Figure 4.12).

In the following we display also the triangular plot for all the estimators when employed on the "vanilla" MC simulations. This type of graph represents a different way to show the correlation between different multipoles of the CB power spectrum. In each sub-panel of the triangular plot it is shown the contour corresponded to 1σ C.L. for at the 2D-distribution of two multipoles: the narrower the region, the greater the correlation between the two considered bins. Given the large number of bins considered, it is difficult to read the numerical values shown in the graphs, however, the main point is the pattern that displays the graph as a whole. In these graphs we re-find the behavior shown by the covariance matrices $V^{BB'}$.

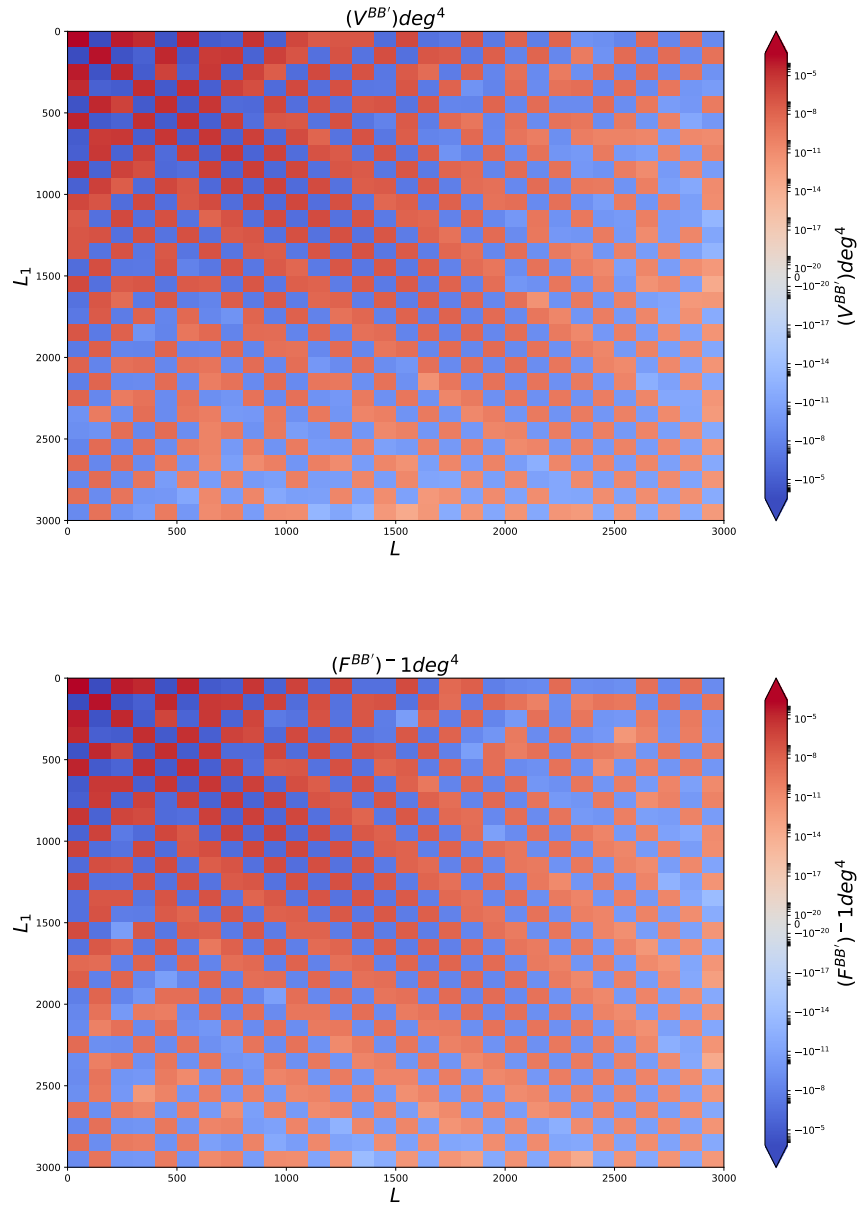


Figure A.1: Upper panel: elements of the covariance matrix built with the simulations for the EE-based linear estimator encoded with a color-map. Lower Panel: elements of the $(F^{BB'})^{-1}$ matrix of the EE-based linear estimator encoded with the same color-map. Note that the $(F^{BB'})^{-1}$ matrix maps very well the pattern of the covariance of estimates even if the amplitudes of the elements could differ (see Figure 4.12).

A.1. CORRELATION BETWEEN CB MULTIPOLES FOR THE "VANILLA" CASE199

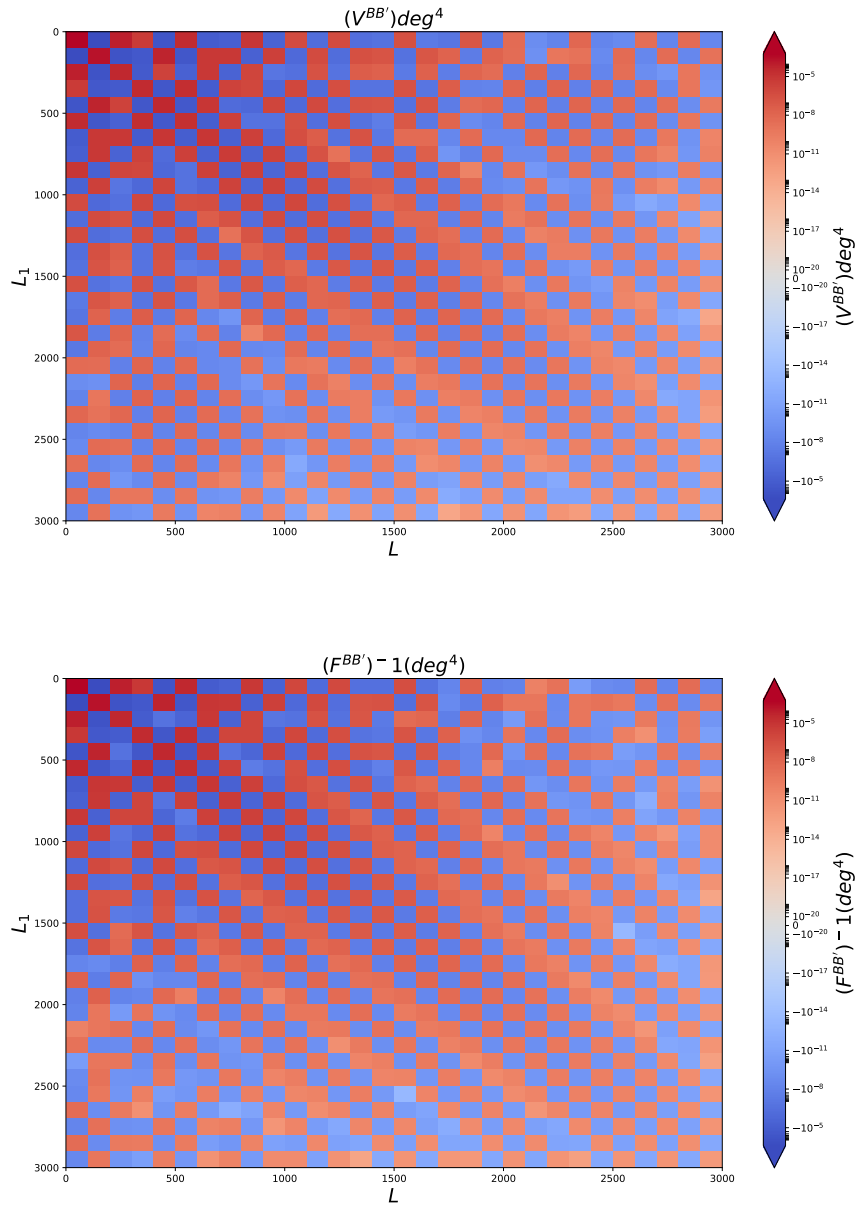


Figure A.2: The same of Figure A.1 but for the EE-based quadratic estimator.

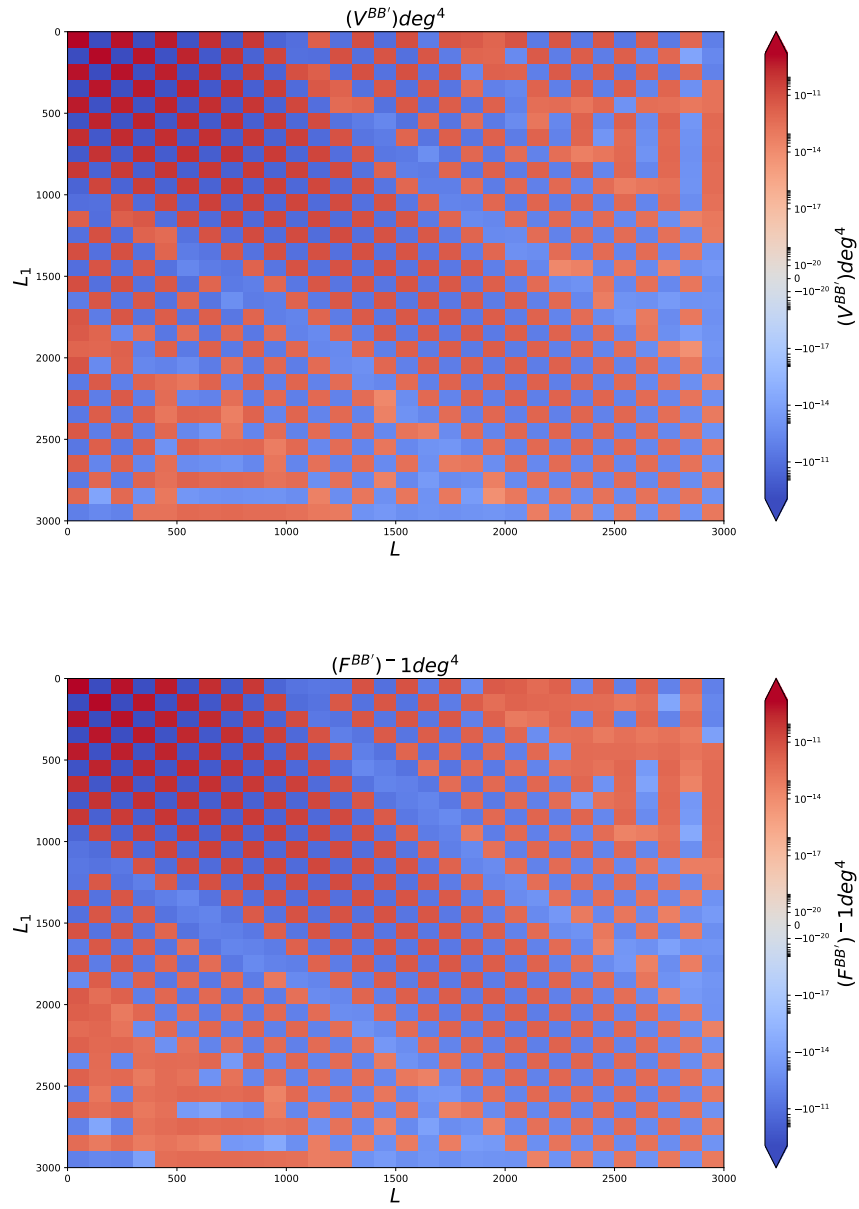


Figure A.3: The same of Figure A.1 but for the BB-based quadratic estimator.

A.1. CORRELATION BETWEEN CB MULTIPOLES FOR THE "VANILLA" CASE201

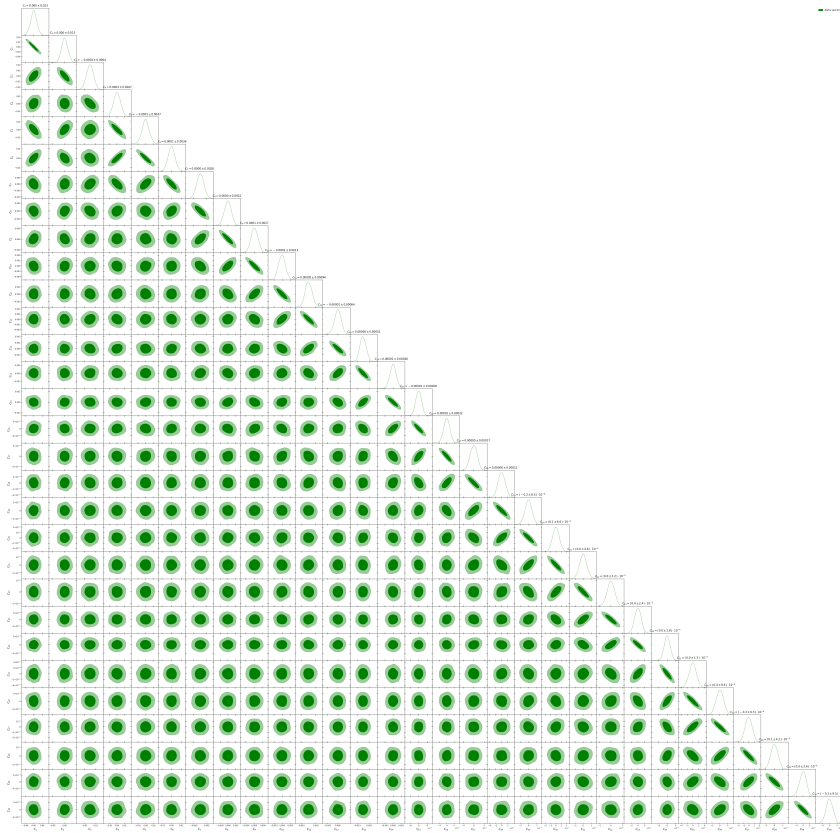


Figure A.4: Triangular Plot for the EE-based linear estimator.

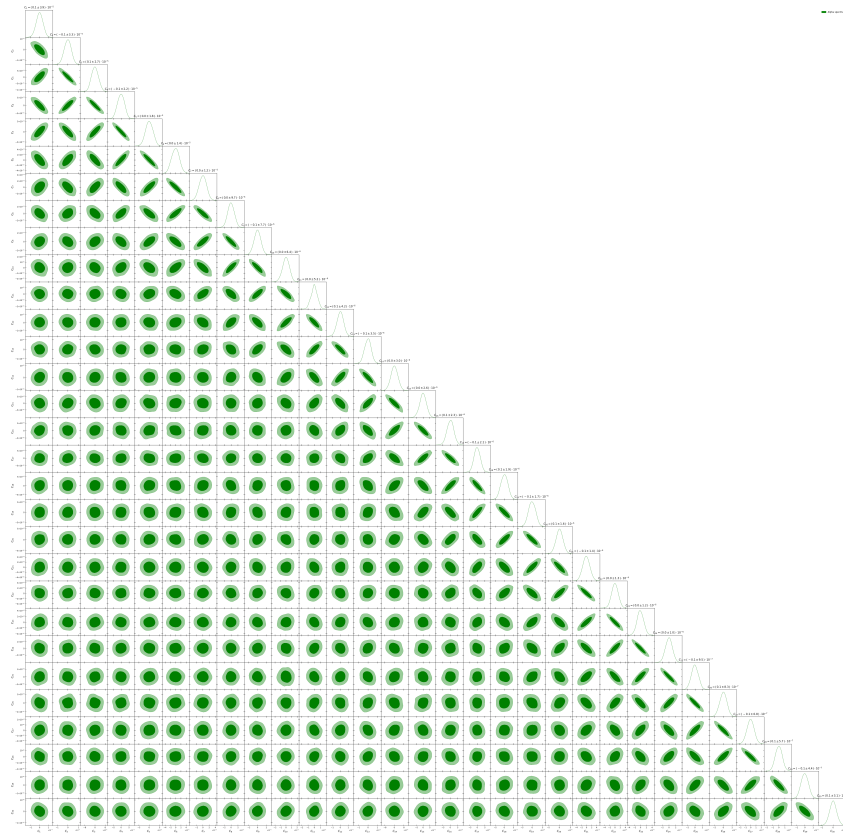


Figure A.5: Triangular Plot for the BB-based linear estimator.

A.1. CORRELATION BETWEEN CB MULTIPOLES FOR THE "VANILLA" CASE203

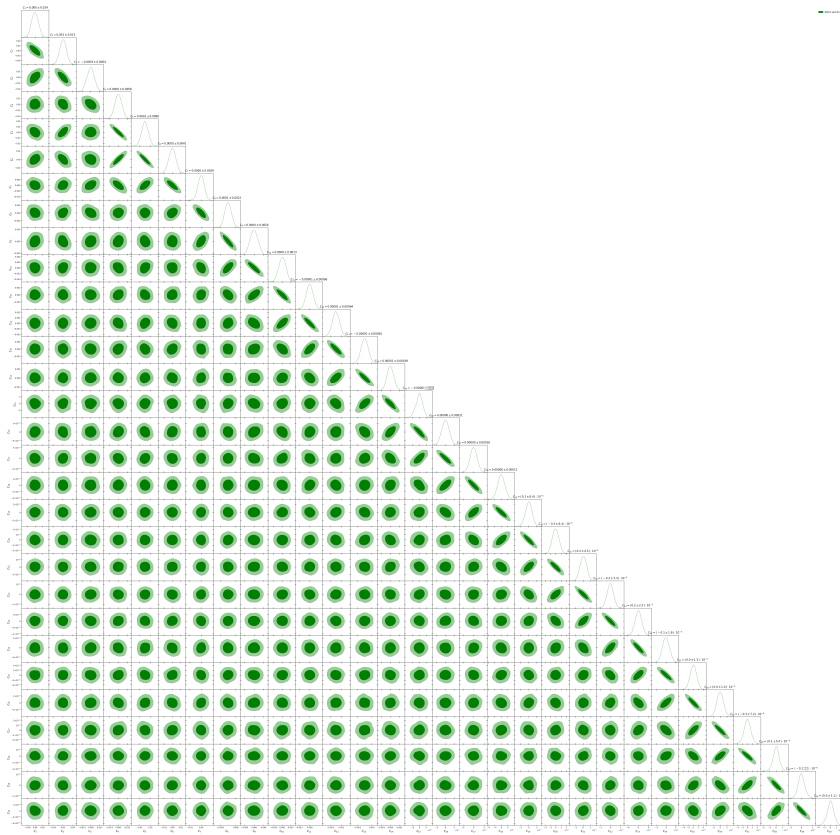


Figure A.6: Triangular Plot for the EE-based quadratic estimator.

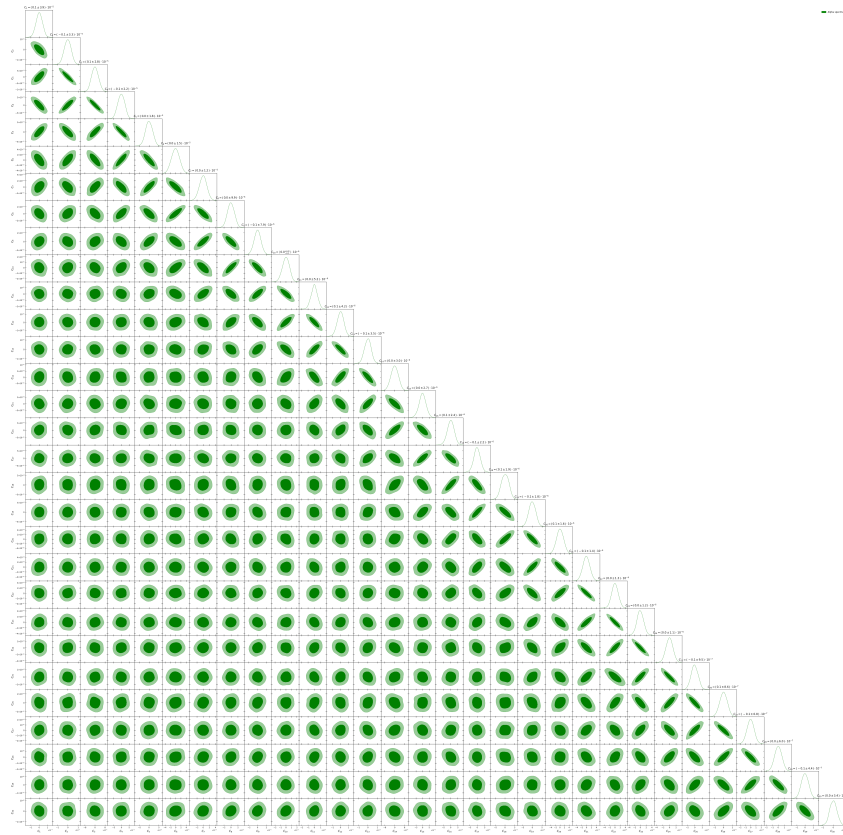


Figure A.7: Triangular Plot for the BB-based quadratic estimator.

A.1. CORRELATION BETWEEN CB MULTIPOLES FOR THE "VANILLA" CASE205

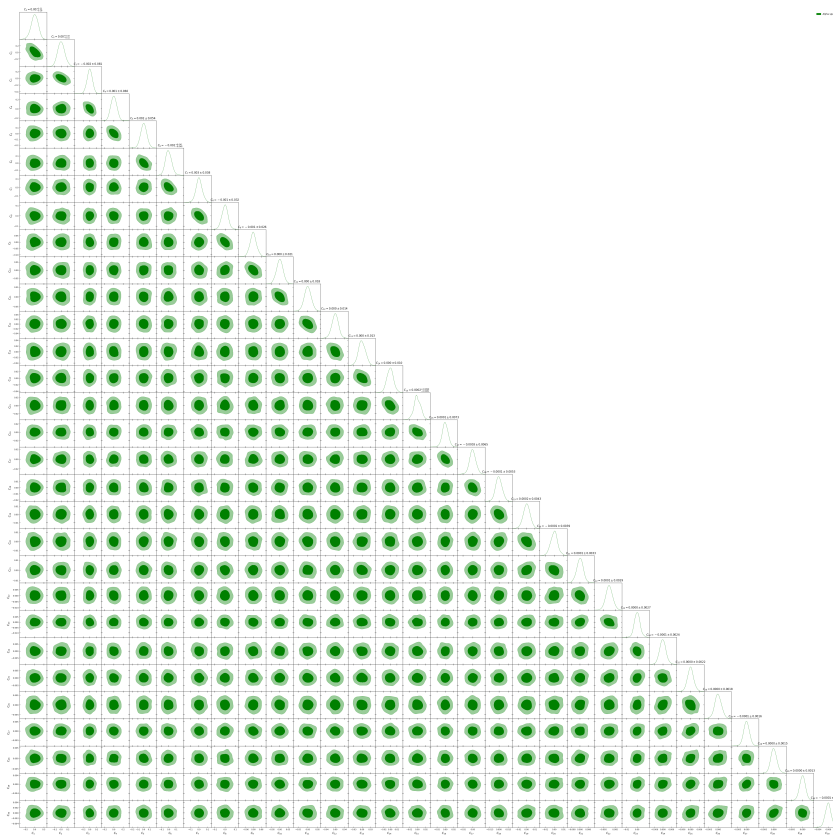


Figure A.8: Triangular Plot for the EB-based quadratic estimator.

A.2 Correlation between F-matrix and uncertainties in the FFP10 analysis

In this appendix we show the ratio between $\sqrt{(F^{BB})^{-1}}$ and the standard deviations for all the C_B^α estimators, see Eqs. 4.174, 4.175, 4.144, 4.151 and 4.157, when employed on the FFP10 simulation adopting the setup reported in table 4.1, section 4.5.3. Figure A.9 displays the results for the linear estimators while figure A.10 the behaviour of the quadratic estimators. From those figures one can note that the uncertainties of all the estimators are underestimated by the inverse of the F matrix, in particular;

- the uncertainties of the EE-based estimators by round 10%;
- the uncertainties of the EB-based estimator by round 10-15%;
- the uncertainties of the BB-based estimators are the ones which are largely underestimated, the linear by a factor 15-25% and the quadratic estimator by 50-60%;

All these estimators, by constructions, are sensible to the covariance matrix¹ used to build their objects. In our analysis, in order to have stable implementations, we employ the `NaMaster`²[125] routine to estimate the gaussian covariance matrix for the CMB band power. However, the latter is an approximation of the covariance matrix of the C_ℓ estimate and that is what it produces such impact on the amplitude of the elements of the F matrix. Anyway, all these results are in reasonable agreement with the behaviour of the estimators characterised with the Vanilla nearly-ideal MC, see section 4.5. The only one that deviates significantly from the expected one is the quadratic BB estimator. As mentioned in the section 4.5.3.3, the treatment of systematics for quadratic estimators is not completely stable yet, and this could impact on the uncertainty of the estimates. In order to better understand this behaviour we need to produce a set of "vanilla" simulation, i.e. without systematic effects, with a Planck-like noise level and repeat the analysis. This analysis is left for future works.

¹To be precise, in the quadratic estimators we use the matrix $D_{\ell\ell'}^{X,Y} = \langle C_\ell^X C_{\ell'}^Y \rangle$, see Eqs. 4.144, 4.151 and 4.157

²<https://github.com/LSSTDESC/NaMaster>

A.2. CORRELATION BETWEEN F -MATRIX AND UNCERTAINTIES IN THE FFP10 ANALYSIS

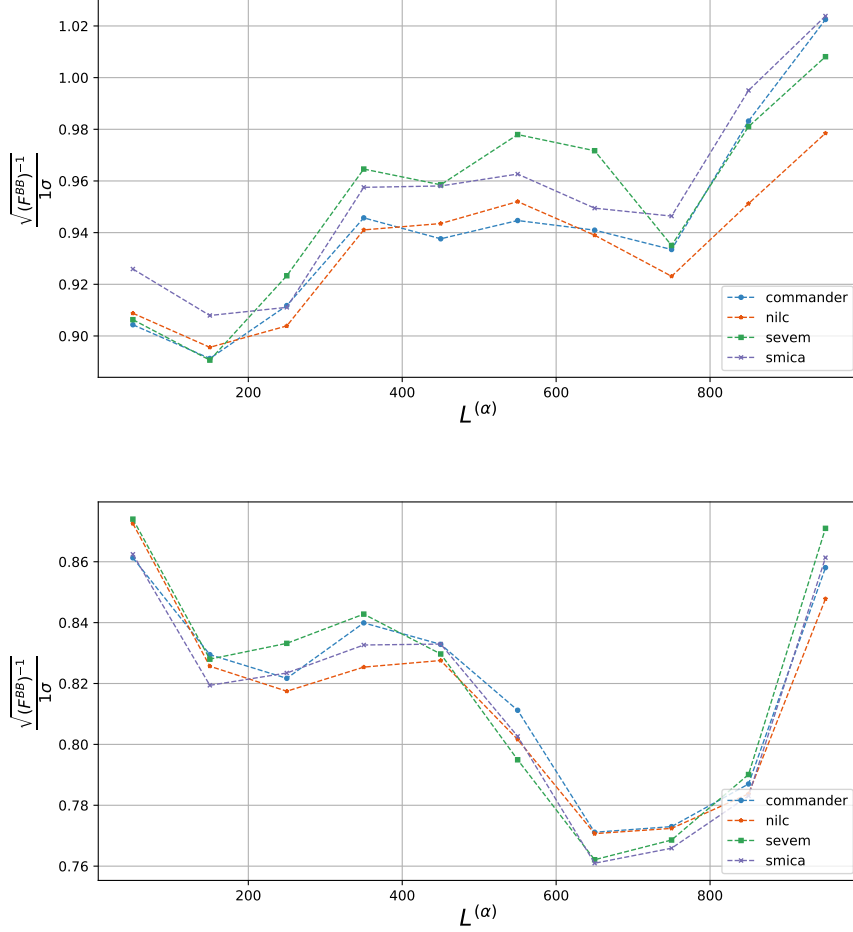


Figure A.9: Ratio between $\sqrt{(F^{BB})^{-1}}$ and the standard deviations for the EE-based (upper panel) and BB-based (lower panel) linear estimators, see Eqs. (4.174) and (4.175), when employed on the FFP10 simulations adopting the setup reported in table 4.1. Note that the uncertainties of the EE- and BB-based estimators are underestimated by the inverse of the F matrix by round 10% and 15-251% respectively.

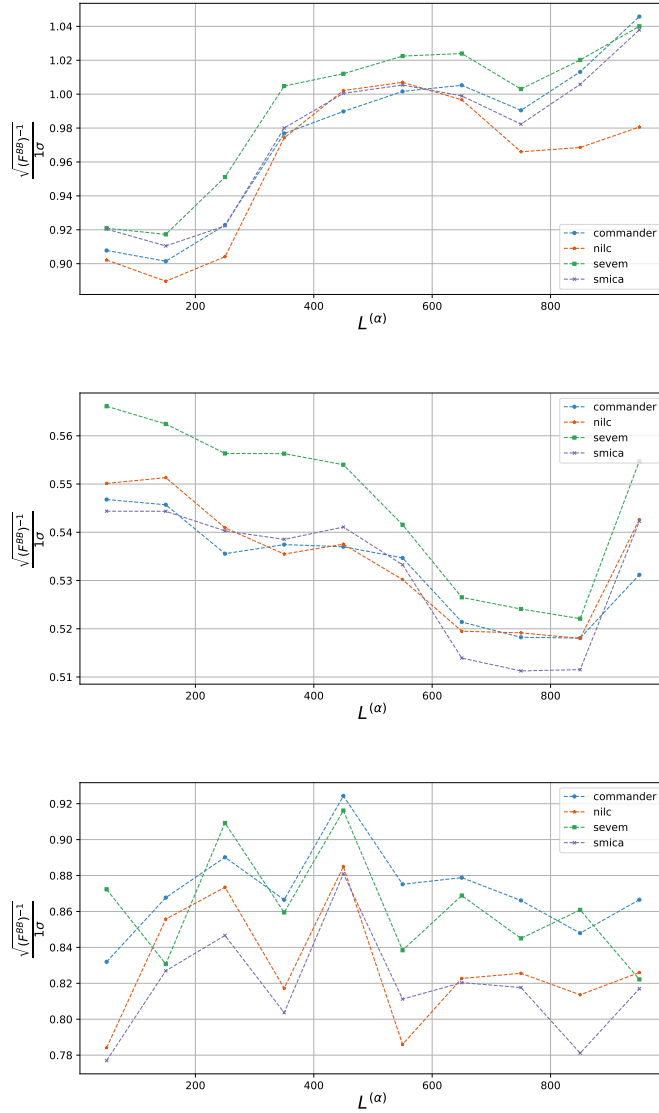


Figure A.10: The same of figure A.9 but for the quadratic estimators, i.e. $\hat{E}_{(EE^2)}^B$ (upper panel), $\hat{E}_{(BB^2)}^B$ (middle panel) and $\hat{E}_{(EB^2)}^B$ (lower panel) when applied on the FFP10 simulations with the setup described in table 4.2.